



**FREEDROP TESTING AND CFD SIMULATION OF ICE MODELS
FROM A CAVITY INTO SUPERSONIC FLOW**

THESIS

Thomas J. Flora, Lieutenant Commander, USN
AFIT/GAE/ENY/12-S15

**DEPARTMENT OF THE AIR FORCE
AIR UNIVERSITY**

AIR FORCE INSTITUTE OF TECHNOLOGY

Wright-Patterson Air Force Base, Ohio

DISTRIBUTION STATEMENT A

APPROVED FOR PUBLIC RELEASE; DISTRIBUTION UNLIMITED.

The views expressed in this document are those of the author and do not reflect the official policy or position of the United States Navy, the United States Air Force, the United States Department of Defense or the United States Government. This material is declared a work of the U.S. Government and is not subject to copyright protection in the United States.

FREEDROP TESTING AND CFD SIMULATION OF ICE MODELS
FROM A CAVITY INTO SUPERSONIC FLOW

THESIS

Presented to the Faculty
Department of Aeronautics and Astronautics
Graduate School of Engineering and Management
Air Force Institute of Technology
Air University
Air Education and Training Command
in Partial Fulfillment of the Requirements for the
Degree of Master of Science in Aeronautical Engineering

Thomas J. Flora, BS Mechanical Engineering
Lieutenant Commander, USN

September 2012

DISTRIBUTION STATEMENT A
APPROVED FOR PUBLIC RELEASE; DISTRIBUTION UNLIMITED.

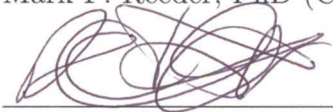
FREEDROP TESTING AND CFD SIMULATION OF ICE MODELS
FROM A CAVITY INTO SUPERSONIC FLOW

Thomas J. Flora, BS Mechanical Engineering
Lieutenant Commander, USN

Approved:

Mark F. Reeder

Mark F. Reeder, PhD (Chairman)



Lt Col Richard E. Huffman, PhD
(Member)

20 August 2012

Date

20 Aug 12

Date

20 August 2012

Date

Capt Chris L. Martin, PhD (Member)

Chris L. Martin

Abstract

Weapon release at supersonic speeds from an internal bay is highly advantageous. For this reason, both experimental and numerical methods were used to investigate store separation from a cavity into Mach 2.94 flow. Both approaches were conducted on an open cavity with a length-to-depth ratio of 4.5. The experimental process used a piezoresistive pressure transducer to capture the time-varying content of the pressure signal, while Schlieren and high speed photography were used to visualize the dynamic response of a store released from the cavity. The computational solution used the OVERFLOW solver with higher-order numerical methods, Chimera grids, and the DDES/SST hybrid turbulence model. Two shapes, a sphere and a Mk-82, scaled to 1:20, were formed using frozen tap water. The sphere model was freedrop tested both experimentally and computationally, while the sub-scale store shaped model was freedrop tested experimentally. In both the experiment and the computation, the total pressure was varied to alter the dynamic response of the model. Computed spectra of pressure signals were in reasonable agreement with those measured experimentally, while the trajectory and dynamics of the CFD sphere release closely matched the experimental freedrop tests. Two sawtooth spoiler devices were tested for effectiveness at high Mach numbers. Pressure measurements showed a detuning of the Rossiter tones at the expense of an increase in the broadband levels. Furthermore, spoiler testing demonstrated the capability to enhance store separation. Mk-82 shapes were also tested, which proved that the experimental process can be used with representations of actual stores. The capability to reduce the test pressure conditions to sub-atmospheric levels allowed sub-scale models to be accurately scaled in mass and moment of inertia using heavy Mach scaling laws.

Acknowledgements

I must begin by expressing a heartfelt *thank you* to my research advisor, Dr. Mark F. Reeder. Whether through a timely *vector* to keep me moving in the right direction or a kind word to strengthen the wind in my sails, his guidance and support proved invaluable to my efforts. I would also like to thank the project sponsors, Rudy Johnson and Jim Grove, from the Air Force Research Labs Air Vehicles directorate, for their financial and professional contributions to the research.

The computational results of this research were made possible by building upon the previous efforts of Dr. Robert Nichols of the University of Alabama-Birmingham. Gratitude is extended to Commander Neal Kraft, Major Andrew Lofthouse, and Captain Chris Martin for guiding this CFD novice to a solution of a complex flow problem. The hardware and software support provided by Dave Doak also greatly aided in obtaining the desired computational results.

I would like to acknowledge the efforts of the laboratory support staff for their critical assistance throughout the experimental phase of my research. Under the adroit leadership of Jay Anderson, John Hixenbaugh, Chris Zickefoose, and Sean Miller each provided much needed support and technical guidance. In addition, a special thanks to Brian Crabtree and Chris Harkless of the AFIT model shop for their dedication to precision and timeliness during the component manufacturing process.

Thomas J. Flora

Table of Contents

	Page
Abstract	iv
Acknowledgements	v
List of Figures	ix
List of Tables	xvii
List of Abbreviations	xviii
I. Introduction	1
1.1 Motivation	2
1.1.1 Advantages of Internal Stores	2
1.1.2 Disadvantages of Internal Stores	2
1.2 Problem Statement	3
1.2.1 CFD Analysis	4
1.2.2 Wind Tunnel Testing	5
1.2.3 Flight Testing	5
1.3 Research Objectives	6
II. Literature Review and Background	8
2.1 Cavity Flow Phenomena	8
2.2 Dynamic Scaling Laws	12
2.3 High Speed Store Separation Testing	19
2.4 Correlating Store Separation Effects to Cavity Dynamics	22
2.5 OVERFLOW Solver	23
2.6 Signal Decomposition and Spectral Analysis	29
III. Methodology	31
3.1 Experimental Setup	31
3.1.1 Supersonic Variable-Density Blowdown Tunnel	31
3.1.2 Test Section and Cavity	33
3.1.3 Release Mechanism	35
3.1.4 Model Fabrication	39
3.1.5 Experimental Components and Data Acquisition	41
3.2 Experimental Methodology	44
3.2.1 Experimental Procedures	44
3.2.2 Test Conditions	45
3.2.3 Sphere Model Freedrop Testing	48
3.3 Computational Methodology	49

	Page
3.3.1 Initial Efforts	50
3.3.2 Final Grid Generation	51
3.3.3 Boundary Conditions	53
3.3.4 Overset Grids and Moving Body Simulation	54
3.3.5 Grid Scaling and Non-Dimensionalization	56
3.3.6 Approach to CFD Solution	58
3.4 Passive Flow Control	65
3.5 Generic Air-to-Ground Store Release	66
IV. Results and Analysis	69
4.1 Cavity Conditions	69
4.1.1 Clean Cavity Flow	69
4.1.2 Captive Sphere Cavity Flow	71
4.2 Sphere Drop Testing	82
4.3 Experimental Investigation of Passive Flow Control	106
4.3.1 Acoustic Effects	106
4.3.2 Store Separation Improvements	109
4.4 Mk-82 Sub-scale Model Testing	123
4.5 Scaling Laws Applied	130
4.5.1 Heavy Mach Scaling	131
4.5.2 Light Mach Scaling	135
V. Conclusions and Recommendations for Future Work	138
5.1 Research Conclusions	138
5.2 Future Opportunities	142
5.2.1 Experimental	142
5.2.2 Computational	143
Appendix A. Post-processing Code .m Files	145
Appendix B. $P_{T,sc}=4$ Psia Sphere Run Images	162
Appendix C. $P_{T,sc}=12$ Psia Sphere Run Images	172
Appendix D. $P_{T,sc}=20$ Psia Sphere Run Images	181
Appendix E. Store Run Images	186
Appendix F. Transducer Calibration Functions	200
Appendix G. Sample OVERFLOW Inputs (Run CT1B.D)	202
Bibliography	206

Vita	209
------------	-----

List of Figures

Figure	Page	
1	Two generations of aircraft representing those which use an internal weapons bay. (a) B-25 Mitchells stand ready to raid the Japanese homeland aboard the USS Hornet while some 60 years later, (b) an F-35 Litening II conducts flight testing over the Chesapeake Bay [1, 2].	1
2	Streamline depictions in open (top) and closed (bottom) cavity flow. Note the highlighted stagnation points.	9
3	Flow mechanism contributing to longitudinal, resonant pressure oscillations.	10
4	Axes and coordinate system.	13
5	HIFEX sled testing demonstrating successful release.	22
6	Illustration highlighting the key components of SVDB wind tunnel.	31
7	Depiction of the (a) prototype and (b) final test section.	33
8	Cutaway along the centerline of the test section top showing cavity dimensions, transducer orifice, and solenoid locations.	34
9	Closeup of cavity with sidewalls removed for clarity. In this experiment, only orifices P_1 , P_2 , and P_6 are fitted with pressure transducers. Cavity nomenclature is also shown.	35
10	Mechanism configured with sphere clamp showing (a) fully closed at release and (b) fully opened, 10 frames later (5 ms). Note the stationary position of the sphere during mechanism release sequence.	37
11	Repeatability checks on sphere ice models. Capture rate = 250 Hz.	37
12	Solenoid and clamp mechanism in the (a) closed position and (b) open position.	39

Figure	Page	
13	Mold fabrication showing (a) silicone material, (b) mixed two-part silicone, (c) store silicone base, (d) and store silicone with male RP store. Also shown (e) is the sphere silicone base filled (f) with the male RP sphere.....	39
14	Model fabrication process.	40
15	Experimental test components.	41
16	Representation of the (a) Schlieren optical and high-speed camera configuration and a close-up (b) of the high-speed digital camera orientation with respect to the defined axis system.	43
17	Solidworks sphere mass and inertial properties.	49
18	First iteration of the domain surrounding the sphere. Interblock boundaries shown in black.	51
19	Computational grid view showing Plate (gray) and Bay (black) domains. Subfigure is an inset of the cavity with front and top Bay surfaces hidden to reveal the contained sphere (yellow) and Yin (blue) grid.	52
20	Boundary condition locations.	54
21	Enlarged view of sphere grid showing (a) Yin (blue) and Yang (red) grids and (b) background Bay grid (black) with a centerline computational surface of the Yen grid, showing grid spacing and I-blank hole cutting.	55
22	OVERFLOW grid coordinate system and bay dimensions (all dimensions are shown in inches).	56
23	Grid relative movement from a 6-DOF run showing translation and rotation of Yin and Yang (sphere) grids.	57
24	Combined residuals (LHS and RHS) for run CT1B.	64
25	Combined residuals (LHS and RHS) for run CT4B_D	65
26	Depiction of (a) long sawtooth spoiler (flow left to right) and (b) streamwise view of short sawtooth spoiler.....	66

Figure	Page
27 Solidworks store mass and inertial properties.....	67
28 Comparison between full-size Mk-82 and 1/20 ice model. All dimensions are in inches.....	68
29 Schlieren imagery of incoming boundary layer at 20 Psia stagnation pressure.....	69
30 Schlieren imagery of shear layer (clean cavity) at (a) 4 Psia and (b) 20 Psia stagnation pressure.	70
31 Image sequence of run 525C1 (4 Psia). Capture rate = 8 kHz, shutter speed = 8 μ s.	72
32 Image sequence of run 525C4 (20 Psia). Capture rate = 8 kHz, shutter speed = 8 μ s.	73
33 SPLs of a clean cavity and a cavity with a captive sphere in the release position.	74
34 SPL (captive sphere in cavity) at 4, 12, and 20 Psia	74
35 Time-varying pressure signal from OVERFLOW at location of P6 showing complete run (a) and a data sample from time 0.05 to 0.054 (b). Subfigure (c) provides a visual comparison with experimental pressures from transducer P6.	76
36 Comparison between OVERFLOW and experimental frequency spectrum.....	77
37 Centerline cut of run CT1B_Long showing vector and y-vorticity contour fields.	78
38 Centerline cut of run CT1B_Long showing non-dimensional pressure and non-dimensional density contour fields.	80
39 Image sequence of run CT1B (4 Psia). Centerline plane density contours show shear layer fluctuations, cavity acoustics, and mass entrainment. $\Delta t=20 \mu$ s. Iteration numbers shown upper right of frame.	81

Figure	Page	
40	Highlight of key features in high-speed and Schlieren camera footage for sphere release.	83
41	Image sequence of run 529S4. 4 Psia stagnation pressure. Frame rate=2kHz, $\Delta t=20\text{ms}$	85
42	Image sequence of run CT1B_D (4 Psia). Centerline plane density contours shown. $\Delta t=20\text{ ms}$	87
43	Image sequence of run 601S2. 12 Psia stagnation pressure. Frame rate=2kHz, $\Delta t=20\text{ms}$	89
44	Image sequence of run CT4B_D (12 Psia). Centerline plane density contours shown. $\Delta t=20\text{ ms}$	91
45	4 Psia numerical and experimental runs ($\Delta t=20\text{ ms}$).	92
46	12 Psia numerical and experimental runs ($\Delta t=20\text{ ms}$).	93
47	Image sequence of run CT2B_D (2 Psia). Centerline plane density contours shown. $\Delta t=20\text{ ms}$	95
48	Image sequence of run CT3B_D (1 Psia). Centerline plane density contours shown. (a) - (e) $\Delta t=20\text{ ms}$	97
49	Plot of sphere non-dimensional X coordinate.	98
50	Plot of sphere non-dimensional Z coordinate.	99
51	Plot of non-dimensional streamwise velocity (u).	100
52	Plot of non-dimensional w velocity.	101
53	Plot of non-dimensional angular velocity of the sphere (Y component).	102
54	Plot of integrated non-dimensional pressure force in X direction.	103
55	Plot of integrated non-dimensional viscous force in X direction (due to shear).	104
56	Plot of non-dimensional moment about Y axis.	105

Figure	Page
57 Image sequence of run 605C5 (12 Psia). Short sawtooth flow control device installed. Capture rate = 8 kHz, shutter speed = 8 μ s.	107
58 4 Psia stagnation pressure frequency response clean, short sawtooth, and long sawtooth.	107
59 12 Psia stagnation pressure frequency response clean, short sawtooth, and long sawtooth.	108
60 20 Psia stagnation pressure frequency response clean, short sawtooth, and long sawtooth.	109
61 Image sequence of run 524S5. Short Sawtooth flow device used. Frame rate=2kHz, Δt =20ms.	111
62 Image sequence of run 604S4. Short sawtooth flow control device used. Frame rate=2kHz, Δt =20ms.	113
63 Image sequence of run 525S4. Short sawtooth flow control device used. Frame rate=2kHz, Δt =20ms.	115
64 Image sequence of run 524S8. Long Sawtooth flow device used. Frame rate=2kHz, Δt =20ms.	117
65 Image sequence of run 604S7. Long sawtooth flow control device used. Frame rate=2kHz, Δt =20ms.	119
66 Image sequence of run 525S7. Long sawtooth flow control device used. Frame rate=2kHz, Δt =20ms.	121
67 4 Psia stagnation pressure (a) clean, (b) SST, and (c) LST.	122
68 12 Psia stagnation pressure (a) clean, (b) SST, and (c) LST.	122
69 Bar graph showing the effectiveness of the tab spoiler device on the separation characteristics of the sphere.	123
70 Image sequence of run 523B1. No flow control device used. $P_{T,sc}$ =4 Psia. Frame rate=2 kHz, Δt =20 ms.	125
71 Image sequence of run 605B4. No flow control device used. $P_{T,sc}$ =4 Psia. Frame rate=2 kHz, Δt =20 ms.	126

Figure	Page
72 Image sequence of run 604B4. Long sawtooth flow control device used. $P_{T,sc}=4$ Psia. Frame rate=2 kHz, $\Delta t=20$ ms.....	128
73 Mk-82 ice model. 4 Psia stagnation pressure (a) clean, (b) SST, and (c) LST.....	129
74 Image sequence of run 524S1. No flow control device used. Frame rate=2kHz, $\Delta t=20$ ms.	163
75 Image sequence of run 524S2. No flow control device used. Frame rate=2kHz, $\Delta t=20$ ms.	164
76 Image sequence of run 529S1. No flow control device used. Frame rate=2kHz, $\Delta t=20$ ms.	165
77 Image sequence of run 529S2. No flow control device used. Frame rate=2kHz, $\Delta t=40$ ms.	166
78 Image sequence of run 529S3. No flow control device used. Frame rate=2kHz, $\Delta t=20$ ms.	167
79 Image sequence of run 529S5. No flow control device used. Frame rate=2kHz, $\Delta t=20$ ms.	168
80 Image sequence of run 524S4. Short Sawtooth flow device used. Frame rate=2kHz, $\Delta t=20$ ms.	169
81 Image sequence of run 524S6. Short Sawtooth flow device used. Frame rate=2kHz, $\Delta t=20$ ms.	170
82 Image sequence of run 524S7. Long Sawtooth flow device used. Frame rate=2kHz, $\Delta t=20$ ms.	171
83 Image sequence of run 601S2. No flow control device used. Frame rate=2kHz, $\Delta t=20$ ms.	173
84 Image sequence of run 601S3. No flow control device used. Frame rate=2kHz, $\Delta t=20$ ms.	174
85 Image sequence of run 604S1. No flow control device used. Frame rate=2kHz, $\Delta t=40$ ms.	175
86 Image sequence of run 604S2. No flow control device used. Frame rate=2kHz, $\Delta t=20$ ms.	176

Figure	Page
87 Image sequence of run 604S3. Short sawtooth flow control device used. Frame rate=2kHz, Δt =20ms.	177
88 Image sequence of run 604S5. Short sawtooth flow control device used. Frame rate=2kHz, Δt =20ms.	178
89 Image sequence of run 604S6. Long sawtooth flow control device used. Frame rate=2kHz, Δt =20ms.	179
90 Image sequence of run 604S8. Long sawtooth flow control device used. Frame rate=2kHz, Δt =20ms.	180
91 Image sequence of run 525S1. No flow control device used. Frame rate=2kHz, Δt =60ms.	182
92 Image sequence of run 525S2. No flow control device used. Frame rate=2kHz, Δt =20ms.	183
93 Image sequence of run 525S5. Short sawtooth flow control device used. Frame rate=2kHz, Δt =20ms.	184
94 Image sequence of run 525S6. Short sawtooth flow control device used. Frame rate=2kHz, Δt =20ms.	185
95 Image sequence of run 605B5. No flow control device used. $P_{T,sc}$ =4 Psia. Frame rate=2 kHz, Δt =20 ms.	187
96 Image sequence of run 605B6. No flow control device used. $P_{T,sc}$ =4 Psia. Frame rate=2 kHz, Δt =20 ms.	188
97 Image sequence of run 605B10. Short sawtooth flow control device used. $P_{T,sc}$ =4 Psia. Frame rate=2 kHz, Δt =20 ms.	189
98 Image sequence of run 605B12. Short sawtooth flow control device used. $P_{T,sc}$ =4 Psia. Frame rate=2 kHz, Δt =20 ms.	190
99 Image sequence of run 605B13. Short sawtooth flow control device used. $P_{T,sc}$ =4 Psia. Frame rate=2 kHz, Δt =20 ms.	191

Figure	Page
100 Image sequence of run 605B1. Long sawtooth flow control device used. $P_{T,sc}=4$ Psia. Frame rate=2 kHz, $\Delta t=20$ ms.....	192
101 Image sequence of run 605B2. Long sawtooth flow control device used. $P_{T,sc}=4$ Psia. Frame rate=2 kHz, $\Delta t=20$ ms.....	193
102 Image sequence of run 601B1. No flow control device used. $P_{T,sc}=12$ Psia. Frame rate=2 kHz, $\Delta t=20$ ms.	194
103 Image sequence of run 604B1. Short sawtooth flow control device used. $P_{T,sc}=12$ Psia. Frame rate=2 kHz, $\Delta t=20$ ms.....	195
104 Image sequence of run 604B2. Short sawtooth flow control device used. $P_{T,sc}=12$ Psia. Frame rate=2 kHz, $\Delta t=20$ ms.....	196
105 Image sequence of run 604B3. Short sawtooth flow control device used. $P_{T,sc}=12$ Psia. Frame rate=2 kHz, $\Delta t=20$ ms.....	197
106 Image sequence of run 525B1. No flow control device used. $P_{T,sc}=20$ Psia. Frame rate=2 kHz, $\Delta t=20$ ms.	198
107 Image sequence of run 525B2. Long sawtooth flow control device used. $P_{T,sc}=20$ Psia. Frame rate=2 kHz, $\Delta t=20$ ms.....	199
108 Transducer calibration functions for cavity and stagnation chamber dynamic pressure transducers.	201

List of Tables

Table	Page	
1	Measured total test conditions and converted values.	46
2	Calculated test freestream conditions	47
3	Test freestream conditions (cont.) and Reynolds numbers.	48
4	Computational domain information.	53
5	Dimensional CFD flow parameters.	58
6	Key OVERFLOW settings.	60
7	OVERFLOW inputs.	62
8	OVERFLOW sphere mass and inertial properties.	62
9	Analytical and experimental frequency comparisons using a captive sphere.	75
10	Sphere heavy Mach scaling results. Mach 2.94, 40k ft, 1/20 th scale.	133
11	Heavy Mach scaling mass and inertial properties for a store shaped ice model. Mach 2.94, 1/20 th scale.	134
12	Light Mach scaling mass and inertial properties for a store shaped ice model. Mach 2.94, 1/20 th scale.	136

List of Abbreviations

Abbreviation		Page
CFD	Computational Fluid Dynamics	4
6-DOF	Six Degree of Freedom	4
CTS	Captive Trajectory System	5
AFIT	Air Force Institute of Technology	6
GPLD	General Purpose Low Drag	6
HIFEX	High-Frequency Excitation Active Flow Control for High-Speed Weapon Release	19
LRSA	Long Range Strike Aircraft	19
PRT	Powered Resonance Tubes	20
JDAM	Joint Direct Attach Munition	21
SLA	Stereo Lithography	23
LU-SGS	Lower Upper-Symmetric Gauss Seidel	24
MPI	Message Passing Interface	24
HLLC	Harten-Lax-van Leer-Contact	24
WENO	Weighted Essentially Nonoscillatory	24
SSOR	Successive Symmetric Over Relaxation	25
RANS/LES	Reynolds Averaged Navier-Stokes/Large Eddy Simulation	25
DCF	Domain Connectivity Function	28
DFT	Discrete Fourier Transform	29
PSD	Power Spectral Density	30
SVDB	Supersonic Variable-Density Blowdown	31
RP	Rapid Prototype	38

Abbreviation	Page
FFT	Fast Fourier Transform 42
WICS	Weapons Internal Carriage and Separation 51
SST/DDES	Shear Stress Transport/Delayed Detached Eddy Simulation 60
SST	Short Sawtooth 66
LST	Long Sawtooth 66
PIV	Particle Induced Velocimetry 69

FREEDROP TESTING AND CFD SIMULATION OF ICE MODELS FROM A CAVITY INTO SUPERSONIC FLOW

I. Introduction

Declaring the complexities of cavity flow would be analogous to a 17th century expedition returning to Europe with proclamations that the earth is round. Entering the eighth decade of formal research [19], what is known is that airflow in and about the cavity can contain a complex amalgamation of unsteady, turbulent, and viscous effects. A deeper understanding of fluid behavior surrounding an exposed cavity is beyond academic with both defense and civil applications. A military application of particular importance to the engineer is the internal weapons bay [5]. From Doolittle's B-25 to the latest 5th generation fighter, many aircraft have been designed to carry and employ weapons from a fuselage cavity (Figure 1).



Figure 1. Two generations of aircraft representing those which use an internal weapons bay. (a) B-25 Mitchells stand ready to raid the Japanese homeland aboard the USS Hornet while some 60 years later, (b) an F-35 Litening II conducts flight testing over the Chesapeake Bay [1, 2].

1.1 Motivation

1.1.1 Advantages of Internal Stores

Many tactical and operational advantages arise from the use of aircraft with internally carried stores. Reducing radar cross section is a critical element to increasing combat survivability of modern aircraft. Pylon mounted stores, with their associated fuses, control surfaces, and geometric protuberances present a vivid electromagnetic signature. Carrying and employing these stores from an internal bay greatly reduces the radar observability, allowing modern fighters such as the F-22 to meet critical radar cross section design objectives [22]. Externally mounted stores can account for up to 30% of total aircraft drag [19]. Minimizing or eliminating external weapons stations can significantly reduce the life-cycle cost of an aircraft, a factor of increasing importance as fiscal considerations become paramount. Carriage limitations, dictated by fuzes, fins, or guidance kits, can limit the operational airspeeds of aircraft carrying external stores. As employment speeds increase, effects such as aerodynamic heating can be detrimental to pylon mounted weapons that are constantly exposed to the freestream. Internal carriage effectively mitigates this particular concern. The advantages of carrying internal stores are significant enough that all 5th generation US attack aircraft are designed to employ weapons from a bay [5].

1.1.2 Disadvantages of Internal Stores

While benefits from internal stores are remarkable, so too are the difficulties for the engineers charged with cavity/store design and integration. From a store design and analysis perspective, externally carried stores offer a degree of simplicity that is absent from internal weapons. Specifically, two effects are especially problematic, acoustic resonance and store separation.

Acoustic resonance refers to the high amplitude, periodic pressure loading that

can occur in and around the cavity. With the bay door opened, internally carried weapons are exposed to a unique flowfield that can be detrimental to both weapon and cavity components [30]. As precision guided weapons contain sensitive guidance and control components, furthering the understanding of this degrading phenomenon is critical to safe and effective carriage of sensitive and sophisticated stores.

While the discipline of assessing safe separation of a weapon is not unique to internally carried stores, the unsteadiness of the flowfield presents unique challenges to the weapons separation verification process. Unsteady flow produces unsteady forces on the surface which ultimately affects the dynamics of the weapon. In his paper, Johnson defines the separation event as “the initial half second of flight after the weapon (or store) is released from the aircraft”[12]. During this time, the weapon must travel through the cavity and penetrate the shear layer before being exposed to the freestream, after which, the risk of impact with the aircraft can be assessed by the translation and rotation response of the store. It is during the first two phases of flight where the weapon is most susceptible to unsteady flow effects. Current weapon designs compound this problem. In an effort to reduce collateral damage and fratricide, increasingly, stores are designed to be lighter and more maneuverable. A negative side effect from this trend is that these weapons are more susceptible to detrimental disturbances by the unsteady flow [5]. Ultimately, to be approved for operational use, the weapon and aircraft configuration must yield consistent, safe separation events.

1.2 Problem Statement

Fundamentally, assessing safe separation of a store released from an aircraft requires predictability and repeatability. An introduction or major modification of a store and/or aircraft requires an appropriate level of analysis for carriage and release

certification [4]. Typically, this is done through three interconnected approaches: computational fluid dynamics (CFD) analysis, flight tests, and wind tunnel testing [4]. This integrated approach to store separation analysis has proven capable to date. Each method has its advantages and limitations, specifically as it applies to separation of stores from a cavity.

1.2.1 CFD Analysis

The benefits of CFD as an approach to understanding cavity flow and store separation are well documented [5, 12, 19]. While far from trivial, a sufficient grid appropriately applied to a robust solver processed by capable computational resources is invaluable to the understanding of fluid behavior in and around the cavity. Coupling CFD with an integrated six degree of freedom (6-DOF) solver allows weapon separation to be simulated. Once a certain degree of confidence is placed on the solution through verification and validation, the simulation can be run over a large parametric range. Salient post-processing on a large dataset allows visualization and analysis of the flow and dynamic response of the store.

Despite the many success stories, even the most ardent users will attest to the limitations of the method. In his paper, Kraft highlights some reasons why CFD is an unlikely candidate to fully replace the wind tunnel during test and evaluation [15]. The first is processing power/algorithm optimization. While access to petaflop (10^{15} floating point operations per second) computers is near at hand, few CFD algorithms are able to handle the massive parallel clusters required for complex flow conditions [15]. Second is the complexity of aircraft weapons systems currently fielded and in development. According to Kraft, “...all of the advances in computer hardware and software have been absorbed in increasing the fidelity of more complex systems” [15]. Lastly, as current tactical platforms are capable of routine operations in envelopes

once thought unreachable, e.g. controlled departed or supersonic flight, even the robust viscous solvers with the latest turbulence modeling are unable to truly predict the time-dependent fluid dynamics.

1.2.2 Wind Tunnel Testing

Wind tunnel testing has been a proven workhorse for assessing the aerodynamic response of a system. Early store separation testing used freedrop testing, however, results were suspect since scaling laws impaired the engineer from accurately predicting the response of a full scale store. To mitigate this limitation [4] the captive trajectory system (CTS) was developed to measure the aerodynamic loading on the store. While effective for time-averaged loading, the CTS is largely ineffective at predicting time-dependent store loading imparted from unsteady flow phenomena. This limitation has led to recommendations that freedrop testing be resumed despite the inherent scaling limitations [5].

1.2.3 Flight Testing

While flight testing is the most accurate assessment of store separation events, it is also the most expensive method [4]. While efficiencies have been made in the flight test process that allows for more data points to be collected on each flight, fiscal limitations preclude multiple drop events from identical release conditions, which is a prerequisite to assessing the effects of unsteady cavity flow on store separation. As budget considerations become the focus of defense initiatives, it is unlikely that flight testing will have a more prolific role in separation analysis, particularly in the research and development phase of a program.

1.3 Research Objectives

A significant amount of investigative efforts have focused on cavity flow [19] yielding a broad foundational knowledge base, yet some aspects of the flow remain unresolved. Given the considerations aforementioned, the original research objective was to utilize the Air Force Institute of Technology (AFIT) high-speed tunnel to test and assess the dynamics of an inertially simple shape. The high-speed lab houses a supersonic, variable-density blowdown tunnel capable of stagnation pressures ranging from 4-35 Psia. This provides the unique opportunity to perform supersonic testing at sub-atmospheric conditions. The ability to reduce the dynamic pressure (q) can positively effect the dynamic scaling laws. The model was to be fabricated from a non-destructive material that would pose little risk to the downstream tunnel components.

The model chosen for the initial tests was a sphere made from frozen tap water. After several successful fabrications of water ice spheres, consideration was given to testing a shape representative of an actual store. Though the mass and inertial properties are more complex, the ice shape in the form of a 500 lb general purpose low drag (GPLD) weapon would provide a dynamic response of a shape used in current tactical applications. Though dynamic scaling laws remain a limitation of freedrop testing, accurate analysis of the response of a sub-scale model to unsteady phenomenon could be assessed.

The sphere shape not only yields a simplified *point mass* problem, it also provides a more tractable shape for CFD simulation. Few opportunities exist for investigators to conduct both experimental testing and numerical simulation within the same research period. Simple, *in-house* validation of 6-DOF CFD solutions with experimental results allows a unique perspective with which to evaluate both the experimental and numerical processes used. A secondary objective of the research was to use the

OVERFLOW CFD suite for modeling a release of a sphere from a geometrically similar cavity into flow conditions consistent with the tunnel experiment.

Controlling the flow over a cavity through various means is a method employed by engineers charged with 1) minimizing the pressure loading and/or 2) ensuring safe weapons separation. Both active and passive flow control devices, with and without feedback loops, have proved effective at positively influencing the shear layer and cavity flowfield to meet both objectives. A tertiary goal of the research was to assess the impact of simple, passive flow control devices in supersonic flow.

II. Literature Review and Background

2.1 Cavity Flow Phenomena

In order to begin a systematic approach to understanding store separation from a cavity, one must be familiar with the common terms regarding supersonic cavity flow.

- L/D - Largely, cavity flow can be categorized by the ratio of length (L) to depth (D).
- Open cavity - At supersonic speeds, cavities with an $L/D \leq 10$ are generally categorized as open flow cavities [28]. These are usually deeper, air-to-ground weapons bays.
- Closed cavity - Cavities exposed to supersonic flow with an $L/D \geq 13$ typical of air-to-air weapons bays on fighter-type aircraft [28].
- Transitional cavity - Cavity configurations between open and closed, $L/D \approx 12$ [28].
- Clean cavity - an empty cavity devoid of stores and flow control devices, generally in a basic rectangular configuration.

Figure 2 is a two-dimensional view of cavity flowfields for a clean open and closed cavity. In open cavities, the incoming boundary layer has sufficient energy to bridge the cavity, creating a shear layer where the dividing streamline impinges on the back wall. Incoming flow seen by a closed cavity separates at the leading edge yet lacks sufficient energy to span the entire cavity. The flow impinges on the cavity ceiling and subsequently separates from the ceiling prior to exiting the cavity. In both open and

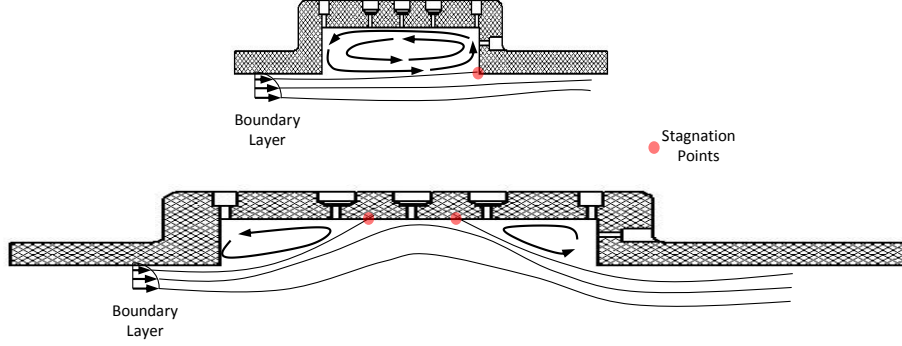


Figure 2. Streamline depictions in open (top) and closed (bottom) cavity flow. Note the highlighted stagnation points.

closed flows, areas of recirculation exists within the cavity (bounded by the dividing streamline).

Many investigations have focused on open cavity flows particularly due to the acoustic resonance that characterizes this cavity geometry. High and low frequency pressure mechanisms can resonate in the cavity area that can significantly impact surrounding components [11]. Arguably, the seminal research on cavity flow was produced by Rossiter, which resulted in a relationship between the dimensionless Strouhal Number and the freestream Mach number. The original relationship proposed by Rossiter is shown below in Equation 1.

$$Str = \frac{fL}{U_\infty} = \frac{n - \beta}{M_\infty + \frac{1}{k_c}}, n = 1, 2, 3 \dots \quad (1)$$

where

Str = Strouhal number

f = modal frequency (Hz)

L = cavity length (ft)

U_∞ = freestream streamwise velocity (ft/s)

n = mode number

M_∞ = freestream Mach number

β = phase delay constant

$$k_c = \text{convection velocity ratio} \left(\frac{U_c}{U_\infty} \right)$$

Since Rossiter's work, acoustic studies have focused on the frequency, amplitude, and dominant mode prediction methods. While various approaches to each have been proposed, the mechanism responsible for the longitudinal pressure oscillations as originally proposed by Rossiter still stands as a likely causal phenomenon of cavity unsteadiness. A two-dimensional depiction of the pressure oscillation sequence is shown below in Figure 3. Heller and Bliss expounded on Rossiter's work by furthering

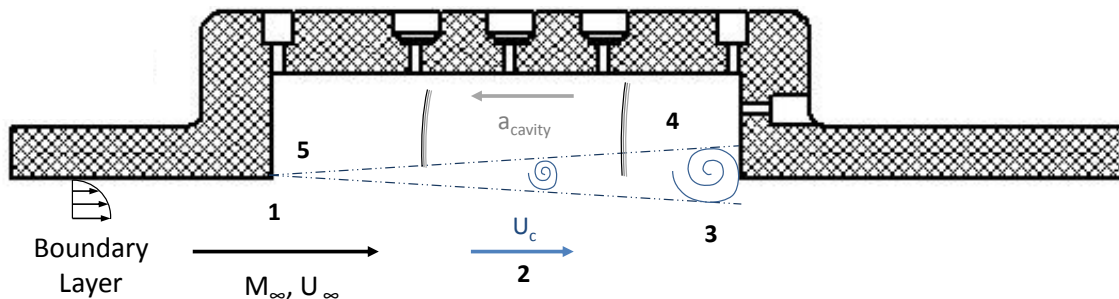


Figure 3. Flow mechanism contributing to longitudinal, resonant pressure oscillations.

the understanding of the physical mechanisms responsible for supersonic cavity flow-fields. According to Heller and Bliss: "Flow-induced cavity oscillations are caused by the interaction of the free shear layer and the cavity internal medium, which involves both acoustic and hydrodynamic mechanisms" [10]. These two mechanisms can be described as:

- Hydrodynamic - As the shear layer develops vertical instability along the cavity face, a process of mass addition and removal occur at the trailing edge of the cavity. This can be visualized by replacing the back wall with a piston-like device that imparts energy to the internal flowfield of the cavity [10].
- Acoustic - As the mass addition and removal process perpetuates, a series of pressure waves develop in the internal field of the cavity. The pressure waves interact with and are affected by the attached shear layer, thereby creating a complex, coupled relationship between the two driving/sustaining mechanisms [10].

Rossiter assumed the temperature difference in the cavity and freestream were negligible. Heller, Holmes, and Covert account for the difference in the speed-of-sound of the cavity and freestream by modifying Rossiter's Equation (Equation 1) to account for the temperature difference [11]. This modification extends the Mach number range of this analytical frequency prediction. Heller's modification to Rossiter's formula is shown below in Equation 2.

$$Str = \frac{fL}{U_\infty} = \frac{n - \beta}{\frac{M_\infty}{\sqrt{1 + \frac{1}{2}(\gamma - 1)M_\infty^2}} + \frac{1}{k_c}}, n = 1, 2, 3\dots \quad (2)$$

In both equations, the empirical constants β and k_c account for the phase delay between the interaction of the oncoming pressure wave with the subsequent shed vortex and the ratio of the vortex convective velocity to the freestream velocity,

respectively. Rossiter, Heller, and more recently Murray [24] agree on the values of these constants at $\beta = 0.25$ and $k_c = 0.57$, respectively (although these values are currently debated [24]).

2.2 Dynamic Scaling Laws

In the case of dynamic release testing, it is necessary to scale not only the applied forces but also the inertial response of the body to these forces [20]. The applied forces are scaled correctly provided the flight Mach and Reynolds numbers can be reproduced in the wind tunnel and geometric similarity between the full-scale and test articles exist. Fundamentally, this is foundational to all static wind tunnel testing. When conducting dynamic tunnel tests, additional scaling relationships exist to extrapolate test results to a full-scale release event [14].

In his paper, Marshall simplifies the equations of motion to 2-DOF to highlight the salient parameters and their impact on the dynamic scaling of the store motion. The frame of reference used in these equations of motion are shown in Figure 4. The origin is along the centerline of the cavity, 3.44 in back and 0.625 in up from the leading edge of the cavity. Positive Z direction in the tunnel reference frame is aligned with the gravity vector. This coordinate system was chosen in order to be consistent with the coordinate system used in the numerical analysis. Using the coordinate system shown in Figure 4, the equations can be simplified as seen below in Equations 3 and

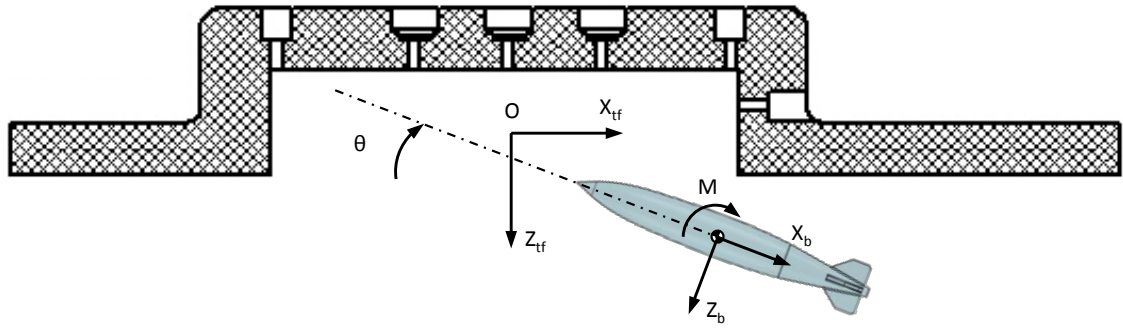


Figure 4. Axes and coordinate system.

4.

$$\left(\frac{\ddot{Z}}{g} \right) = 1 - \left[C_{N\alpha} \left(\theta + \frac{\dot{Z}}{V_\infty} + \Delta\alpha \right) \cos \theta - C_A \sin \theta \right] \left(\frac{q_\infty S}{mg} \right) + \left(\frac{F_{ej}}{mg} \right) \cos \theta \quad (3)$$

$$\ddot{\theta} = \left[C_{m\alpha} \left(\theta + \frac{\dot{Z}}{V_\infty} + \Delta\alpha \right) + C_{mq} \left(\frac{d\dot{\theta}}{2V_\infty} \right) + \Delta C_m \right] \left(\frac{q_\infty S d}{I} \right) - \left(\frac{F_{ej} X_{ej}}{I} \right) \quad (4)$$

where

\ddot{Z} = vertical acceleration (ft/s²)

g = gravitational acceleration (ft/s²)

$C_{N\alpha}$ = derivative of normal force coefficient with angle of attack (1/rad)

θ = pitch attitude, positive pitch nose up (rad)

\dot{Z} = vertical velocity (ft/s)

V_∞ = freestream velocity (ft/s)

$\Delta\alpha$ = incremental angle of attack from streamline inclination (rad)

C_A = axial force coefficient

q_∞ = freestream dynamic pressure (lb/ft²)

S = store reference area (ft²)

m = mass (slug)

F_{ej} = ejector force (lb)

$\ddot{\theta}$ = angular acceleration (rad/s²)

$C_{m\alpha}$ = derivative of pitch moment coefficient with angle of attack (1/rad)

C_{mq} = pitch damping derivative (1/rad)

$\dot{\theta}$ = angular velocity (rad/s)

ΔC_m = incremental pitch moment coefficient from streamline inclination

d = reference length (ft)

I = pitch moment of inertia (slugs·ft²)

X_{ej} = distance from store c.g. to ejector line of action (ft)

The quantities in square brackets represent the aerodynamic properties of the store

while the parenthetical quantities represent the geometric and inertial properties. Key assumptions to Marshall's equations are 1) C_N and C_m vary linearly with AOA and 2) C_A , $C_{N\alpha}$, $C_{m\alpha}$, and C_{mq} are all constant and represent the characteristics of the store in an undisturbed freestream airflow.

From Equations 3 and 4, a series of relationships can be utilized to predict full-scale store motion from sub-scale models in the wind tunnel. Unfortunately, without significantly altering the test gravity, it is impossible to satisfy both the aerodynamic and inertial scaling laws simultaneously [14]. To this end, compromises must be made between the two scaling paradigms when performing freedrop tunnel testing.

Marshall assesses the three primary approaches to dynamic scaling. The first, Froude scaling, is suitable for subsonic ($M < 0.3$) flight conditions involving test airspeeds much lower than flight conditions. Second, heavy Mach scaling, where simulation relationships that retain the test Mach number equal to the flight Mach number allowing compressibility affects to be accounted in the aerodynamic scaling. Last is light Mach scaling, which can be used when angular motion is the primary concern [20].

Ideally, the relationships represented in Equations 5 to 12 will accurately scale

dynamics of scaled store to full-scale results.

$$Z' = Z(\lambda) \quad (5)$$

$$\theta' = \theta \quad (6)$$

$$m' = m(\rho'_\infty / \rho_\infty)(V'_\infty / V_\infty)^2 \lambda^2 (g/g') \quad (7)$$

$$I' = I(\rho'_\infty / \rho_\infty)(V'_\infty / V_\infty)^2 \lambda^4 (g/g') \quad (8)$$

$$F'_{ej} = F_{ej}(\rho'_\infty / \rho_\infty)(V'_\infty / V_\infty)^2 \lambda^2 \quad (9)$$

$$X'_{ej} = X_{ej}(\lambda) \quad (10)$$

$$V'_\infty = V_\infty \sqrt{\lambda(g'/g)} \quad (11)$$

$$t' = t(\lambda) / (V'_\infty / V_\infty) \quad (12)$$

where

$(\)'$ = sub-scale parameter

$(\)_\infty$ = freestream parameter

Z = store c.g. from origin (ft)

λ = model scale factor (L_{model} / L_{actual})

ρ = density (slug/ft³)

T = temperature ($^{\circ}R$)

To simulate flight testing at low Mach numbers, Froude scaling is the preferred method. Since the gravitational ratio (g'/g) has yet to be adequately altered in tunnel testing, Equation 11 requires the test be conducted at a tunnel velocity well below flight airspeeds, (factored by $\sqrt{\lambda}$), thereby reducing the test Mach number. At low airspeeds, where compressibility is negligible, this scaling compromise is acceptable.

For transonic and supersonic testing, compressibility effects must be accounted

for. When using Mach scaling, compromises are made as one retains the flight Mach number (and essentially the velocity) in the tunnel. This provides aerodynamic similitude while compromising the dynamic scaling laws. The first Mach scaling method, heavy Mach scaling, assumes that the test gravitational field is equal to earth's gravity. The scaling relationships for heavy scaling are shown below in Equations 13 - 18.

$$Z' = Z(\lambda) \quad (13)$$

$$\theta' = \theta \quad (14)$$

$$m' = m(q'_\infty/q_\infty)(\lambda^2) \quad (15)$$

$$I' = I(q'_\infty/q_\infty)(\lambda^4) \quad (16)$$

$$V'_\infty = V_\infty \sqrt{T'_\infty/T_\infty} \quad (17)$$

$$t' = t(\lambda)/(\nu) \quad (18)$$

$$F'_{ej} = F_{ej}(\rho'_\infty/\rho_\infty)(V'_\infty/V_\infty)^2 \lambda^2 \quad (19)$$

$$X'_{ej} = X_{ej}(\lambda) \quad (20)$$

where

$$q = \text{dynamic pressure (lbs/ft}^2\text{)}$$

Here, the tunnel velocity is higher than prescribed for correct motion scaling. Although each term in Equations 3 and 4 are degraded to the extent of the error of the velocity parameter (Equation 17), the primary effect is that the sub-scale angular rates are higher than those seen in full-scale flight. Heavy Mach scaling retains the g ratio at unity (Equation 7) and requires either a drastic decrease in tunnel dynamic

pressure or increased model density for correct dynamic scaling.

Light Mach scaling alleviates the requirement for sub-scale models to be constructed of high-density materials, especially at lower scales ($\leq 1/20^{th}$). This is accomplished by assuming the gravitational acceleration can be changed in the wind tunnel. Currently, no acceptable method [14] exists for altering the gravitational field. One tack toward influencing the vertical acceleration (*effective g*) is to augment the ejection force to account for the test gravitational deficiency. Another, more straightforward approach is to allow the weapon to freefall from the cavity and account for the reduced vertical displacement using a correction factor [14]. Using this approach, g/g' remains at unity and the vertical acceleration will be in error by the amount shown in Equation 21 [20].

$$\Delta g' = g' - g = g \left[\frac{(V'_\infty/V_\infty)^2}{\lambda} - 1 \right] \quad (21)$$

It is imperative for the reader to understand that Mach scaling laws are founded on a series of compromises as one retains the flight Mach number during scaled testing. In their paper, Deslandes and Donauer answer the question as to whether what is seen at sub-scale matches accurately predicts the full-scale store response [6]. As with Marshall, they assess the three scaling laws and determine how accurately the sub-scale results match full scale. Their findings indicate that heavy Mach scaling reproduced trajectories that were in better agreement with full-scale translation as opposed to orientation. Even with a significant ejection mechanism, models constructed under light Mach scaling conditions failed to accurately reproduce the vertical translation (model remained closer to the release point) yet showed a higher degree of accuracy in pitch response [6]. The result of the above discussions highlights the need for those conducting freedrop tests to understand the trade-offs between the various dynamic scaling laws.

2.3 High Speed Store Separation Testing

The complexities of cavity flow increase with Mach number. The High-Frequency Excitation Active Flow Control for High-Speed Weapon Release (HIFEX) program was initiated by the Defense Advanced Research Projects Agency in 2001 to demonstrate the capabilities of an active flow control device on store separation at Mach 2.5 [3]. According to Bower et al.: “The need for enhanced weapons bay flow control is more crucial for weapons release at Mach 2 to 3 flight speeds than for release in the transonic flight regime” [3]. The program began with assessment of various flow control devices and their effectiveness at suppressing the acoustic tones in the cavity, while hoping that such suppression would positively affect store separation. Testing transitioned to scaled weapon tunnel tests using both CTS and freedrop testing. At the time of the report (2004), full-scale sled testing was planned at Holloman AFB. The operational objective of the program was to develop a technology that could be utilized for safe separation of stores from the Long Range Strike Aircraft (LRSA) platform.

Predominantly, passive control devices, usually in the form of a spoiler, have been used to alter the flowfield about a weapons bay during the release sequence. Passive flow control uses fixed mechanisms in an open-loop system, usually as a palliative solution. The advantages of a passive control device is the ease of implementation into an already complex weapons system. The drawback to the passive flow device is that the design range is fixed and narrow, reducing or even negating the effects outside of the optimum band. Active flow control devices utilize a feedback input in a closed-loop system to vary the parameters of the device. This allows the control device to be varied and optimized over a larger operational band.

The HIFEX program began investigative efforts assessing the four types of active flow control devices on a deep weapons bay. All tunnel tests were conducted on an

$L/D=5$ cavity at $M_\infty=2.5$ in the Boeing Polysonic Wind Tunnel. A brief description of the various control approaches are as follows:

- Powered Resonance Tubes (PRT) - Traditional approaches to active flow look to excite the shear layer within the frequency band where the large scale vortices are expected. In a departure of conventional methods, PRTs can be used to excite the dissipative scales an order of magnitude higher, which can alter the larger scale structures and the mean flow [3]. Instead of reducing the amplitude of the resonant tones, "high-frequency excitation destroys the organization of the initial shear layer that is necessary to sustain flow-induced resonance" [3].
- Jet screens - This device injects air normal to the incoming flow through a slit upstream of the cavity. The jet screen not only provides shear layer control, but also shock control, which can drastically alter the weapon as it transverses the near-body flowfield.
- Supersonic microjet actuators - An array of jets located upstream the leading edge used to inject mass flow into the incoming boundary layer. The objective is to disrupt the feedback mechanism required for acoustic resonance by a) disrupting the interaction of the forward traveling acoustic wave the shear layer near the leading edge and/or b) generating streamwise vorticity, thus making more the shear layer more stable and less susceptible to influence from the cavity acoustic disturbances [3].

Wind tunnel acoustic testing revealed that the PRT and microjet actuators reduced the level of modal and broadband tones in the cavity.

Using the insight gained in acoustic testing, the HIFEX investigators looked to assess the influence of the active control devices on the pitching moment of a store as it exits the cavity. Testing was conducted on a sting-mounted 10% scale Mk-82

Joint Direct Attack Munition (JDAM) model [3]. Schlieren optics were used to gain insight into the flowfield structures that affected the weapon as it transversed from the cavity. Of note, a spoiler device was used for comparison between a traditional passive device and the active devices under investigation. Results indicated that the PRT and jet-screen positively affected the pitching characteristics of the weapon as it transitioned through the shear layer. It was further assessed that the PRT combined with the jet screen positively influenced weapon release characteristics [3].

Freedrop testing of the Mk-82 JDAM model was conducted using light scaling laws. According to Bower et al.:

“Light scaling was used in the drop testing, where the relative importance of weapon weight is decreased compared to the aerodynamic and ejector forces. As a result of this, with regard to similarity variables, the weapon will tend to be closer to the aircraft for a longer time than would be experienced in flight. For this reason, the light scaling is conservative. That is, if safe separation occurs with a light-scaled weapons model, then a safe separation with the full-scale weapon is essentially certain.” [3]

Trajectory analysis was conducted using illuminated target markers processed through photogrammetric software while flowfield visualization was provided via Schlieren photography. Freedrop testing revealed that weapons released from the forward and middle bay position were unsuccessful without flow control and successful with the device in place. Further drop tests were conducted that revealed that the tandem configuration of microjet arrays provided the best weapon release characteristics while having the lowest mass flow requirement of all devices investigated. For this reason, the tandem microjet array was selected as the actuator to be used during full-scale sled testing.

Scaled experimental results were validated using the test track at Holloman AFB. Due to test constraints, the release speed was limited to Mach 2. A test sled and release mechanism were designed to best simulate the flow conditions expected with

the LRSA aircraft. A full-scale HIFEX bay was fitted with the tandem microjet configuration that proved to be the most effective active flow control device in wind tunnel tests. The release was successful and groundbreaking as it became the first successful test release of an air delivered weapon at Mach 2 [18].



Figure 5. HIFEX sled testing demonstrating successful release.

2.4 Correlating Store Separation Effects to Cavity Dynamics

Flow physics have been investigated to determine the pressure environment in the cavity, the shear layer behavior over the cavity, and the store separation characteristics from a cavity. Murray et al. look to determine the coupled response between the three as they suspect a relationship between the shear layer motion and the store dynamics [23].

Murray et al. used a 1/15th scale model of a 500 lb JDAM from a rectangular $L/D=6$ bay into Mach 1.5 flow. A key component of the research was the ability to

synchronize the release event with the cavity acoustics to determine the phase relationship between the fluctuating pressure and the store dynamics. This capability was made possible by a repeatable ejection mechanism that provided synchronization capability with the time-dependent pressure signal. The JDAM model was constructed of stereo lithography (SLA) plastic filled with assorted metal washers for ballast. This allowed the mass and moment of inertia to be finely tuned. Light scaling was used in the design of the ejection mechanism to compensate for the gravitational acceleration deficiency.

Results of Murray's work showed a clear resonant peak at 810 Hz, which he assessed to be consistent with Rossiter's formula (Equation 1). This resonance was observed in the clean bay and with a store in the carriage position [23]. Consistent with the objective of the research, five runs showed similar displacements in the vertical and streamwise direction, yet drastically different pitch angles. After comparison of the release event timing with the time-dependent pressure signal, it was found that the release initiation occurred during different phases of the pressure oscillation. This strongly suggests a phase relationship between the oscillating pressure signal and the release initiation, thereby affecting the store dynamic response [23].

2.5 OVERFLOW Solver

Limitations inherent to Mach scaling laws prohibit complete accuracy when determining the full-scale results based on scaled tunnel tests. Assuming an accurate solution, augmenting freedrop testing with a capable CFD solver provides further insight into the physics of cavity flow and the response of a released store. The OVERFLOW solver was chosen to supplement the experimental testing for the following reasons:

- A baseline case was provided from previous work conducted at AFIT, allowing efficient user startup of a complex flow problem.
- The overset, structured methodology (i.e Chimera) facilitates the use of structured grids defining the computational domain around complex objects while providing the capability of modeling relative motion between bodies.
- The OVERFLOW solver has been used extensively among CFD users to model complex flow problems such as unsteady flow, turbulent flow, and moving body simulations.

The following summarizes the key features of the OVERFLOW solver, with excerpts from the OVERFLOW 2.1 User's Manual [26]. OVERFLOW is a three-dimensional time-marching implicit Navier-Stokes code that uses structured overset grid systems. Tracing its lineage through a family of flow solvers dating back to 1976 [26], the current CFD solver package of edition 2.1 provides a robust degree of performance. Some of the recent upgrades provide a snapshot into the capabilities of the solver:

- Lower Upper-Symmetric Gauss Seidel (LU-SGS) implicit solution algorithm and a Roe upwind inviscid flux scheme.
- Multigrid solution procedure, low-Mach number preconditioning, and a central difference/matrix dissipation scheme.
- Parallelization with OpenMP and Message Passing Interface (MPI).
- Dual time stepping implicit solution algorithm.
- Harten-Lax-van Leer-Contact (HLLC) inviscid Riemann flux algorithm.
- Two Weighted Essentially Nonoscillatory (WENO) inviscid Riemann flux algorithms.

- An unfactored Successive Symmetric Over Relaxation (SSOR) implicit solution algorithm.
- Three hybrid Reynolds Averaged Navier-Stokes/Large Eddy Simulation (RANS/LES) turbulence models
- Wall functions for the transport equation turbulence models.

OVERFLOW 2.1 solves the full Navier-Stokes equations in generalized coordinates.

The Navier-Stokes equations may be written as:

$$\frac{\partial \vec{q}}{\partial t} + \frac{\partial \vec{E}}{\partial \xi} + \frac{\partial \vec{F}}{\partial \eta} + \frac{\partial \vec{G}}{\partial \zeta} = 0 \quad (22)$$

where q represents the vector of conserved variables as shown in Equation 23

$$\vec{q} = V \begin{bmatrix} \rho \\ \rho u \\ \rho v \\ \rho w \\ \rho e_o \end{bmatrix} \quad (23)$$

where V represents the volume. The linearized Euler implicit form of Equation 22, including sub-iterations, is represented as

$$\begin{bmatrix} I + \frac{\Delta t}{(1+\theta)\Delta\tau} + \frac{\Delta t}{1+\theta}(\partial_\xi A + \partial_\eta B + \partial_\zeta C) \\ (q^{n+1,m} - q^n) - \frac{\theta}{1+\theta}\Delta q^n + \frac{\Delta t}{1+\theta}RHS^{n+1,m} \end{bmatrix} \Delta q^{n+1,m+1} \quad (24)$$

The explicit viscous and inviscid fluxes are included in the term RHS given by

$$RHS = \frac{\partial \vec{E}}{\partial \xi} + \frac{\partial \vec{F}}{\partial \eta} + \frac{\partial \vec{G}}{\partial \zeta} \quad (25)$$

Equation 24 has the general matrix form $\mathbf{A}x = \vec{b}$. Solving the system of discrete equations requires inversion of the \mathbf{A} matrix. Direct inversion of the matrix for three-dimensional flows requires a large amount of computational time and memory. OVERFLOW 2.1 incorporates various numerical schemes to solve for the \mathbf{A} matrix making the code one of the fastest available for attaining steady state solutions.

In addition to a wide variety of the latest numerical methods, OVERFLOW 2.1 incorporates grid sequencing to acceleration the initial solution. With grid sequencing invoked, the solution begins on a course grid, with every 4th point removed from the original grid, then performs the calculations on a intermediate grid (every other point removed) with the final solution being performed on the original input grid.

OVERFLOW 2.1 solves the non-dimensional Navier-Stokes, turbulence, species, and motion equations. As with other flow solvers, non-dimensionalization is an important aspect of the OVERFLOW suite. In addition to conventional dimensionless flow quantities, OVERFLOW also requires dimensionless parameters for the moving body simulation. Some of the non-dimensional quantities used by OVERFLOW include

$$V^* = V/a_\infty \quad (26)$$

$$t^* = ta_\infty/L \quad (27)$$

$$\rho^* = \rho/\rho_\infty \quad (28)$$

$$p^* = p/(\gamma_\infty p_\infty) \quad (29)$$

$$m^* = m/(\rho_\infty L^3) \quad (30)$$

$$I^* = I/(\rho_\infty L^5) \quad (31)$$

$$M^* = M/(\rho_\infty V_\infty^2 L^3) \quad (32)$$

where

$()^*$ = dimensionless variable

L = unit grid length

t = time (sec)

V = velocity (ft/s)

ρ = density (slug/ft³)

p = pressure (lb/ft²)

m = mass (slug)

I = moment of inertia (slug·ft²)

M = moment (ft·lb)

It is imperative that the OVERFLOW user properly non-dimensionalize the flow inputs in order to arrive at the correct solution. Flow and dynamic motion solutions are also output using dimensionless parameters.

As with any CFD solution, a poorly constructed or insufficiently refined grid can lead to inaccurate, misleading results. Overset grid methodology that utilizes relative motion adds unique challenges to the grid generation process. When using a Chimera scheme, one must be familiar with the following terms:

- Blanked-out points - points inside bodies or holes, where the solution is not computed or is ignored.
- Field points - points on the grid where the differential equations are solved.
- Fringe points - points adjacent to the grid boundary whose solutions rely on interpolated values from overlapping grids.

- Donor points - points from the overlapping grid that passes information to the underlying fringe points.
- Orphan points - fringe points without a valid donor, usually a result of insufficient grid overlap.

OVERFLOW begins the simulation process by splitting the input grids to individual MPI processes for load balancing. This is followed by hole-cutting and interpolation for the overlapping grids, performed using the software routine Domain Connectivity Function (DCF). DCF cuts blanked-out points (called *X-Rays*) on the inner portions of the overlapping grids, on which the solution is either not computed or ignored. With the input grid and the hole-cutting file, OVERFLOW uses DCF to assemble the complete grid system. When assembling the grid, it is recommended to maintain enough layers between the overlapping grids to maintain the full stencil of the flux algorithm (e.g. three layers of fringe points are needed for a 4th or 5th-order stencil). Insufficient overlap between grids can result in orphan points. The OVERFLOW manual recommends minimizing the amount of orphan points by allowing sufficient overlap of neighboring grids [26].

Additional input files are required when performing moving body simulations. When simulating 6-DOF motion, the user specifies which grids will be subject to dynamic motion and the initial conditions of the dynamics (location, orientation, and force/moment). Using a program within the overflow suite (*misxur*), the user defines the surface over which forces and moments are integrated. The final input required by OVERFLOW for 6-DOF motion provides the program with the non-dimensional mass and inertial properties of the moving body.

2.6 Signal Decomposition and Spectral Analysis

As demonstrated first with Rossiter's work and nearly every open supersonic cavity study henceforth, the environment is dominated by a series of periodic pressure signals that reside in certain frequency bands (i.e. Rossiter modes). As with other engineering problems, this periodic signal leads "quite naturally to a decomposition by a basis consisting of sines and cosines". The Fourier transform is the mechanism used to perform this decomposition [9].

All digital, observed signals are discrete and finite. These discrete temporal signals can be converted to frequency space using the discrete Fourier transform (DFT). Equation 33 is used to compute the DFT, transitioning a discrete time signal to the frequency domain.

$$F_k = \frac{1}{N} \sum_{n=0}^{N-1} x_n \cdot e^{-2\pi i \frac{\omega}{N} nk} \quad (33)$$

where

N = number of time domain samples

n = time domain sample index

k = frequency domain index (0, 1, 2, ..., N-1)

A byproduct of the transformation process is spectral leakage, or a misrepresentation of spectral components of the signal. Spectral leakage occurs when a harmonic frequency does not precisely correspond to a discrete bin of the DFT, resulting in a non-zero amplitude *leaking* to other bins [9]. Harris presents an analysis of various windows functions used to reduce the undesirable leakage influenced by sampling process.

Welch proposes using Hamming windows to divide the time signal into overlapping

sections. The modified periodograms are calculated for each section using the DFT and subsequently averaged. The resultant average is the power spectral density (PSD) [31].

III. Methodology

3.1 Experimental Setup

3.1.1 Supersonic Variable-Density Blowdown Tunnel

The AFIT high-speed aerodynamics lab houses the Supersonic Variable-Density Blowdown (SVDB) wind tunnel. A graphical depiction of the facility is shown in Figure 6. Key components of the SVDB tunnel are listed below, corresponding to the

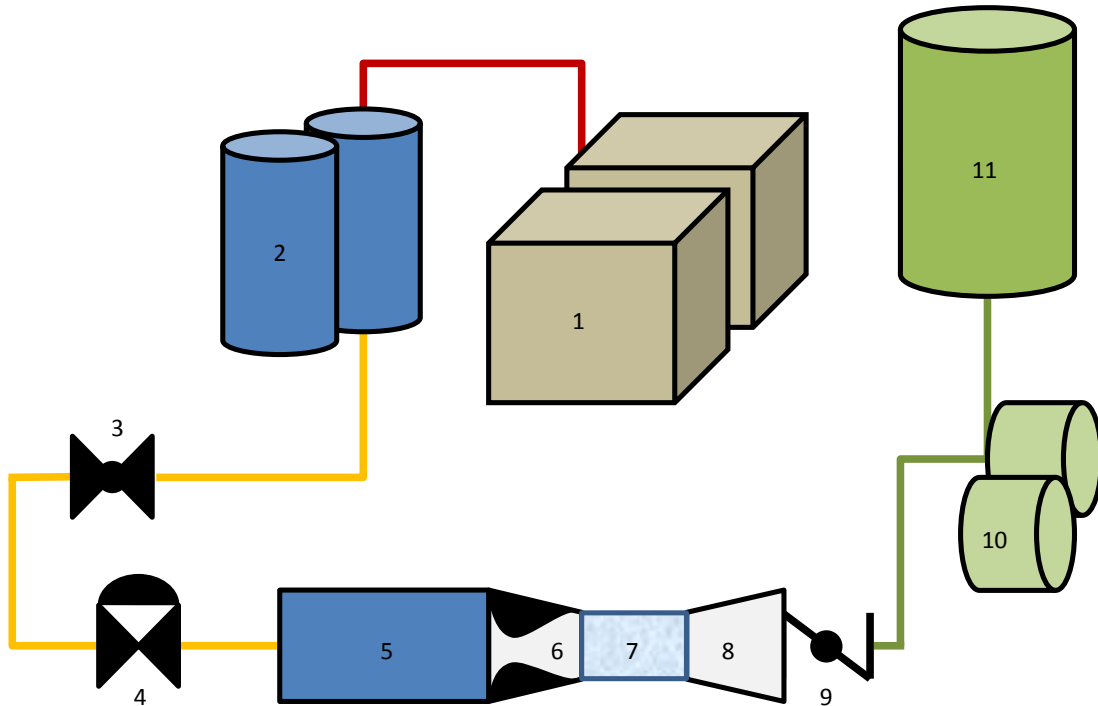


Figure 6. Illustration highlighting the key components of SVDB wind tunnel.

labels of Figure 6.

1. High pressure air compressors - Two Ingersoll Rand® Model UP6-50PE-200 compressors supply up to 170 CFM air at 200 Psig.

2. Air dryers - Donaldson® Regenerative Air Dryers® remove moisture from the compressed air prior to tunnel entry.
3. Pressure-side valve - El-O-Matic® pilot actuator controls the high pressure supply via a ball-type valve.
4. Regulating valve - Pressure controlled Leslie® diaphragm-type valve provides the mechanism to vary the pressure conditions in the settling chamber and test section.
5. Settling chamber - Cylindrical chamber for conditioning the flow upstream of nozzle. Stagnation conditions are provided via a dynamic pressure transducer and thermocouple.
6. Nozzle Block - Various freestream Mach numbers can be discretely set using two separate nozzle blocks designed for Mach 1.8 and 2.94 flow. This research used the Mach 2.94 nozzle exclusively.
7. Test Section - A custom acrylic test section was designed and fabricated to allow easy access for model placement and configuration changes, modularity, and optical access.
8. Diffuser - An adjustable ramp diffuser allowed control of downstream throat conditions to ensure consistent, supersonic flow in the test section.
9. Vacuum-side valve. Pilot actuated butterfly-type valve isolates vacuum conditions required to attain sub-atmospheric stagnation pressures *and* supersonic flow.
10. Vacuum pumps - A Stokes® Microvac® vacuum pump with second-stage boost pump draws a near vacuum on the low pressure side of the system.

11. Vacuum tank - Vacuum accumulator drawn down by the vacuum pumps used to charge the flow through the test section.

3.1.2 Test Section and Cavity

The SVDB is configured with a 2.5 in square test section approximately 16 in long. The test section top piece, which housed the cavity, and sidewalls were manufactured from solid acrylic. The floor of the test section was an acrylic window framed with aluminum to provide structural rigidity to the test section. To allow access to the test section, the sidewalls were removable, held in place by toggle clamps during tunnel operation. Figure 7 shows both a prototype test section and the final test section. The first iteration consisted of a $L/D=2.66$ cavity. The tunnel dimensions,

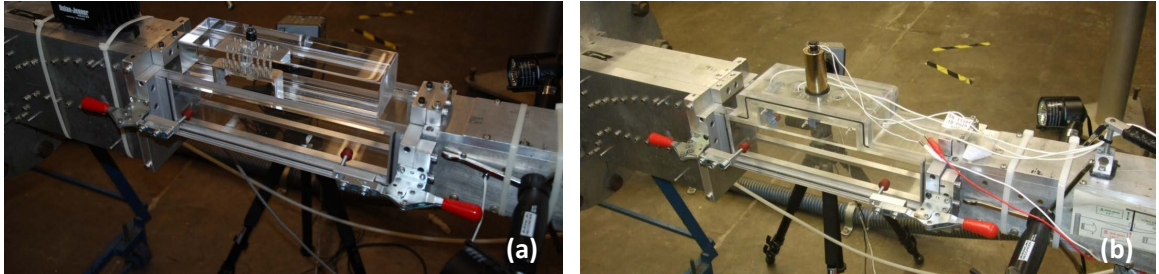


Figure 7. Depiction of the (a) prototype and (b) final test section.

$D=1.5$, $W=1.75$, and $L=4$, were sized for a 1/30th scale model. The prototype cavity was milled from a solid piece of acrylic (test section top) which yielded machined, opaque faces on the cavity sidewalls, thereby precluding Schlieren access through the cavity. No pressure transducers were mounted in the cavity. Capitalizing on the initial successful tests and an accommodating time line, a second test section was designed and fabricated using lessons learned from the prototype piece. The new cavity maintained the same depth but a longer length, yielding an $L/D=4.5$.

To provide Schlieren optical access through the cavity, the acrylic tunnel sides were mated with the acrylic cavity sidewalls providing an clear unobstructed view through the side of the cavity. The new test section was also designed with orifices for dynamic pressure transducers. Tunnel dimensions with orifice locations are shown below in Figure 8 Five threaded orifices provided transducer mounts along the centerline on

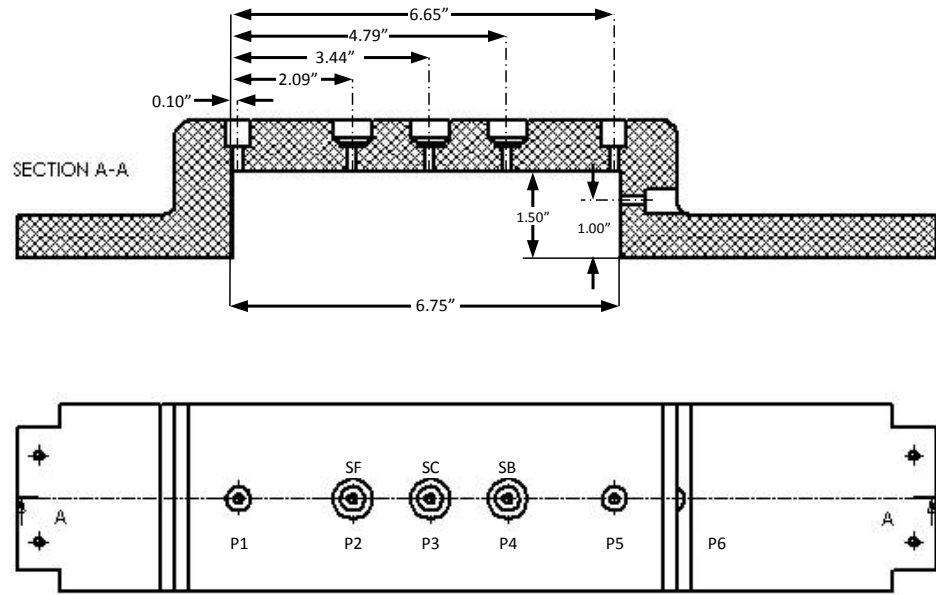


Figure 8. Cutaway along the centerline of the test section top showing cavity dimensions, transducer orifice, and solenoid locations.

the cavity top ($P1-P5$). Orifice $P6$ was located on the centerline of the aft wall, where the pressure fluctuations were greatest. $P2-P4$ could accept either a pressure transducer or the actuation solenoid. Although not used in this research, this provides the capability of moving the store release point within the cavity. Figure 9 provides a narrow view of the cavity section. While the cavity was capable of fitting six pressure transducers, only three were used in this experiment ($P1$, $P2$, and $P6$). Although pressure measurements were taken at these three locations, only transducer $P6$ was

used during data analysis. Also shown is the nomenclature for the cavity faces (*front wall, ceiling, back wall*).

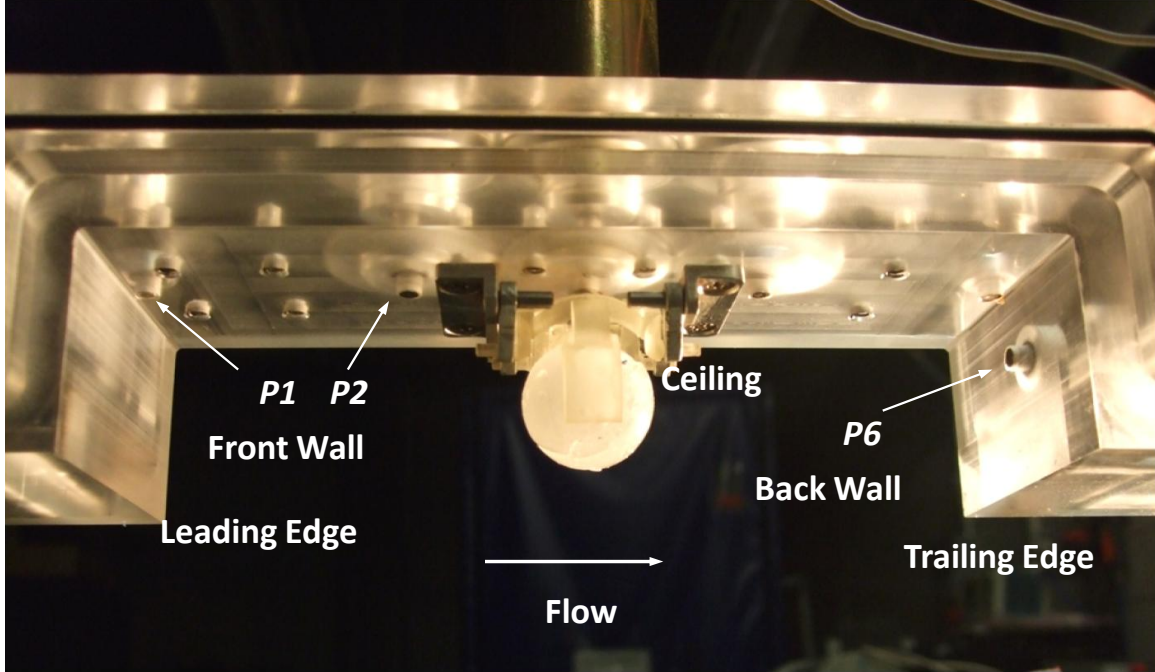


Figure 9. Closeup of cavity with sidewalls removed for clarity. In this experiment, only orifices P_1 , P_2 , and P_6 are fitted with pressure transducers. Cavity nomenclature is also shown.

3.1.3 Release Mechanism

Both the sphere and store model were released from the cavity under gravity acceleration only. Although most aircraft that employ from a cavity use an ejector, this mechanism was not used in this experiment for the following reasons:

1. Scope - Adding an ejection mechanism increases the complexity of the experiment. The ejection force and moment must be consistently imparted to the store. Eliminating the ejector force reduced a variable in the data.
2. Current trends - As modern weapons become lighter and more precise, the

technology housed within the store does so as well. Modern guidance kits, seeker heads, and control mechanisms are more susceptible to carriage and release damage than previous versions. High ejector forces intended to minimize the dwell time in the shear layer increase the potential for damage to sensitive equipment.

3. Model material - The ice model might not withstand a significant ejection force imparted on the store at release. Consideration was given to adding a hardback attachment to the release mechanism in order to distribute an ejector load yet ultimately not incorporated.
4. Research objectives - One critical question is “how does unsteady cavity flow affect weapons separation”. For this reason, minimizing the resident time of the weapon in the shear layer is counter to the goals of the experiment. Although advantageous in the applied sense, the ejector mechanism impedes meeting some goals of the experiment.

To this end, the linkage mechanism was designed such that the initial release position and attitude were repeatable and the clamp mechanism would neither impart a force or interfere with the falling store. Figure 10 depicts a release sequence with a sphere model. The release sequence is captured in the raw video with initiation occurring at frame 340 and ending at frame 350. The release sequence lasts approximately 5 ms. The sphere remains in the same position with the mechanism fully open, indicating no force is imparted to the sphere in the opening process on this run.

One key factor of freedrop testing is to maintain repeatability in the release sequence, whether using an ejection mechanism or allowing a freefall release. Figure 11 provides comparison of three static drop tests. Subfigures (a1), (b1), and (c1) all show the beginning of sphere freefall event for three separate drop tests. Each test

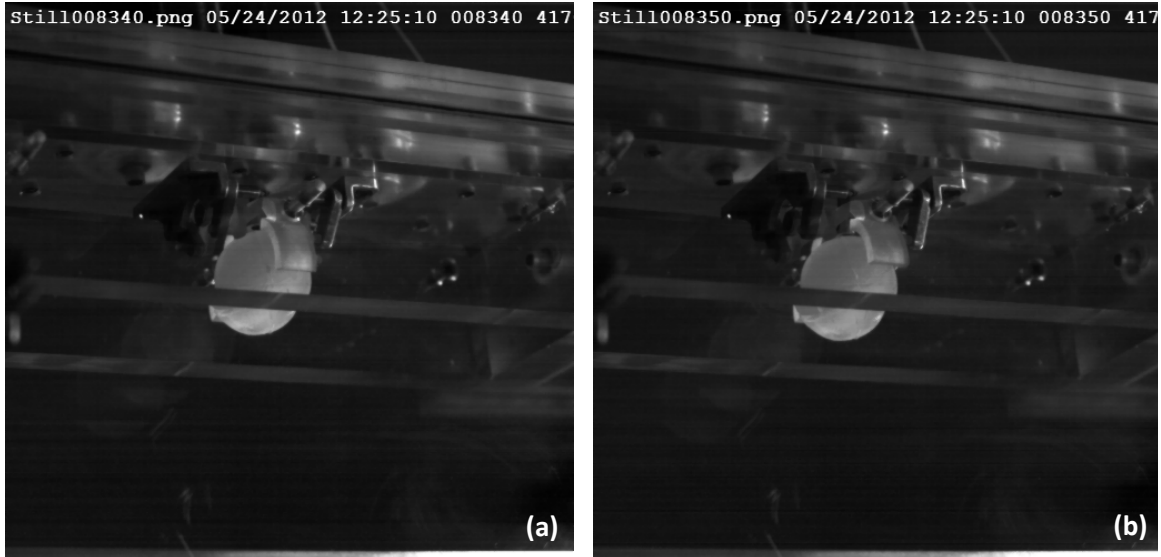


Figure 10. Mechanism configured with sphere clamp showing (a) fully closed at release and (b) fully opened, 10 frames later (5 ms). Note the stationary position of the sphere during mechanism release sequence.

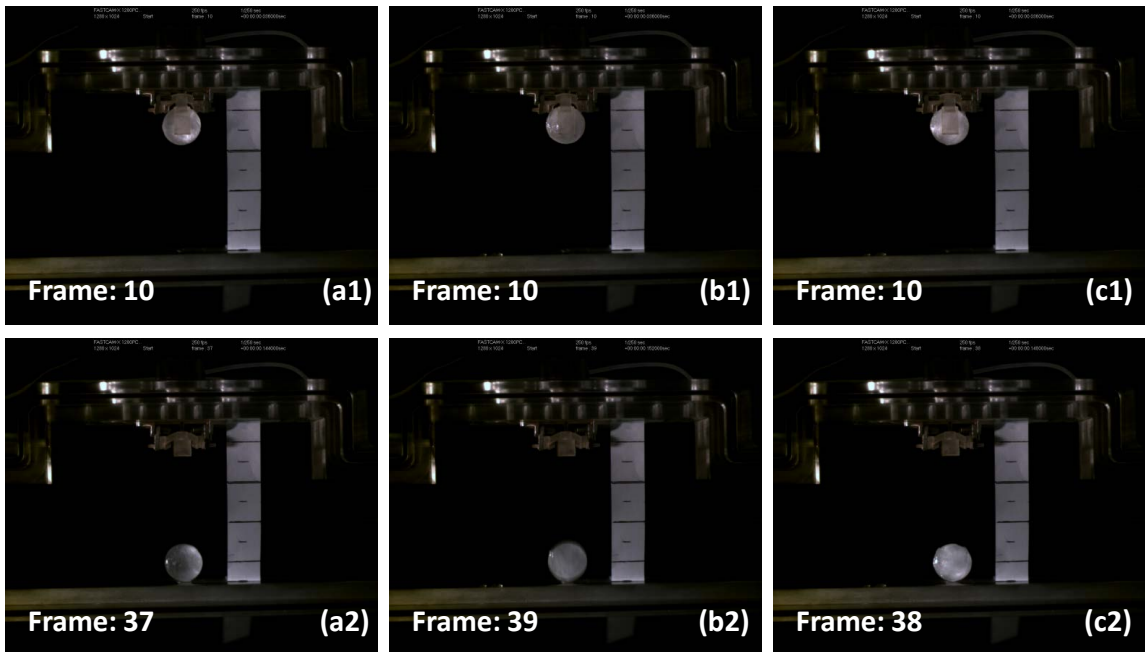


Figure 11. Repeatability checks on sphere ice models. Capture rate = 250 Hz.

began with the sphere held at the release position, with the c.g. centered at 3.44 in from the leading edge of the cavity and 0.63 in from the cavity face. The imagery captured the event from release to impact on the tunnel floor, a total c.g. fall distance

of 2.66 in. Using the high-speed imagery, the drop time was calculated to be 0.108, 0.116, and 0.112 sec for tests a, b, and c, respectively. This test indicates a high degree of repeatability between sphere release events. For reference purposes, calculated freefall of an object traveling 2.66 in in a vacuum (considered a valid assumption) was calculated to be 0.117 sec, consistent with test release times, indicating no ejection force was imparted to the sphere by the release mechanism.

Two clamp sets were fabricated in an Objet®3-D printer. The sphere pieces contained clamp arms with concave faces to hold the sphere in place. The store clamp arms were fashioned in a similar manner without the concave surface on the clamp arm face. Originally, the mechanism was manufactured using steel arms, however, the rapid prototype (RP) clamp pieces were preferred for the following reasons:

1. Melting - Metal arms that cradled the model placed sufficient pressure on the model to initiate melting, creating an irregular surface on the model.
2. Position - The RP clamps enabled a more repeatable and precise release location and orientation.
3. Interference - Because the RP clamps held the models on the sides, the opening action pulls the clamps outward and up, releasing the model while minimizing force or interference from the mechanism.

Mechanism actuation was accomplished using a synchronized DC input to a Magnetic Sensor Systems®push-type tubular solenoid. A 12 volt, 2 amp electric current providing approximately 60 oz of downward force to the linkage at a stroke length of 0.5 in. Figure 12 illustrates how the actuation force is translated to the clamps, which open outward. This allows a clean release to occur without imparting an ejection force to the sphere.

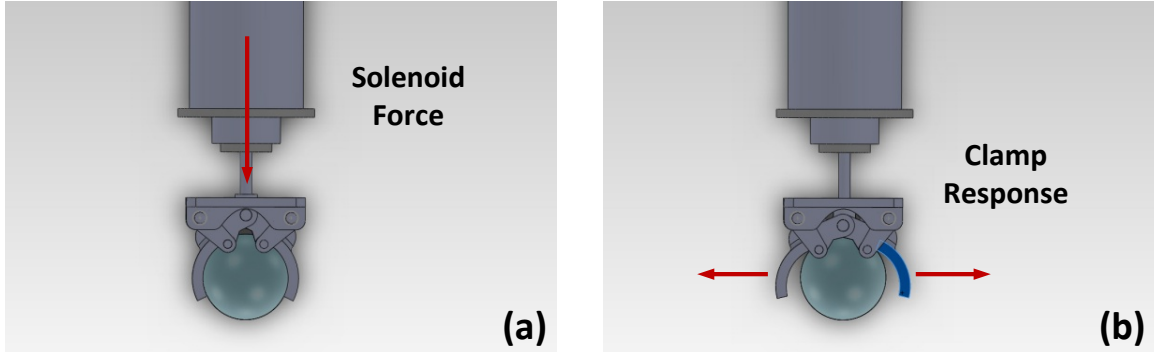


Figure 12. Solenoid and clamp mechanism in the (a) closed position and (b) open position.

3.1.4 Model Fabrication

Fabricating small finned axis of rotation models or spheres from water ice proved no trivial task. The material required a mold soft enough to allow expansion during freezing while yet able to hold a rigid shape. Silicone was chosen after a brief trade study of various mold materials. The silicone used was a two-part silicone putty that hardened when mixed. Figure 13 shows the mold fabrication process. After the two-

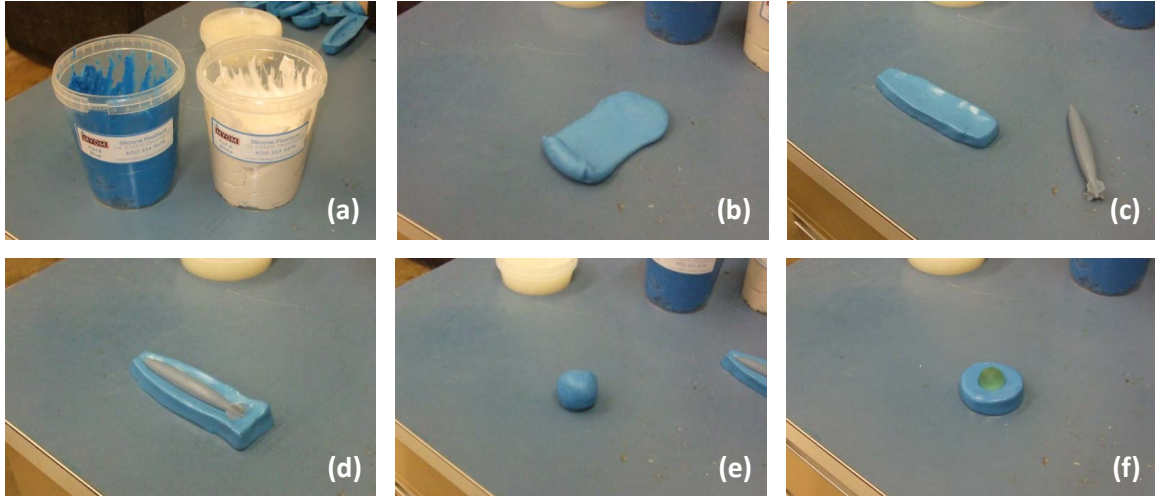


Figure 13. Mold fabrication showing (a) silicone material, (b) mixed two-part silicone, (c) store silicone base, (d) and store silicone with male RP store. Also shown (e) is the sphere silicone base filled (f) with the male RP sphere.

part silicone was thoroughly kneaded, silicone bases were formed and the male RP component was pressed into the base. After approximately two hours, the silicone had dried and the RP male piece could be removed revealing the mold cavity. Petroleum jelly was applied to the silicone base and model to allow release of the silicone top.

Formation of the ice model is depicted in Figure 14. Vacuum grease was applied to

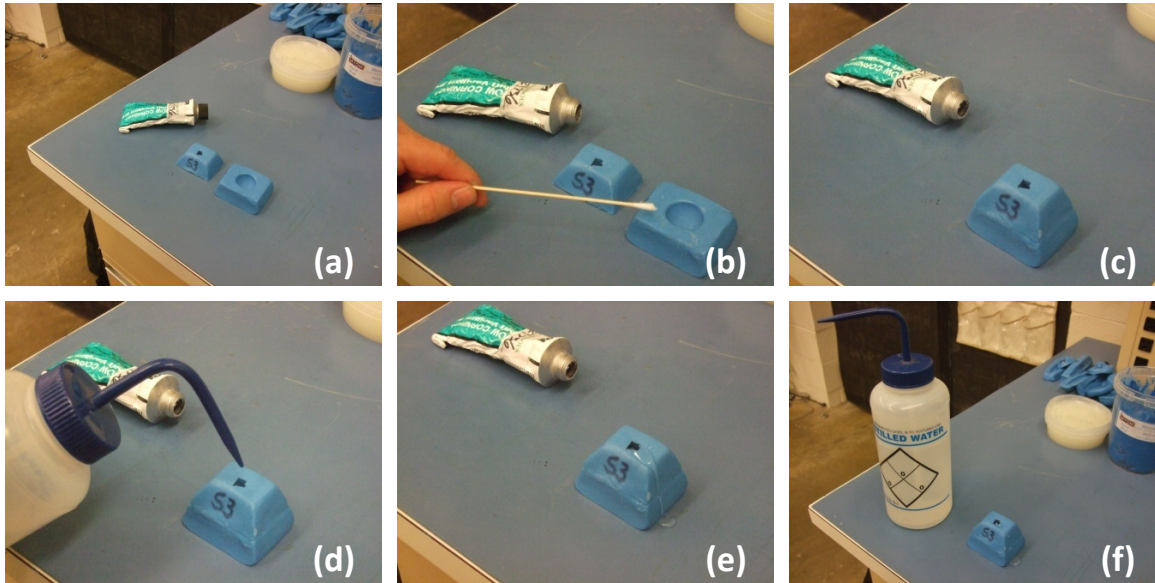


Figure 14. Model fabrication process.

the parting surface of the mold to ensure a proper seal during the freezing process. As shown in Subfigure (d) of 14, liquid tap water was poured into a large, fill hole in the top portion of the mold. Early testing of model fabrication used distilled water, yet the models proved ineffective as the lack of impurities actually weakened the model itself and led to premature fracturing during the testing process. As the impurities of tap water strengthened the frozen ice model, tap water was selected as the preferred model material. In order to ensure consistent mass distribution of the ice models, it was imperative that all trapped air bubbles were released from the sphere prior to the freezing process.

Once the mold was completely filled and all voids were eliminated from the mold, the model was inserted into an SPT®UF-150SS refrigeration unit. The unit temperature range, measured using an Omega®K-Type thermocouple, was 4.7° F - 12.0° F. The coldest setting was used during the freezing process, which proved to mitigate the mass loss due to melting during the transfer process from the refrigeration unit to the test section.

3.1.5 Experimental Components and Data Acquisition

Tunnel control, image capture, store release, and data acquisition were all sequenced using a National Instruments®NI PXI-1042 computer via a *virtual interface* program. Figure 15 provides visualization of the some of the wind tunnel and data acquisition components:

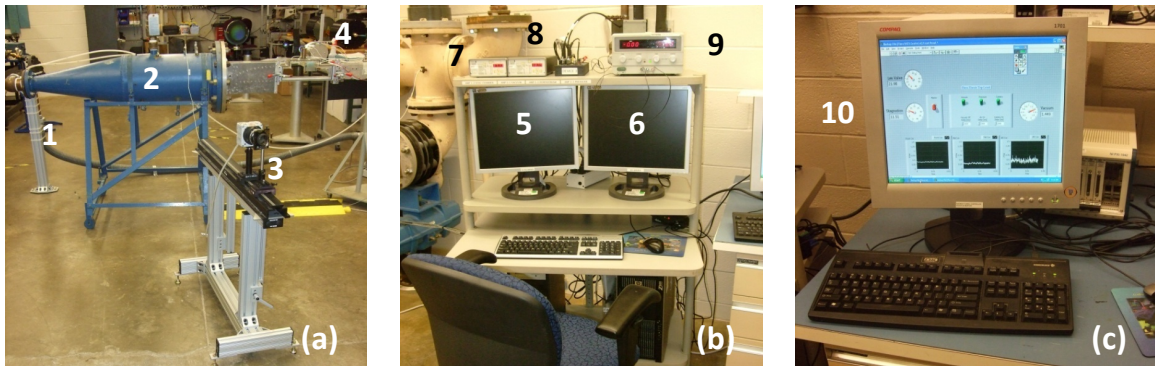


Figure 15. Experimental test components.

1. Pressure regulating valve and incoming high-pressure feed line.
2. Stagnation chamber chamber with pressure relief valve and affixed $M=2.94$ nozzle block.

3. Schlieren camera - A Photron FASTCAM-X®digital camera was used to capture Schlieren images at both 2 kHz and 8 kHz. Shutter speeds for all runs was set to $8 \mu\text{s}$. A Nikon®Series-E 50mm lens was used with an aperture setting of f/1.8.
4. Test section in situ between the nozzle block and the diffuser section.
5. Desktop station for Schlieren image post-processing using the Photron FASTCAM®software.
6. Desktop station for the high speed imagery post-processing using the IDT®Motion Studio software.
7. Two Endevco®Model 136 DC differential voltage amplifiers condition the voltage output from the transducers to the data acquisition software.
8. National Instruments®data acquisition card for signal throughput to the data acquisition system.
9. GW Instek®GPR-3510HD DC power supply providing 12 v, 2 amp current to the release mechanism solenoid.
10. National Instruments®NI PXI-1042 computer providing tunnel control, camera/release sequencing, and data collection.

Not shown in Figure 15 are the following components:

- Agilent®35670A spectral analyzer used to capture the frequency content of the pressure signal from transducer $P6$. Using the spectral analyzer, a fast Fourier transform (FFT) was performed on the pressure signal over the 0-6400 Hz frequency band averaging 20 samples using a rectangular (*flat-top*) window.
- Dantec®X4MPG-4 high-speed digital camera was used to capture imagery of the release events at a frame rate of 2 kHz. Shutter speed for each image

sequence was set to 497 μ s. A Nikon[®]AF NIKKOR 28mm lens was used with an aperture setting of f/2.8.

Figure 16 provides a depiction of the image acquisition components. Subfigure (a)

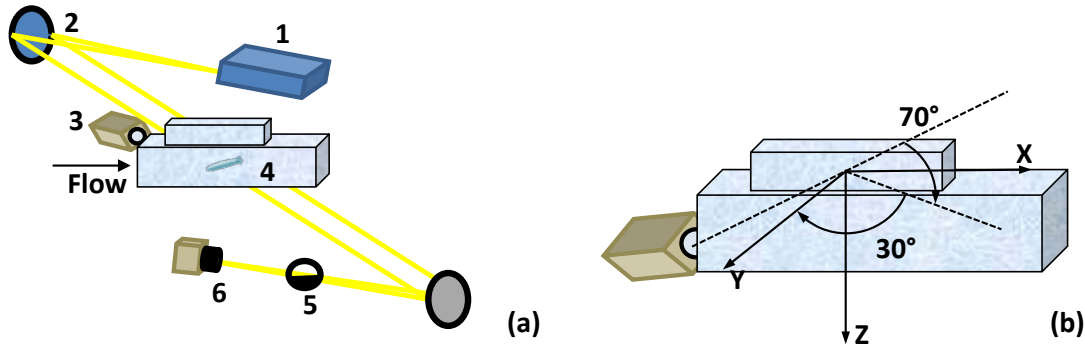


Figure 16. Representation of the (a) Schlieren optical and high-speed camera configuration and a close-up (b) of the high-speed digital camera orientation with respect to the defined axis system.

provides representation of the following:

1. Light source passing through an aperture towards a parabolic mirror set at a focal distance of 80 in.
2. The focal mirror collimates the light source through the test section.
3. The Dantec[®]high-speed camera is situated behind the test section (as viewed in Subfigure (a)) capturing high-speed imagery of the release event.
4. Acrylic test section providing optical access through the cavity and test section for Schlieren and high-speed image capture.
5. Horizontal knife edge to capture the density gradients.
6. Photron[®]high-speed camera for Schlieren image acquisition.

Subfigure (b) illustrates the orientation of the Dantec®high-speed camera with respect to the tunnel section. As depicted, with flow passing left to right, the high-speed camera is on the back side of the test section oriented 70° to the XY plane and 30° to the YZ plane.

Total pressure and temperature values were collected in the stagnation chamber using an Endevco®50 Psia piezoresistive pressure transducer and an Omega®K-Type thermocouple, respectively. Pressure measurements were also collected along the centerline of the cavity ceiling and back wall at orifices $P1$, $P2$ and $P6$ using three 15 Psia Endevco®piezoresistive pressure transducers. Calibration was performed on each transducer using a BetaGauge®330 hand-held pressure calibrator. Calibration functions of the pressure transducers can be found in Appendix F.

3.2 Experimental Methodology

3.2.1 Experimental Procedures

The typical testing process began with model fabrication, where the ice models were allowed to freeze for approximately one hour. Once the models had solidified, they were weighed using a MyWeigh®Durascale 50 gram digital scale. A set of identical molds were used for freezing to improve efficiency and model output. Samples were routinely tested using the scale and calipers to ensure consistent model fabrication. Mold number and model weight were manually noted in an experimental log. Once model quality had been visually inspected and weight verified to be consistent with mold averages, the model was returned to the refrigeration unit while the data acquisition system was prepared.

Prior to testing initiation, the Schlieren system was verified to be functioning properly. After verifying camera shutter speed and frame rate, the horizontal knife-edge was adjusted to adequately capture the density gradients. The tripod mounted

Dantec®high-speed camera was also inspected for a properly oriented view with the correct frame and exposure rates.

Upon verification of the readiness of the testing components, the ice model was removed from the refrigeration unit and transferred to the test section. Gloves and RP tongs were used to reduce the melting rate during transfer. Once the model and sidewalls were properly in place, the DC amplifier readout was used to ensure proper pressure conditions upstream the regulator valve and on the downstream vacuum side. With the pressure conditions verified, the tunnel run was initiated from the tunnel control console. With a properly setup test configuration and an experienced user, the average elapsed time from removing the model from the freezer to test completion was 15 seconds. During this time, model melting was negligible.

The National Instruments®program sequenced tunnel startup and store release. After a 4 sec delay to account for tunnel startup transients, the release was activated by the tunnel control program via the DC power supply to the solenoid. Schlieren image capture was synchronized with the solenoid operation to properly time the drop event. The Dantec®high-speed camera was manually activated using the Motion Studio software along with the FFT spectral analyzer. Both events were timed to adequately capture the release sequence. Upon each successful test, the testing pressure, temperature, and frequency conditions were manually noted in the experimental log.

3.2.2 Test Conditions

Experimentally, drops were assessed at three test conditions, $P_{T,sc}=4, 12$, and 20 Psia. Measured tunnel values for the three test conditions are shown in Table 1. Assuming a calorically perfect gas at $M=2.94$ and isentropic expansion through the nozzle, the following freestream conditions can be determined using the relations in

Table 1. Measured total test conditions and converted values.

M	$P_{T,sc}$ (Psia)	$T_{T,sc}$ ($^{\circ}$ C)	P_T (lb/ft 2)	T_T ($^{\circ}$ R)
2.94	4	25	576	536.7
2.94	12	27	1728	540.3
2.94	20	29	2880	543.8

Equations 34 through 36.

$$\frac{T_{T,sc}}{T_{\infty}} = 1 + \frac{\gamma - 1}{2} M_{\infty}^2 \quad (34)$$

$$\frac{P_{T,sc}}{P_{\infty}} = \left(1 + \frac{\gamma - 1}{2} M_{\infty}^2 \right)^{\gamma/(\gamma-1)} \quad (35)$$

$$a = \sqrt{\gamma R T} \quad (36)$$

where

$(\cdot)_{T,sc}$ = total stilling chamber measured value

$(\cdot)_{\infty}$ = freestream value

T = temperature ($^{\circ}$ R)

M = Mach number

P = pressure (lb/ft 2)

γ = ratio of specific heats

a = speed of sound (ft/s)

R = specific gas constant (ft \cdot lbs/(slug \cdot $^{\circ}$ R))

The values used for R and γ are 1716 and 1.4, respectively. The calculated freestream values are shown below in Table 2. From the calculated values for the freestream

Table 2. Calculated test freestream conditions

P_∞ (lb/ft ²)	T_∞ (°R)	a_∞ (ft/s)	q_∞ (lb/ft ²)
17.2	196.7	687.4	104.3
51.5	198.0	689.7	312.4
85.8	199.3	692.0	519.4

flow, Stokes' law can be used to determine the freestream viscosity.

$$\frac{\mu_\infty}{\mu_o} = \left(\frac{T_\infty}{T_o} \right)^{3/2} \left(\frac{T_o + S}{T_\infty + S} \right) \quad (37)$$

(38)

where

$()_o$ = reference value

T = temperature (K)

μ = dynamic viscosity (N·s/m²)

S = Sutherland's constant (K)

Here, Stokes' law is represented in SI units. The values for μ_o , T_o , and S are 1.716×10^{-5} , 273, and 111, respectively. From there, the following pertinent freestream values could then be determined using Equations 39 and 40 as shown in Table 3.

$$\rho_\infty = \frac{P_\infty}{RT_\infty} \quad (39)$$

$$Re_\infty = \frac{\rho_\infty V_\infty L}{\mu_\infty} \quad (40)$$

where

$$\rho = \text{density (slug/ft}^3\text{)}$$

$Re_{\infty,ft}$ = Reynolds number

L = characteristic length (ft)

Table 3. Test freestream conditions (cont.) and Reynolds numbers.

μ_{∞} (slug/(ft·s))	ρ_{∞} (slug/ft ³)	V_{∞} (ft/s)	$Re_{\infty,ft}$
1.58x10 ⁻⁷	5.11x10 ⁻⁵	2020.9	649600
1.59x10 ⁻⁷	1.52x10 ⁻⁴	2027.6	1929000
1.60x10 ⁻⁷	2.51x10 ⁻⁴	2034.4	3183000

3.2.3 Sphere Model Freedrop Testing

The original research objective was to assess the dynamic response of a sphere released from a cavity into supersonic flow at various q (dynamic pressure) conditions. As previously stated, this was controlled by varying the stagnation pressure of the SVDB. The sphere shape was chosen because of its simple inertial properties, consistent mass distribution, and ease of model fabrication. The 0.94 in diameter sphere was modeled in Solidworks® for RP geometry (mold fabrication) and to determine the mass properties. The mass and inertial properties of the sphere can be seen in Figure 17. Using a sample size of 28, the average measured weight of the sphere was 0.015 lb with a standard deviation of 0.00034 lb. The 5% difference between the measured value and the predicted value is likely due to expansion during the freezing process, where the actual sphere size was slightly larger than the sphere modeled

```

Mass properties of Sphere 46rad ( Part Configuration - Default )

Output coordinate System: -- default --

Density = 57.25 pounds per cubic foot

Mass = 0.0143 pounds

Volume = 0.000250 cubic feet

Surface area = 0.0192 square feet

Center of mass: ( feet )
  X = 0.00000000
  Y = 0.00000000
  Z = 0.00000000

Principal axes of inertia and principal moments of inertia: ( pounds * square feet )
Taken at the center of mass.
  Ix = (1.00000000, 0.00000000, 0.00000000) Px = 0.00000872
  Iy = (0.00000000, 1.00000000, 0.00000000) Py = 0.00000872
  Iz = (0.00000000, 0.00000000, 1.00000000) Pz = 0.00000872

Moments of inertia: ( pounds * square feet )
Taken at the center of mass and aligned with the output coordinate system.
  Lxx = 0.00000872      Lxy = 0.00000000      Lxz = 0.00000000
  Lyx = 0.00000000      Lyy = 0.00000872      Lyz = 0.00000000
  Lzx = 0.00000000      Lzy = 0.00000000      Lzz = 0.00000872

```

Figure 17. Solidworks sphere mass and inertial properties.

in Solidworks®. The low standard deviation validates the consistency between the various models used for testing.

Initially, it was hoped that the sphere might exit the cavity provided the stagnation pressure could be set to the lowest available pressure in the tunnel (4 Psia). This proved not to be the case, as the following chapter shows that at all pressures, the sphere failed to exit the cavity, unless the release was augmented with flow control. The response of the sphere was consistent in that, once translating within the shear layer and impinging on the freestream flow, the sphere returned upward into the cavity, striking the back wall at various displacements in the -Z direction.

3.3 Computational Methodology

To supplement the experimental effort, CFD was used to model the cavity flowfield and the sphere freedrop release event. The OVERFLOW solver was selected because

of its robust capabilities provided by the overset gridding method and the capability to model relative motion between bodies. This lends the OVERFLOW solver well suited for store separation application. Initial efforts were facilitated through a baseline grid generated by Dr. Robert Nichols, a leading coding contributor and expert of the OVERFLOW suite [26]. The grid and validated input files were provided by CDR Neal Kraft, a resident doctoral student. Kraft used OVERFLOW to investigate the unsteady cavity flowfield and its effect on store separation trajectories [16]. The guidance and initial trajectory provided by Kraft proved invaluable at getting the initial numerical solution off the ground.

3.3.1 Initial Efforts

The initial phase of the computational research focused on establishing a baseline case from the grid and inputs provided by Nichols and Kraft, respectively. Although the ultimate objective was to model the same dimensions and flow conditions used within the experimental portion of the research, it was important to build upon the previous efforts for the author to become familiar with the CFD process, specifically using the OVERFLOW solver. Early runs were successfully conducted at $M=0.95$ using a prototype sphere grid. The first iteration of the sphere grid consisted of twelve blocks in a *butterfly* arrangement. Figure 18 is a two-dimensional view of the sphere grid situated in the flow, with the block boundaries highlighted in black. Two major problems were discovered using the initial grid:

1. Insufficient grid overlap - Overset grids require a specific amount of grid overlap between adjacent blocks. The first sphere grid consisted of adjacent blocks with no grid overlap, resulting in an excessive amount of orphan points. This led to non-physical flow discontinuities at the grid boundaries, as highlighted in Figure 18.

2. Improper geometry - The original object, intended to be a sphere, was modeled incorrectly, resulting in a shape similar to a *round football*.

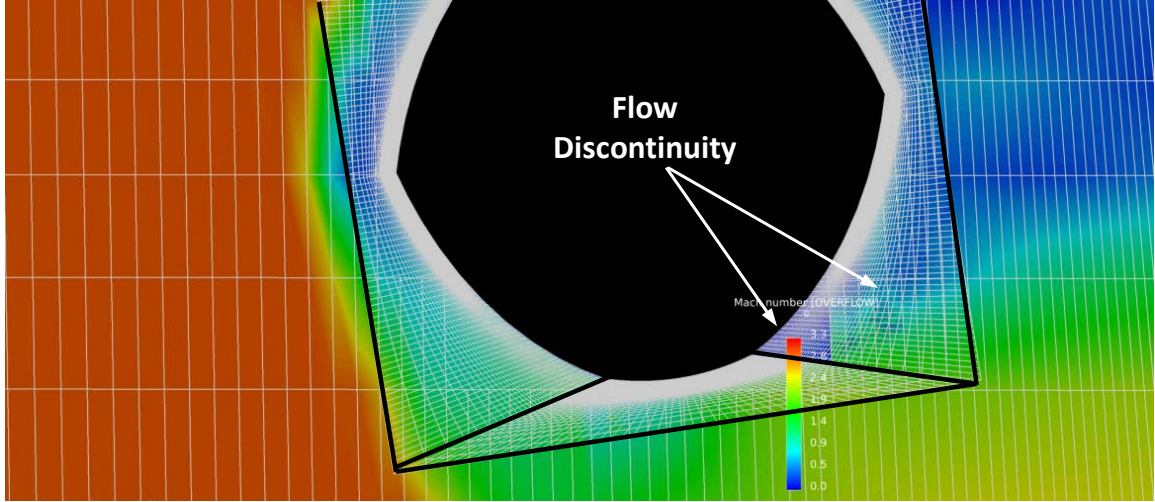


Figure 18. First iteration of the domain surrounding the sphere. Interblock boundaries shown in black.

3.3.2 Final Grid Generation

The multiblock grid used for the computational solution consisted of four separate structured grids (blocks). The first and second blocks were provided in the original Nichols grid [25], named *Plate* and *Bay* respectively. This grid is modeled after the Weapons Internal Carriage and Separation (WICS) tunnel configuration. The WICS dataset has been used extensively to validate cavity specific CFD research [25]. The geometry of the $L/D=4.5$ WICS cavity is 18 in long and 4 in in width and depth. Wall spacing for the *Plate* grid upstream the cavity was set to 0.0075 in. The bay grid had a reduced wall spacing of 0.075 in due to the lower wall shear stress within the cavity [25].

Pointwise[®] was used to generate the grid geometry surrounding the sphere. The

sphere was modeled with the same proportions within the cavity as the experimental setup. In order to minimize skewness and grid distortion along the surface of the sphere, two structured grids were used to define the domain surrounding the sphere. The two overlapping C-type grids, named *Yin* and *Yang*, are based upon the approach proposed by Kageyama and Sato [13]. They consist of identical grids, opposing in orientation, that completely envelope the sphere while providing sufficient overlap required by an overset computational domain. The wall normal grid spacing at the sphere boundary was set to 0.005 in, with a growth rate of 1.2, extruded out to 0.5 in from the surface of the sphere.

The final, multiblock grid input into the OVERFLOW solver is shown in Figure 19. In this figure, the *Bay* grid is shown in black with the *Plate* grid depicted in gray. The inset image provides an enlarged view of the sphere at the release point within the

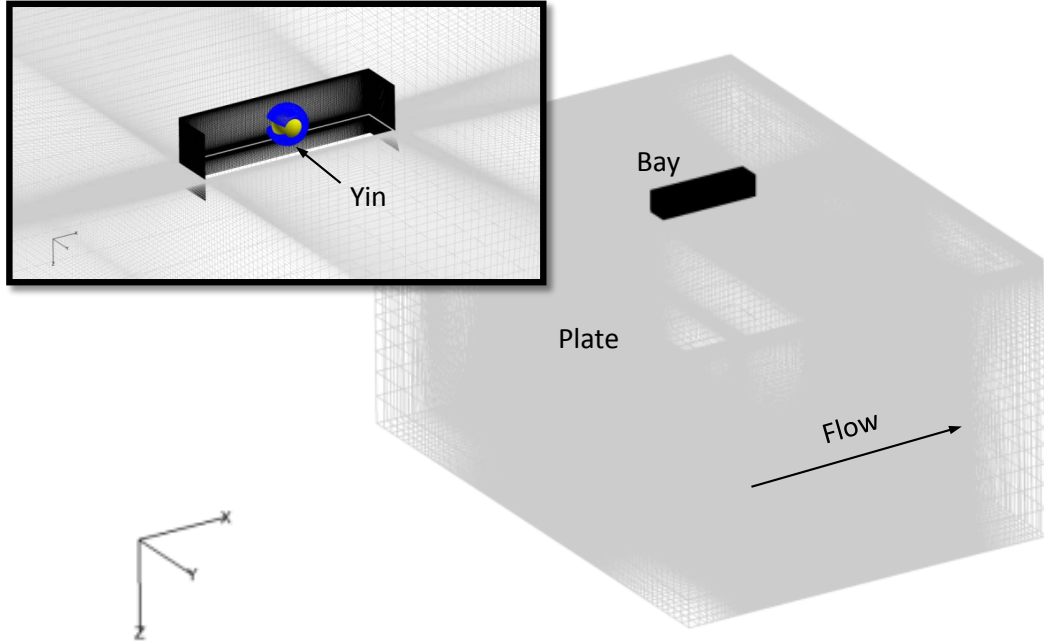


Figure 19. Computational grid view showing Plate (gray) and Bay (black) domains. Subfigure is an inset of the cavity with front and top Bay surfaces hidden to reveal the contained sphere (yellow) and Yin (blue) grid.

cavity. Shown is the *Yin* grid (blue), with the front and ceiling grid surfaces hidden for clarification purposes. The reader should note the orientation of the axis system within the computational domain (X→streamwise, Z→out of the cavity, aligned with the gravity vector). Grid information is summarized in Table 4.

Table 4. Computational domain information.

Block	Name	Cells	Dimensions
1	Plate	5600000	351x201x81
2	Bay	1920000	201x81x121
3	Yin	140000	41x71x51
4	Yang	140000	41x71x51

3.3.3 Boundary Conditions

Figure 20 illustrates the various boundary conditions delineated in the flow solution.

1. Impose freestream
2. Characteristic outflow condition based on Riemann invariants with freestream imposed on incoming characteristics
3. Outflow (pure extrapolation)
4. Inviscid adiabatic wall
5. Viscous adiabatic wall
6. *BC201*

Not depicted in Figure 20 are the *surfaces* of the sphere and the cavity walls, both defined using a viscous adiabatic boundary condition. The *BC201* boundary condi-

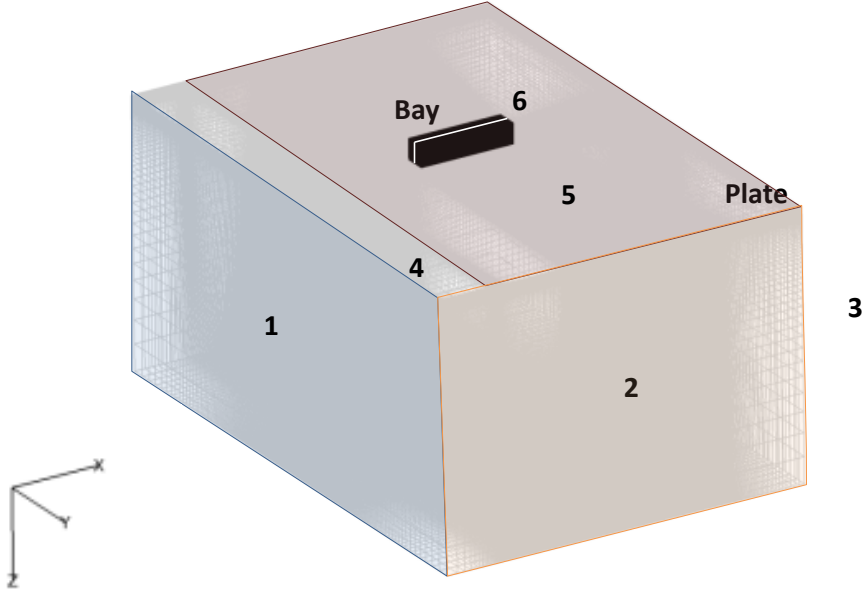


Figure 20. Boundary condition locations.

tion defines a line along the centerline of the cavity, on the front, ceiling, and back faces. This boundary condition provides an output of the conserved variables at each time step.

3.3.4 Overset Grids and Moving Body Simulation

As previously stated, the entire computational grid consisted of four separate blocks (*Plate*, *Bay*, *Yin*, *Yang*). A single, multiblock grid file (*grid.in*) discretized the entire flowfield required for numerical execution. In order to maintain a full 5-point stencil, sufficient grid overlap must yield three layers of fringe points at each block boundary. The sufficient overlap eliminated all orphan points within the multiblock grid, as per the recommendation of the OVERFLOW user's manual. [26]. Figure 21 provides a view of the grid overlap between the *Yin* and *Yang* grids.

Grid *I-blank* regions are set either using a special type of boundary condition or through an entity referred to as an *X-ray*. Boundary condition blanked-out regions are

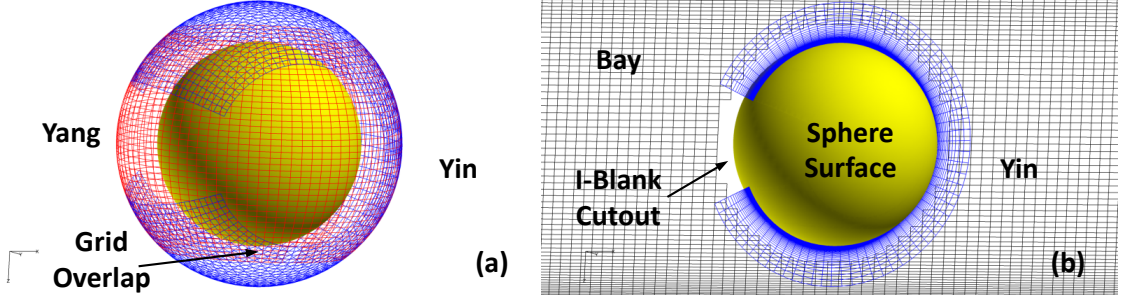


Figure 21. Enlarged view of sphere grid showing (a) Yin (blue) and Yang (red) grids and (b) background Bay grid (black) with a centerline computational surface of the Yen grid, showing grid spacing and I-blank hole cutting.

used for situations where both grids are static, as is the case with a blanked-out region of the *Plate* grid (overlapped by *Bay* in the vicinity of the shear layer. An x,y array of pierce points (*X-ray*), is tied to the moving body entities and translates/rotates with the body, providing dynamic hole cutting during 6-DOF simulations. Figure 21 (b) provides a view of the centerline computational surface of the *Yin* grid and the blanked out region of the background *Bay*. Recommended practice [26] is to specify an *X-ray* distance such that the hole is cut outside the moving body boundary layer while providing the required overlap for the fringe point requirement of the given flux algorithm. This approach was followed as suggested.

The original location of the sphere blocks within the *grid.in* file was at the origin, shown in Figure 22. The prescribed motion capability of OVERFLOW was invoked to move the sphere to the center of the cavity (24.0, 0.0, -2.0). The sphere inertial and mass properties were non-dimensionalized in accordance with the scheme presented in Chapter II and specified in the input file *scenario.xml*. A delay of 1000 time steps (approximately 350 iterations) allowed initial solution transients to subside prior to release. Once the initial numerical transients subsided, the sphere was allowed to freefall (using a non-dimensional gravity term) in the +*Z* direction. Figure 23 provides visualization of the moving sphere grids during a full 6-DOF dynamic run. Subfigure (a) depicts the sphere at the release location, centered in the cavity. Subfigures (b) and

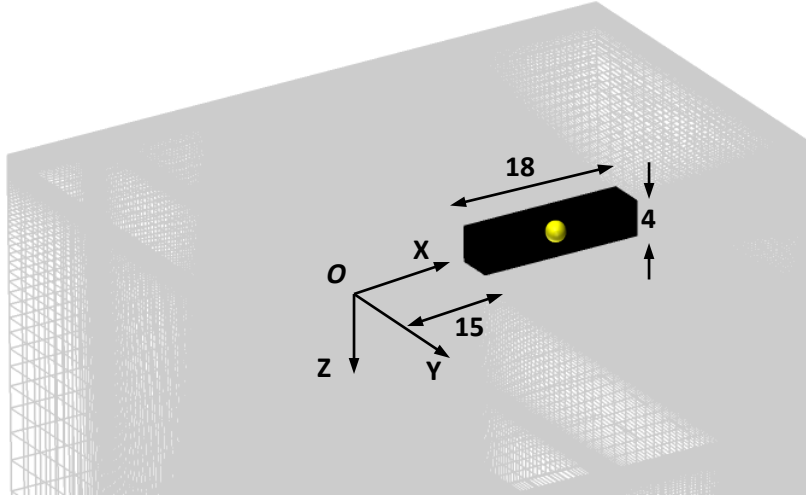


Figure 22. OVERFLOW grid coordinate system and bay dimensions (all dimensions are shown in inches).

(c) depict relative grid movement of the sphere throughout a full dynamic run. Once dynamic motion was initiated for the run, OVERFLOW calculated the forces and moments every 10th iteration and repositioned the associated sphere grids according the full 6-DOF equations of motion. With each grid reposition, DCF reassembled a new computational domain based upon the updated position of the moving *Yin* and *Yang* grids, while also cutting the holes of the background grid according to the specifications of the *X-rays* assigned to the sphere body.

3.3.5 Grid Scaling and Non-Dimensionalization

This research attempted to validate a numerical solution by comparing the WICS computational bay the dimensionally similar SVDB cavity. The experimental scale of the SVDB cavity ($L=6.75$, $D,W=1.5$) was 3/8th scale the physical WICS bay. In computational space, the cavity spanned 15.0 to 33.0 in X , -2.0 to +2.0 in Y , and 0.0 to -4.0 in Z . When scaling dimensionally, the key parameter is L_{ref} (ft/grid unit). For all runs, L_{ref} was equal to 0.0313 ft/grid unit. L_{ref} is used throughout

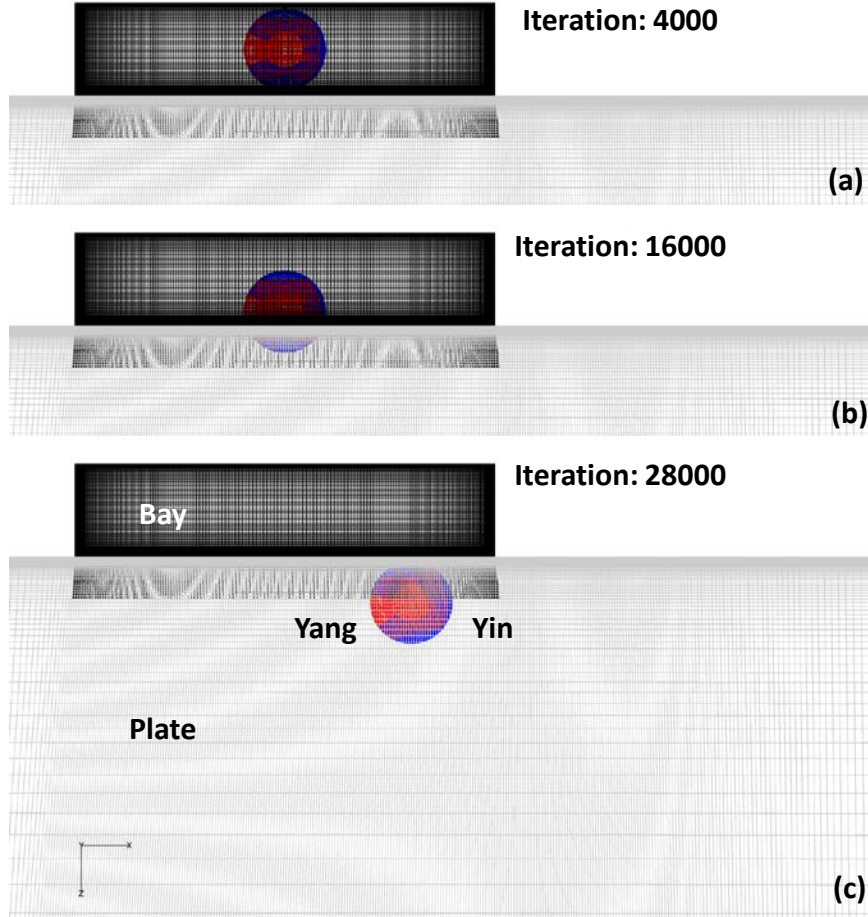


Figure 23. Grid relative movement from a 6-DOF run showing translation and rotation of Yin and Yang (sphere) grids.

the non-dimensionalization of both the flow and mass/inertial properties, as seen in Chapter II. The primary mechanism of changing the scale of the cavity from the WICS dimensions to the SVDB cavity was through the Reynolds number. OVERFLOW specifies Reynolds number per unit grid length, therefore, to scale down the numerical bay *dimensions* to actual SVDB tunnel dimensions, the input Reynolds number was converted from physical space (Re_{ft}) to computational space ($Re_{gridunit}$) using L_{ref} .

Not only must the aerodynamic properties be scaled correctly from computational to physical space, but the inertial properties must be properly non-dimensionalized

as well. The model properties (mass and inertial) are specified non-dimensionally in the input file *scenario.xml*. The dimensional properties used in the calculations were based upon the actual sphere size as tested in the tunnel (radius = 0.47 in). Using a model density equal to frozen tap water ($\rho_{ice}=1.94$ slugs/ft³), the weight was calculated to be 0.0156 lb. This weight corresponded well with the average, measured model weight (0.015 lbs) and the Solidworks® mass property output. Using Equation 41, the moment of inertia was calculated (in the pitch plane) to be $I_{yy} = 2.96 \times 10^{-7}$ slugs · ft².

$$I_{yy} = \frac{2}{5}mr^2 \quad (41)$$

This value also corresponds well with the values produced by Solidworks®.

3.3.6 Approach to CFD Solution

Flow and inertial inputs were chosen to correspond with the operating pressures and temperatures of the wind tunnel along with the dimensions and properties of the experimentally tested sphere. The dimensional values used in calculating the non-dimensional OVERFLOW inputs are given below in Table 5. Run CT1B was

Table 5. Dimensional CFD flow parameters.

Run	Δt (sec)	M	P_T (lb/ft ²)	T_T (°R)	$Re_{\infty,ft}$
CT1B	5.0×10^{-6}	3	576	533	640000
CT1B_D	5.0×10^{-6}	3	576	533	640000
CT4B_D	5.0×10^{-6}	3	1728	537	1930000
CT2B_D	5.0×10^{-6}	3	288	537	320000
CT3B_D	5.0×10^{-6}	3	144	528	161000

initiated as the *baseline* numerical solution, corresponding with the lowest test pressure in the wind tunnel ($P_{T,sc}=4$ Psia). This run was a static run, with the store

suspended, centered in the cavity. Run CT1B_D was run under the same flow conditions while invoking a dynamic release of the store.

The reader should note that the tested sphere release point was not precisely at the same corresponding position in computational space. Experimentally, the release mechanism held the sphere in the captive position with the sphere c.g. located 3.44 in aft the leading edge and 0.625 up from the cavity face. In computational space, the sphere was released from the coordinates (24.0, 0.0, -2.0) (as measured from the grid origin). This corresponded with a dimensional equivalent of 3.38 in from the leading edge and 0.75 up from the face of the cavity. This difference was noticed during post processing, yet considered negligible as the sphere did not interfere with the shear layer in the captive position either in the experiment or the CFD simulation.

Run CT4B_D corresponds with the $P_{T,sc}=12$ Psia runs. Although consideration was given to matching a numerical solution with the the 20 Psia experimental runs, the additional run was not performed for the following reasons: 1) further increasing the Reynolds number would require grid refinement for an accurate solution and 2) the sphere failed to exit the cavity at the lower stagnation pressures, meaning no further insight to the model dynamics would be gained at the higher pressures.

Runs CT2B_D and CT3B_D were both run at stagnation pressures of 2 and 1 Psia, respectively. These runs were conducted at pressures below those capable in the SVDB tunnel in an effort to attain a successful separation event from the cavity.

The flow inputs varied between runs, yet all other settings specified in the OVERFLOW .in input file were consistent from run to run. Most settings were previously set in the baseline case provided by Nichols. These settings take advantage of the latest numerical and computational capabilities of OVERFLOW version 2.1. Some of the primary settings can be seen in Table 6. The reader is referred to the work of Pulliam [27] for further detail in the finite-difference, numerical schemes available

Table 6. Key OVERFLOW settings.

Parameter	Setting
Numerical Method (RHS)	HLLC Upwind Scheme with van Albada limiters 5 th -order spatial terms
Numerical Method (LHS)	SSOR 2 nd -order in time with Newton subiterations
Viscous Terms	2 nd -order differencing for convection terms including all viscous cross-terms
Turbulence Modeling	DDES with SST RANS model

to OVERFLOW, particularly, those incorporated in the computational efforts of this research.

As previously stated, the background grid and baseline input settings were verified by Nichols and validated against the WICS dataset [25]. In his paper, Nichols assessed various hybrid RANS/LES models using the WICS geometry. Research was performed using the OVERFLOW 2.1 solver with a 2nd-order time and 5th-order spatial flux algorithms. Flow conditions used in his modeling were $M=0.95$ ($Re_{ft}=2.5 \times 10^6$) and 1.75 ($Re_{ft}=2.5 \times 10^6$) The Shear Stress Transport/Delayed Detached Eddy Simulation (SST/DDES) hybrid RANS/LES turbulence model was compared against other hybrid turbulence models, showing promising results at accurately modeling the unsteady flow of the WICS cavity [25].

Selection of the appropriate turbulence model (and associated settings) is critical when assessing flow around a cavity due to the massive separation that can occur in the shear layer and the general unsteadiness of the flowfield. The research uses the power of the SST/DDES hybrid turbulence model, a combination shown to accurately model the physics of cavity flow [25]. Recognizing the optimum zones for the $\kappa - \omega$ and the $\kappa - \epsilon$, Menter and Rumsey proposed a turbulence model that used a blended function to force the model to perform as a $\kappa - \omega$ in the near wall region and a $\kappa - \epsilon$ model away from the wall and in the region of the shear layer [21]. In addition

to Menter's SST RANS model, the latest version of DES was used to simulate the large scale, anisotropic turbulent structures. *Delayed* DES improves upon the original version by ensuring the LES branch is not invoked early (within the boundary or shear layer) by improperly spaced grids. For further information of SST/DDES hybrid turbulence model, the reader is referred to the work of Spalart et al. [29]. Wall functions were used in the solution with plate grid spacing providing a Y^+ value of 5 at $P_o=1$ Psia and 27 at 12 Psia. The sphere grid spacing, when subject to the freestream flow, yielded a Y^+ value < 1 (1 Psia) and 2 (12 Psia).

Using the Nichols generated background grids (*Plate*, *Bay*) and the grids (*Yin*, *Yang*) generated during this research, the solution was initiated at the flow conditions of the baseline input files previously verified by Kraft [16]. The solution was progressively stepped from Mach 0.95 to 3.0 through a series of *.restart* files. After 3000 combined iterations, the solution was stable enough for the higher Mach number flow (3.0). This solution file, *q.3000*, was for each subsequent computational run. This *restart* file allowed the solver to be initialized using a previous solution, thereby improving the initial stability of the solution.

The physical time step was initially 5.0×10^{-5} , consistent with the timing used by Nichols [25]. This time step yielded temporal residuals on the order of 10^{-2} to 10^{-1} , assessed to be too high. Because the objective was to attain a reasonable solution, vice one that was computationally efficient, the time step was reduced to 5.0×10^{-6} for all final runs.

The primary OVERFLOW flow parameters input to the solver can be seen in Table 7. The time step is non-dimensionalized in accordance with the scheme of Chapter II, while the Reynolds number is converted to grid units via L_{ref} . These inputs correspond with physical values of Table 5.

In addition to the flow inputs, the mass and inertial properties were non-dimensionalized

Table 7. OVERFLOW inputs.

Run	Δt^*	M	T_∞ (°R)	Re_∞ (1/grid unit)
CT1B	0.32	3	190.36	20000
CT1B_D	0.32	3	190.36	20000
CT4B_D	0.326	3	191.79	60300
CT2B_D	0.326	3	191.79	10000
CT3B_D	0.323	3	188.6	5030

in accordance with Chapter II and delineated in the input file *scenario.xml*. The sphere properties for each dynamic release computation run are shown in Table 8.

Table 8. OVERFLOW sphere mass and inertial properties.

Run	Re_d	g^*	m^*	I^*
CT1B_D	5.00x10 ⁴	2.44x10 ⁻⁷	3.31x10 ⁵	2.07x10 ⁵
CT4B_D	1.51x10 ⁵	2.42x10 ⁻⁷	1.11x10 ⁵	6.94x10 ⁴
CT2B_D	2.50x10 ⁴	2.42x10 ⁻⁷	6.64x10 ⁵	4.17x10 ⁵
CT3B_D	1.26x10 ⁴	2.47x10 ⁻⁷	1.31x10 ⁶	8.19x10 ⁵

Fieldview® was used to analyze to time-dependent and time-average solution files *q.iteration*. Excel® and MATLAB® were used to analyze the data that were produced in the files *animate.out*, *resid.out* and the output from the *BC201* file. The *BC201* file is unique in that it provides the solution (conserved variables) at each time step. This was used for a time-varying analysis of the pressure along the centerline of the cavity. The MATLAB files used during post-processing are provided in Appendix A.

The reader should note that the *BC201* file produces the conserved variables of the Navier-Stokes equation. As shown in Equation 23, pressure is not an explicit output of the *BC201* file. The non-dimensional pressure was derived from the following equation:

$$p^* = (\gamma - 1)\rho^*(e_o^* - \frac{1}{2}\vec{V}^2) \quad (42)$$

where

$()^*$ = non-dimensional value

p^* = pressure

γ = ratio of specific heats

ρ^* = density

e_o^* = total energy

\vec{V} = velocity (0 - stagnation point at no-slip wall)

The non-dimensional pressure was converted to physical pressure according to Chapter II.

As with any computational solution, the residual values of the solution provide a qualitative view of the stability of the numerical solution. With an unsteady flow solution such as cavity flow, true convergence will never be attained, yet stability may be assessed from the residuals of the higher-order numerical algorithms. Figure 24 shows the residual history of run CT1B (no drop). Plotted in Figure 24 is the combined L_2 Norm of both the temporal and spatial residuals for each grid. As previously stated, the solution begins using a *restart* file at iteration 3000. The first 300 iterations are stepping through the grid sequencing process, indicated by the residual spike. Iterations 3500-4600 contain the period where both the numerical and physical (shear layer) are reaching a *stabilized* state. At iteration 4600, with the residuals fluctuating between 10^{-4} and 10^{-6} , the solution can be assessed as stable, but not converged.

Figure 25 provides a view of the residuals from a dynamic release solution. Again,

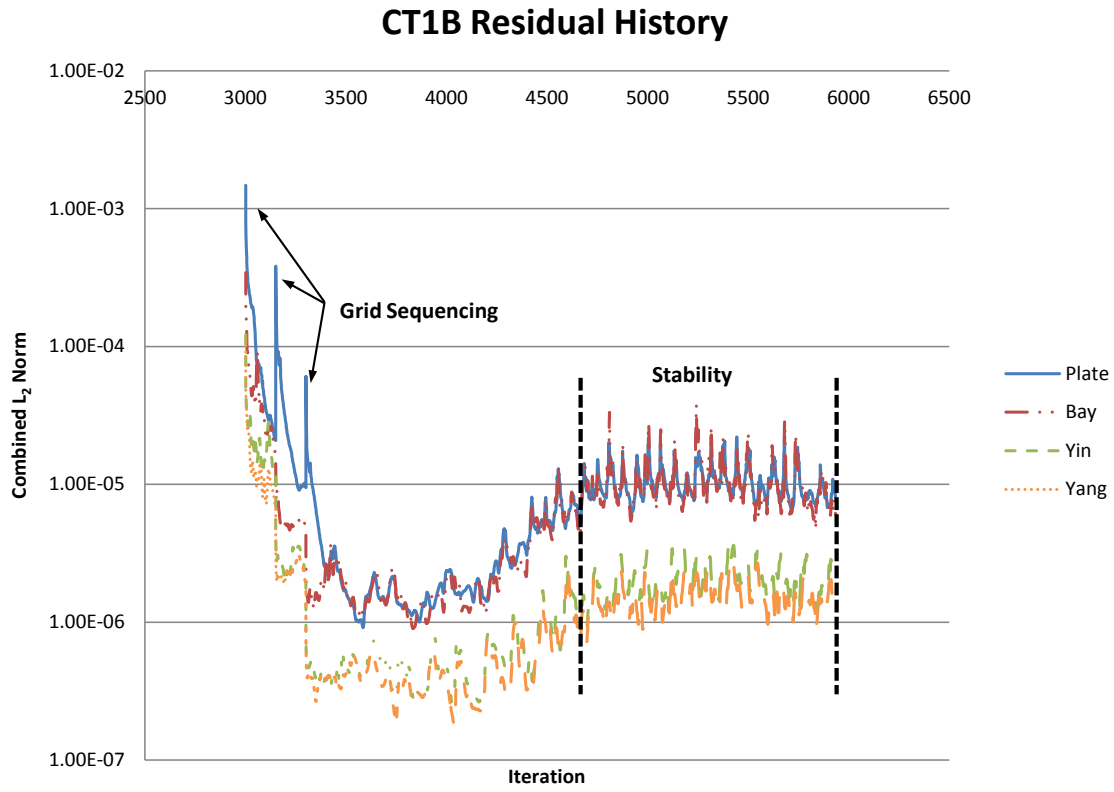


Figure 24. Combined residuals (LHS and RHS) for run CT1B.

the stability region begins at iteration 4600 and continues through the end of the run, with a slight spike as the sphere penetrates the shear layer. As the sphere enters the shear layer, massive separation occurs within the flow, yielding the residual spike around iteration 17500.

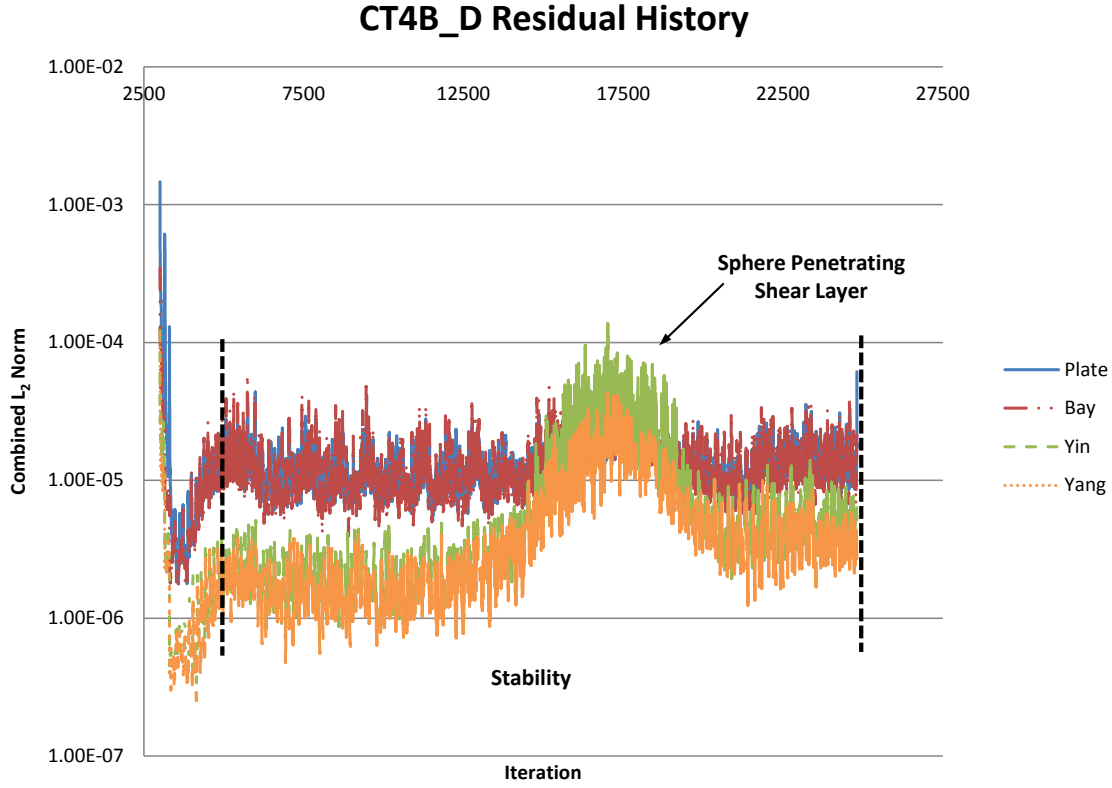


Figure 25. Combined residuals (LHS and RHS) for run CT4B_D

3.4 Passive Flow Control

One important experimental research objective was to determine sphere translation and rotation response as a function of dynamic pressure. Ideally, the tunnel stagnation pressure could be lowered enough for clean separation to occur. For this research, the tunnel was unable to reach stagnation pressures low enough for a clean release.

The test section cavity was designed with the capability to incorporate a leading edge spoiler device. In keeping with the scope and time constraints of the research, a passive spoiler was chosen as the flow control device over more effective, active means [3, 30]. The spoiler design consisted of two spoilers, both spanning $1/3^{\text{rd}}$ the width of the cavity and consisting of a sawtooth edge (Fig. 26). The shorter of the two, *short*

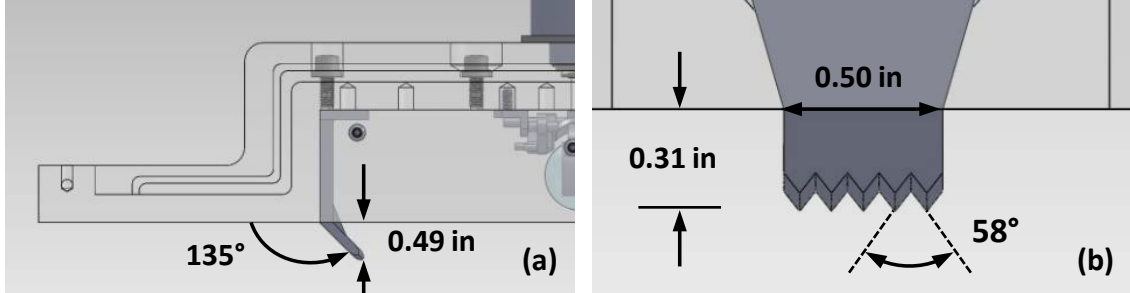


Figure 26. Depiction of (a) long sawtooth spoiler (flow left to right) and (b) streamwise view of short sawtooth spoiler.

sawtooth (SST), protruded into the freestream flow 0.31 inches, or approximately 1δ . The longer *tab* tested protruded into the freestream at approximately twice the height of the incoming boundary layer (2δ). This device is referred to as *long sawtooth* (LST). Both the SST and LST had five teeth on the tip of the device.

The sawtooth design has been shown to be effective at reducing the cavity acoustic levels [7] and possibly enhancing store separation. The reader should note that past research suggests the effectiveness of the spoiler device is maximized in the subsonic and transonic regime, with limited usefulness in supersonic flow [7]. Where Dix assessed a sawtooth device that spanned the width of the cavity, this research used a tab style design with hopes that the device would induce streamwise vortices in the shear layer and cavity, possibly creating a downward force ($+Z$) force on the store. Both the streamwise vortices and the turbulent structures created by the sawtooth would likely contribute to the destabilization of the shear layer, ultimately disrupting the feedback mechanism required for Rossiter tones.

3.5 Generic Air-to-Ground Store Release

While the sphere model presents a shape that simplifies the scaling laws and eliminates pitch considerations, the applied purpose of scaled model testing is to simulate a geometrically similar full-size store. To this end, the ice model process was

applied to a shape more representative of an actual air-to-ground store, in this case a Mk-82 500 lb class general purpose weapon.

In the case of the sphere, each model was consistent, one to the next, in both weight and c.g. Fabricating a 1/20th scale Mk-82 out of ice was not as repeatable. An acceptable model (all fins in tact) was produced approximately 3 of 4 builds. The average model weight, using five separate molds, was calculated to be 0.030 lbs, with a standard deviation of 0.00073 lbs. While model weight proved to be consistent, variations existed between each model in surface roughness and nose shape. Likely, the c.g. varied between models.

The ice store was modeled in Solidworks® and displayed in Figure 27. The notable

Mass properties of Mk-82_05 (Part Configuration - Default)

Output coordinate System: -- default --

Density = 57.251 pounds per cubic foot

Mass = 0.0283 pounds

Volume = 0.000495 cubic feet

Surface area = 0.0521 square feet

Principal axes of inertia and principal moments of inertia: (pounds * square feet)
Taken at the center of mass.

lx = (1.00000000, 0.00000000, 0.00000000)	Px = 0.00000758
ly = (0.00000000, 0.70710678, -0.70710678)	Py = 0.00019517
lz = (0.00000000, 0.70710678, 0.70710678)	Pz = 0.00019517

Moments of inertia: (pounds * square feet)
Taken at the center of mass and aligned with the output coordinate system.

Lxx = 0.00000758	Lxy = 0.00000000	Lxz = 0.00000000
Lyx = 0.00000000	Lyy = 0.00019517	Lyz = 0.00000000
Lzx = 0.00000000	Lzy = 0.00000000	Lzz = 0.00019517

Figure 27. Solidworks store mass and inertial properties.

properties are weight and moments of inertia, which are used when calculating the scaling laws. Figure 28 provides a comparative illustration between the ogive nose/-conical fin Mk-82 variant (dimensions at full scale) and the ice store model (1/20th

scale). The c.g. of the actual store is $0.42L$, while the ice model c.g. is located 48% the length of the model, therefore, the ice model is less stable in pitch than the full-scale article.

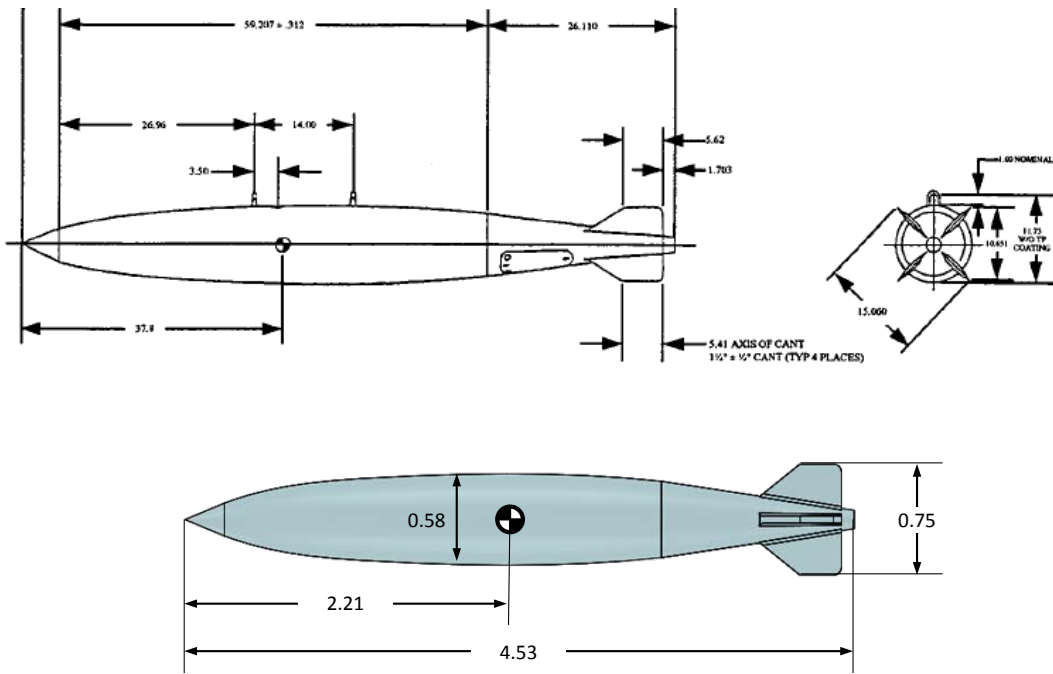


Figure 28. Comparison between full-size Mk-82 and 1/20 ice model. All dimensions are in inches.

IV. Results and Analysis

4.1 Cavity Conditions

4.1.1 Clean Cavity Flow

The first step of the experimental process was to assess the character of the shear layer at the three primary test conditions ($P_{T,sc} = 4, 12$, and 20 Psia). Cavity shear layer behavior may be dependent on the state of the incoming boundary layer (laminar/turbulent) [19] and therefore it was important to assess the condition of the upstream boundary layer as shown in Figure 29. This image was captured at the

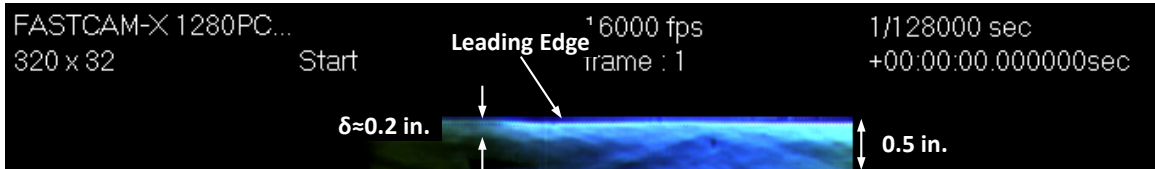


Figure 29. Schlieren imagery of incoming boundary layer at 20 Psia stagnation pressure.

highest test condition (20 Psia) due to the higher density gradients being more distinct in the flow when compared with the lower pressures tested. Qualitative analysis of the density (and therefore velocity) gradients on the Schlieren imagery yielded an estimated boundary layer depth of approximately 0.2 in (5 mm). For reference purposes, the height of the Schlieren image corresponds with 0.5 in displacement from the tunnel ceiling/cavity face. Using an Re_{ft} on the order of 3 million (corresponding with the 20 Psia total pressure), turbulent boundary layer theory yields $\delta_{99}=0.22$ in. Greene used particle image velocimetry (PIV) to assess the boundary layer within the SVDB at test conditions similar to those shown in Figure 29, resulting in a measured boundary layer thickness of 6 mm, or 0.24 in [8]. The satisfactory agreement

between Schlieren imagery, analytical estimates, and PIV confirms the presence of a fully developed, turbulent boundary layer upstream the leading edge of the cavity.

Figure 30 provides comparison between the Schlieren imagery taken at 4 Psia and 20 Psia stagnation pressures. As previously discussed, the higher stagnation pressures yielded sharper visualization of the pressure gradients, providing a higher degree of contrast of the flow structures visualized in the Schlieren photography. Also shown in

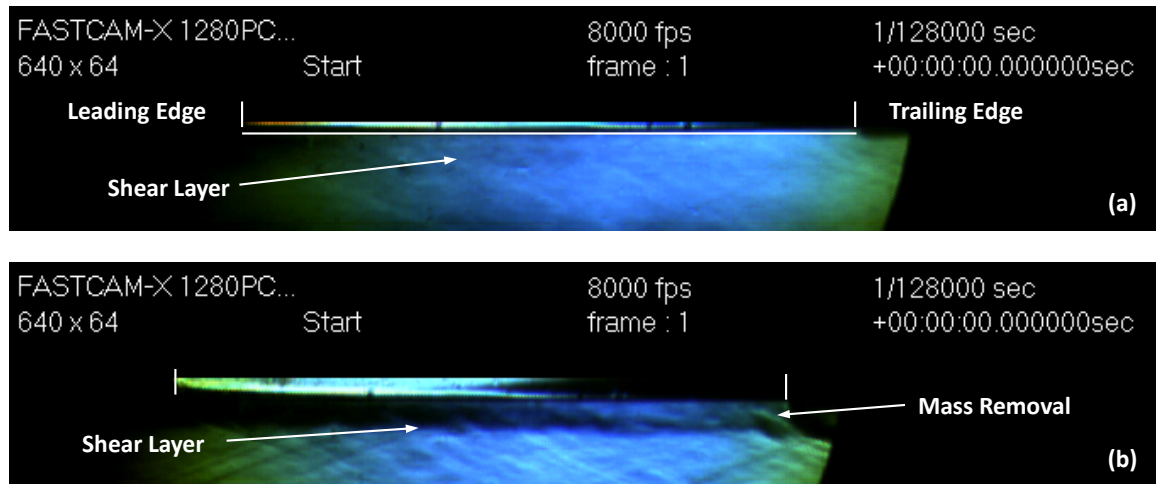


Figure 30. Schlieren imagery of shear layer (clean cavity) at (a) 4 Psia and (b) 20 Psia stagnation pressure.

Figure 30 are the reference points of the cavity, which provide visual context in the proceeding images of the cavity shear layer (flow direction left to right). In Subfigure (a), the shear layer is barely visible along the cavity face. Subfigure (b), the highest tested stagnation pressure, provides better visualization of the flow. Both images are captured at 8 kHz, yielding a image resolution of 640 x 64, proving sufficient to capture the entire cavity length. Clearly visible in Subfigure (b) is the cavity shear layer, contrasted in black against the blue freestream. Also visible is a flow structure at the trailing edge of the cavity, likely due to the mass removal phase associated with the hydrodynamic process of the fluctuating shear layer.

Figures 31 and 32 are all captured at a frame rate of 8 kHz using an 8 μ s shutter speed. This frame rate provides adequate temporal resolution to capture the expected time scales of the vortical structures (3 kHz) while providing full imaging of the entire cavity. Each image sequence contains five frames spanning 0.5 ms.

One fundamental mechanism contributing the sustainment of periodic oscillation seen in the shear layer is the hydrodynamic effect due to mass entrainment into and out of the cavity. While the shear layer is not distinctly shown in Figure 31, frames 2 and 3 show flow structures likely due to the mass flow exiting the cavity (*cavity exhale*).

The highest stagnation pressure tested (20 Psia) affords the clearest view of the flow structures dominating the flow about the cavity face. Although increasing the total pressure increases the Reynolds number, from a qualitative perspective, the oscillatory nature of the shear layer remains unchanged. This is consistent with the finding of Heller and Bliss [10]. Figure 32 clearly shows a variety of flow features captured in the Schlieren image sequence. First, the shear layer is easily distinguishable. Second, the shock waves created by the vortical structures are clearly seen as lighter, linear structures at the lower center of each frame (especially visible in frame 4). Also seen are the reflected shocks from the tunnel floor, shown as darker, linear features towards the leading edge of each frame (Fig. 32).

4.1.2 Captive Sphere Cavity Flow

To supplement the qualitative representations of the shear layer provided by Schlieren, the content of the cavity pressure signal provides a quantitative perspective on the time-dependent nature of the local conditions within the cavity. For an $L/D=4.5$, longitudinal oscillations dominate the cavity whereby transducer *P6*, located on the back wall, was the ideal location for sensing these pressure variations.

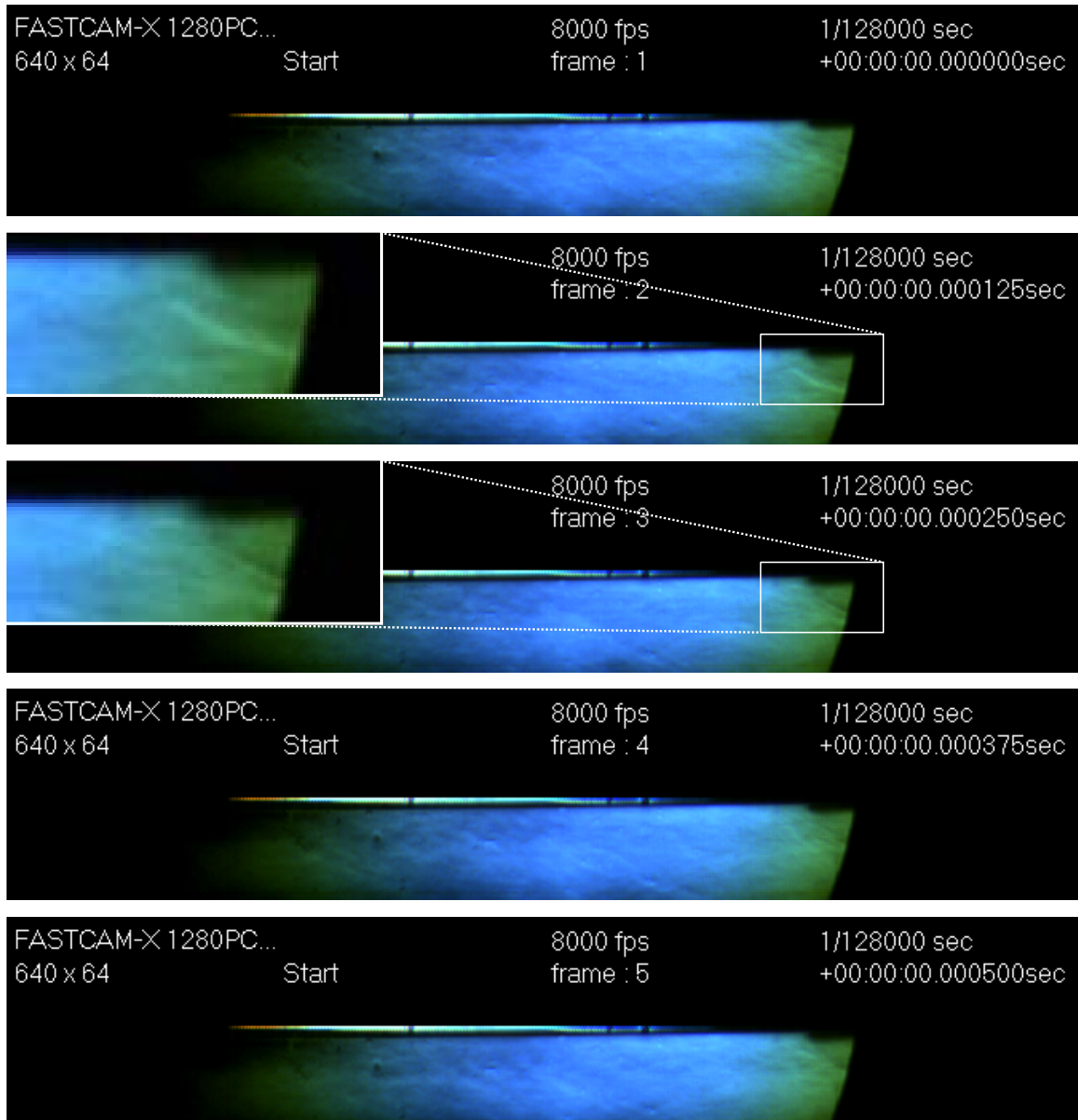


Figure 31. Image sequence of run 525C1 (4 Psia). Capture rate = 8 kHz, shutter speed = 8 μ s.

The preceding Schlieren images captured a clean cavity configuration. To be more consistent with the CFD cavity analysis, which was conducted with a sphere in the release position, experimental frequency data was collected with a captive sphere in the release position. Figure 33 indicates that the acoustic levels within the cavity are

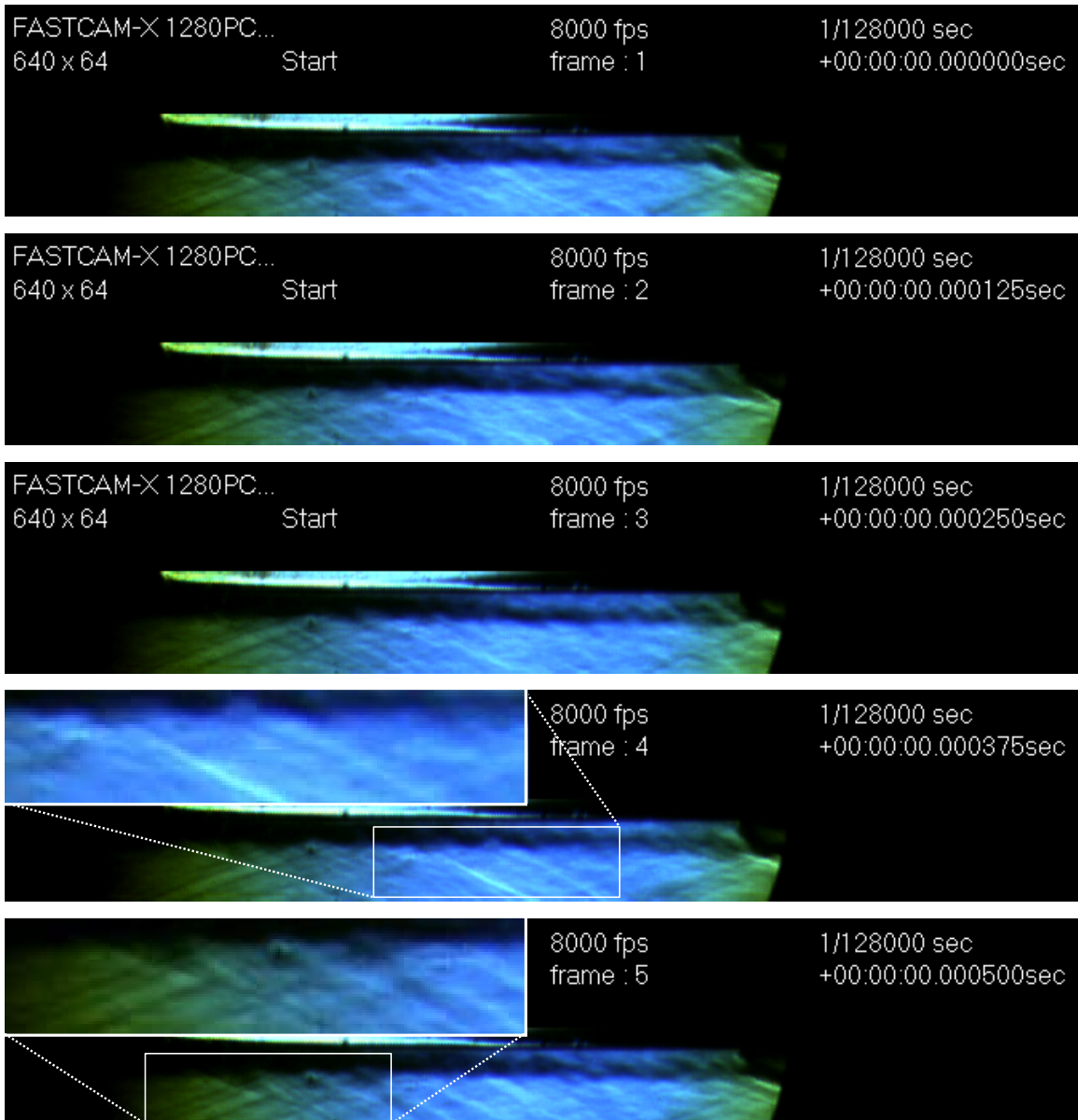


Figure 32. Image sequence of run 525C4 (20 Psia). Capture rate = 8 kHz, shutter speed = 8 μ s.

nearly identical in amplitude and frequency in both configurations (clean and captive sphere).

The PSD of the $P6$ pressure signal was provided by converting the signal output (V_{rms}) from the spectral analyzer, averaging over 20 samples, and plotting against frequency. As shown in Figure 34, strong periodic frequency content is clearly present

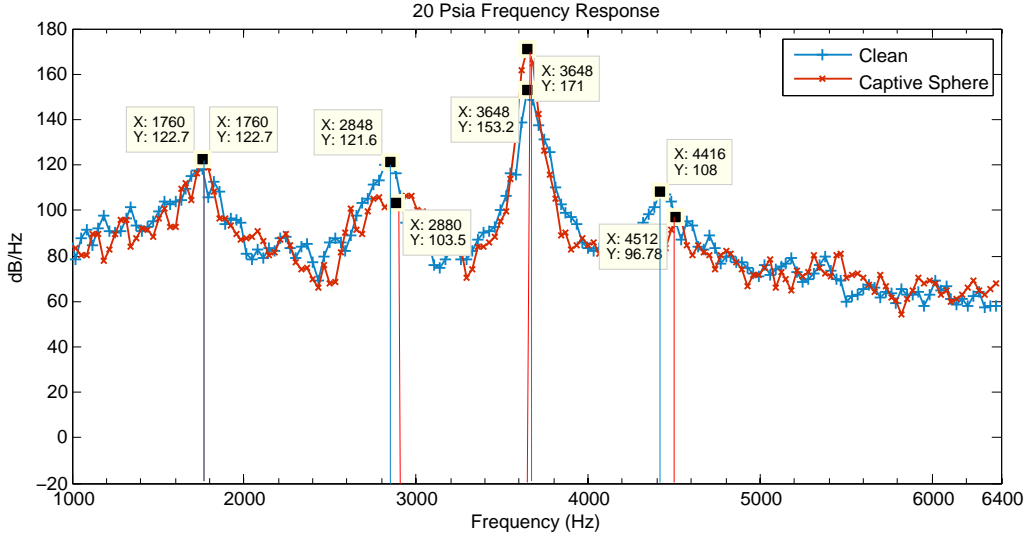


Figure 33. SPLs of a clean cavity and a cavity with a captive sphere in the release position.

in modes 2 and 4, with slight spectral peaks in modes 3 and 4. For comparison,

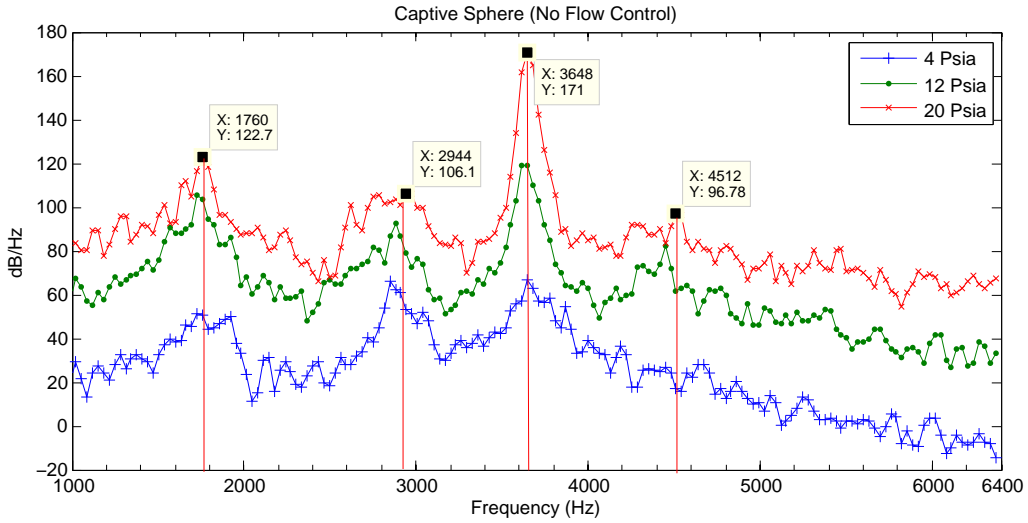


Figure 34. SPL (captive sphere in cavity) at 4, 12, and 20 Psia

Heller's equation (Eq. 2) provides expected modal frequency spikes. Equation 2 was computed with the following inputs: $L=0.56$ ft, $M=2.94$, $\beta=0.25$, and $k_c=0.57$. Velocities of 2015, 2025, and 2035 ft/s were used as the velocities calculated at 4, 12,

and 20 Psia, respectively. Strong correlation exists between the predicted dominant

Table 9. Analytical and experimental frequency comparisons using a captive sphere.

4 Psia

mode	<i>Str</i>	Heller et al	Experimental
		<i>f</i> (Hz)	<i>f</i> (Hz)
1	0.21	760	No distinct peak
2	0.50	1774	1760
3	0.78	2787	2848
4	1.06	3801	3648
5	1.34	4814	No distinct peak
6	1.63	5828	No distinct peak

12 Psia

mode	<i>Str</i>	Heller et al	Experimental
		<i>f</i> (Hz)	<i>f</i> (Hz)
1	0.21	764	No distinct peak
2	0.50	1783	1728
3	0.78	2801	2880
4	1.06	3820	3616
5	1.34	4839	4448
6	1.63	5857	No distinct peak

20 Psia

mode	<i>Str</i>	Heller et al	Experimental
		<i>f</i> (Hz)	<i>f</i> (Hz)
1	0.21	767	No distinct peak
2	0.50	1791	1760
3	0.78	2815	2976
4	1.06	3839	3648
5	1.34	4862	No distinct peak
6	1.63	5886	No distinct peak

frequencies and those measured experimentally. Measured mode 2 peaks lie within 1-3% of analytical values while at the higher modes (3 and 4), the values diverge to approximately 7% difference between predicted and measured frequencies.

Analyzing the time-dependent pressure signal provides a quantitative means by which to compare the experimental and computational results. Figure 35 shows the temporal comparison of the time-varying pressure output from the *BC201* file and the $P(t)$ signal from tunnel *P6* transducer. Subfigure (a) shows the entire time signal

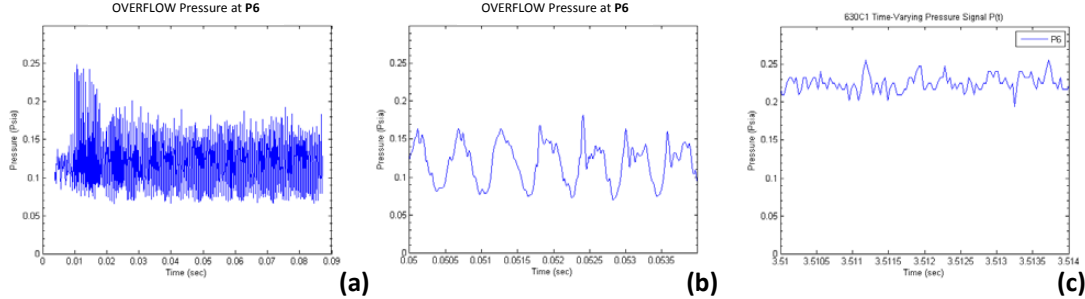


Figure 35. Time-varying pressure signal from **OVERFLOW** at location of **P6** showing complete run (a) and a data sample from time 0.05 to 0.054 (b). Subfigure (c) provides a visual comparison with experimental pressures from transducer **P6**.

for the complete CT1B_Long run, while (b) is an enlarged view of the computational pressure solution over a 4 ms segment. Periodicity of the pressure signal is clearly seen in Subfigure (b), with peak values corresponding to the second Rossiter mode. Subfigure (c) shows the experimental time signal segment beginning at 3.51 sec (to allow tunnel transients to settle), also over a 4 ms interval. While the pressure fluctuations measured experimentally are not as clear as the numerical solutions, the pressure amplitude corresponds adequately with the pressure amplitude of the CFD results (slightly under predicted numerically). The amplitude discrepancy between the numerical and computational results is likely due to the signal sensitivity limits of the transducer/digital data acquisition system combined with the low absolute mean pressure (≈ 0.22 Psia).

A common way of comparing time-varying outputs is to decompose the signal from temporal basis to a frequency spectrum. As discussed in Chapter III, run CT1B_Long

was allowed to run for roughly 17000 iterations to provide a longer time duration from which to process the spectral density using Welch's method [31]. The graph in Figure 36 shows a plot of an experimental run at 4 (green) and 12 (red) Psia total pressures (captive sphere) compared against the OVERFLOW pressure output from the back wall location corresponding to experimental transducer *P6* (also run at 4 Psia stagnation pressure). This highlights the capability to validate the numerical results with experimental values collected in the same research effort. Although the 12 Psia plot does not correspond with the total pressure input to OVERFLOW (4 Psia), it does provide a stronger signal with which to compare the frequency content between experimental runs and numerical simulation.

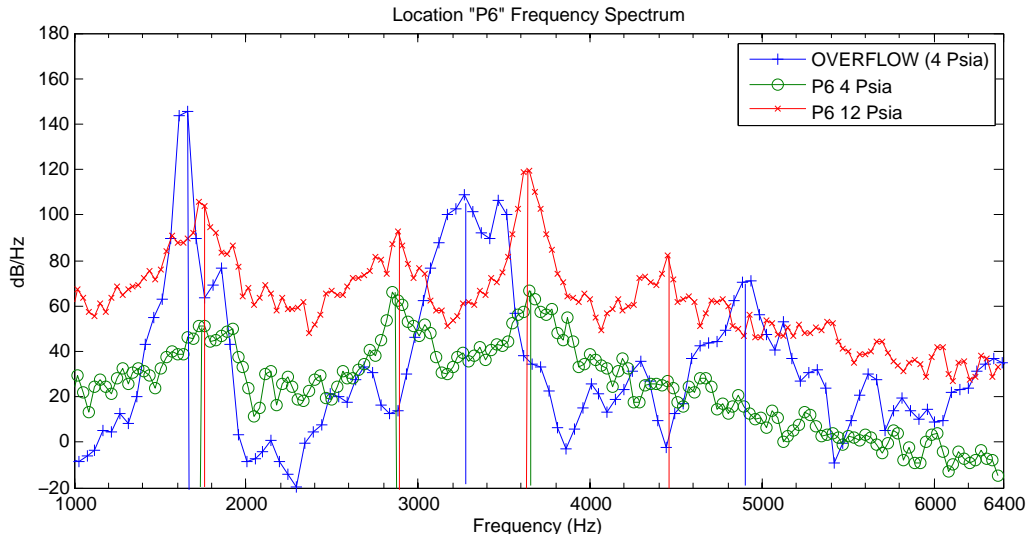


Figure 36. Comparison between OVERFLOW and experimental frequency spectrum.

Strong frequency correlation exists in the second Rossiter mode (3.5% error at 4 Psia, 3.9% error at 12 Psia), although the numerical results over predict the amplitude of the pressure oscillations. There exists no corresponding third mode on the numerical solution, with marginal matching of the frequencies at the higher modes (4

and 5). Broadband spectra amplitudes (on the order of 20 dB) correlate well between numerical and experimental results.

CFD solutions yield a vast dataset providing insight into the flow physics within and around a cavity. The two OVERFLOW runs, CT1B and CT1B_Long, were both run with the sphere in the captive position (no release) in order to gain a better understanding of the flow phenomenon of the cavity. Details of the grid composition and flow conditions were given in Chapter II. Figure 37 provides a two dimensional view of the centerline plane (XZ) at $Y=0$. The two figures both present a time-averaged solution beginning at iteration 1000 through run completion. The top figure

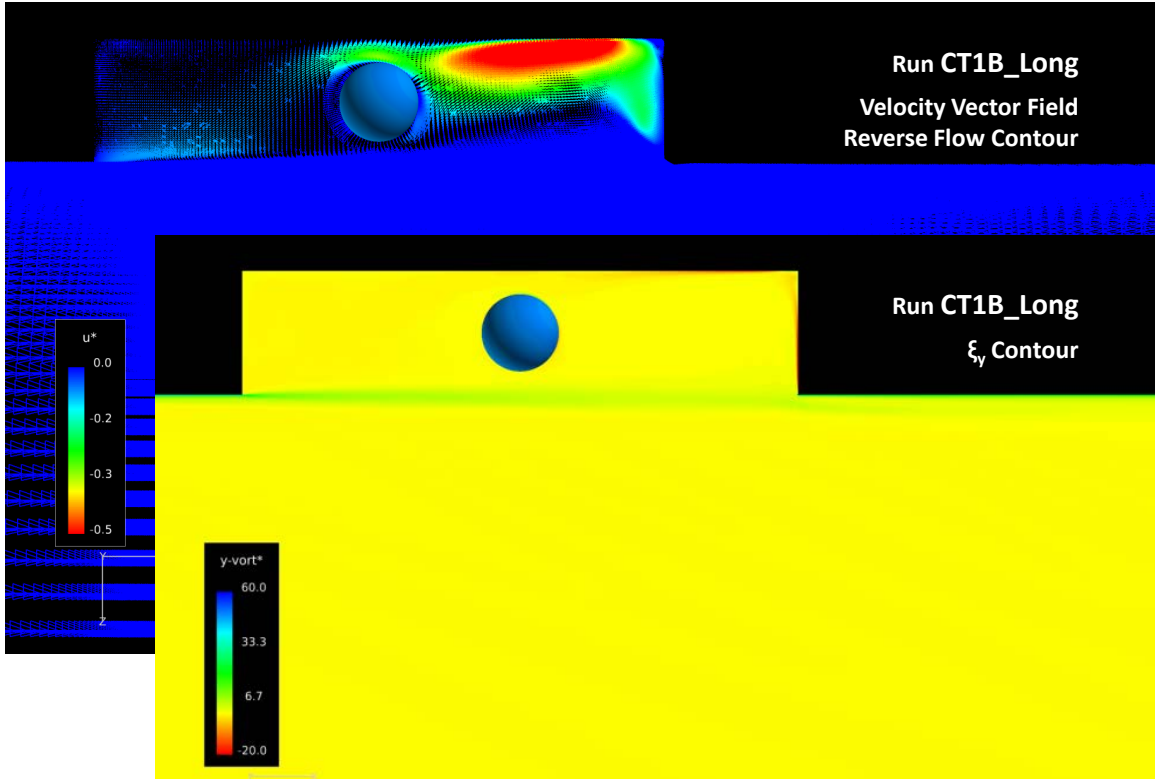


Figure 37. Centerline cut of run CT1B_Long showing vector and y-vorticity contour fields.

is a velocity vector plot colored with reverse streamwise flow ($-u^*$). This and all

subsequent planar CFD views provide a computational surface depicting the face of the sphere colored with density. The top view provides highlights the area of recirculation at the back wall and near the ceiling (aft of the sphere). This is due to the impingement of the shear layer on the back wall, contributing to the mass flow addition into the cavity, the energy addition phase of the hydro mechanical process [10]. The bottom figure is the same centerline view, colored with spanwise vorticity (+ out of page). As expected, high shear stress levels are present in the incoming boundary layer while continuing, though dissipating, in the free shear layer adjacent the face of the cavity. The large velocity gradient between the incoming supersonic flow and the relative stationary cavity flow causes a counterclockwise angular rotation within the shear layer, contributing to the energy addition of the large scale, turbulent, vortical structures. Also seen on the lower image, along the ceiling of the cavity, is the counterrotating (with respect to the shear layer) vorticity, also an indication of reverse flow in the upper region behind the sphere.

Figure 38 shows the non-dimensional pressure and density for the same dataset, shown in the top and bottom image, respectively. Seen in both images is the flow variations across the leading edge and trailing edge shock waves. In the upper image, the stagnation region on the lower back wall, near the trailing edge, highlights the average point of impingement as the shear layer contacts the back wall. The lower image of Figure 38 is shaded with density, which provides visualization comparable to the density gradients from the experimental Schlieren. One key feature seen in the time-averaged view of the density field is the weak compression wave present beneath the shear layer at the midpoint of the cavity. It is unlikely that this is a result of the suspended sphere within the cavity, as the sphere location does not impinge of the vertical motion of the shear layer, but likely due to the interacting longitudinal pressure waves within the cavity.

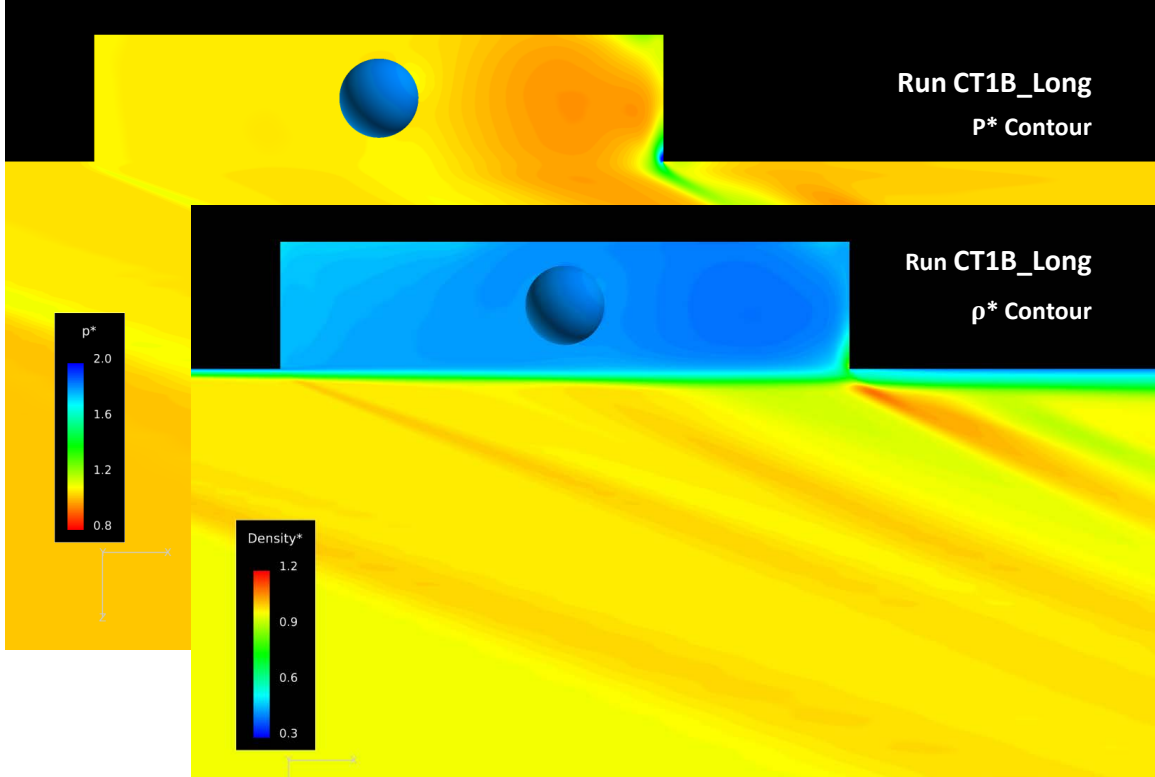


Figure 38. Centerline cut of run CT1B_Long showing non-dimensional pressure and non-dimensional density contour fields.

While a time-averaged solution file provides a clear depiction of the mean flow properties, a time-dependent solution gives insight to the unsteady nature of the physics of the flow. Figure 39 is an image set of 14 sequential flow solutions, each separated by 4 iterations. A centerline view colored with density provides a qualitative depiction of the fluid dynamics within the tunnel. Using a time-step of $5 \mu\text{s}$, Figure 39 yield an effective *computational frame rate* of 50 kHz, sufficient to capture the time scales of the cavity and shear layer dynamics. Total time span of the image sequence is $280 \mu\text{s}$. One feature to note from the image sequence is the pair of longitudinal pressure waves present within the cavity. Subfigures (a) - (g) show the first longitudinal wave traveling upstream, forward of the sphere, with the second traveling aft, located just behind the sphere in Subfigures (h) - (n). T_∞ for the CT1B run was set to 190.36°R corresponding to a speed of sound approximately 675

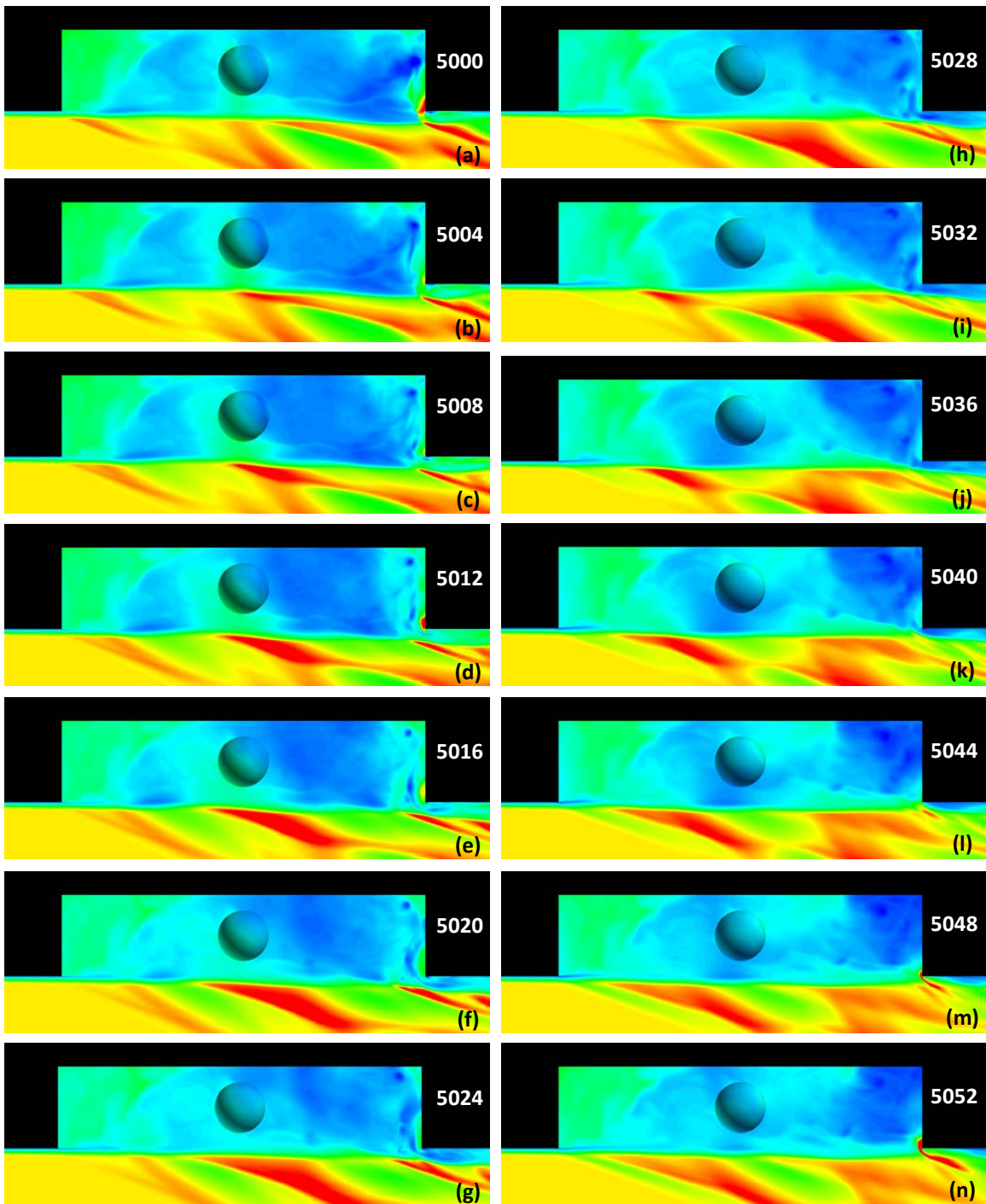


Figure 39. Image sequence of run CT1B (4 Psia). Centerline plane density contours show shear layer fluctuations, cavity acoustics, and mass entrainment. $\Delta t=20 \mu\text{s}$. Iteration numbers shown upper right of frame.

ft/s. The OVERFLOW solution indicates speed of sound levels of roughly $1.5a_\infty$. Both pressure waves move approximately 1 in within the 140 μs time span, which corresponds with a wave velocity of 600 ft/s, indicating that these entities shown moving longitudinally within the cavity are sound pressure waves.

Also present is the stagnation point on the aft wall of the cavity, shown in red. Again, Heller's description of the hydrodynamic process [10], is seen at the trailing edge of the cavity. Beginning with Subfigure (a), the high-density region is indicative of the mass flow addition process brought about by shear layer interaction with the back wall. Through Subfigures (b) - (l), as the trailing edge of the shear layer is displaced downward ($+Z$), the mass imbalance within the cavity is corrected through mass removal at the trailing edge.

Another phenomenon shown in the density contour images of Figure 39 is the acoustic wave/shock interaction that occurs within the shear layer. Below the shock wave are clearly time-dependent shock structures that travel both upstream and downstream the lower face of the shear layer. This is a clear indication of the unsteady disturbances inherent in cavity flow.

4.2 Sphere Drop Testing

Before commencing a discussion of the experimental drop tests, the following definitions were used to qualitatively describe the sphere release events.

- Successful separation: a drop event where the model did not impact either the top of the tunnel or the cavity area (within the camera field of view).
- Marginal separation: a drop event where the model impacted the trailing edge of the cavity or top of the tunnel but did not break apart, continuing downstream out of the camera field of view.

- Unsuccessful separation: A drop event which satisfies none of the above criteria (e.g. returns to the cavity, impacts the back wall and breaks apart, etc.).

Figure 40 provides an example of the synchronized high-speed and Schlieren imagery, highlighting the key components within the image field-of-view. Seen on the left of

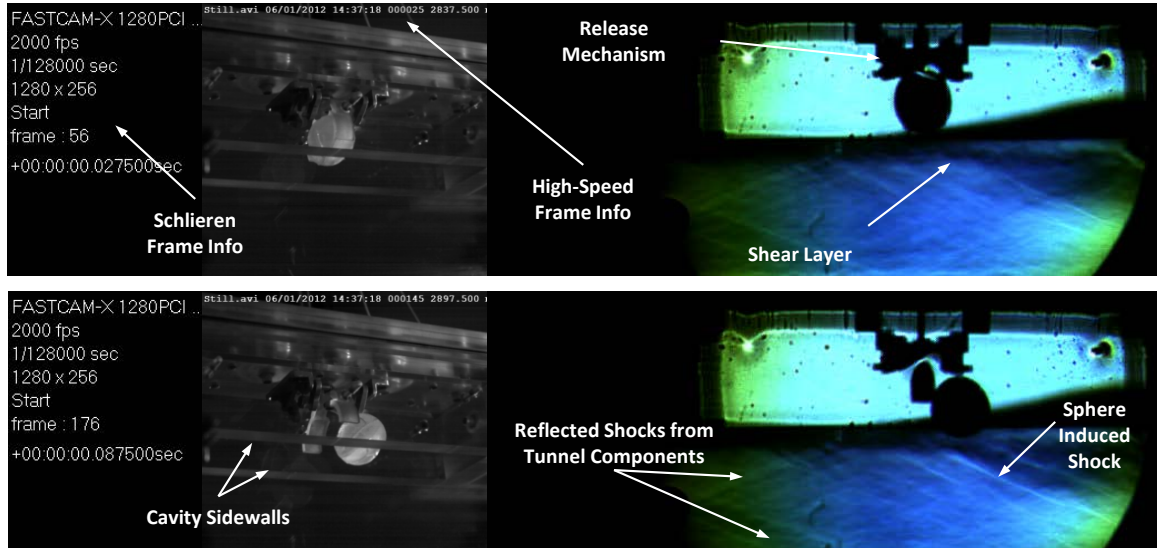


Figure 40. Highlight of key features in high-speed and Schlieren camera footage for sphere release.

the frame is the image tag provided by the Photron® software. To the right of the Schlieren tag is the high-speed camera imagery with an image tag atop the frame. Of note, though the Dantec® high-speed camera was placed on the *back* side of the tunnel (Fig. 16), the image was horizontally flipped to remain consistent with the orientation of the Schlieren footage. In the image pair, the flow proceeds left to right.

As previously stated, one original objective was to release an inertially simple object from a cavity at various tunnel conditions. From the scaling laws [20], a sphere provides a simple model from which to approach dynamic scaling. One assumption is that the rotational considerations (pitch, pitch rate) are negligible, thus further simplifying Marshall's scaling law to a 2-DOF model (X, Z). The negligible rotation,

demonstrated experimentally at all test conditions, validated the assumption that rotational rates had little effect on the translational dynamics of the sphere.

Since the model density, flow velocity, and gravitational constant were fixed (see Eqs. 7 and 15), the simplest way to vary conditions was to vary the stagnation pressure, which in turn changed the dynamic pressure within the test section. The low stagnation pressure reduced the aerodynamic forces and moments on the sphere. As previously stated, drop testing was performed at the three stagnation pressures ($P_{T,sc}=4, 12, \text{ and } 20$), with intentions of tracking the separation event of the sphere. Initial tests proved that even at the lowest densities available to the SVDB tunnel, q could not be reduced enough to enable successful separation from the cavity. Hardware modifications to the tunnel would likely reduce the stagnation pressure below 4 Psia, yet time constraints prohibited tunnel configuration changes during this research period.

An unsuccessful separation of the sphere model is shown in Figure 41. This run (529S4) was performed at a stagnation pressure of 4 Psia. Image capture rate of both cameras was set to 2 kHz, with a shutter speed of $8 \mu\text{s}$. Each frame is separated by 20 ms, with a total elapsed time of 0.1 sec for the total run. Here, the sphere releases cleanly from the mechanism, falls in the $+Z$ direction, and partially penetrates the free shear layer. As seen from the image pair at Schlieren frame 126, as soon as the sphere surface contacts the freestream, $\dot{Z} \rightarrow 0$, while the sphere accelerates in the streamwise direction ($+X$) and translates up into the cavity, ultimately striking the aft wall approximately 0.5 inches from the trailing edge of the cavity.

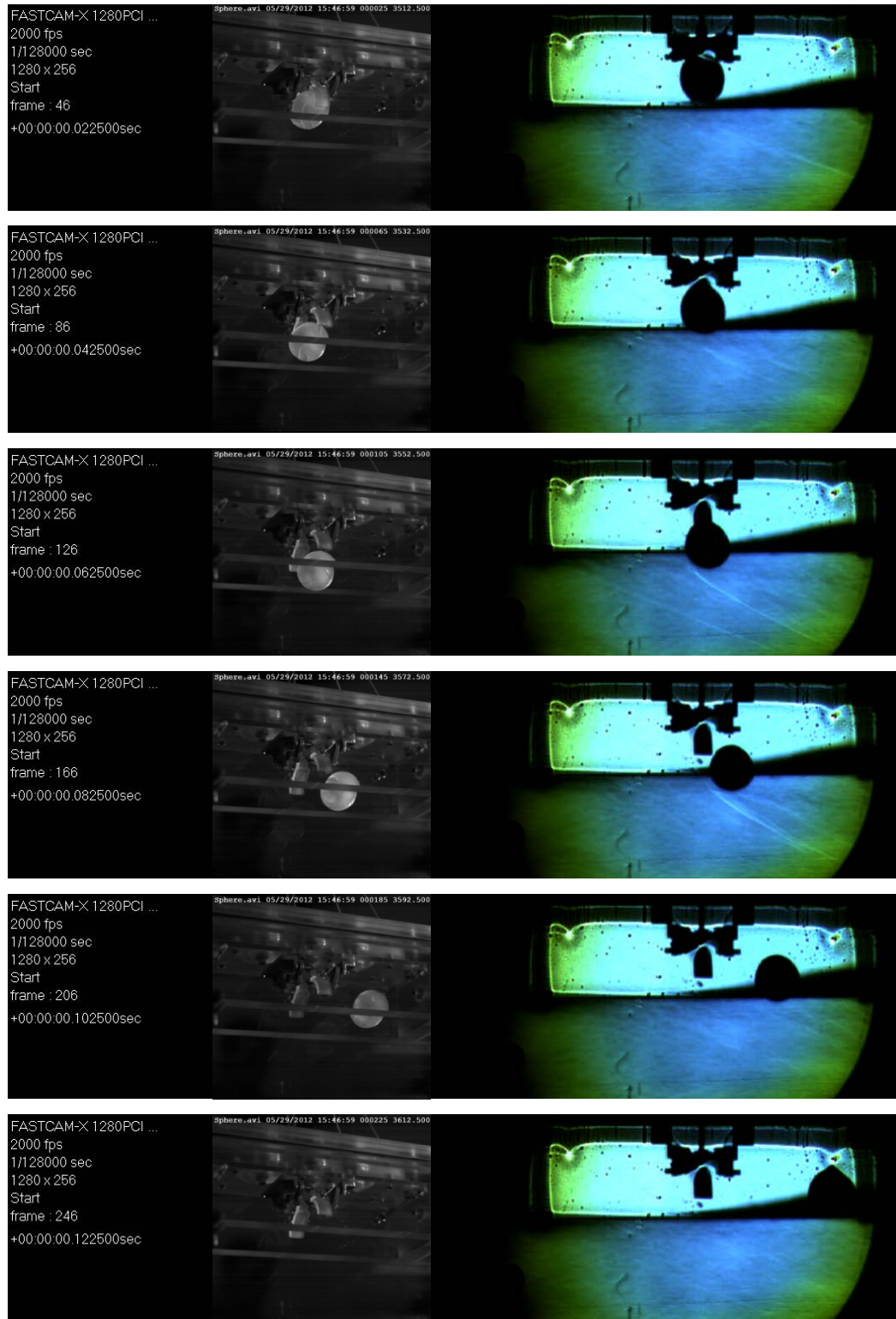


Figure 41. Image sequence of run 529S4. 4 Psia stagnation pressure. Frame rate=2kHz, $\Delta t=20$ ms.

Again, demonstrating the power of a CFD solution, Figure 42 provides the computational equivalent of the previous experimental run shown in Figure 41. In the CFD imagery, a centerline plane shaded with density provides a visualization of the release event modeled in OVERFLOW. The values input into the solver for run CT1B_D correspond with the measured and calculated test conditions of run 529S4. Each image is a density colored solution separated by 4000 iterations. This provides a Δt of 20 ms between images, the same timing depicted in the experimental image sequence shown in the previous image (for comparison purposes). Here, the solution at iteration 4000 corresponds to the release of the sphere via the input file, at which the relative time is set to zero. As with the experimental run, the sphere initially falls in the $+Z$ direction, with dynamics quite similar to the sphere drops within the SVDB tunnel.

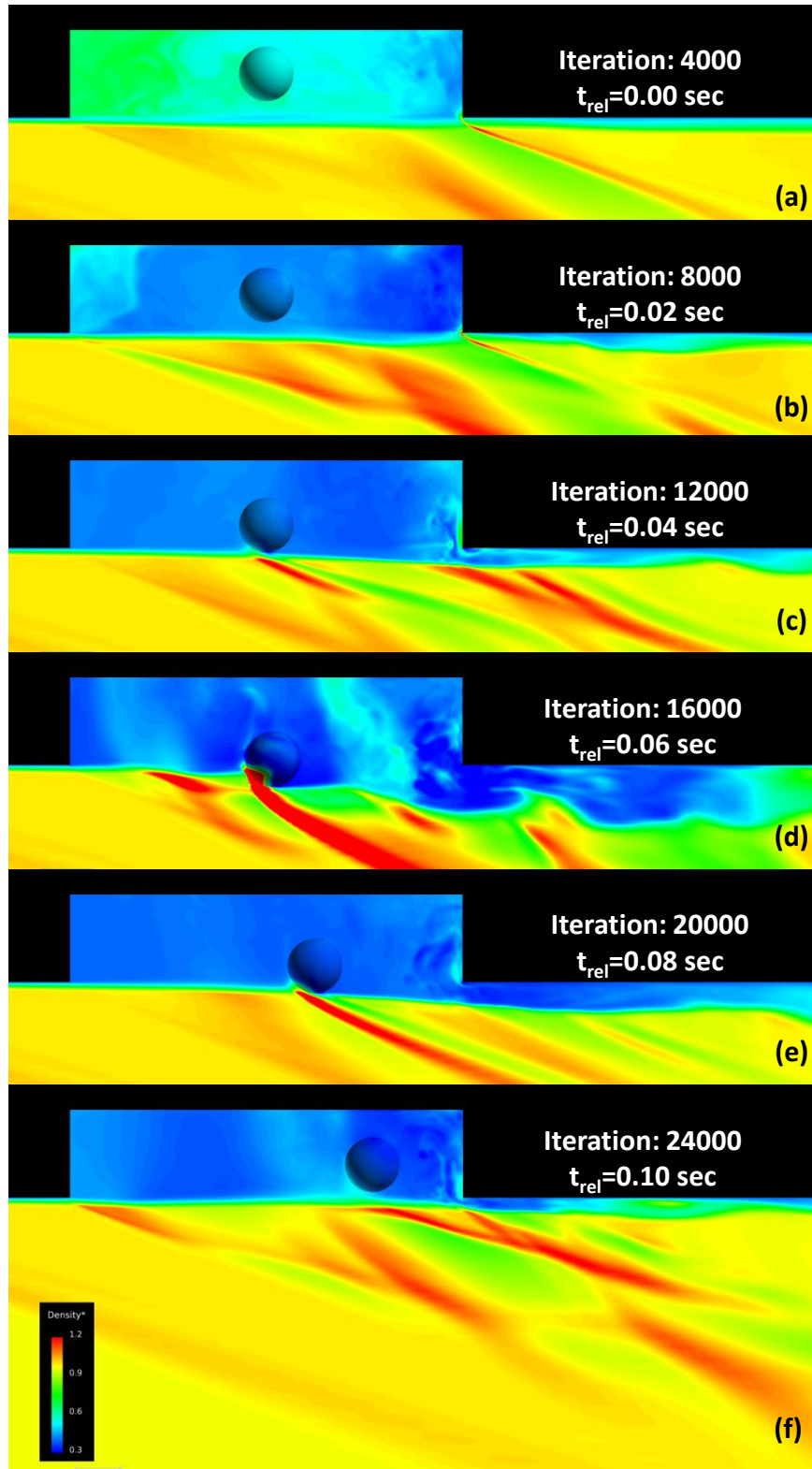


Figure 42. Image sequence of run CT1B_D (4 Psia). Centerline plane density contours shown. $\Delta t=20 \text{ ms}$.

Although experimental assessments showed that the spherical ice model would not cleanly separate from the cavity at the lowest available stagnation chamber of the SVDB (4 Psia), further sphere testing was conducted at the higher stagnation pressures. While increasing the stagnation pressure decreases the likelihood of a successful separation event, the higher density gradients allow better visualization of the flow structures present during the drop. Figure 43 is another example of a clean release of the sphere model that leads to an unsuccessful separation. This test (601S2) was conducted at $P_{T,sc}=12$ Psia. Again, each image pair is separated by 20 ms, with a total event elapsed time of 0.1 sec. As with the lower stagnation pressure, the ice sphere cleanly releases from the mechanism and freefalls partially through the shear layer. Again, once the surface of the sphere impinges on the free shear layer/freestream boundary, the higher dynamic pressure of the freestream propels the sphere back into the cavity, impacting the aft wall.

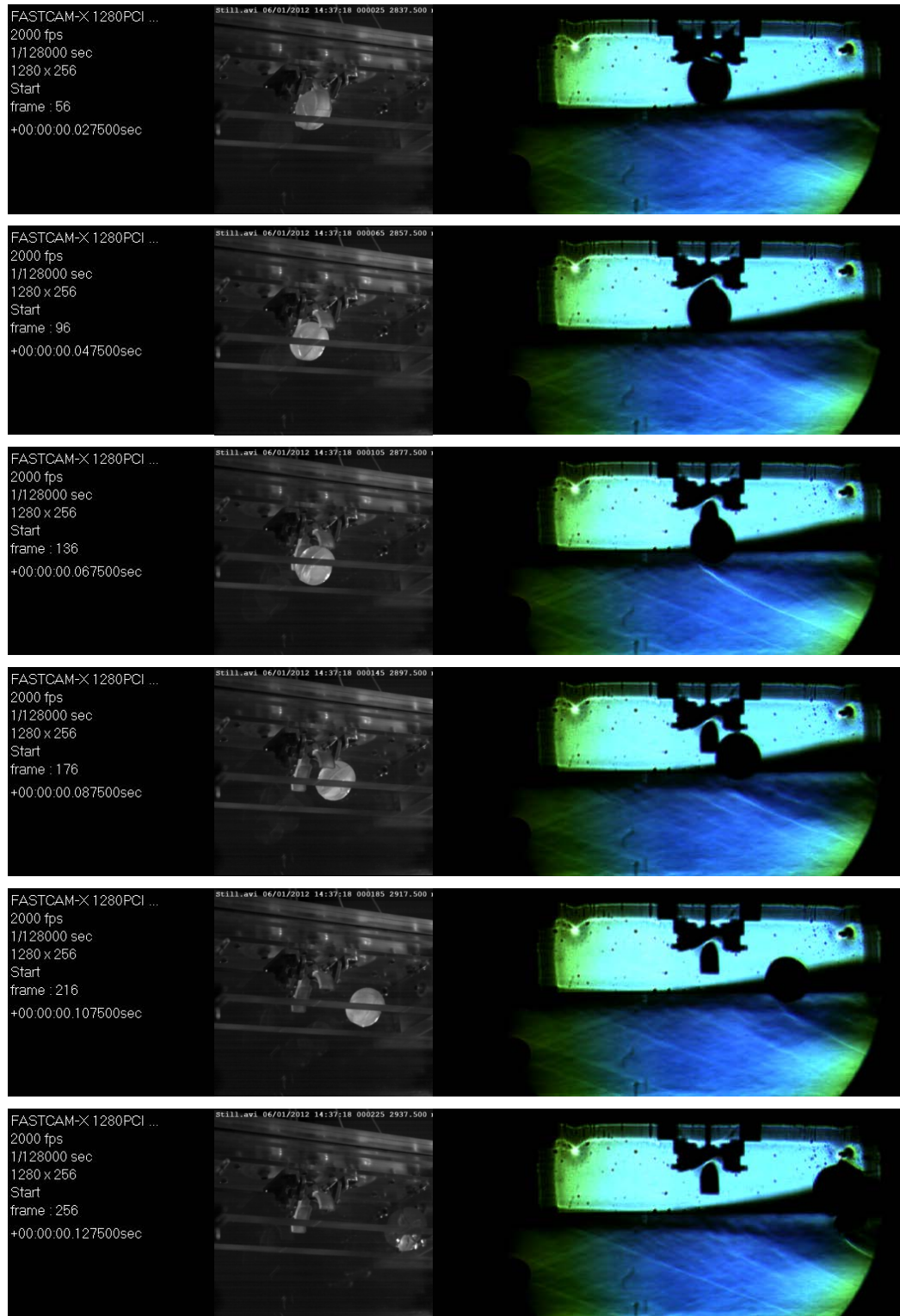


Figure 43. Image sequence of run 601S2. 12 Psia stagnation pressure. Frame rate=2kHz, $\Delta t=20$ ms.

In keeping with the intention of validating experimental and numerical freedrop events, OVERFLOW was used to model a sphere release at a stagnation pressure of 12 Psia, using identical flow conditions as seen in run 601S2. Again, at these flow conditions, similitude can be seen between the two runs. Like run CT1B_D, the image sequence begins at the solution of iteration 4000, where the relative time sequence is initiated ($t_{rel}=0$), after the dynamic motion begins. As seen in the centerline plane, colored by density, the event is an unsuccessful drop, as the sphere returns into the cavity and translates towards the back wall. Like the 4 Psia case, good correlation exists between the experimental tests and numerical simulations.

The reader should note the two experimental runs (529S4 and 601S2) were selected among a total of 15 sphere runs without a flow control device. The reader is referred to Appendices B through D for further image sequences at the various tunnel operating conditions. Due to the trajectory sensitivity to initial conditions, some variation existed from run-to-run, though most sphere drop test results were reasonably repeatable. In the absence of any flow control device, each experimental sphere release test was an unsuccessful separation event. One notable aspect from the sphere release imagery contained within the appendices is the forward ($-X$) movement of the model at release. Recirculatory flow clearly seen in Figure 37 or the pressure waves apparent in Figure 39 likely contributed to this forward movement of the sphere. This forward motion was not observed in the numerical simulations.

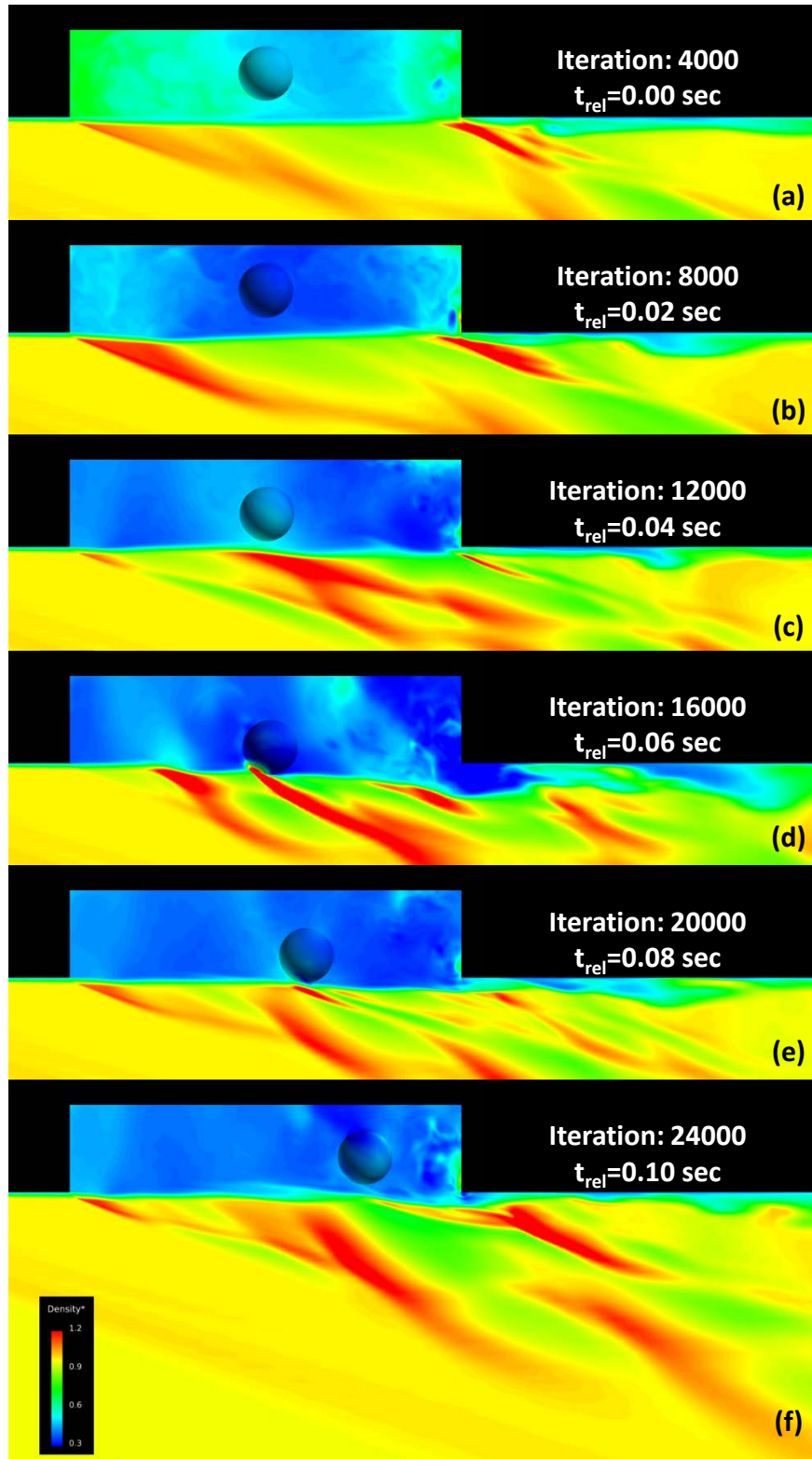


Figure 44. Image sequence of run CT4B_D (12 Psia). Centerline plane density contours shown. $\Delta t=20$ ms.

Figures 45 and 46 provide vertically aligned views of the previously presented experimental and numerical runs. At both stagnation conditions (4 and 12 Psia), the runs correlated well between computational and tested dynamics of the sphere model.

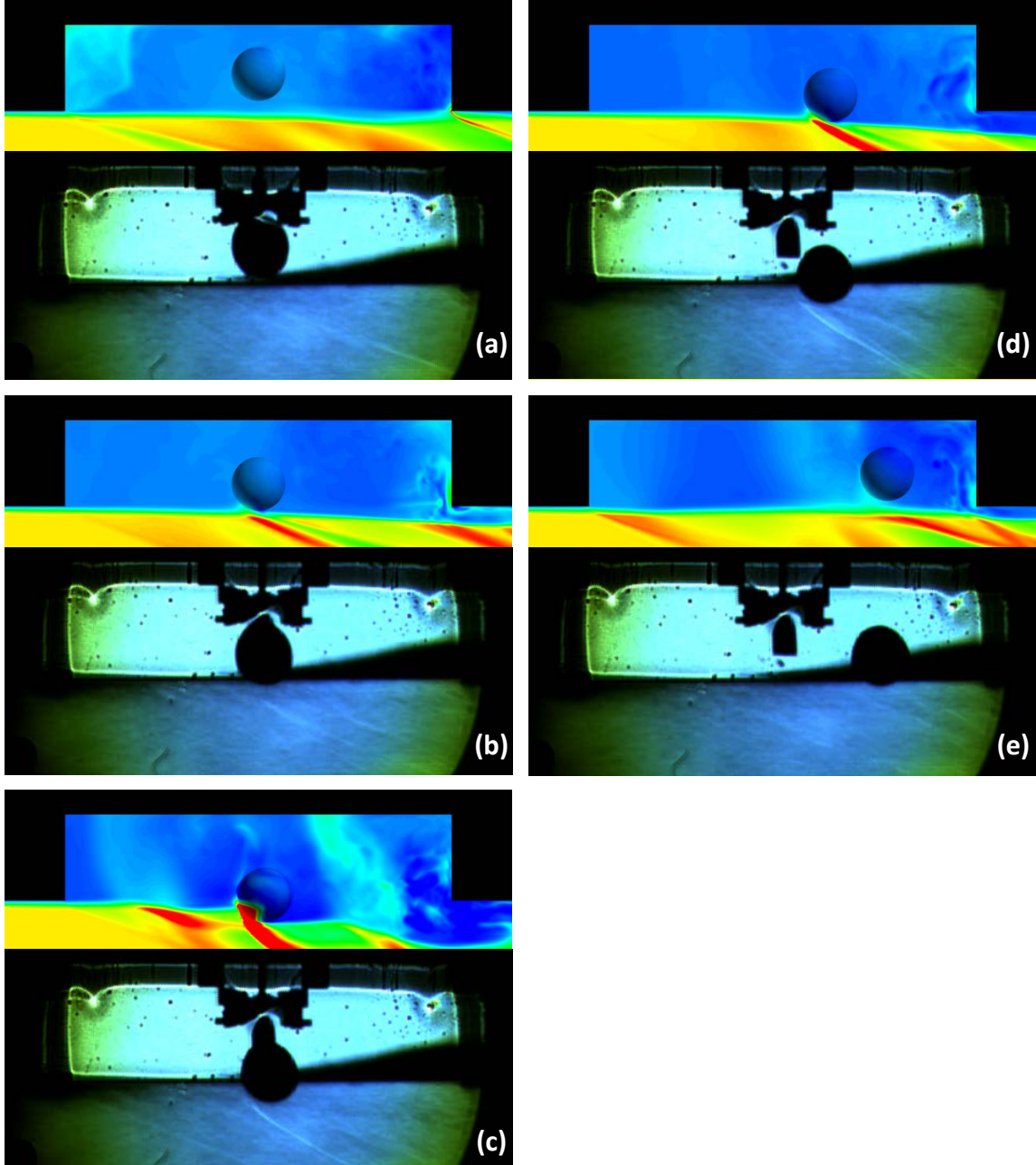


Figure 45. 4 Psia numerical and experimental runs ($\Delta t=20$ ms).

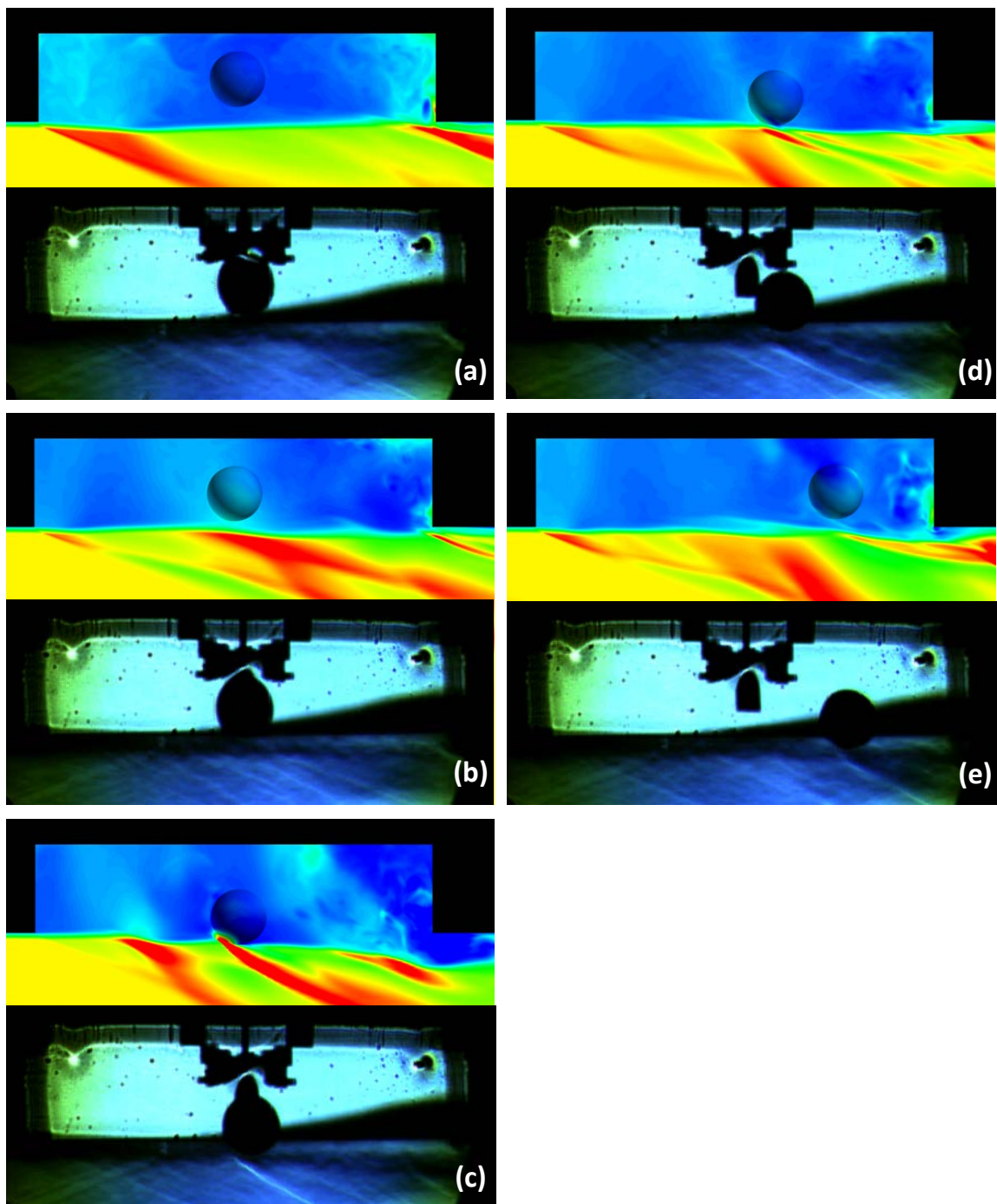


Figure 46. 12 Psia numerical and experimental runs ($\Delta t=20$ ms).

As previously mentioned, for the research, it was not possible to reduce the tunnel stagnation pressure below 4 Psia, which would likely have enabled a successful separation event of the sphere. However, using OVERFLOW, the flowfield could be modeled with lower pressure conditions in the effort towards attaining a successful release. To this end, cases were modeled for $P_T=2$ Psia, shown in Figure 47, and for $P_T=1$ Psia (Fig. 48). As with the other OVERFLOW relative motion runs, Figures 47 and 48 are centerline plane images colored in non-dimensional density.

In order to capture the entire release event on a single figure, the image sequence depicting run CT2B_D begins at iteration 8000. Subfigure (a) depicts the solution just after the release event, which occurs at iteration 4000. While the dynamic pressure of the tunnel was lowered by a factor of two from the baseline 4 Psia case, the sphere still lacks the momentum to completely penetrate the shear layer and successfully separate from the cavity.

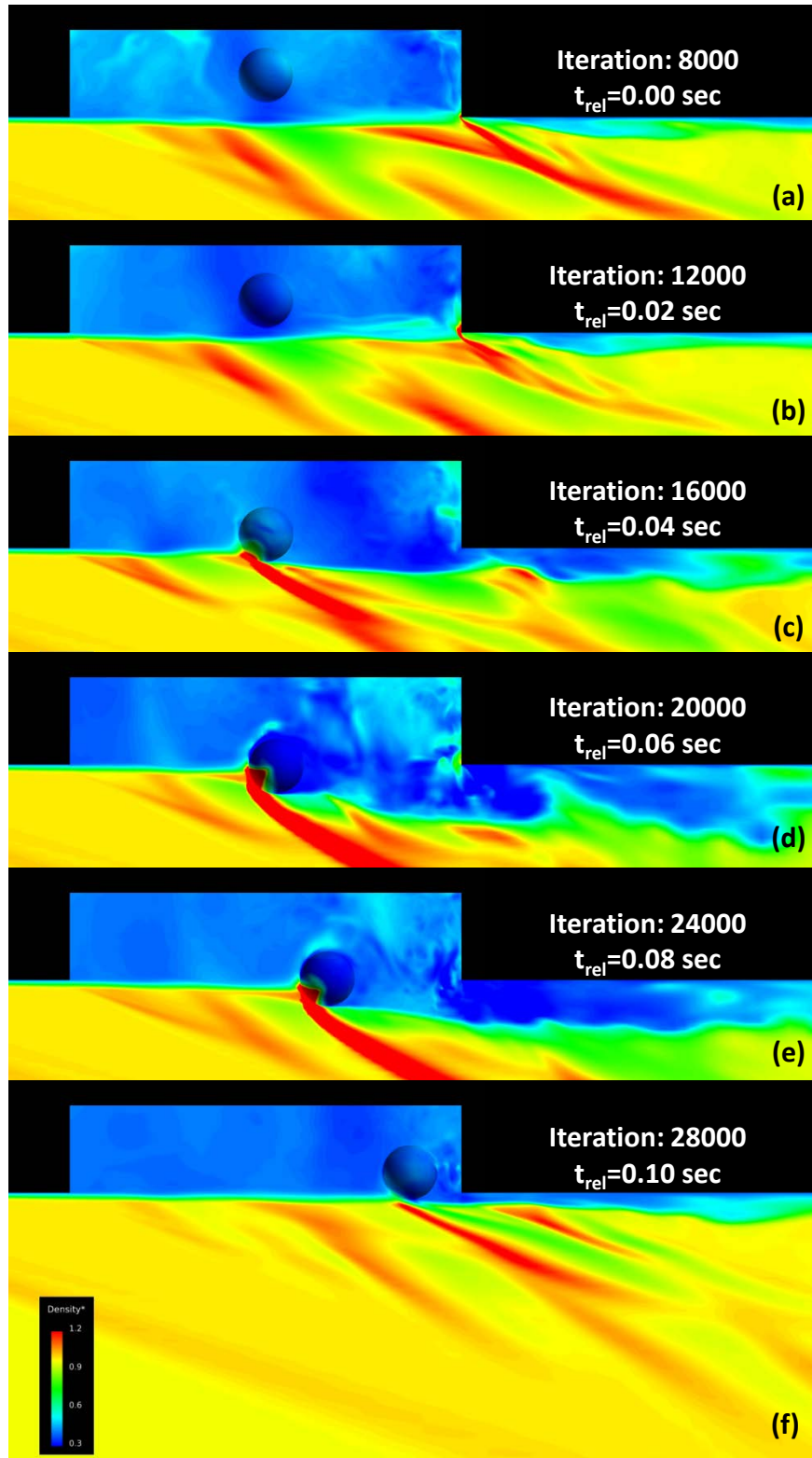


Figure 47. Image sequence of run CT2B_D (2 Psia). Centerline plane density contours shown. $\Delta t=20 \text{ ms}$.

Figure 48 shows the release event for run CT3B_D, the computational solution at the lowest stagnation pressure (1 Psia). Here, the sequence begins at 12000, seen in Subfigure (a), and continues to iteration 29500. In this simulation, the sphere penetrates the shear layer and successfully clears the trailing edge of the cavity. One interesting result is the stability of the shear layer as seen in Subfigure (a). Compared to numerical simulations at higher Reynolds numbers where the instability of the shear layer is well developed prior to sphere/shear layer interaction, here the shear layer (as seen at iteration 12000) is laminar and stable, resulting in a relatively benign cavity environment.

Another notable feature seen beginning in Subfigure (c) continuing through (e) is the shock train that develops within the cavity as a result of the bow shock from the blunt spherical surface. With sufficient shear layer penetration, the bow shock induced by the sphere face penetrates the higher temperature region of the cavity and forms into a shock train.

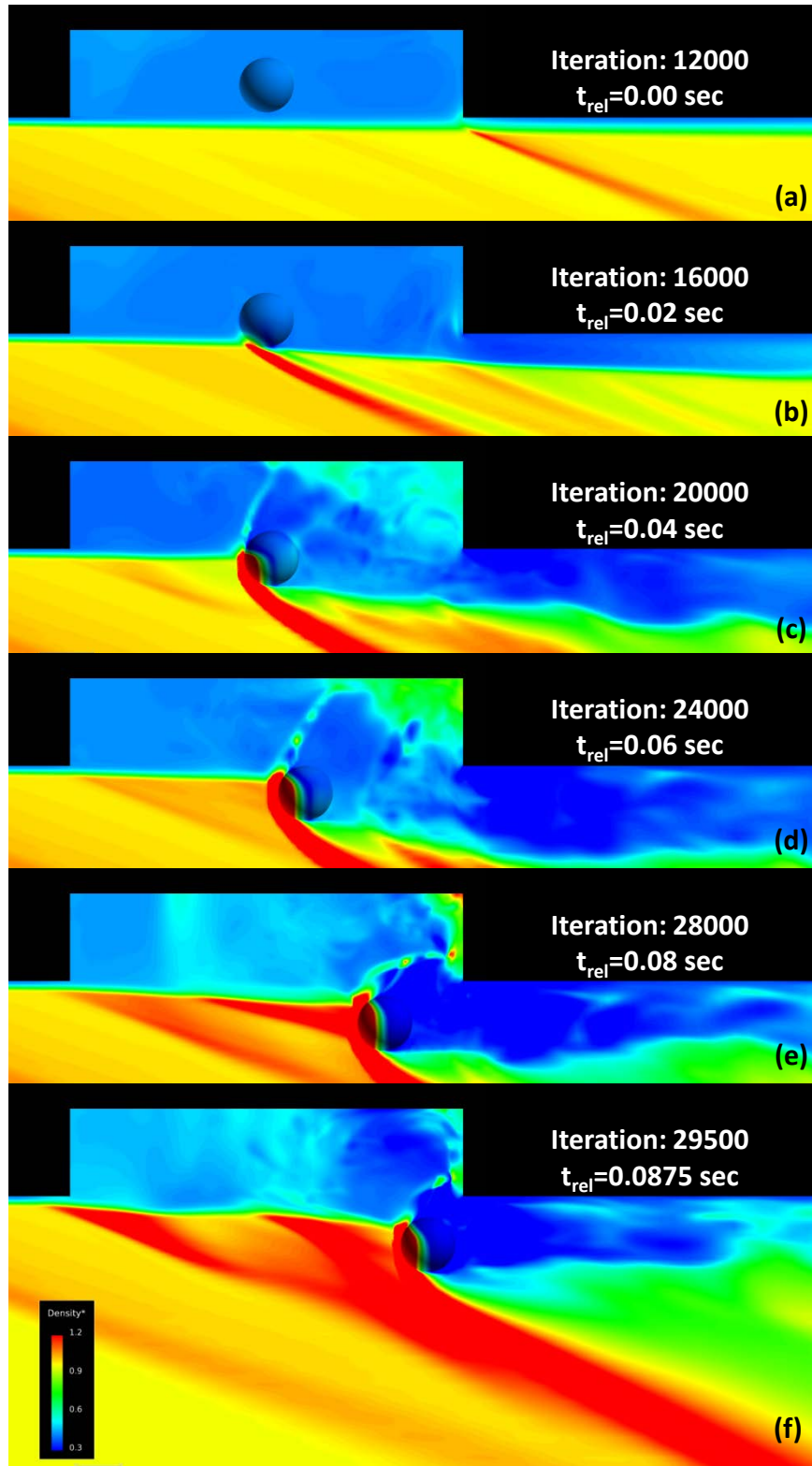


Figure 48. Image sequence of run CT3B_D (1 Psia). Centerline plane density contours shown. (a) - (e) $\Delta t=20 \text{ ms}$.

While qualitative views of the computational flow solution yield a vast degree of insight into the physics of cavity flow, the relative motion of the sphere is better assessed through a quantitative approach. The following graphs are all outputs from the OVERFLOW CFD solver, contained in the output file *animate.out*. This output file provides the solutions to the equations of motion, both in the body fixed and inertial frame of reference.

Figure 49 begins with the sphere at the release position. As discussed in Chapter III, the CFD release point, anchored in the computational reference frame, is (24.0, 0.0, -2.0). Using the same origin, the computational bay spans from 15.0 to 33.0 in X , -2.0 to +2.0 in Y , and -4.0 to 0.0 in Z . Transforming the CFD coordinates

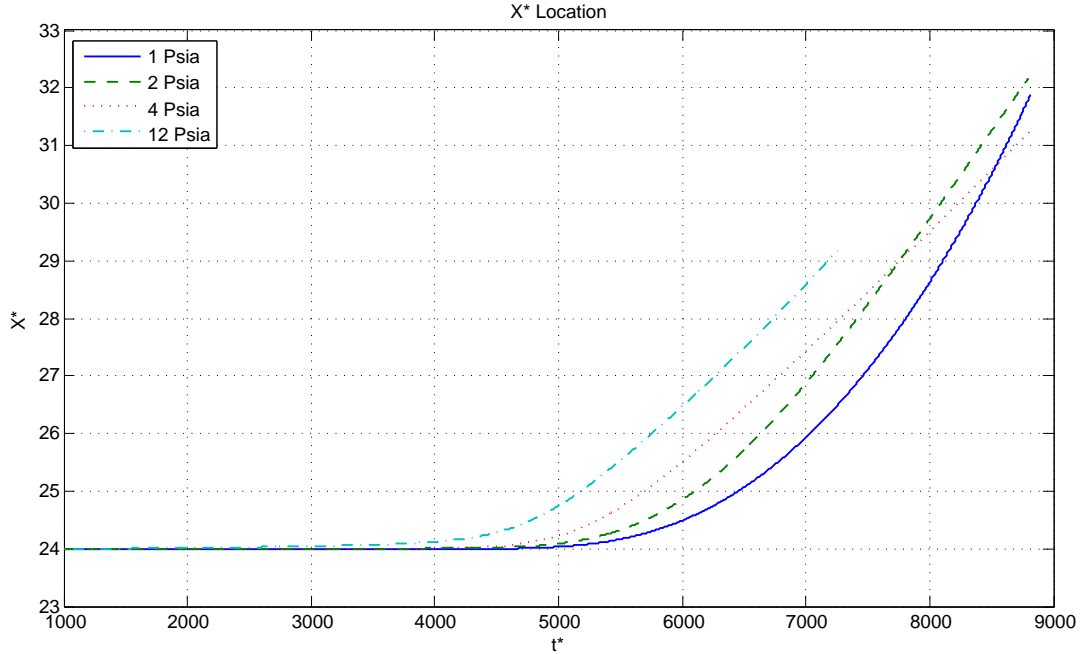


Figure 49. Plot of sphere non-dimensional X coordinate.

to the experimental scale, using the release point as the origin, the physical tunnel

dimensions span from -3.44 to 3.31 in along X , -0.75 in to +0.75 in in Y , and -0.87 in to 0.63 in in the Z direction.

Streamwise location of the sphere c.g. is shown in Figure 49. The ordinate is non-dimensional streamwise location plotted against the non-dimensional time step. In each of the following plots, the legend begins with the lowest pressure (1 Psia). Here, as the dynamic pressure is increased, the sphere translates more rapidly in the $+X$ direction.

Vertical displacement is shown below in Figure 50. As can be seen in the qualitative Figures (42 - 48), the vertical displacement out of the cavity is inversely proportional with q , leading to complete shear layer penetration and continued $+Z$ translation at the lowest simulated pressure. Shown here, at each of the three higher

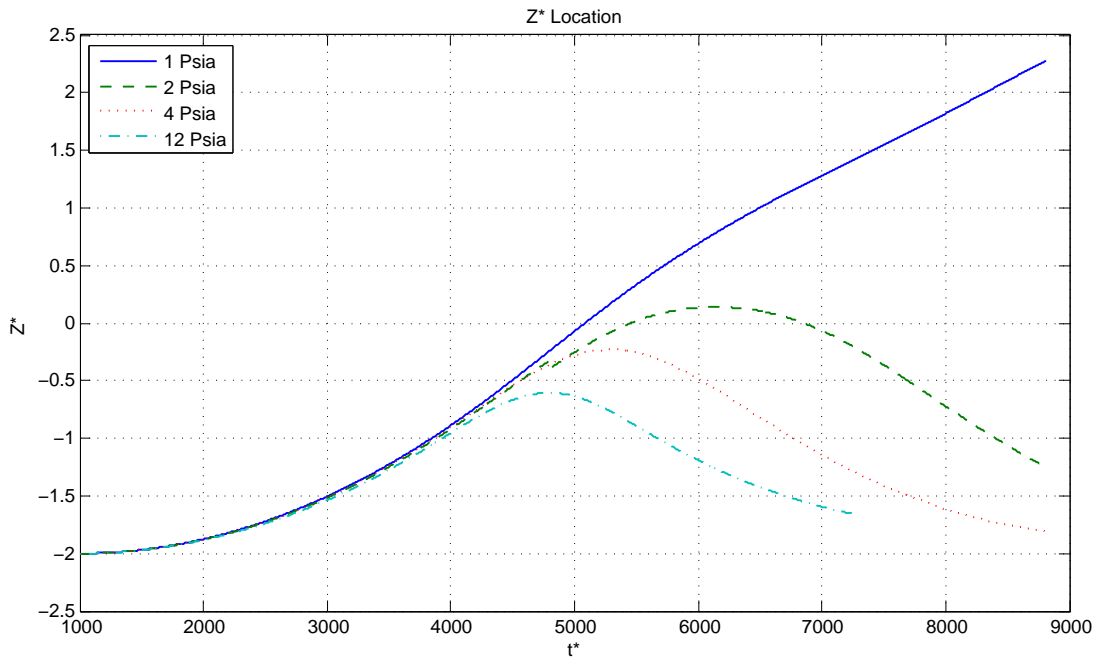


Figure 50. Plot of sphere non-dimensional Z coordinate.

pressures, is the arrested downward displacement as the shear layer imparts momentum to the sphere, causing the sphere to return to the cavity.

Velocities, forces, and moments output from OVERFLOW are all provided in non-dimensional values, as outlined in Chapter II. Figure 51 provides the non-dimensional streamwise velocity of the sphere c.g. plotted against the non-dimensional time. As

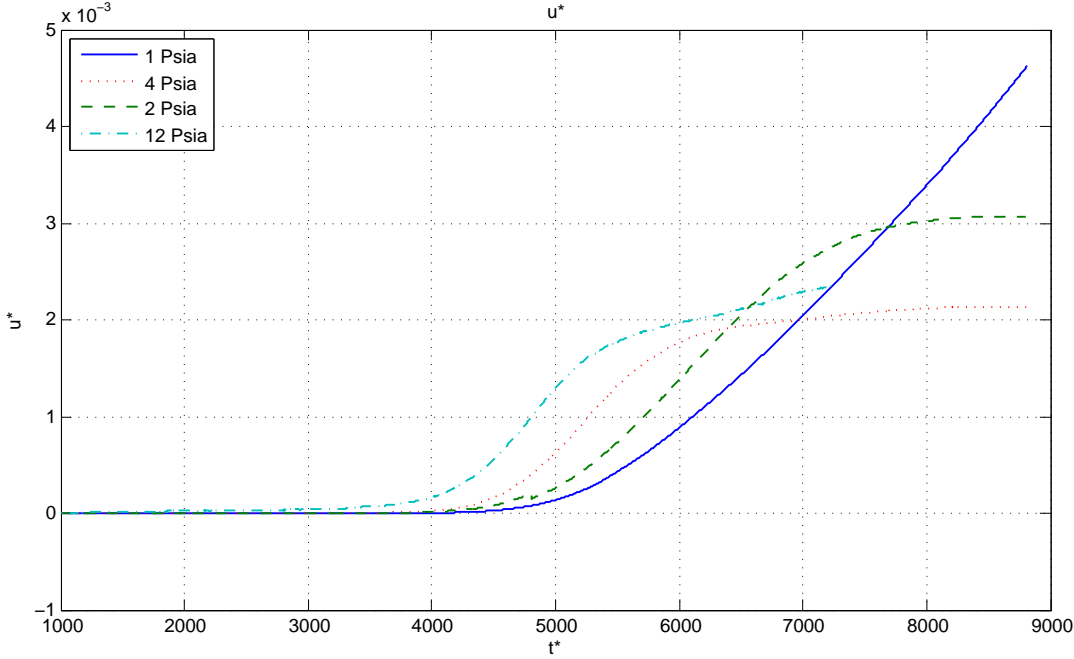


Figure 51. Plot of non-dimensional streamwise velocity (u).

expected, the initial acceleration increases with increasing q and decreases as the sphere returns to the cavity (with the exception of the 1 Psia case).

The dimensional value of the final velocity of run CT1B_D, using a $V_\infty=2020$ ft/s, was found to be 4.04 ft/s. For comparison purposes, as seen in Figure 41, experimentally, the sphere translates in the streamwise direction approximately 1 in between the final two frames (separated by 20 ms). This corresponds with $u \approx 4$ ft/s, in strong agreement with the numerical results.

Downward non-dimensional velocity (w^*), is shown in Figure 52. For the three

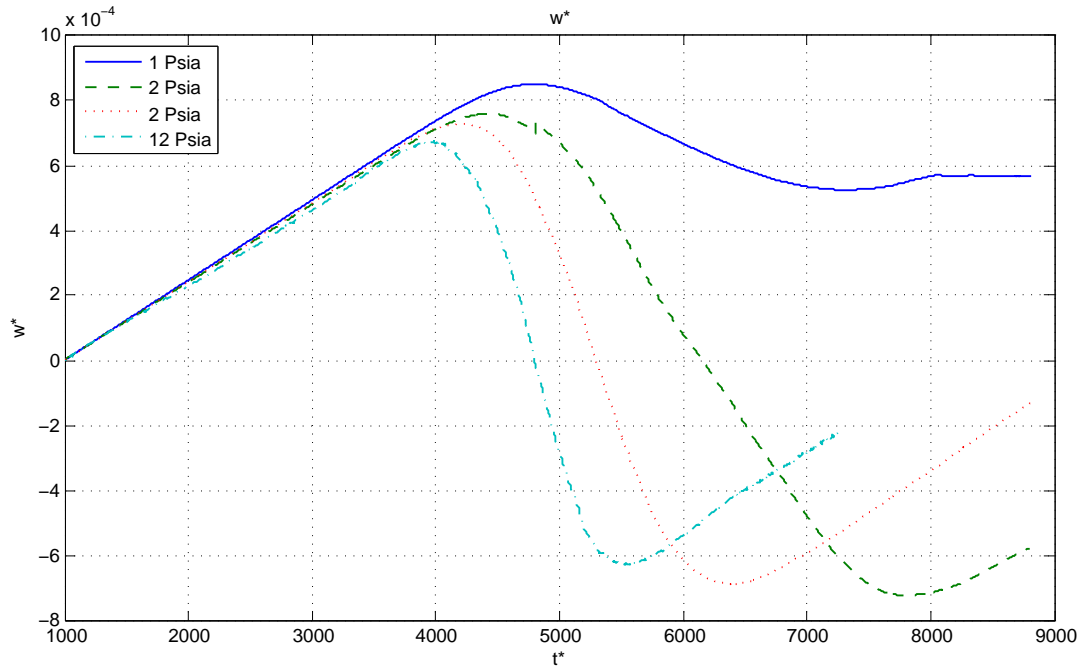


Figure 52. Plot of non-dimensional w velocity.

higher pressures, positive acceleration increases until the sphere contacts the freestream, upon which the vertical acceleration decreases until velocity becomes negative. Once the sphere has completely returned to the cavity, gravitational acceleration overcomes the negative acceleration from the freestream interaction. As run CT3B_B escapes the shear layer, the sphere continues to fall as the vertical velocity stabilizes at 6.00×10^{-4} .

Angular velocity ($+Y$) was assumed negligible, eliminating any applied forces on the sphere due to Magnus effect. Figure 53 validates this assumption. The peak angular velocity of run CT1B_D corresponds to a dimensional angular velocity of 2.6 rad/s. As the time scale of each release was approximately 0.1 sec, the angular component was minimal. This can be visualized by the sphere *skipping* off the shear layer, vice spinning once the surface contacted the freestream.

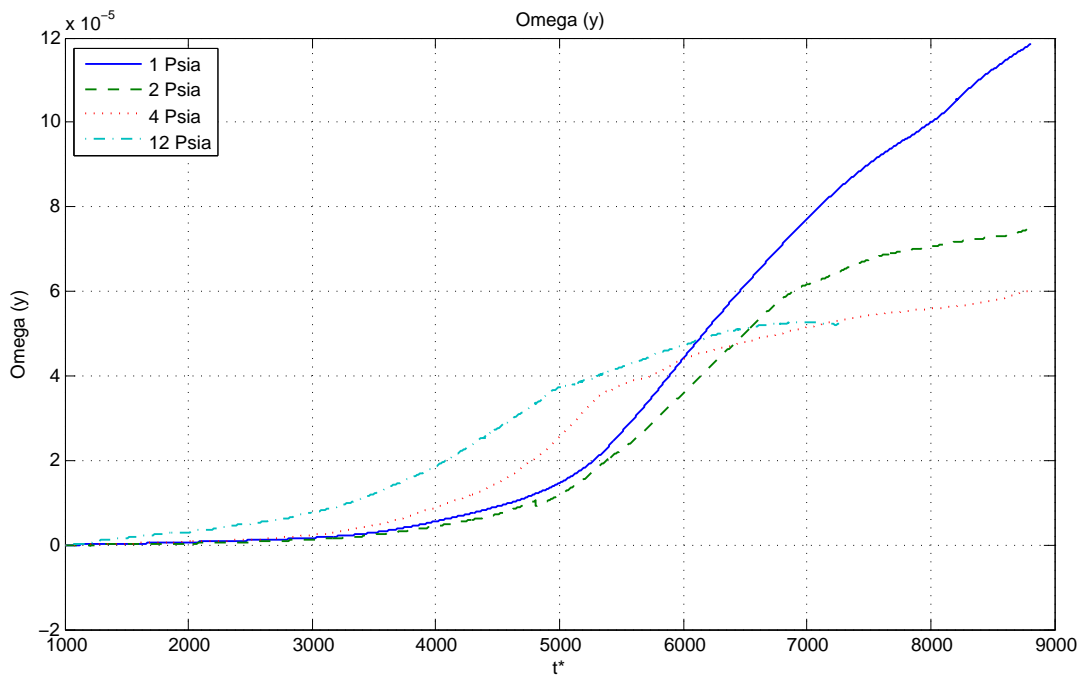


Figure 53. Plot of non-dimensional angular velocity of the sphere (Y component).

The integrated non-dimensional pressure values clearly show the oscillatory nature of the flowfield within the cavity and once the sphere has penetrated the shear layer (Fig. 54). In some of the experimental runs, the sphere moved upstream ($-X$)

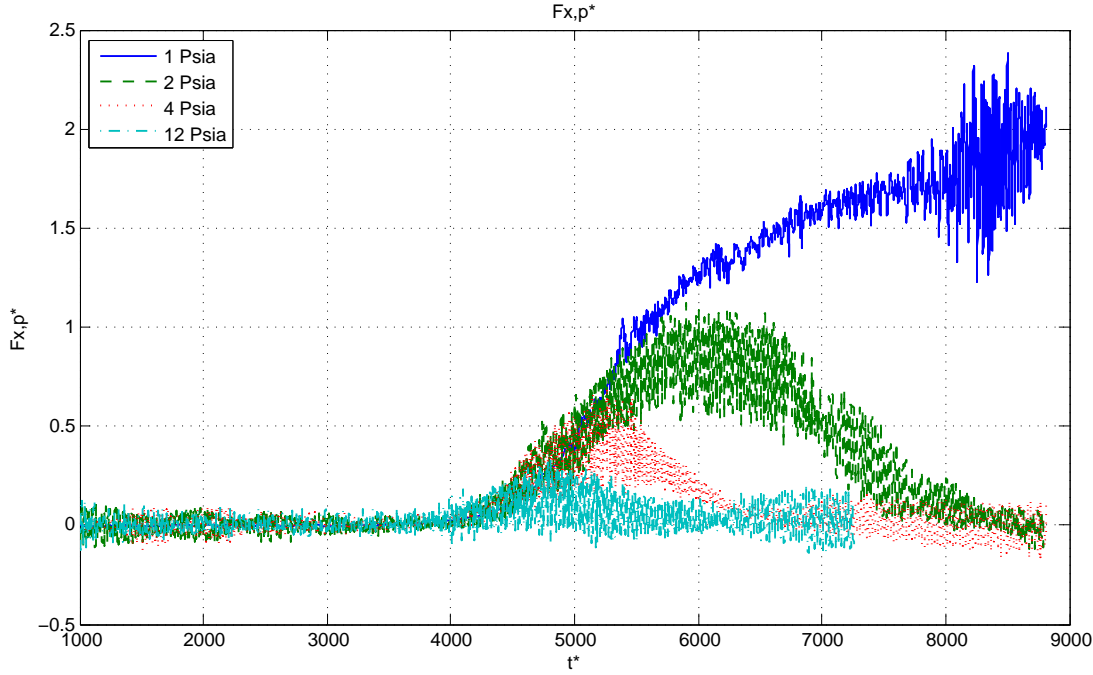


Figure 54. Plot of integrated non-dimensional pressure force in X direction.

immediately upon release (as seen in Appendices B to D). This is likely due to a $-X$ force from the recirculatory flow within the cavity. As seen in the plot of the non-dimensional pressure and viscous forces (Figs. 54 and 55), the mean force applied to the sphere was essentially zero. This would explain why each computational release resulted in a purely downward translation at the beginning of each run.

An interesting result shown in Figure 55 is the relatively steady viscous force acting on the seen in cavity region of run CT3B_D. As previously mentioned, and verified here, the shear layer (and cavity flow) remains stable at this lower Reynolds number, even through iteration 12000. Once the sphere penetrates the shear layer,

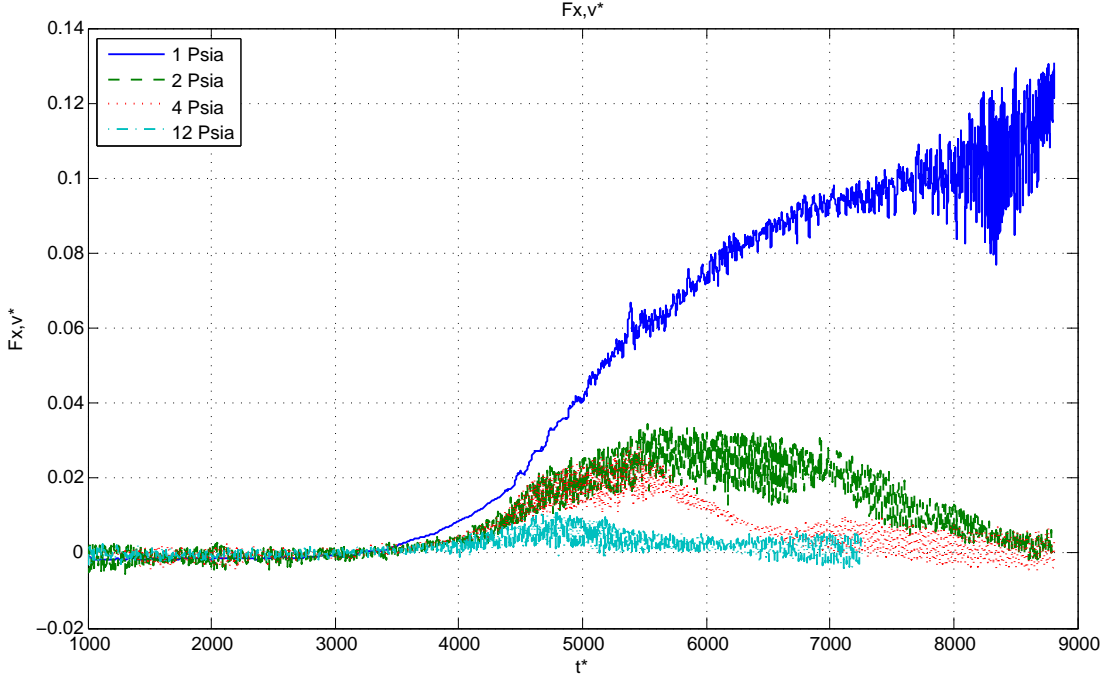


Figure 55. Plot of integrated non-dimensional viscous force in X direction (due to shear).

the shear layer is excited and unsteady flow ensues. This is shown as the oscillations increase in magnitude at $t^*=5000$.

Figure 56 is a plot of the non-dimensional moment about the Y axis (positive out-of-page). Seen here is the increase in angular momentum about the sphere c.g. as the bottom surface of the sphere penetrates the shear layer and contacts the freestream. The magnitude of the oscillations is greatly increased during the dwell time of the sphere within the shear layer. Again, the steady nature of run CT3B_D within the cavity indicates a relatively benign cavity flowfield at the lower Reynolds number. For this run, the moment increases as the lower portion of the sphere interacts with the freestream. The higher forces imparted to the sphere from the freestream flow rotates the sphere counter-clockwise (as viewed), corresponding to the positive moment seen in Figure 56. Once the sphere penetrates the shear layer, the flow is deflected above and beneath the sphere, reducing the magnitude of the positive moment (time steps

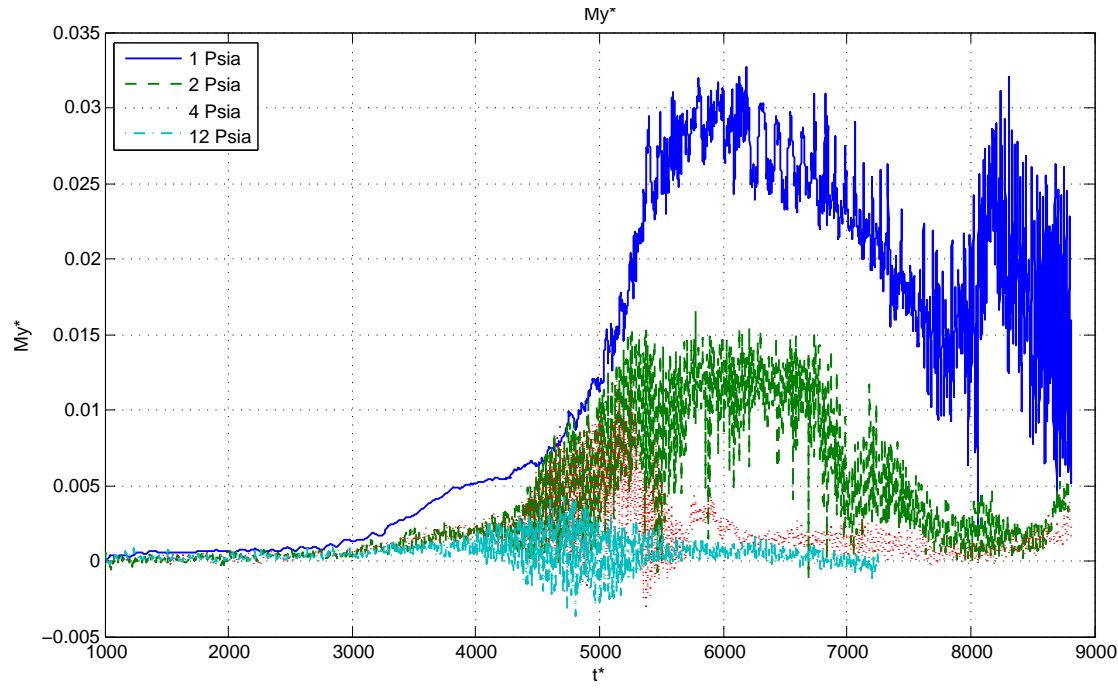


Figure 56. Plot of non-dimensional moment about Y axis.

5500 - 8000). Once the bow shock interacts with the back wall of the cavity (time step > 8000), the magnitude of the oscillations greatly increases.

4.3 Experimental Investigation of Passive Flow Control

Flow control devices have traditionally been used as palliative solutions, i.e. they are incorporated after the initial design has been tested and proved inadequate by some performance measure. In this same vein, this research sought to incorporate a simple passive flow control device to impel the sphere out of the cavity. The purpose of a flow control device used in concert with a cavity weapons bay is twofold. First, the flow control device should be able to reduce the acoustic loading seen in the cavity. Second, the flow control device should enhance the store separation characteristics in that particular device/cavity/store configuration. The optimum flow control device would accomplish both objectives simultaneously.

Both the SST and LST tab designs were tested with the sphere model. The difference between the two was that the SST penetrated the incoming flow at approximately the height of the boundary layer (δ), while the LST protruded roughly 2δ into the flow. Figure 57 provides a Schlieren image sequence showing the influence of the SST on the surrounding flowfield. One can see the extreme shock wave as the incoming flow impacts the protruding spoiler. Also, when compared with the original shear layer, the effect of the spoiler is to thicken the shear layer considerably, creating a wake in the freestream flow.

4.3.1 Acoustic Effects

The preferred method to assess the flow control device's capability to reduce the acoustic loading is to analyze the SPL within the cavity. The following figures (Figs. 58 - 60) provide the acoustic response seen at transducer $P6$, the best available location within the cavity to capture the longitudinal pressure disturbances.

Figure 58 shows the acoustic response of the cavity, as measured at $P6$, at a stagnation pressure of 4 Psia. The SPLs are plotted with respect to frequency for

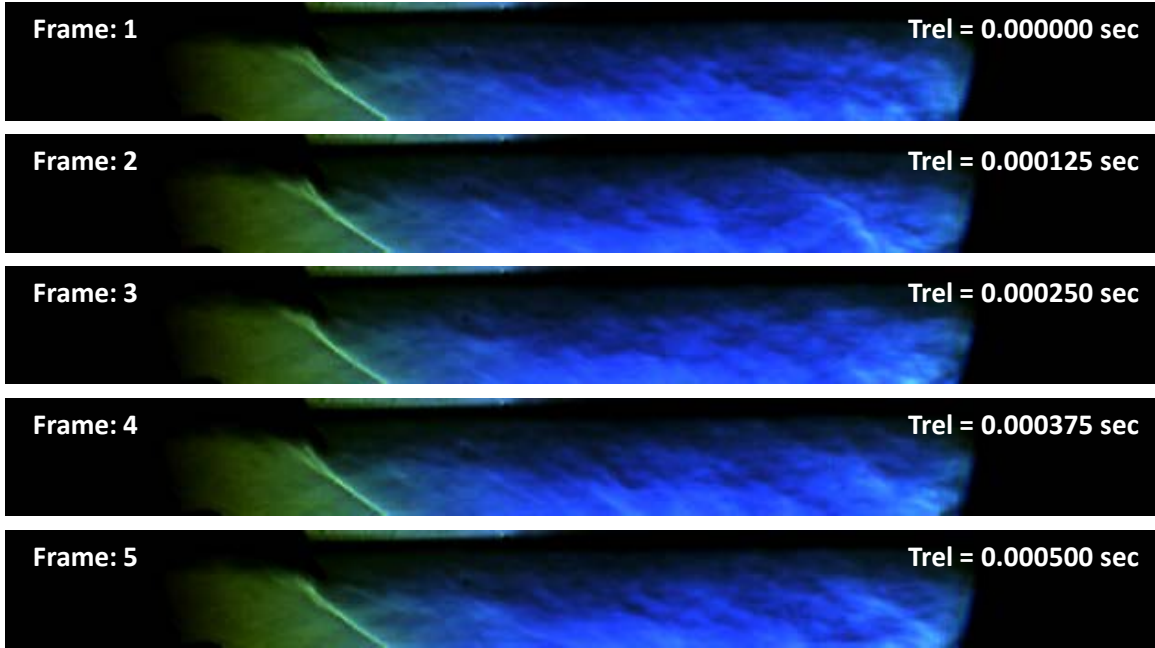


Figure 57. Image sequence of run 605C5 (12 Psia). Short sawtooth flow control device installed. Capture rate = 8 kHz, shutter speed = 8 μ s.

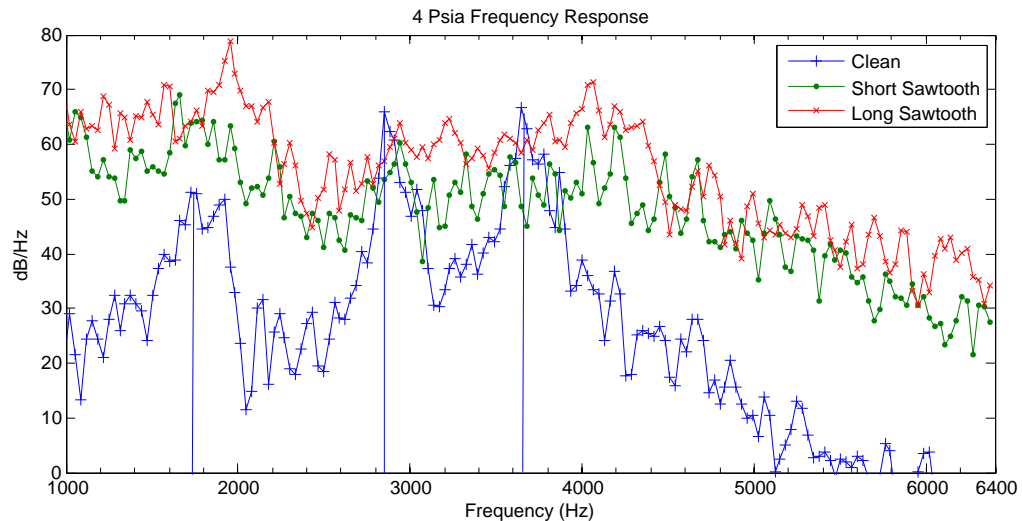


Figure 58. 4 Psia stagnation pressure frequency response clean, short sawtooth, and long sawtooth.

the cavity without a spoiler device, with the SST, and with the LST. Of note, in this context, the term *clean* denotes cases where no flow control is applied. In all

spoiler configurations, the sphere is held captive in the release position. This allows assessment of spoiler effectiveness on a cavity with a *store* in place.

At 4 Psia, the clean cavity (+) has clear spikes corresponding to Rossiter modes 2, 3, and 4. The broadband levels are approximately 20 dB, with the highest amplitude of 65 dB occurring in mode 4 (3650 Hz). At the lowest stagnation pressure, the spoilers effectively detune the modal spikes but at the expense of elevating the entire broadband noise level, a highly undesirable trade-off.

The 12 Psia acoustic response is similar to that shown in Figure 58. In Figure 59, the clean configuration shows clear spikes in modes 2, 3, and 4 with a possible excitation of mode 5 (4200 Hz). Again, the SST and LST data (• and x) show no indication

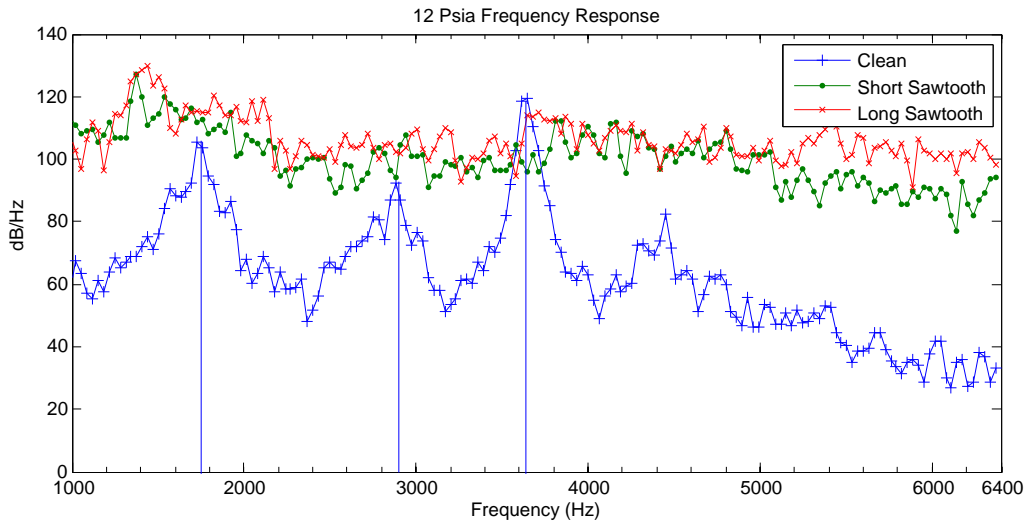


Figure 59. 12 Psia stagnation pressure frequency response clean, short sawtooth, and long sawtooth.

of exciting any Rossiter modes. The broadband noise is raised approximately 40 dB, nearing the amplitude of the 4th Rossiter mode (118 dB).

While the spoiler was largely ineffective at reducing the acoustic levels within

the cavity at the lower pressures, Figure 60 shows that, at increased q , the spoilers begin to accomplish some acoustic tone reduction. Although the broadband tones

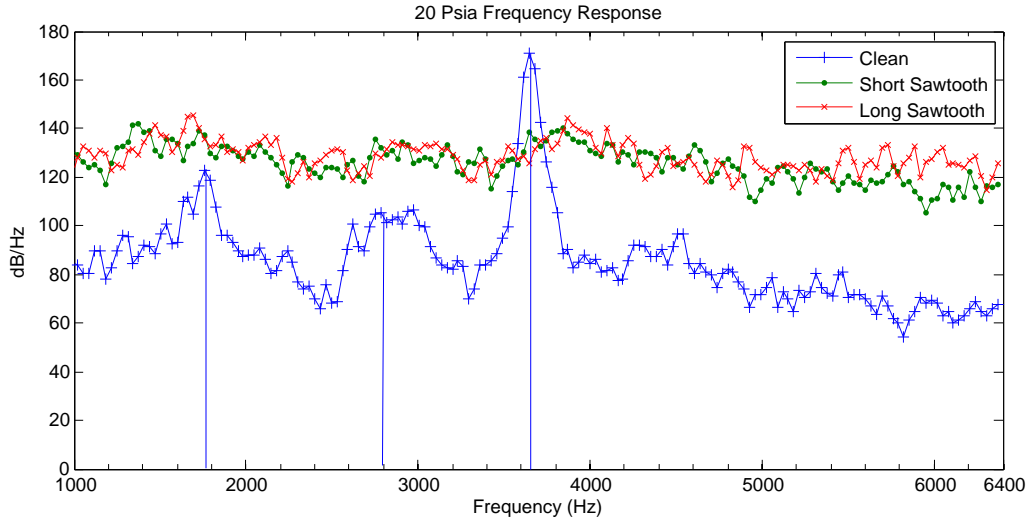


Figure 60. 20 Psia stagnation pressure frequency response clean, short sawtooth, and long sawtooth.

are increased by about 50 dB, the median signal strength is still well below (40 dB) the extreme amplitude of the 4th modal spike. Here, at a $P_{T,sc}=20$ Psia, the spoilers begin to have a positive impact on the acoustic tones, seen as a detuning of the 4th Rossiter mode.

4.3.2 Store Separation Improvements

While improving the acoustic environment of the cavity will decrease the possibility of excessive loading or vibrations on the enclosed equipment, one must consider the requirements to safely release the weapon from the aircraft. Again, one important question is whether a specific flow control device positively influences the separation characteristics of a weapon.

Figures 61 through 66 all show image sequences similar to the sphere drops previously shown, where the stagnation pressure is varied from 4 to 20 Psia. The difference is the implementation of both the short and long sawtooth spoiler passive flow control devices. These figures provide qualitative visualization of the impact of the tab spoiler on the dynamic response of the sphere model. Figure 61 shows the sphere response using the SST spoiler at $P_{T,sc}=4$ Psia. Here, the thickened shear layer can be seen growing along the cavity face. In this run, the sphere has enough vertical momentum to completely exit the cavity (frame 4) through the enlarged shear layer (wake). As in the unaided runs, as soon as the sphere surface encounters the shear layer/freestream boundary, the freestream imparts energy to the sphere and propels it back towards the face of the cavity ($-Z$). Figure 61 (run 524S5) is categorized as a marginal separation, as the sphere contacts the trailing edge, yet does not reenter the cavity.

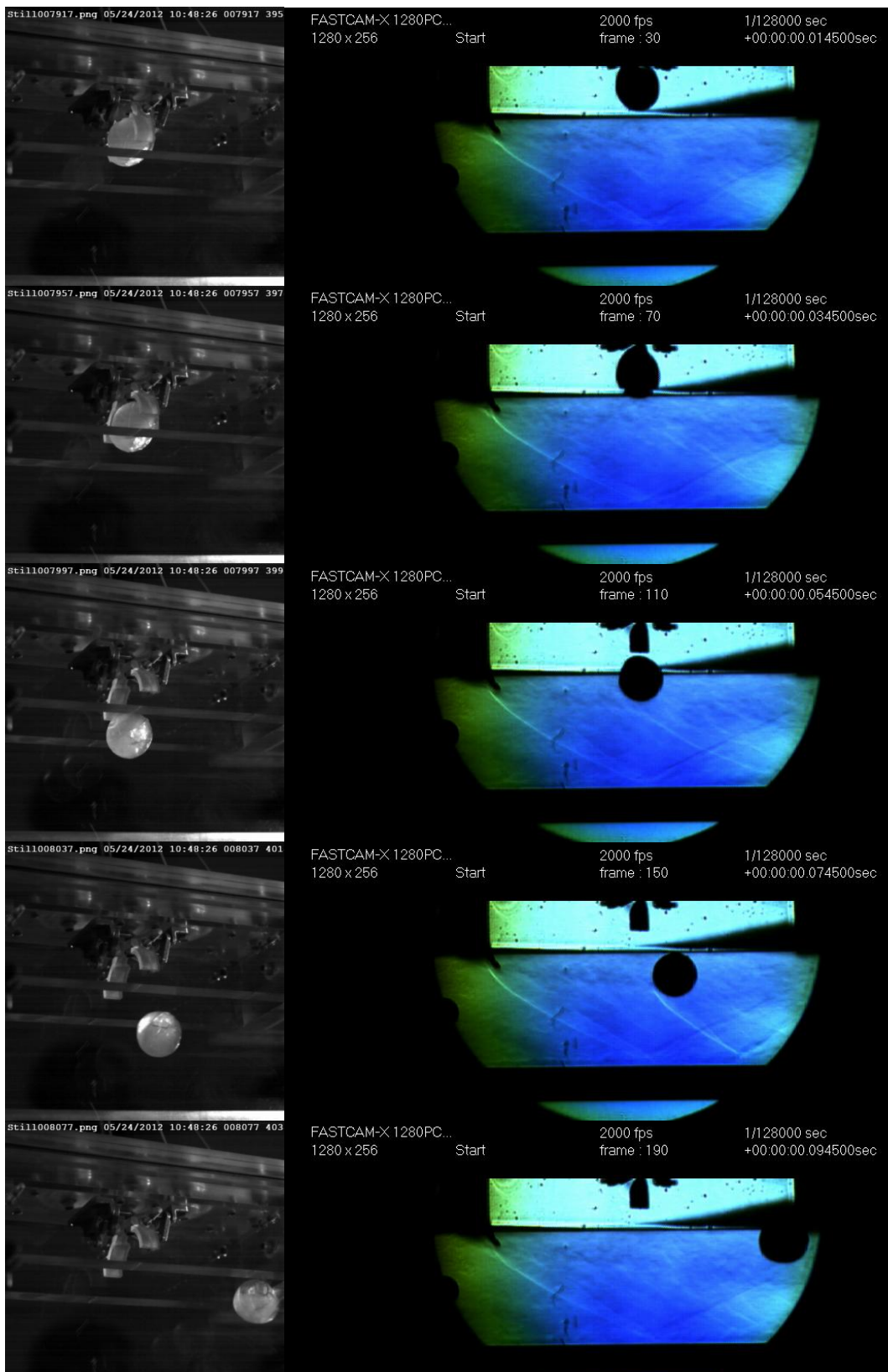


Figure 61. Image sequence of run 524S5. Short Sawtooth flow device used. Frame rate=2kHz, $\Delta t=20$ ms.

Figure 62 shows a sphere release with the SST spoiler at a stagnation pressure of 12 Psia. The shear layer growth is similar at the higher pressure as seen at 4 Psia. Again, the higher density gradients of the flow allow a more definitive view of the flow features. Seen at this pressure is the compression shock off the tab, along with the reflected shock off the boundary layer/tunnel floor. The reader should note that, with the SST configuration, the reflected shock off the tunnel floor does not interfere with the shear layer or sphere dynamics until after the trailing edge. Here, the sphere clears the cavity face as it descends into the wake and is propelled back towards the cavity, impacting the trailing edge, resulting in a marginal separation event, similar to the dynamic response shown in Figure 61.

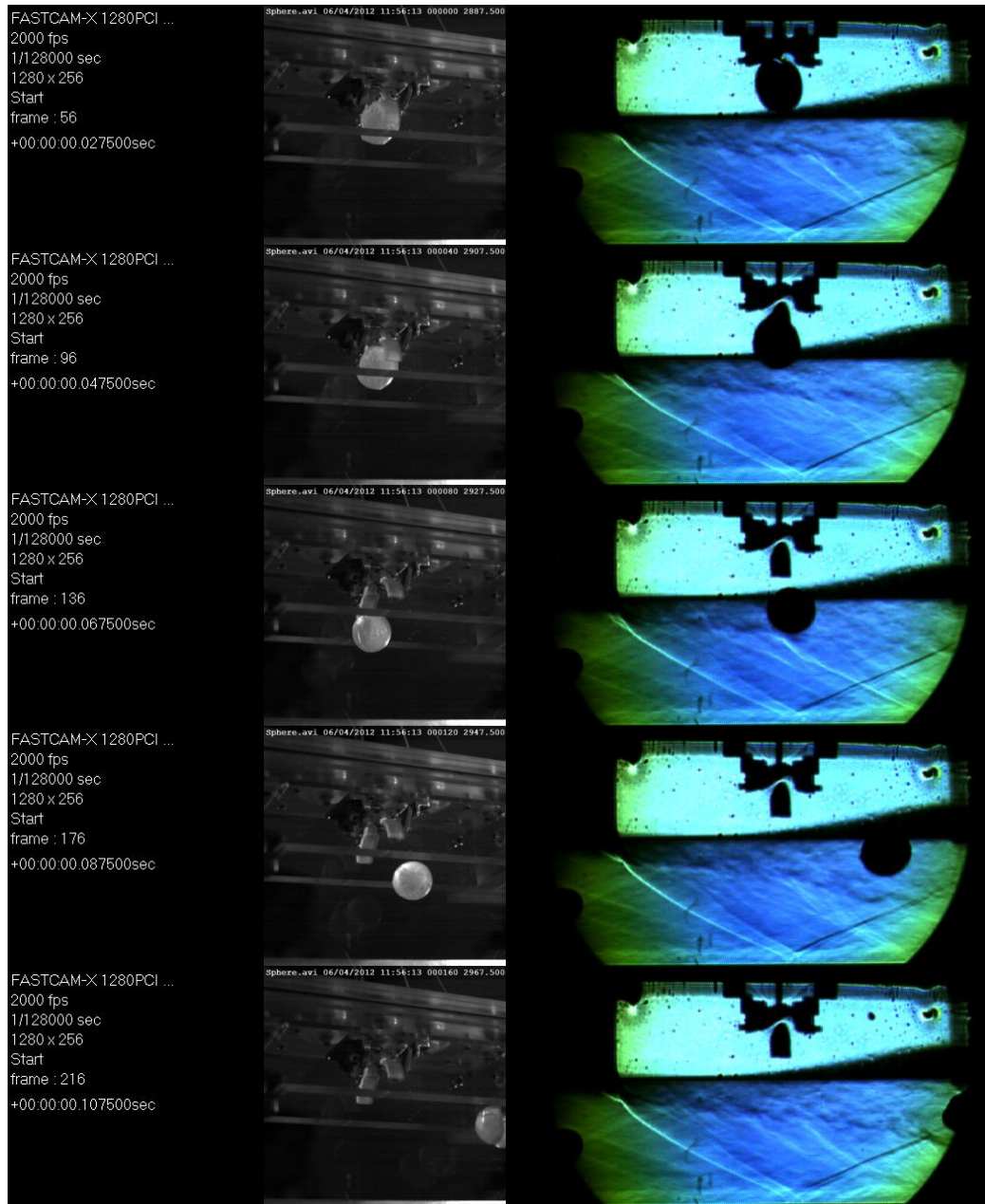


Figure 62. Image sequence of run 604S4. Short sawtooth flow control device used. Frame rate=2kHz, $\Delta t=20$ ms.

The 20 Psia run affords the clearest visualization of the flow features. The reader should note the distinct shock structures that occur in frames 1,2, and 4. These shock waves are indicative of the complex interaction between the large scale structures within the shear layer and the compressibility effects of the freestream. At all three pressures tested, the SST was sufficient to *drop* the shear layer and disrupt the organization enough to positively alter the sphere dynamics. As with the two preceding cases, the result of run 525S4 was a marginal separation.

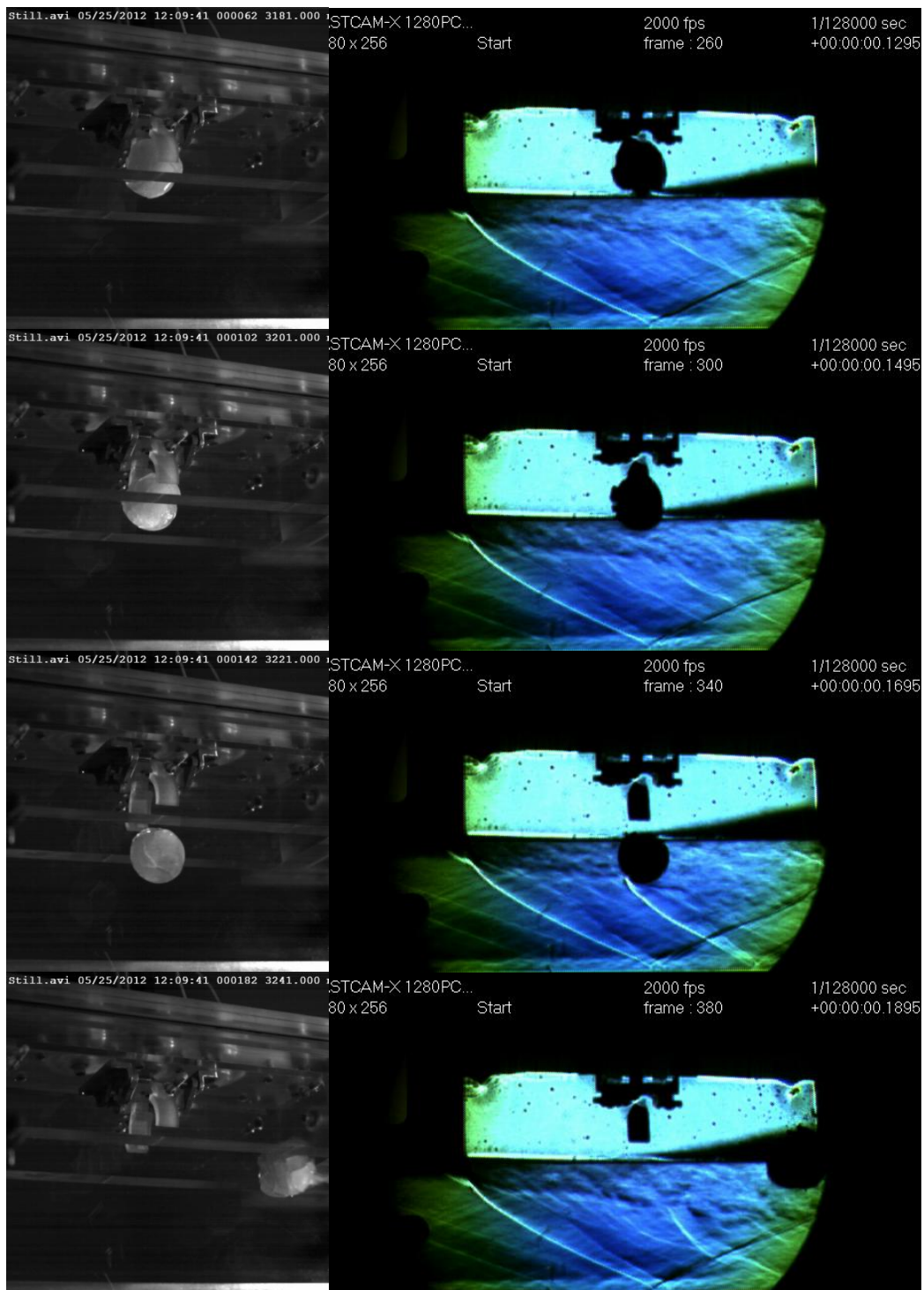


Figure 63. Image sequence of run 525S4. Short sawtooth flow control device used. Frame rate=2kHz, $\Delta t=20\text{ms}$.

The SST and LST are identical with the exception that the LST protrudes further into the incoming flow (2δ). Figure 64 shows the effect of the longer spoiler. Compared with the SST, the LST increases the shock angle off the tab, as seen by the reflected shock beginning forward of the sphere (and interfering with the shear layer prior to the trailing edge). This 4 Psia run represents one of only two successful sphere separation events seen in the wind tunnel.

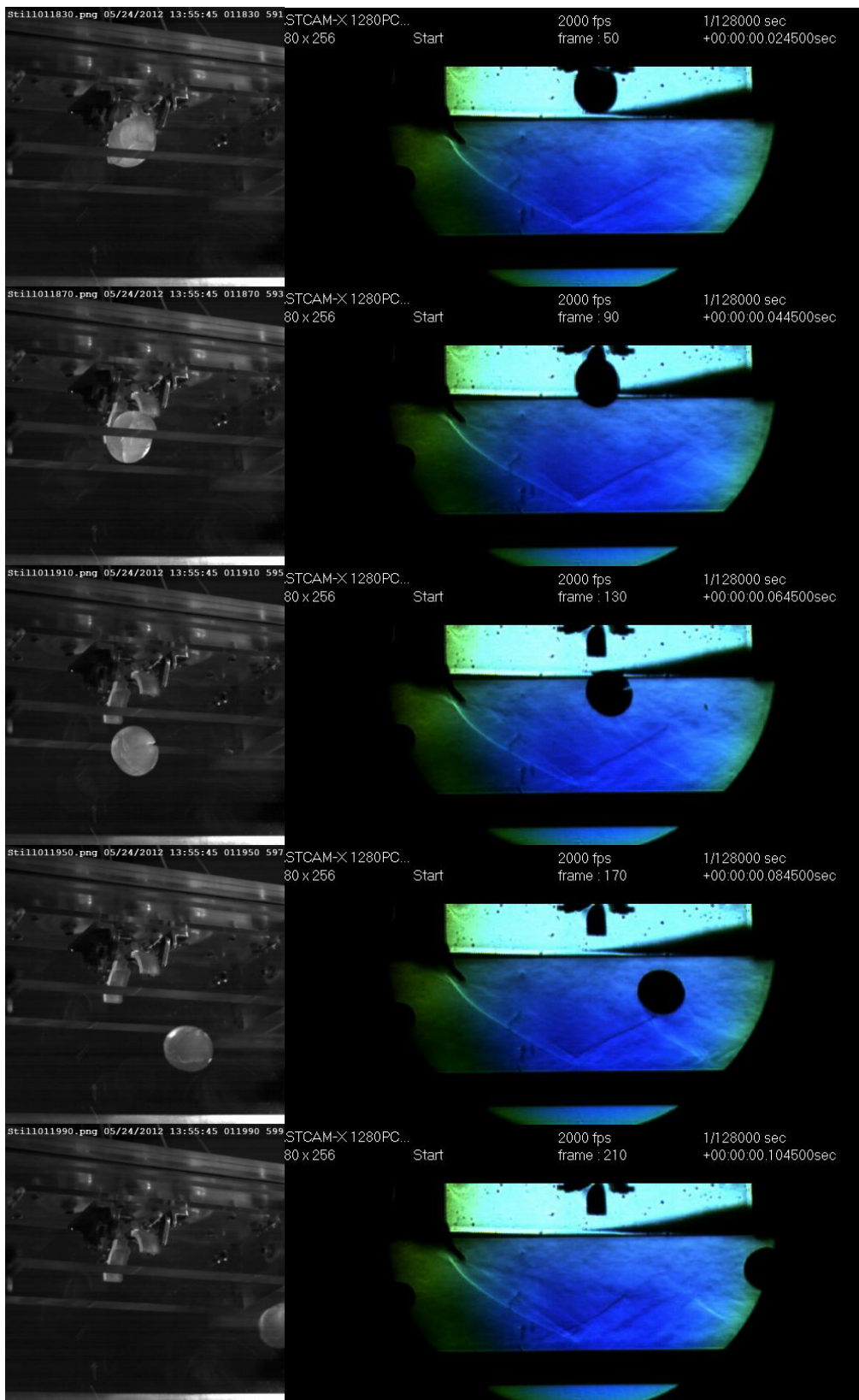


Figure 64. Image sequence of run 524S8. Long Sawtooth flow device used. Frame rate=2kHz, $\Delta t=20$ ms.

Figure 65 shows the 12 Psia sphere drop using the LST. Here, the sphere falls into the tab wake and begins translating downstream. As with the 4 Psia LST run, the shear layer is thickened, the wake is deeper, and the sphere translates further in $+Z$ than with the shorter spoiler. However, the release is unsuccessful, as the sphere impacts the trailing edge and breaks apart. Compared with the the 4 Psia LST case (run 524S8) where the dynamic pressure was lower, the higher aerodynamic forces imparted to the sphere by the freestream flow increases the upward velocity ($-w$), propelling the sphere back into the aft wall of the cavity.

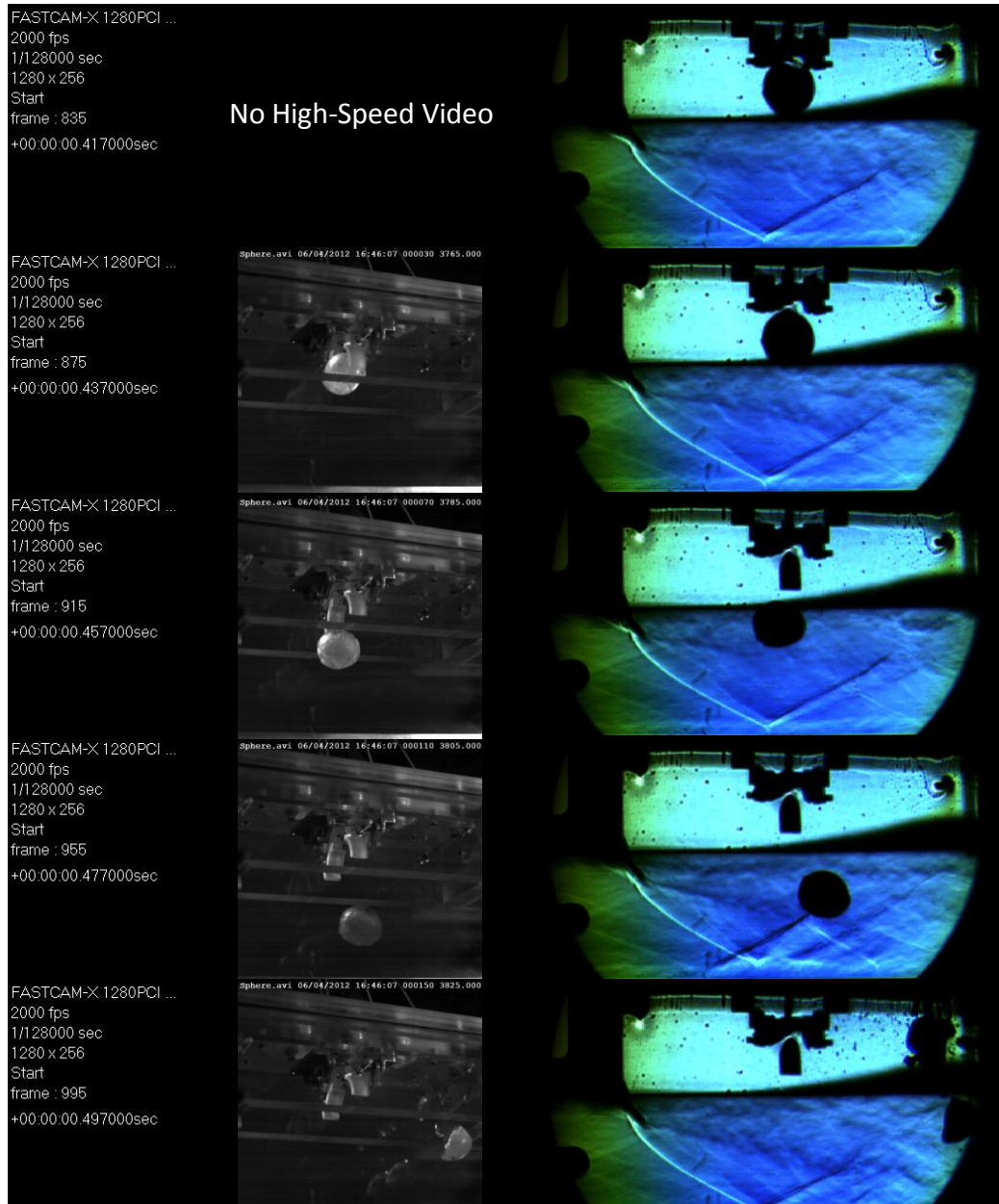


Figure 65. Image sequence of run 604S7. Long sawtooth flow control device used. Frame rate=2kHz, $\Delta t=20$ ms.

At the highest pressure, the shear layer displacement due to the LST is clearly seen. While the sphere does return to impact the trailing edge, this image sequence provides a clear depiction of the influence of the spoiler device on store separation. For further examples of sphere drops used in conjunction with flow control devices, the reader is referred to Appendices B through D.

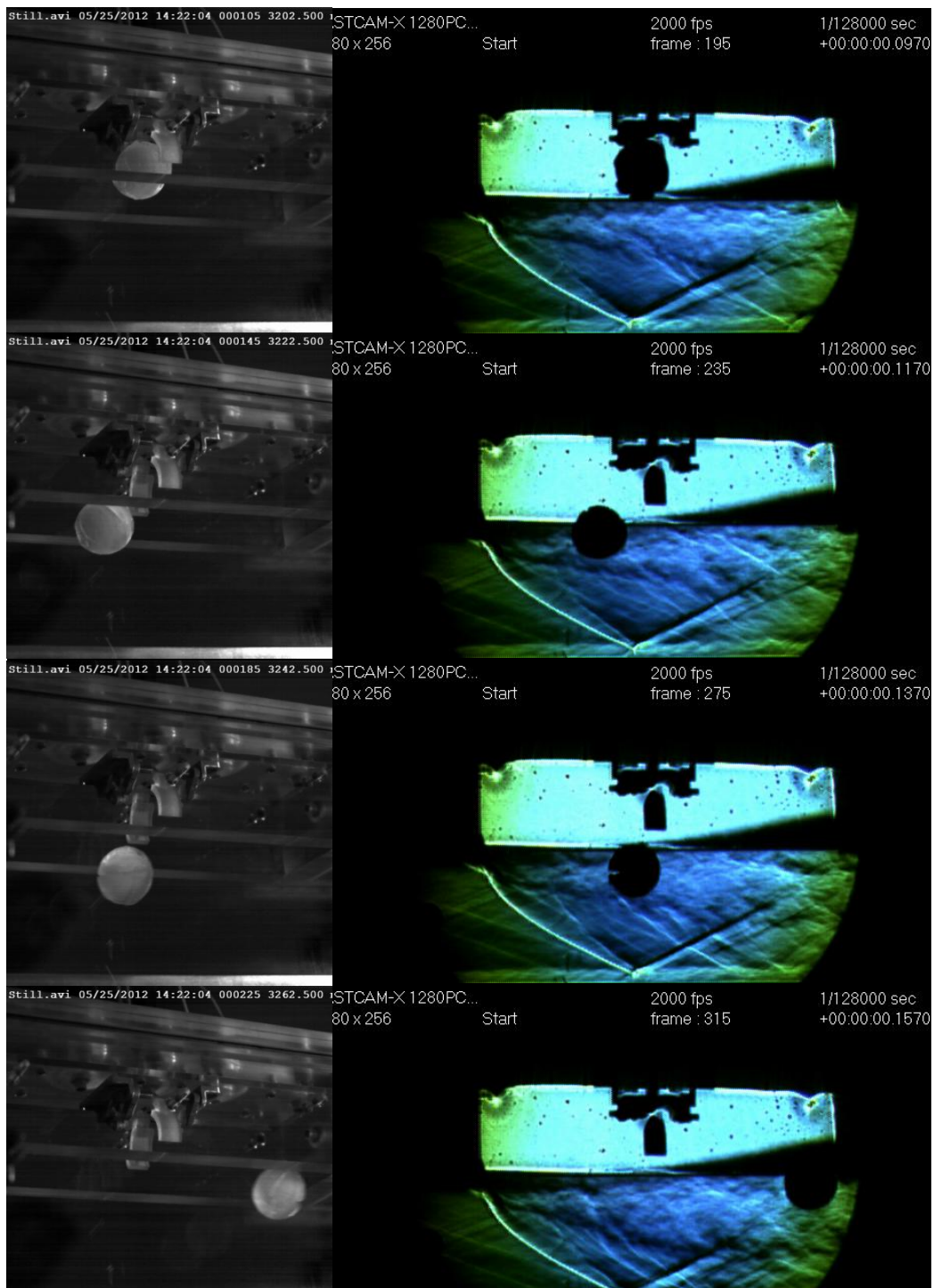


Figure 66. Image sequence of run 525S7. Long sawtooth flow control device used. Frame rate=2kHz, $\Delta t=20$ ms.

Figures 67 and 68 provide side-by-side comparison between runs without a spoiler, with an SST, and with an LST. Figure 67 is a $P_{T,sc}=4$ Psia condition while Figure 68 are $P_{T,sc}=12$ Psia runs. The three images in each figure show the instance where

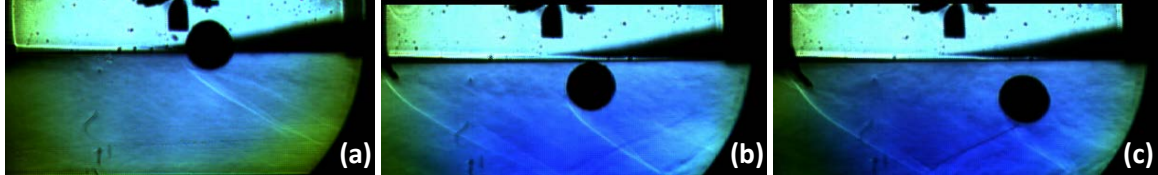


Figure 67. 4 Psia stagnation pressure (a) clean, (b) SST, and (c) LST.

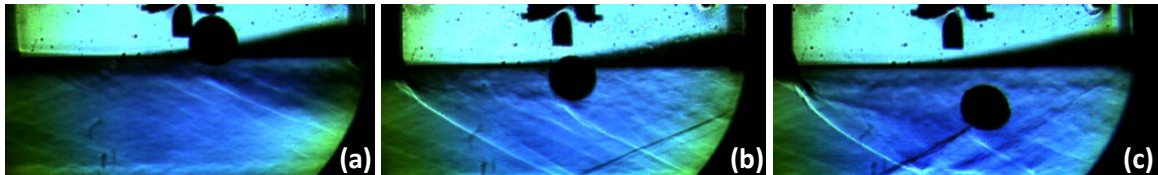


Figure 68. 12 Psia stagnation pressure (a) clean, (b) SST, and (c) LST.

the sphere is at its lowest point in the test section. Both figures clearly show the influence of the spoiler devices on the dynamics of the sphere. At both 4 and 12 Psia total pressures, the spoiler thickens the shear layer, creating a deeper wake, thereby increasing the vertical separation of the model during the separation event.

The effectiveness of the spoiler device on the separation of the sphere can be seen in Figure 69. From the bar graph, one can see that in all cases, without the aid of a flow control device, the resultant separation event was unsuccessful. Incorporating a simple spoiler tab increases the vertical displacement of the sphere, aiding in the separation of the model. While only two test cases resulted in a completely successful release, the data and imagery clearly indicate that a simple spoiler device is effective at positively altering the dynamics of a sphere model at high supersonic speeds.

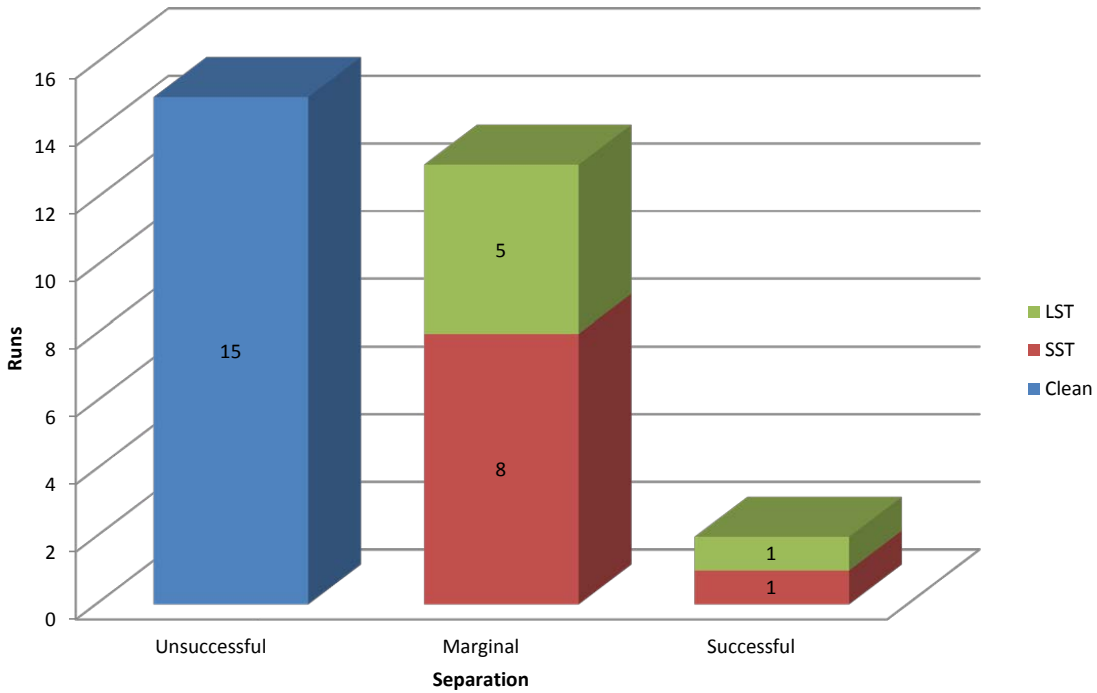


Figure 69. Bar graph showing the effectiveness of the tab spoiler device on the separation characteristics of the sphere.

4.4 Mk-82 Sub-scale Model Testing

The applied power of ice model testing method is seen when models are representative of shapes seen in current (and future) air-to-ground stores. Although the method demonstrated provides little flexibility in mass and inertial property specification, it does provide a rapid, inexpensive testing procedure that could prove viable for front-end risk reduction during the research and development of a new store or aircraft configuration. As with all other freedrop tests, applying the results to full-scale predictions is limited by compromises one makes in the application of the scaling laws.

Both of the following figures (Figs. 70 and 71) depict two repeated releases of an ice store, modeled after the Mk-82 GPLD weapon, at $P_{T,sc}=4$ Psia. When scaling up in mass and inertia, both the light and heavy Mach scaling laws benefit from a

reduced tunnel dynamic pressure (q). For this reason, the primary testing focus was at the lowest stagnation pressure. Here, both figures (70 and 71) depict a consistent, clean release from the mechanism. However, once the store body encounters the shear layer/freestream boundary, the resultant high-pressure differential experience by the lower forebody of the model induces a pitch nose-up ($-M_y$). This positive AOA increases the lifting force on the store with the resultant motion developing into a collision between the store and the release mechanism for both cases.

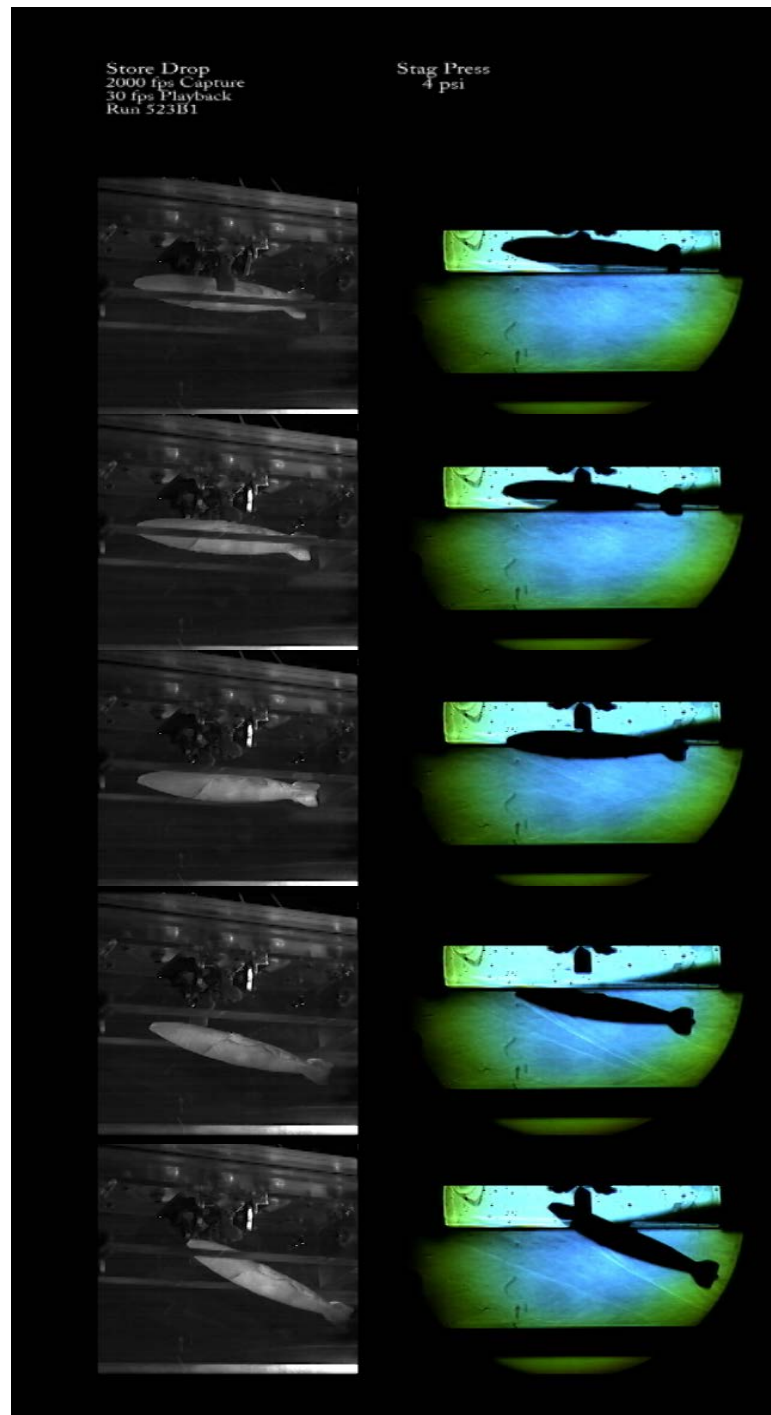


Figure 70. Image sequence of run 523B1. No flow control device used. $P_{T,sc}=4$ Psia. Frame rate=2 kHz, $\Delta t=20$ ms.

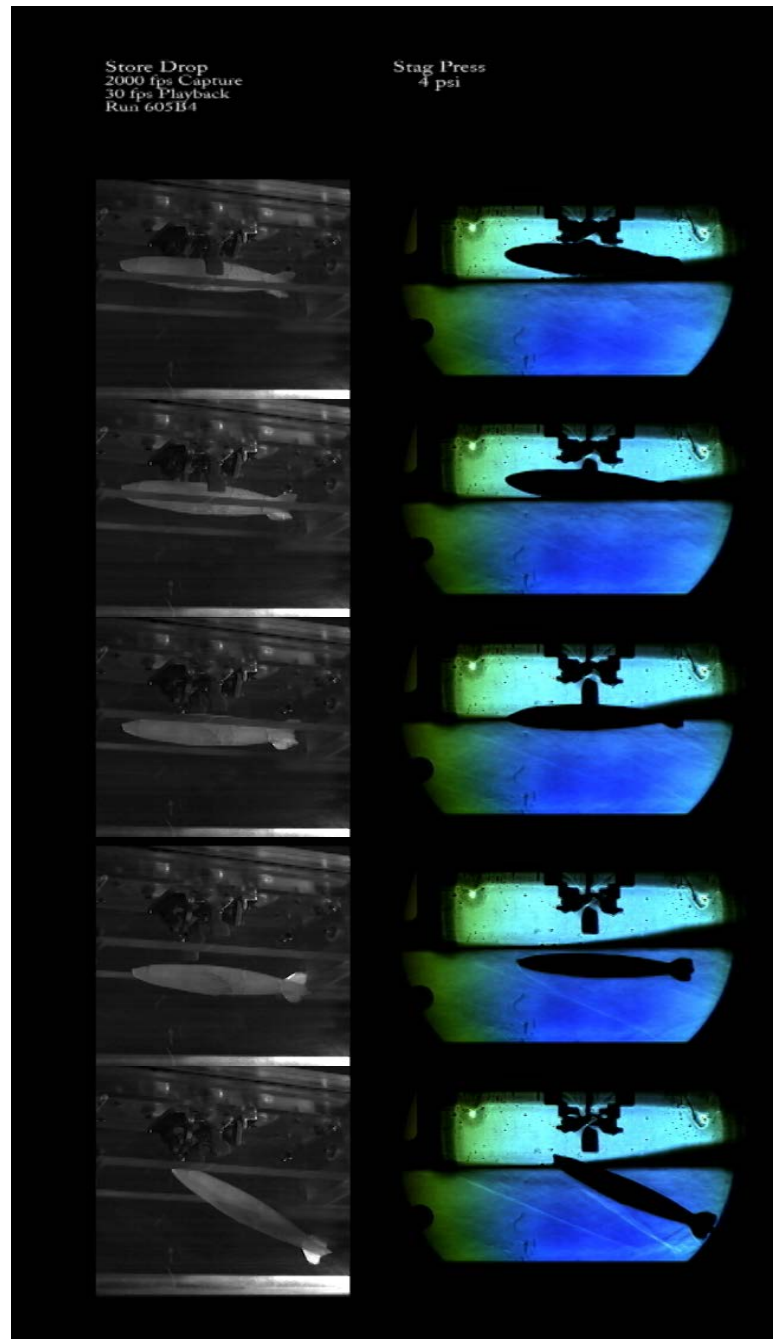


Figure 71. Image sequence of run 605B4. No flow control device used. $P_{T,sc}=4$ Psia. Frame rate=2 kHz, $\Delta t=20$ ms.

The following image sequence (Figure 72) represents the ultimate example of the flexibility of the non-destructive model testing process. Here, the Mk-82 ice store is released at the lowest dynamic pressure available in the SVDB tunnel. The LST is installed to alter the flowfield within and around the cavity. A clean release from the mechanism results in a level orientation of the weapon longitudinal axis with respect to the flow ($\theta=0$). This orientation of the store model is maintained as it passes through the shear layer into the freestream. The end result is a successful separation event of the store, ultimately impacting the floor of the test section. These three preceding figures of the store model represent the runs where shear layer entry occurs without a remarkable amount of pitch. This is an example of an acceptable degree of repeatability between release events. For further examples of Mk-82 ice-model releases, the reader is referred to Appendix E.

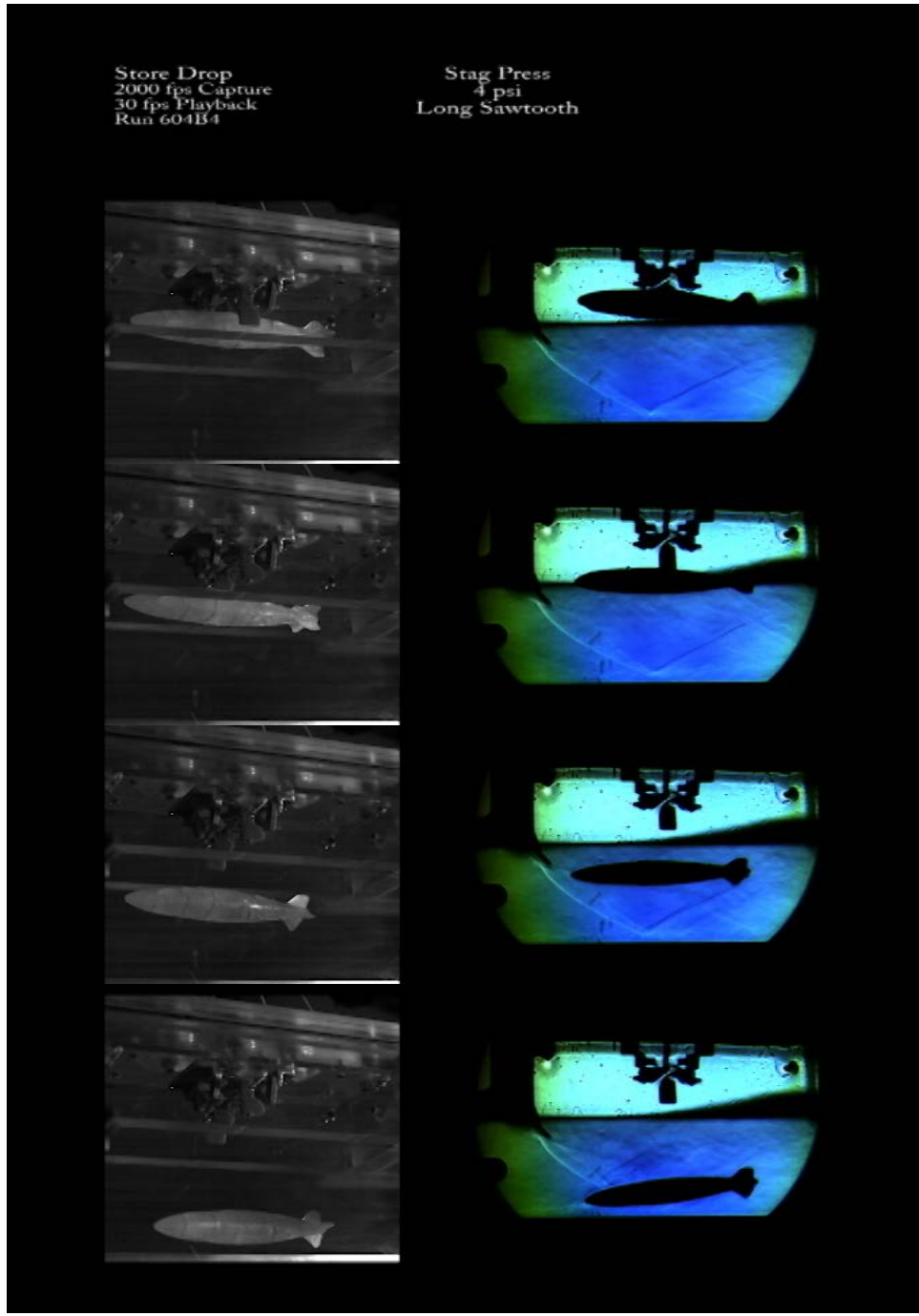


Figure 72. Image sequence of run 604B4. Long sawtooth flow control device used.
 $P_{T,sc}=4$ Psia. Frame rate=2 kHz, $\Delta t=20$ ms.

Figure 73 shows the store ice model released under the influence of the spoiler device. Figure 73 (a) shows the unassisted release of the store at the moment where the bottom surface impinges the freestream, having passed through the shear layer. It is at this point the store begins a pitch nose up angular rate. Subfigure (b) shows

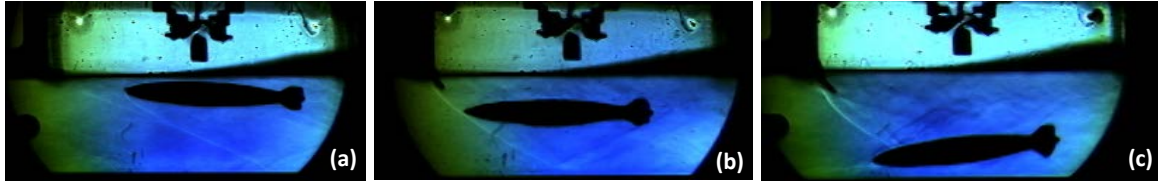


Figure 73. Mk-82 ice model. 4 Psia stagnation pressure (a) clean, (b) SST, and (c) LST.

the store release using the SST device. The wake of the SST allows the store greater vertical displacement from the cavity prior to the increasing angular rates in pitch. Lastly, the LST device produce an even thicker shear layer (or deeper wake), allowing the store to gain enough vertical momentum to completely penetrate the shear layer and continue through the freestream maintaining a level pitch ($\theta=0$). This store release suggests that a spoiler device can be effective at improving the store separation characteristics of a weapon released in high supersonic flow.

As with the sphere, the Mk-82 ice model was freedrop tested at the three total pressures (4, 12, and 20 Psia) in the clean, SST, and LST configurations. The total number of Mk-82 releases was 15. Remaining image sequences can be found in Appendix E. Because of the inconsistency of the model shape (fin quality) and the poor release repeatability (pitch), salient statistics could not be gleaned from the small population of Mk-82 releases.

4.5 Scaling Laws Applied

While the sub-scale testing presented proves a compelling case of what occurs at miniature scales, the apposite question is “how can these results be applied to full-scale articles released at flight conditions”. The answer lies in a clear understanding of the scaling laws and the compromises one must make during application of those laws in sub-scale \rightarrow full-scale extrapolation.

As developed by Keen, Morgret, and Arterbury [14] and summarized in Chapter II, the primary constraint on the freedrop experimentalist can be shown in the following relationships:

$$\text{Aerodynamic Scaling} \implies M'_\infty = M_\infty \quad (43)$$

$$\text{Motion Scaling} \implies M'_\infty = M_\infty \sqrt{\lambda \frac{g'}{g} \frac{T_\infty}{T'_\infty}} \quad (44)$$

For context, the values used in the experimental research will provide a framework for understanding this scaling *contradiction*. For acceptable aerodynamic scaling of a cavity release at $M=2.94$, the tunnel Mach number must also be set to $M=2.94$, otherwise compressibility effects are compromised. For truly accurate aerodynamic scaling, Reynolds number must also be matched, yet store aerodynamic properties are far less dependent on Reynolds number than Mach number [14] (also, attaining actual Reynolds number in a test condition is limited to highly specialized tunnels).

For proper dynamic scaling (Equation 44), the test Mach number would be set to some value less than Mach 2.94. Using a scaling factor of 1/20th, a gravity ratio of 1 ($g' = g$), and a temperature ratio of 0.8, the test Mach number would need to be set at 0.6. This example shows the fundamental contradiction between the two scaling laws, as the aerodynamic scaling and motion scaling cannot be simultaneously attained in a wind tunnel.

For this reason, compromises must be applied between the two scaling requirements. For subsonic flow, matching the Mach number of test conditions and actual flight is not critical, therefore the motion Mach number requirement can be readily attained at the expense of aerodynamic scaling. This is the essence of Froude scaling. As compressibility effects become significant in transonic and supersonic flow, it becomes critical to maintain the aerodynamic relationship (Equation 43) at the expense of the motion scaling Mach requirement. These flow regimes *force* the engineer to effectively choose between the two Mach dynamic scaling laws, heavy and light Mach scaling. Here, the term *Mach* scaling refers to the two primary motion scaling laws used in transonic/supersonic flow.

Two important parameters that must be accounted for in the dynamic scaling laws are the equivalent mass and moment of inertia. While other parameters must also be scaled appropriately [14], these represent a intuitive basis for the scaling laws. For proper mass and moment of inertia scaling, Equations 7 and 8 must be satisfied between sub-scale (') and full-scale values. That means, for the engineer conducting freedrop testing, the test conditions must be varied appropriately to correctly scale dynamically (in both mass and moment of inertia). For a known weapon at a given release altitude and airspeed, ρ_∞, V_∞ , and m are fixed. Generally, the scale of the model is determined by the physical size of the wind tunnel. Therefore, when scaling in mass and moment of inertia, the test conditions can either be modified by varying the model weight or the tunnel density.

4.5.1 Heavy Mach Scaling

When using heavy Mach scaling laws, the key assumption is that a) the sub-scale gravity cannot be altered ($g'/g=1$) and b) the velocity ratio is fixed by the test Mach number. Due to these assumptions, the following mass and moment of inertia

relationships, developed in Chapter II, are reiterated below:

$$m' = m(q'_\infty/q_\infty)(\lambda^2) \quad (45)$$

$$I' = I(q'_\infty/q_\infty)(\lambda^4) \quad (46)$$

The term *heavy* refers to typical model weights that result from this relationship. With a dynamic pressure ratio at unity and a gravitational constant of 32.2 ft/s², in order to properly model the weight of the Mk-82, the 1/20th model must weigh 1.25 lb. The average density of a Mk-82 (4 ft³) is 125 lb/ft³. A 1/20th model would need to be composed of a material with an average density of 2525 lb/ft³. For comparison sake, the density of platinum is 1350 lb/ft³. This illustrates why heavy Mach scaling is generally limited to larger tunnel facilities with larger sub-scale models (> 1/20th) constructed of high-density materials such as lead or gold.

For the current research, instead of using a model density significantly higher than actual weapon densities, the weight of the model was fixed by the density of frozen tap water (57.3 lb/ft³). This, however, was compensated by the capability of the AFIT blowdown tunnel to reduce q'_∞ , thereby modeling the actual weapon mass and moment of inertia properties. The following example uses the sphere model to demonstrate how the test dynamic pressure influences the heavy Mach scaling relationships.

The notional sphere represents a model that further simplifies Marshall's presentation of similitude [20] using only 1-DOF, that is the vertical component (\ddot{Z}). This configuration eliminates pitch considerations and angular rates, focusing on scaling in translation only. The example uses a release altitude of 40000 ft, Mach 2.94, with a dynamic pressure equal to 2378 lb/ft². The 1/20th sphere (d=0.938 in) scales up to a full-size notional, spherical store with a diameter of 1.56 ft. The corresponding volume is approximately 2 ft³. Rearranging the terms in Equation 45 and changing

the test dynamic pressure effectively changes the heavy scaled weight of this notional store at this flight condition.

Table 10 presents the heavy Mach scaling (in mass) results of this notional, spherical store. Scaling a 1/20th ice model to a full-size fixed volume sphere by changing the dynamic pressure effectively results in a store *constructed* from various materials. While the 1 Psia case was not experimentally tested, it is included for comparison with the numerical simulations. At a stagnation pressure of 1 Psia, the full-scale

Table 10. Sphere heavy Mach scaling results. Mach 2.94, 40k ft, 1/20th scale.

$P_{T,sc}$ (Psia)	q'_∞/q_∞	Weight (lb)	Density (lb/ft ³)	Material
1	0.011	550	225	Titanium
4	0.044	138	69	Rubber
12	0.13	46	23	Pine
20	0.22	28	14	Balsa

equivalent effective weight is 550 lb, or approximately the density of titanium. At the highest stagnation pressure tested, the notional sphere effective weight is only 28 lb, with an equivalent density of 14 lb/ft³. At this tunnel condition, the ice model scales up to a full-size article made of balsa wood. While these values illustrate the mass scaling relationship of heavy Mach scaling, with the exception of the 1 Psia case, they result in store densities unrealistic to actual weapons. This is a key reason why heavy Mach scaling is used in larger tunnels, where $\lambda > 1/20$.

Having laid out this example for heavy Mach scaling using a simple sphere, one can transition to applying heavy Mach scaling to the Mk-82 shaped ice model. The sphere example targeted a fixed release altitude and allowed the variable dynamic pressure ratio obtained in the SVDB to change the scaled weight of the notional full-size article. In the following example, the Mk-82 shaped ice model is compared

against an actual Mk-82 with known mass and moment of inertia properties [17]. In the sphere example, changing the tunnel conditions changed the heavy scaled weight of the notional store released at a fixed altitude (40000 ft). The Mk-82 example below (Tab. 11) shows how an experimentalist can alter the tunnel dynamic pressure to change the simulated release altitude of a full-size weapon. While the sphere example assumed the angular components were of no consequence, the store shaped weapon scaling must be assessed using the vertical component and the pitch component ($\ddot{Z}, \ddot{\theta}$). To this end, both mass and moment of inertia scaling components must be accounted for in the dynamic Mach scaling laws.

Table 11 shows the effect of scaling up a 1/20th Mk-82 model to a full-scale Mk-82 using heavy Mach scaling. The properties of an actual Mk-82 and the ice model are

Table 11. Heavy Mach scaling mass and inertial properties for a store shaped ice model. Mach 2.94, 1/20th scale.

Actual Properties			
	Weight (lb)	Mass (slug)	I_{yy} (slug·ft ²)
Full-Size Mk-82	500	15.5	37
1/20 th Uniform Ice Model	0.031	0.00097	6.0x10 ⁻⁶

$P_{T,sc}=1$ Psia		Scaled Values		
Simulated Altitude (ft)	q'_∞/q_∞	Weight (lb)	Mass (slug)	I_{yy} (slug·ft ²)
20k	0.0044	2813	87	218
40k	0.011	1136	35	88
57625	0.0248	500.0	15.5	38.7
60k	0.028	436	14	34

$P_{T,sc}=4$ Psia		Scaled Values		
Simulated Altitude (ft)	q'_∞/q_∞	Weight (lb)	Mass (slug)	I_{yy} (slug·ft ²)
20k	0.018	703	22	54
27905	0.0248	500.0	15.5	38.7
40k	0.044	284	9	22
60k	0.11	109	3	8

included at the top of the table as a reference. To properly heavy scale in both mass and moment of inertia, the q ratio (q'_∞/q_∞) must be reduced to 0.0248. From Table 11 one can see that at the lowest stagnation pressure available in the SVDB tunnel, the ice model scales properly in mass *and* moment of inertia, commensurate with a Mk-82 released at 27905 ft. The $P_{T,sc}=1$ Psia condition is included in the table to reinforce the consequence of further reducing the tunnel dynamic pressure. Were this condition attainable in the tunnel, the simulation would model a Mk-82 release at 57625. From Table 11, it is evident that the capability of achieving realistic release altitudes under heavy Mach scaling laws is possible, even with a light sub-scale model, if the tunnel dynamic pressure can be sufficiently reduced.

4.5.2 Light Mach Scaling

Light Mach scaling assumes that the gravitational constant can be changed such that the Mach number requirement can be matched both aerodynamically *and* dynamically. Under typical test conditions, this requires a significant increase in the test gravitational constant. Though generally insufficient, various approaches have been attempted, to include augmenting the ejection force or simply accepting the errors from from the gravitational deficiency. Because this test was conducted without an ejection mechanism, any light Mach scaling results must account for this gravitational deficiency. Accounting for the variable gravitational term, the light Mach scaling mass and moment of inertia relationships are given below [20]:

$$m' = m(\rho'_\infty/\rho_\infty)(\lambda^3) \quad (47)$$

$$I' = I(\rho'_\infty/\rho_\infty)(\lambda^5) \quad (48)$$

As with heavy Mach scaling, light Mach scaling can be strongly influenced by changing the tunnel total conditions, here resulting in a changing freestream density.

Table 12 provides the mass and inertial scaling properties using light Mach scaling laws for the store shaped model. In this example, the fixed properties of the Mk-

Table 12. Light Mach scaling mass and inertial properties for a store shaped ice model. Mach 2.94, 1/20th scale.

	Weight (lb)	Mass (slug)	I_{yy} (slug·ft ²)
Full-Size Mk-82	500	15.5	37
1/20 th Uniform Ice Model	0.031	0.00097	6.0x10 ⁻⁶

$P_{T,sc}=4$ Psia		Scaled Values		
Simulated Altitude (ft)	ρ'_∞/ρ_∞	Weight (lb)	Mass (slug)	I_{yy} (slug·ft ²)
20k	0.040	6182	192	479
40k	0.087	2865	89	222
60k	0.23	1100	34	85
77050	0.496	500.0	15.5	38.7

$P_{T,sc}=12$ Psia		Scaled Values		
Simulated Altitude (ft)	ρ'_∞/ρ_∞	Weight (lb)	Mass (slug)	I_{yy} (slug·ft ²)
20k	0.12	2074	65	161
40k	0.26	961	30	74
54225	0.496	500.0	15.5	38.7
60k	0.67	369	12	29

$P_{T,sc}=20$ Psia		Scaled Values		
Simulated Altitude (ft)	ρ'_∞/ρ_∞	Weight (lb)	Mass (slug)	I_{yy} (slug·ft ²)
20k	0.20	1253	39	97
40k	0.43	581	18	45
43125	0.496	500.0	15.5	38.7
60k	1.12	223	7	17

82 provide a reference from which to scale up to an effective altitude (vice weight). Targeting the known properties of the Mk-82, the scaling laws allow the freedrop experimentalist to simulate a release from various altitudes. Three total pressures are included in the table to reinforce how a change in total pressure affects the simulated release altitude of a full-scale store. Setting $P_{T,sc}$ to 4, 12, and 20 Psia changes the

simulated release altitude to 77050, 54225, and 43125, respectively. The reader should note that applying the light Mach scaling laws to the Mk-82 model provides proper scaling in both mass and moment of inertia.

From Table 12, one might be tempted to make the erroneous conclusion that light Mach scaling is the preferred method for predicting full-scale dynamics from sub-scale ice models. The results, using the light Mach relationships in Equations 47 and 48, provide realistic release altitudes at each of the tested stagnation pressures. The difference between heavy Mach and light Mach scaling is the gravitational constant used during testing. As previously stated, light Mach scaling requires an increase in test gravity. This is usually accomplished by augmenting the ejection force to account for the gravitational deficiency (Equation 21). With a velocity ratio of unity, a 1/20th scale test would require an ejection force 19 times earth's gravitational field.

This research did not impart an ejection force to the weapon model. Even with an augmented ejection force, light Mach scaled tests yield weapons trajectories that are generally closer to the parent *aircraft* than full-scale results [3]. Therefore, it is reasonable to assume that a successful release of a light Mach scale model (frozen tap water) without an ejection force would guarantee a successful release in full-scale flight. It is for this reason that the ice model process demonstrated in this research would yield a conservative approach to initial risk reduction studies on store separation from an internal bay.

V. Conclusions and Recommendations for Future Work

5.1 Research Conclusions

Given the operational and tactical advantages of internal weapons bays and supersonic flight, it is natural to consider combining these two entities. However, carriage and release from a cavity at supersonic speeds poses unique technical challenges. One of the most prominent issues is achieving safe store separation, and separation of a body from a cavity into a Mach 2.94 freestream is the focus of this research.

The difficulties in predicting separation of a body from a cavity into a supersonic freestream are manifold. Foremost is that the fluid impinging the body is non-uniform and highly time-dependent during the release due to the complex flowfield within the cavity and the freeshear layer. The presence of the shock or expansion wave emanating from the cavity lip further complicates the problem. In addition, a sound computational model needs to include the motion of the store and also properly track the reaction to the forces, integrated from pressure and shear stress acting over the entire body.

Traditional approaches to assessing store separation include flight testing, CFD, and wind tunnel tests. Since flight tests are expensive, it behooves the DoD research community to improve wind tunnel testing and computational resources used for store separation. To this end, one objective of the current research was to develop and utilize non-destructive models of a very simple geometry and freedrop them in the wind tunnel while using appropriate diagnostics. The non-destructive nature of the models enabled the use of a blowdown facility with a vacuum attached downstream of the diffuser. In turn, this setup enabled a wide range of stagnation pressures, and hence dynamic pressures in the test section. A second objective was to apply the

OVERFLOW CFD solver in a manner which allowed direct comparison to the wind tunnel experiment.

To an extent, one could consider the study a limited form of validation for the OVERFLOW code. After establishing this robust experimental procedure, additional experiments were carried out using flow control, in the form of spoilers, and more representative store models. Results were categorized as follows: (1) initial runs (computational and experimental) without store release, (2) CFD and freedrop testing of sphere models for varied stagnation pressure, and (3) freedrop testing of sphere and Mk-82 models with and without flow control applied.

When a stationary store was mounted, pressure tap data acquired within the cavity compared reasonably well with the computational results. Spectra showed that Rossiter modes in modes 2, 3, and 4 were present in both. Furthermore, Schlieren visualization generally matched the trends shown in the CFD results.

Spheres composed of ice were experimentally dropped from a cavity with $P_{T,sc}=4$, 12, and 20 Psia. At each of these three conditions, the sphere initially descended into the shear layer but then returned upward, back into the cavity. CFD simulation of the store showed similar dynamics when released at 4 and 12 Psia total pressure. One of the most critical findings of the research was that the computational and the experimental showed excellent correlation in this result.

The OVERFLOW solver was used to model sphere releases at stagnation pressures lower than those available experimentally. At $P_T=2$ Psia, the dynamic path of the sphere was similar to that of the higher pressures, as the sphere returned back into the cavity. However, at a stagnation pressure of 1 Psia, the sphere successfully separated from the cavity, aligned with the expectation that the sphere would clear the cavity if the pressure was sufficiently reduced.

Two passive flow control devices were investigated. Both devices used an angled,

tab-shaped spoiler with a sawtooth edge. The shorter device extended 1δ into the flow, while the longer one protruded 2δ . The impact of the devices were assessed by measuring the time-varying pressure signal at the back wall. For all three stagnation pressure conditions, the spoiler effectively eliminated the resonant peaks but raised the broadband noise levels. In this respect, the effect of the spoiler on the cavity acoustics is similar to other noise attenuating devices.

A critical aspect of the investigation into flow control was the effect of the spoiler on store separation. The spoiler did alter the cavity flowfield in a way that positively enhanced store separation. As suggested by the Schlieren imagery, the tab produced a low momentum wake behind the spoiler, thus thickening the shear layer. Sphere freedrop tests demonstrated that this wake increased the vertical separation of the sphere. Of the fifteen sphere drops augmented by a flow control device, all proved effective at enhancing the model separation characteristics. Thirteen resulted in marginal separations, while two separation events were successful, in which the sphere separated from the cavity without impacting the cavity or test section.

An ice model shape similar to a Mk-82 was released at each of the test stagnation pressures, both with and without the spoiler device. The key result from this aspect of the experiment is the capability of conducting non-destructive sub-scale freedrop testing of an ice model in the shape of a real store. This research found that model repeatability was difficult to assess from one Mk-82 ice model to the next. In addition to model consistency, a method of determining the c.g. and moment of inertia of each model would need to be implemented. As demonstrated with the sphere model, the spoiler devices proved effective at increasing the initial vertical displacement of the Mk-82 model, a key component to a successful separation event.

The concluding section of the results and analysis was an application of the two dynamic Mach scaling laws. Because heavy Mach scaling does not require changing

the test gravity and the model translations are more consistent with actual results, it is the preferred scaling law when operating in larger tunnels. In order to properly scale in mass and moment of inertia, either the model weight must be significantly increased when compared with the actual weapon or the tunnel dynamic pressure must be drastically reduced. Using the sphere model, Table 10 demonstrated that changing the dynamic pressure within the test section effectively increased the actual mass of the full-size, notional sphere store. By changing the dynamic pressure, the experimentalist *controls* the weight (and material) of the full-size article. In the Mk-82 example, the full-scale properties were known, thereby allowing a changing dynamic pressure to affect the scaled altitude of the full-size store. It was found that operating the tunnel at the lowest stagnation pressure properly simulated the mass and moment of inertia properties under heavy Mach scaling.

The alternative scaling law when operating in the transonic and supersonic regime is light Mach scaling. Light Mach scaling provides a more accurate pitch response when compared with full-size release, yet requires some method of changing the gravitational field in the test section. Table 12 indicates that under light scaling laws, the Mk-82 ice model scales up to realistic release altitudes at all tested total conditions. While Table 12 would lead one to believe that, using a Mk-82 shaped model consisting of a light material, light Mach scaling should be used to predict full-scale trajectories at the various altitudes. It should be reiterated that light Mach scaling assumes the gravitational field in test section is significantly increased. Under increased gravitational acceleration, the fixed mass ice model would be *heavier*. Even with augmenting gravity using an increased ejection force, light Mach scaled models underpredict the vertical separation from the aircraft (i.e. they *float* compared with full scale weapons). This is why light Mach scaling is a conservative approach to separation analysis. If, under light Mach scaling laws, the weapon successfully separates

in the test condition, then it virtually guarantees that safe separation will occur in flight.

This research did not use an ejection mechanism in the release process. Therefore, gravity is not augmented, deficient by the scale factor (19 g 's). For this reason, this research represents an even more conservative approach than seen in normal Mach scaling. If a safe separation occurs in the SVDB, then even more confidence can be given to the prediction that a full-scale store released at altitude would successfully separate from the aircraft. It is not inferred the concepts presented in this research will be the quintessential store separation analysis technique for all stores released from an internal bay. It is proposed that this rapid, flexible, freedrop testing method could build an extensive dataset from which to make sound decisions early in the research and development phase of current and future store/aircraft designs.

5.2 Future Opportunities

The following is a brief discussion of the various improvements that can be applied to increase the viability of the research.

5.2.1 Experimental

- Model fabrication - The current process should be modified to improve the consistency and repeatability of the ice models. This is especially needed when constructing store shaped models with fins, strakes, or other detailed components.
- Release mechanism - For this research effort, it was acceptable to allow a weapon to free fall from the release mechanism. While the sphere releases were highly repeatable, the Mk-82 shaped model releases tended to vary in location and orientation from one run to the next. In addition to improving the release

repeatability between runs, an ejection force could be implemented to more closely adhere to the light Mach scaling laws.

- Optical tracking technique - While Schlieren and high-speed imagery provide qualitative diagnoses of separation events, incorporating an optical tracking system would allow a greater degree of quantitative precision for assessing various dynamic parameters.
- Decreased stagnation pressures - Tunnel modifications should be made to further reduce the stagnation pressure below the current capability. This would allow validation of the computational sphere release that resulted in a successful separation and provide dynamic pressure ratios with which to attain proper heavy Mach scaling.
- Spoiler configurations - Various spoiler designs could be tested both for acoustic improvement and store separation enhancement.
- Release location - Using the current cavity design, the release location of the store can be varied both longitudinally and vertically to assess the impact of cavity release location on store dynamics.

5.2.2 Computational

- Dedicated CFD effort - A dedicated, thesis level investigation could further explore the multifaceted intricacies of computationally simulating store releases from a cavity.
- Turbulence modeling - Because cavity flow can be dominated by turbulence and massive separation, a more rigorous investigation into the turbulence models and their various settings is warranted.

- Grid generation - This research relied on a previously configured background grid which was scaled down to match the dimensions of the experimental cavity. A dedicated grid, matching the dimensions of the current cavity should be constructed, along with an analysis of various sphere overset gridding approaches.
- Time step study - As with any rigorous computational effort, an investigation should be made to determine the optimum time step for the given flow conditions.
- Spoiler incorporation - An overset domain surrounding the spoiler would allow validation of the experimental spoiler configuration.

Appendix A. Post-processing Code .m Files

The following section consists of the MATLAB®.m files used for data post-processing.

A brief description of each program is included at the beginning of each listing.

Listing A.1. Generate time signal from the OVERFLOW BC 201 boundary condition. Location corresponds with experimental transducer location (P6).

```
1 %Date: 15 May 12
%Author: T.J. Flora
%Description: Opens the cavity top BC_201 file and reads the ...
    information
%at pressure orifices 6

6 %% Clear the Data
clc,clear all,close all

%% Read the File
fid = fopen('CT1B_L_Back_BC.out');

11 %% Set indexing values
Nruns=20000; %Total number of iterations for the run
Stp_idx=1; %Index for each computational step

16 %% Run until end of file
while ~feof(fid)
    tline = fgetl(fid); %Read in the first line

    if strfind(tline, ' 2 ')==5 %If "2" is in space 5, start new ...
        step
21    Iter_inf=sscanf(tline,'%f %f %f %f %f %f %f %f %f');
        %Read...
        %entire step info line
        %Read iteration data
        Top.Block = Iter_inf(1);
        Top.Step(Stp_idx) = Iter_inf(2);
        Top.jmax = Iter_inf(3);
26        Top.kmax = Iter_inf(4);
        Top.lmax = Iter_inf(5);
        Top.Qvars = Iter_inf(6);
        Top.Svars = Iter_inf(7);
        Top.Nd_Sim(Stp_idx) = Iter_inf(8);
        Top.Nd_Tstep(Stp_idx) = Iter_inf(9);
31        end

        % Find line corresponding to orifice "P6"
        if strfind(tline,'2.694')==52
36            Stp_idx=Stp_idx+1;
            P6XYZ=sscanf(tline,'%f %f %f'); %Read xyz comp
```

```

        tline = fgetl(fid); %Next line
        P6Q_1=sscanf(tline,'%f %f %f'); %Read q data line 1
41
        tline = fgetl(fid); %Next line
        P6Q_2=sscanf(tline,'%f %f %f'); %Read q data line 2

        tline = fgetl(fid); %Next line
46
        P6Q_3=sscanf(tline,'%f %f'); % Read q data line 3

        Top.P6.xyz=P6XYZ; %Read location

        % q variables
51
        Top.P6.Dens(Stp_idx-1)=P6Q_1(1);
        Top.P6.Umom(Stp_idx-1)=P6Q_1(2);
        Top.P6.Vmom(Stp_idx-1)=P6Q_1(3);
        Top.P6.Wmom(Stp_idx-1)=P6Q_2(1);
        Top.P6.Stag_e(Stp_idx-1)=P6Q_2(2);
56
        Top.P6.Gamma(Stp_idx-1)=P6Q_2(3);
        Top.P6.Turb1(Stp_idx-1)=P6Q_3(1);
        Top.P6.Turb2(Stp_idx-1)=P6Q_3(2);

        end
61

        %% Stop loop after specified number of iterations
        if Stp_idx==Nruns
            break
66        end
        end

        %Flow parameters
        Gam = 1.4; %Constant gamma
71        V_inf = 2029.1; %fps
        L_char = .0313; %ft/grid unit
        p_inf = 15.68; %psf

        %Calculate non-dim press
76        e_o = Top.P6.Stag_e./Top.P6.Dens; %calc stag energy
        Nd_press = (Gam-1)*Top.P6.Dens.*e_o; %calc Non-Dim pressure
        Press = Nd_press*Gam*p_inf/144; %psia

        %Calculate dim time
81        Time = Top.Nd_Sim*L_char/V_inf;

        fclose(fid);

        %Calculate the fourier transform
86        %L=length(Press); %find length of Press vec
        %NFFT = 2^nextpow2(L);
        %Y=fft(Press,NFFT)/L; %compute fft of Press
        %SR = 200000; %sample rate = 200kHz (5e-6)
        %f=SR/2*linspace(0,1,NFFT/2+1); %pressure in frequency domain

```

```

91
%% Plot the stuff
% Create figure
figure1 = figure('Name','CFD Dynamic Pressure (P6)Time Signal',...
    'Color',[1 1 1]);

96 % Create axes
axes1 = axes('Parent',figure1,'YScale','linear','YMinorTick','on',...
    ;

    ylim(axes1,[0.00 0.3]);
101 %xlim(axes1,[0.05 0.054]);

    box(axes1,'on');
    hold(axes1,'all');

106
% Create title
title('OVERFLOW Dynamic Pressure');

% Create xlabel
111 xlabel(axes1,'Time (sec)');

% Create ylabel
ylabel(axes1,'Pressure (Psia)');

116 % Create semilogy
semilogy(Time,Press,'Parent',axes1,'Color',[0 0 1],...
    'DisplayName','P6');

% Create legend
121 %legend(axes1,'show');
% hold all
% subplot(2,1,2);
% plot(Time,Press);

126 %subplot(212);
%xlim(axes1,[0.01 0.014]);
%semilogy(Time,Press,'Parent',axes1,'Color',[0 0 1],...
    % 'DisplayName','P6');

131 %figure
%plot(TotalMass,'.-')
%grid on

```

Listing A.2. Generate frequency signal from the OVERFLOW BC 201 boundary condition. Location corresponds with experimental transducer location P6.

%Date: 15 May 12

```

2 %Author: T.J. Flora
%Description: Opens the cavity top BC_201 file and reads the ...
    information
%at pressure orifices 6

%% Clear the Data
7 clc,clear all,close all

%% Read the File
fid = fopen('CT1B_L_Back_BC.out');

12 %% Set indexing values
Nruns=20000; %Total number of iterations for the run
Stp_idx=1; %Index for each computational step

%% Run until end of file
17 while ~feof(fid)
    tline = fgetl(fid); %Read in the first line

    if strfind(tline, ' 2 ')==5 %If "2" is in space 5, start new ...
        step
        Iter_inf=sscanf(tline,'%f %f %f %f %f %f %f %f'); %Read...
            entire step info line
22    %Read iteration data
        Top.Block = Iter_inf(1);
        Top.Step(Stp_idx) = Iter_inf(2);
        Top.jmax = Iter_inf(3);
        Top.kmax = Iter_inf(4);
27    Top.lmax = Iter_inf(5);
        Top.Qvars = Iter_inf(6);
        Top.Svars = Iter_inf(7);
        Top.Nd_Sim(Stp_idx) = Iter_inf(8);
        Top.Nd_Tstep(Stp_idx) = Iter_inf(9);
32    end

    % Find line corresponding to orifice "P6"
    if strfind(tline,'2.694')==52
        Stp_idx=Stp_idx+1;
37    P6XYZ=sscanf(tline,'%f %f %f'); %Read xyz comp

        tline = fgetl(fid); %Next line
        P6Q_1=sscanf(tline,'%f %f %f'); %Read q data line 1

42    tline = fgetl(fid); %Next line
        P6Q_2=sscanf(tline,'%f %f %f'); %Read q data line 2

        tline = fgetl(fid); %Next line
        P6Q_3=sscanf(tline,'%f %f'); % Read q data line 3
47    Top.P6.xyz=P6XYZ; %Read location

        % q variables

```

```

Top.P6.Dens(Stp_idx-1)=P6Q_1(1);
52 Top.P6.Umom(Stp_idx-1)=P6Q_1(2);
Top.P6.Vmom(Stp_idx-1)=P6Q_1(3);
Top.P6.Wmom(Stp_idx-1)=P6Q_2(1);
Top.P6.Stag_e(Stp_idx-1)=P6Q_2(2);
Top.P6.Gamma(Stp_idx-1)=P6Q_2(3);
57 Top.P6.Turb1(Stp_idx-1)=P6Q_3(1);
Top.P6.Turb2(Stp_idx-1)=P6Q_3(2);

    end

62 %% Stop loop after specified number of iterations
if Stp_idx==Nruns
    break
end
67 end

%Flow parameters
Gam = 1.4; %Constant gamma
V_inf = 2029.1; %fps
72 L_char = .0313; %ft/grid unit
p_inf = 15.68; %psf

%Calculate non-dim press
e_o = Top.P6.Stag_e./Top.P6.Dens; %calc stag energy
77 Nd_press = (Gam-1)*Top.P6.Dens.*e_o; %calc Non-Dim pressure
Press = Nd_press*Gam*p_inf/144; %psia

%Calculate dim time
Time = Top.Nd_Sim*L_char/V_inf;
82 fclose(fid);

%Calculate the fourier transform
L=length(Press); %find length of Press vec
87 NFFT = 2^nextpow2(L);
Y=fft(Press,NFFT)/L; %compute fft of Press
SR = 200000; %sample rate = 200kHz (5e-6)
f=SR/2*linspace(0,1,NFFT/2+1); %pressure in frequency domain

92 %% Plot the stuff
% Create figure
figure1 = figure('Name','CFD Dynamic Pressure (P6)Time Signal',...
    'Color',[1 1 1]);

% Create axes
97 axes1 = axes('Parent',figure1,'YScale','log','YMinorTick','on');

%ylim(axes1,[0.00 0.3]);
%xlim(axes1,[0.05 0.054]);

```

```

102
    box(axes1,'on');
    hold(axes1,'all');

107 % Create title
    title('OVERFLOW Dynamic Pressure (Frequency Spectrum)');

    % Create xlabel
    xlabel(axes1,'Frequency (Hz)');

112
    % Create ylabel
    ylabel(axes1,'|fft P^2|');

    % Create semilogy
117 semilogy(f,2*abs(Y(1:NFFT/2+1)),'Parent',axes1,'Color',[0 0 1],...
    'DisplayName','P6');

    % Create legend
    %legend(axes1,'show');

122 % hold all
    % subplot(2,1,2);
    % plot(Time,Press);

    %subplot(212);
127 %xlim(axes1,[0.01 0.014]);
    %semilogy(Time,Press,'Parent',axes1,'Color',[0 0 1],...
    %    'DisplayName','P6');

    %figure
132 %plot(TotalMass,'.-')
    %grid on

```

Listing A.3. Generate time signal from the OVERFLOW BC201 boundary condition. Location corresponds with experimental transducer locations P1.

```

%Date: 15 May 12
2 %Author: T.J. Flora
%Description: Opens the cavity top BC_201 file and reads the ...
    %information
%at pressure orifices 1-5

%% Clear the Data
7 clc,clear all,close all

%% Read the File
fid = fopen('BC_CT1A_Top.out');

12 %% Set indexing values
Nruns=3000;    %Total number of iterations for the run

```

```

    Stp_idx=1; %Index for each computational step

    %% Run until end of file
17 while ~feof(fid)
    tline = fgetl(fid); %Read in the first line

    if strfind(tline, ' 2 ')==5 %If "2" is in space 5, start new ...
        step
        Iter_inf=sscanf(tline,'%f %f %f %f %f %f %f %f %f'); %Read...
            entire step info line
22 %Read iteration data
    Top.Block = Iter_inf(1);
    Top.Step(Stp_idx) = Iter_inf(2);
    Top.jmax = Iter_inf(3);
    Top.kmax = Iter_inf(4);
27    Top.lmax = Iter_inf(5);
    Top.Qvars = Iter_inf(6);
    Top.Svars = Iter_inf(7);
    Top.Nd_Sim(Stp_idx) = Iter_inf(8);
    Top.Nd_Tstep(Stp_idx) = Iter_inf(9);
32    Stp_idx=Stp_idx+1;
    end

    % Find line corresponding to orifice 1
    if strfind(tline,'15.252')==4
37        P1XYZ=sscanf(tline,'%f %f %f'); %Read xyz comp

        tline = fgetl(fid); %Next line
        P1Q_1=sscanf(tline,'%f %f %f'); %Read q data line 1

42        tline = fgetl(fid); %Next line
        P1Q_2=sscanf(tline,'%f %f %f'); %Read q data line 2

        tline = fgetl(fid); %Next line
        P1Q_3=sscanf(tline,'%f %f'); % Read q data line 3
47        Top.P1.xyz=P1XYZ; %Read location

        % q variables
        Top.P1.Dens(Stp_idx-1)=P1Q_1(1);
52        Top.P1.Umom(Stp_idx-1)=P1Q_1(2);
        Top.P1.Vmom(Stp_idx-1)=P1Q_1(3);
        Top.P1.Wmom(Stp_idx-1)=P1Q_2(1);
        Top.P1.Stag_e(Stp_idx-1)=P1Q_2(2);
        Top.P1.Gamma(Stp_idx-1)=P1Q_2(3);
57        Top.P1.Turb1(Stp_idx-1)=P1Q_3(1);
        Top.P1.Turb2(Stp_idx-1)=P1Q_3(2);
        end
        % Find line corresponding to orifice 2
        if strfind(tline,'20.607')==4
62            P2XYZ=sscanf(tline,'%f %f %f'); %Read xyz comp

```

```

tline = fgetl(fid); %Next line
P2Q_1=sscanf(tline,'%f %f %f'); %Read P*Q data line 1
67
tline = fgetl(fid); %Next line
P2Q_2=sscanf(tline,'%f %f %f'); %Read P*Q data line 2

tline = fgetl(fid); %Next line
72
P2Q_3=sscanf(tline,'%f %f'); % Read P*Q data line 3

Top.P2.xyz=P2XYZ; %Read location

% q variables
77
Top.P2.Dens(Stp_idx-1)=P2Q_1(1);
Top.P2.Umom(Stp_idx-1)=P2Q_1(2);
Top.P2.Vmom(Stp_idx-1)=P2Q_1(3);
Top.P2.Wmom(Stp_idx-1)=P2Q_2(1);
Top.P2.Stag_e(Stp_idx-1)=P2Q_2(2);
82
Top.P2.Gamma(Stp_idx-1)=P2Q_2(3);
Top.P2.Turb1(Stp_idx-1)=P2Q_3(1);
Top.P2.Turb2(Stp_idx-1)=P2Q_3(2);
end
% Find line corresponding to orifice 3
87
if strfind(tline,'24.153')==4

P3XYZ=sscanf(tline,'%f %f %f'); %Read xyz comp

tline = fgetl(fid); %Next line
92
P3Q_1=sscanf(tline,'%f %f %f'); %Read P*Q data line 1

tline = fgetl(fid); %Next line
P3Q_2=sscanf(tline,'%f %f %f'); %Read P*Q data line 2

tline = fgetl(fid); %Next line
97
P3Q_3=sscanf(tline,'%f %f'); % Read P*Q data line 3

Top.P3.xyz=P3XYZ; %Read location

% q variables
102
Top.P3.Dens(Stp_idx-1)=P3Q_1(1);
Top.P3.Umom(Stp_idx-1)=P3Q_1(2);
Top.P3.Vmom(Stp_idx-1)=P3Q_1(3);
Top.P3.Wmom(Stp_idx-1)=P3Q_2(1);
Top.P3.Stag_e(Stp_idx-1)=P3Q_2(2);
107
Top.P3.Gamma(Stp_idx-1)=P3Q_2(3);
Top.P3.Turb1(Stp_idx-1)=P3Q_3(1);
Top.P3.Turb2(Stp_idx-1)=P3Q_3(2);
end
112
% Find line corresponding to orifice 4
if strfind(tline,'27.791')==4

P4XYZ=sscanf(tline,'%f %f %f'); %Read xyz comp

```

```

117      tline = fgetl(fid); %Next line
P4Q_1=sscanf(tline,'%f %f %f'); %Read P*Q data line 1

121      tline = fgetl(fid); %Next line
P4Q_2=sscanf(tline,'%f %f %f'); %Read P*Q data line 2
122      tline = fgetl(fid); %Next line
P4Q_3=sscanf(tline,'%f %f'); % Read P*Q data line 3

127      Top.P4.xyz=P4XYZ; %Read location

132      % Find line corresponding to orifice 5
      % q variables
      Top.P4.Dens(Stp_idx-1)=P4Q_1(1);
      Top.P4.Umom(Stp_idx-1)=P4Q_1(2);
      Top.P4.Vmom(Stp_idx-1)=P4Q_1(3);
      Top.P4.Wmom(Stp_idx-1)=P4Q_2(1);
      Top.P4.Stag_e(Stp_idx-1)=P4Q_2(2);
      Top.P4.Gamma(Stp_idx-1)=P4Q_2(3);
      Top.P4.Turb1(Stp_idx-1)=P4Q_3(1);
      Top.P4.Turb2(Stp_idx-1)=P4Q_3(2);
137      end

141      if strfind(tline,'32.714')==4

142      P5XYZ=sscanf(tline,'%f %f %f'); %Read xyz comp

146      tline = fgetl(fid); %Next line
P5Q_1=sscanf(tline,'%f %f %f'); %Read P*Q data line 1

147      tline = fgetl(fid); %Next line
P5Q_2=sscanf(tline,'%f %f %f'); %Read P*Q data line 2

151      tline = fgetl(fid); %Next line
P5Q_3=sscanf(tline,'%f %f'); % Read P*Q data line 3
152      Top.P5.xyz=P5XYZ; %Read location

157      % q variables
      Top.P5.Dens(Stp_idx-1)=P5Q_1(1);
      Top.P5.Umom(Stp_idx-1)=P5Q_1(2);
      Top.P5.Vmom(Stp_idx-1)=P5Q_1(3);
      Top.P5.Wmom(Stp_idx-1)=P5Q_2(1);
      Top.P5.Stag_e(Stp_idx-1)=P5Q_2(2);
      Top.P5.Gamma(Stp_idx-1)=P5Q_2(3);
162      Top.P5.Turb1(Stp_idx-1)=P5Q_3(1);
      Top.P5.Turb2(Stp_idx-1)=P5Q_3(2);
      end

167      %% Stop loop after specified number of iterations
      if Stp_idx==Nrns

```

```

        break
    end
end

172 %Flow parameters
Gam = 1.4; %Constant gamma
V_inf = 2029.1; %fps
L_char = .0313; %ft/grid unit
p_inf = 15.68; %psf
177
%Calculate non-dim press
e_o = Top.P5.Stag_e./Top.P5.Dens; %calc stag energy
Nd_press = (Gam-1)*Top.P5.Dens.*e_o; %calc Non-Dim pressure
Press = Nd_press*Gam*p_inf;
182
%Calculate dim time
Time = Top.Nd_Sim*L_char/V_inf;

fclose(fid);
187
%% Plot the Data
close all
figure
plot(Time,Press)
192
%subplot(212)
%plot(w(:,2),'.-')
%grid on

197 %figure
%plot(TotalMass,'.-')
%grid on

```

Listing A.4. Plot spectral analyzer output for clean cavity configuration at 4 12 20 Psia stagnation pressures.

```

1 %Date: 15 May 12
%Author: T.J. Flora
%Description: Read frequency data for 12 psi case

%% Clear the Data
6 clc,clear all,close all

%% Read the Files
F1x = fopen('605C1x.x'); %4psi clean
F1y = fopen('605C1y.txt');
11 F2x = fopen('605C2x.x'); %12psi clean
F2y = fopen('605C2y.txt');
F3x = fopen('605C3x.x'); %20psi clean
F3y = fopen('605C3y.txt');

```

```

16 %% Run until end of file

for i=1:200
    tline1x = fgetl(F1x); %Read in the first line of x
    tline1y = fgetl(F1y); %Read in the first line of y
21    tline2x = fgetl(F2x);
    tline2y = fgetl(F2y);
    tline3x = fgetl(F3x);
    tline3y = fgetl(F3y);
    freq1(i)= sscanf(tline1x,'%f'); %Store column 1
26    amp1(i)= sscanf(tline1y,'%f'); %Store column 1
    freq2(i)= sscanf(tline2x,'%f');
    amp2(i)= sscanf(tline2y ,'%f');
    freq3(i)= sscanf(tline3x,'%f');
    amp3(i)= sscanf(tline3y ,'%f');
31    tline1x = fgetl(F1x); %Increment
    tline1y = fgetl(F1y);
    tline2x = fgetl(F2x);
    tline2y = fgetl(F2y);
    tline3x = fgetl(F3x);
36    tline3y = fgetl(F3y);
end

fclose(F1x);
fclose(F1y);
41 fclose(F2x);
fclose(F2y);
fclose(F3x);
fclose(F3y);

46 %% Plot the Data
close all
% Create figure
figure1 = figure('Name','Clean Frequency Response','Color',[1 1 ...
    1]);

51 % Create axes
axes1 = axes('Parent',figure1,'YScale','log','YMinorTick','on',...
    'YMinorGrid','on',...
    'YGrid','on');

56 xlim(axes1,[1000 6000]);
box(axes1,'on');
hold(axes1,'all');

% Create multiple lines using matrix input to semilogy
61 semilogy1 = semilogy(freq1,amp1,freq2,amp2,freq3,amp3,'Parent',...
    axes1);
set(semilogy1(1),'MarkerFaceColor','auto','Marker','+',...
    'DisplayName','4 Psia');
set(semilogy1(2),'Marker','.', 'DisplayName','12 Psia');

```

```

    set(semilogy1(3), 'Marker', 'x', 'DisplayName', '20 Psia');
66
% Create xlabel
xlabel('frequency (Hz)');

% Create ylabel
71 ylabel('Amplitude (mV) rms');

% Create title
title('Clean Frequency Response');

76 % Create legend
legend(axes1, 'show');
set(legend, ...
    'Position', [0.73 0.84 0.26 0.14]);

```

Listing A.5. Plot spectral analyzer output for clean SST and LST configuration at 4 Psia.

```

1 %Date: 15 May 12
%Author: T.J. Flora
%Description: Opens the cavity top BC_201 file and reads the ...
    information
%at pressure orifices 6

6 %% Clear the Data
clc, clear all, close all

%% Read the Files
F1x = fopen('605C2x.x');
11 F1y = fopen('605C2y.txt');
F2x = fopen('605C5x.x');
F2y = fopen('605C5y.txt');
F3x = fopen('605C8x.x');
F3y = fopen('605C8y.txt');

16 %% Run until end of file

    for i=1:200
        tline1x = fgetl(F1x); %Read in the first line of x
21        tline1y = fgetl(F1y); %Read in the first line of y
        tline2x = fgetl(F2x); %Read in the first line of x
        tline2y = fgetl(F2y); %Read in the first line of y
        tline3x = fgetl(F3x); %Read in the first line of x
        tline3y = fgetl(F3y); %Read in the first line of y
26        freq1(i)= sscanf(tline1x, '%f'); %Read entire step info line
        amp1(i)= sscanf(tline1y, '%f'); %Read entire step info line
        freq2(i)= sscanf(tline2x, '%f'); %Read entire step info line
        amp2(i)= sscanf(tline2y, '%f'); %Read entire step info line
        freq3(i)= sscanf(tline3x, '%f'); %Read entire step info line

```

```

31     amp3(i)= sscanf(tline3y ,'%f'); %Read entire step info line
      tline1x = fgetl(F1x); %Increment tline
      tline1y = fgetl(F1y); %Increment tline
      tline2x = fgetl(F2x); %Increment tline
      tline2y = fgetl(F2y); %Increment tline
36     tline3x = fgetl(F3x); %Increment tline
      tline3y = fgetl(F3y); %Increment tline
end

fclose(F1x);
41 fclose(F1y);
fclose(F2x);
fclose(F2y);
fclose(F3x);
fclose(F3y);
46
%% Plot the Data
close all
% Create figure
figure1 = figure('Name','12 psi Frequency Response','Color',[1 1 ...
1]);
51
% Create axes
axes1 = axes('Parent',figure1,'YScale','log','YMinorTick','on',...
'YMinorGrid','on',...
'YGrid','on');
56
xlim(axes1,[1000 6000]);
box(axes1,'on');
hold(axes1,'all');

61 % Create multiple lines using matrix input to semilogy
semilogy1 = semilogy(freq1,amp1,freq2,amp2,freq3,amp3,'Parent',...
axes1);
set(semilogy1(1),'MarkerFaceColor','auto','Marker','+',...
'DisplayName','Clean');
set(semilogy1(2),'LineStyle',':','DisplayName','Short Sawtooth');
66 set(semilogy1(3),'LineStyle','--','DisplayName','Long Sawtooth');

% Create xlabel
xlabel('frequency (Hz)');

71 % Create ylabel
ylabel('Amplitude (mV)');

% Create title
title('12 Psia Frequency Response');
76
% Create legend
legend(axes1,'show');
set(legend,...
'Position',[0.73 0.84 0.26 0.14]);

```

Listing A.6. Plot spectral analyzer output for clean SST and LST configuration at 12 Psia.

```
%Date: 15 May 12
%Author: T.J. Flora
%Description: Read frequency data for 12 psi case

5 %% Clear the Data
clc,clear all,close all

%% Read the Files
F1x = fopen('605C2x.x'); %12psi clean
10 F1y = fopen('605C2y.txt');
F2x = fopen('605C5x.x'); %12psi SST
F2y = fopen('605C5y.txt');
F3x = fopen('605C8x.x'); %12psi LSt
F3y = fopen('605C8y.txt');

15 %% Run until end of file

for i=1:200
    tline1x = fgetl(F1x); %Read in the first line of x
20    tline1y = fgetl(F1y); %Read in the first line of y
    tline2x = fgetl(F2x);
    tline2y = fgetl(F2y);
    tline3x = fgetl(F3x);
    tline3y = fgetl(F3y);
25    freq1(i)= sscanf(tline1x,'%f'); %Store column 1
    amp1(i)= sscanf(tline1y,'%f'); %Store column 1
    freq2(i)= sscanf(tline2x,'%f');
    amp2(i)= sscanf(tline2y,'%f');
    freq3(i)= sscanf(tline3x,'%f');
30    amp3(i)= sscanf(tline3y,'%f');
    tline1x = fgetl(F1x); %Increment
    tline1y = fgetl(F1y);
    tline2x = fgetl(F2x);
    tline2y = fgetl(F2y);
35    tline3x = fgetl(F3x);
    tline3y = fgetl(F3y);
end

fclose(F1x);
40 fclose(F1y);
fclose(F2x);
fclose(F2y);
fclose(F3x);
fclose(F3y);

45 %% Plot the Data
close all
% Create figure
figure1 = figure('Name','12 psi Frequency Response','Color',[1 1 ...
    1]);
```

```

50
% Create axes
axes1 = axes('Parent',figure1,'YScale','log','YMinorTick','on',...
    'YMinorGrid','on',...
    'YGrid','on');

55
xlim(axes1,[1000 6000]);
ylim(axes1,[.001 .1]);
box(axes1,'on');
hold(axes1,'all');

60
% Create multiple lines using matrix input to semilogy
semilogy1 = semilogy(freq1,amp1,freq2,amp2,freq3,amp3,'Parent',...
    axes1);
set(semilogy1(1),'MarkerFaceColor','auto','Marker','+',...
    'DisplayName','Clean');
65 set(semilogy1(2),'Marker','.', 'DisplayName','Short Sawtooth');
set(semilogy1(3),'Marker','x','DisplayName','Long Sawtooth');

% Create xlabel
xlabel('frequency (Hz)');
70
% Create ylabel
ylabel('Amplitude (Vrms)');

% Create title
75 title('12 Psia Frequency Response');

% Create legend
legend(axes1,'show');
set(legend, ...
80    'Position',[0.73 0.84 0.26 0.14]);

```

Listing A.7. Plot spectral analyzer output for clean SST and LST configuration at 20 Psia.

```

%Date: 15 May 12
%Author: T.J. Flora
%Description: Reads frequency reponse files for 20psi case

5 %% Clear the Data
clc,clear all,close all

%% Read the Files
F1x = fopen('605C3x.x'); %20psi clean
10 F1y = fopen('605C3y.txt');
F2x = fopen('605C4x.x'); %20psi SST
F2y = fopen('605C4y.txt');
F3x = fopen('605C9x.x'); %20psi LSt
F3y = fopen('605C9y.txt');

```

15

```
%% Run until end of file

for i=1:200
    tline1x = fgetl(F1x); %Read in the first line of x
20    tline1y = fgetl(F1y); %Read in the first line of y
    tline2x = fgetl(F2x);
    tline2y = fgetl(F2y);
    tline3x = fgetl(F3x);
    tline3y = fgetl(F3y);
25    freq1(i)= sscanf(tline1x,'%f'); %Store column 1
    amp1(i)= sscanf(tline1y,'%f'); %Store column 1
    freq2(i)= sscanf(tline2x,'%f');
    amp2(i)= sscanf(tline2y ,'%f');
    freq3(i)= sscanf(tline3x,'%f');
30    amp3(i)= sscanf(tline3y ,'%f');
    tline1x = fgetl(F1x); %Increment
    tline1y = fgetl(F1y);
    tline2x = fgetl(F2x);
    tline2y = fgetl(F2y);
35    tline3x = fgetl(F3x);
    tline3y = fgetl(F3y);
end

fclose(F1x);
40 fclose(F1y);
fclose(F2x);
fclose(F2y);
fclose(F3x);
fclose(F3y);
45 %% Plot the Data
close all
% Create figure
figure1 = figure('Name','20 psi Frequency Response','Color',[1 1 ...
    1]);
50 % Create axes
axes1 = axes('Parent',figure1,'YScale','log','YMinorTick','on',...
    'YMinorGrid','on',...
    'YGrid','on');
55 xlim(axes1,[1000 6000]);
box(axes1,'on');
hold(axes1,'all');

60 % Create multiple lines using matrix input to semilogy
semilogy1 = semilogy(freq1,amp1,freq2,amp2,freq3,amp3,'Parent',...
    axes1);
set(semilogy1(1),'MarkerFaceColor','auto','Marker','+',...
    'DisplayName','Clean');
set(semilogy1(2),'Marker','.', 'DisplayName','Short Sawtooth');
```

```
65 set(semilogy1(3), 'Marker', 'x', 'DisplayName', 'Long Sawtooth');

% Create xlabel
xlabel('frequency (Hz)');

70 % Create ylabel
ylabel('Amplitude (Vrms)');

% Create title
title('20 Psia Frequency Response');

75
% Create legend
legend(axes1, 'show');
set(legend, ...
    'Position', [0.73 0.84 0.26 0.14]);
```

Appendix B. $P_{T,sc}=4$ Psia Sphere Run Images

The following figures are the image sequences of the sphere freedrop tests at $P_{T,sc}=4$ Psia. The figures include testing in the clean configuration, with the SST, and the LST installed.

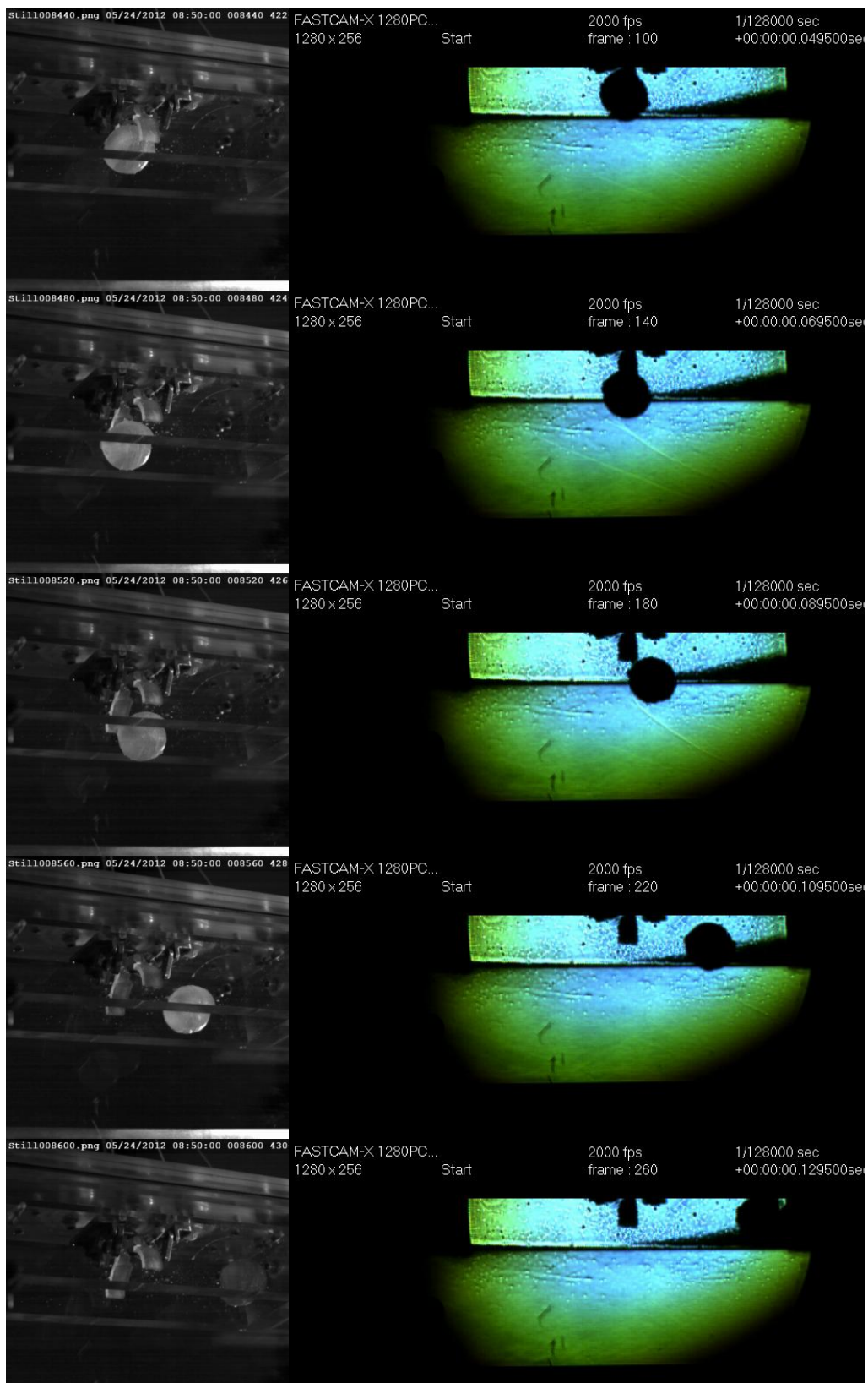


Figure 74. Image sequence of run 524S1. No flow control device used. Frame rate=2kHz, $\Delta t=20$ ms.

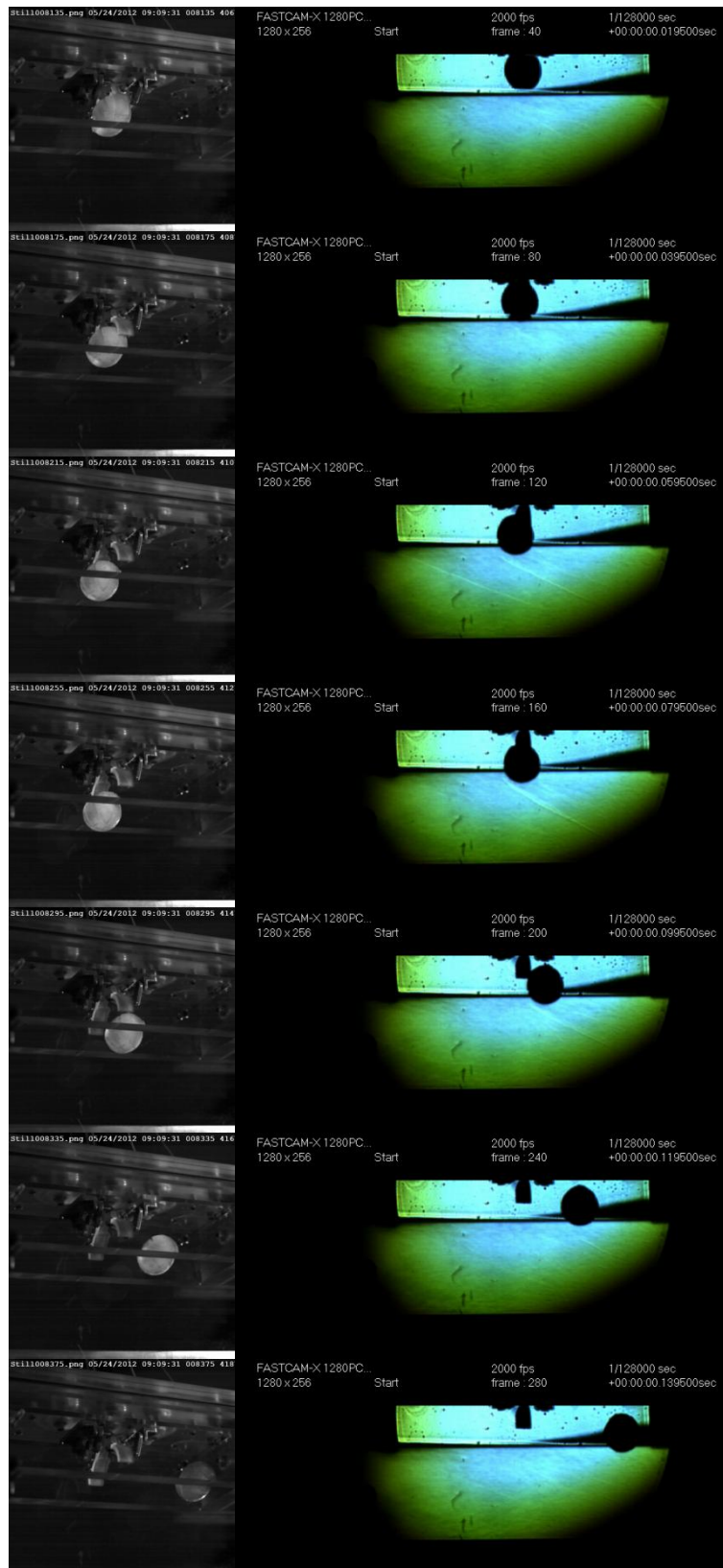


Figure 75. Image sequence of run 524S2. No flow control device used. Frame rate=2kHz, $\Delta t=20$ ms.

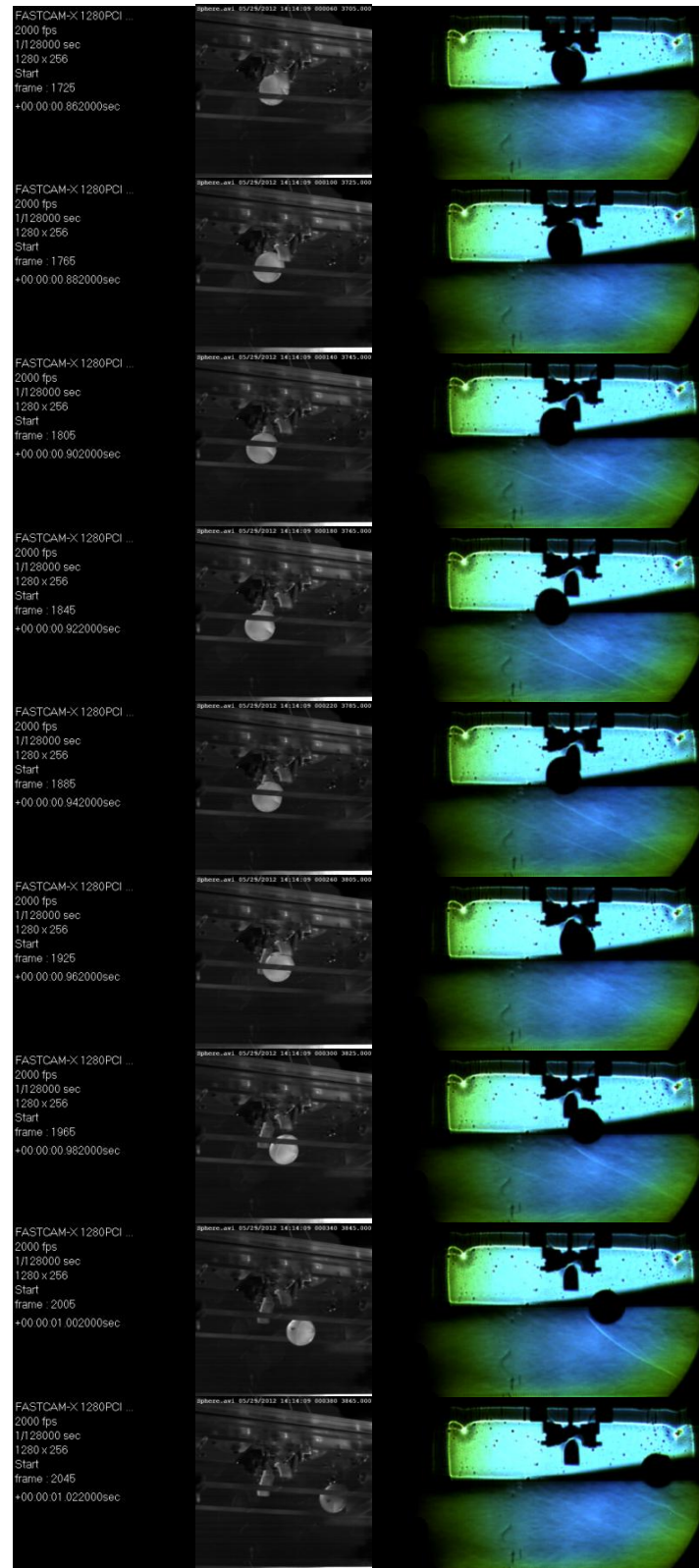


Figure 76. Image sequence of run 529S1. No flow control device used. Frame rate=2kHz, $\Delta t=20\text{ms}$.

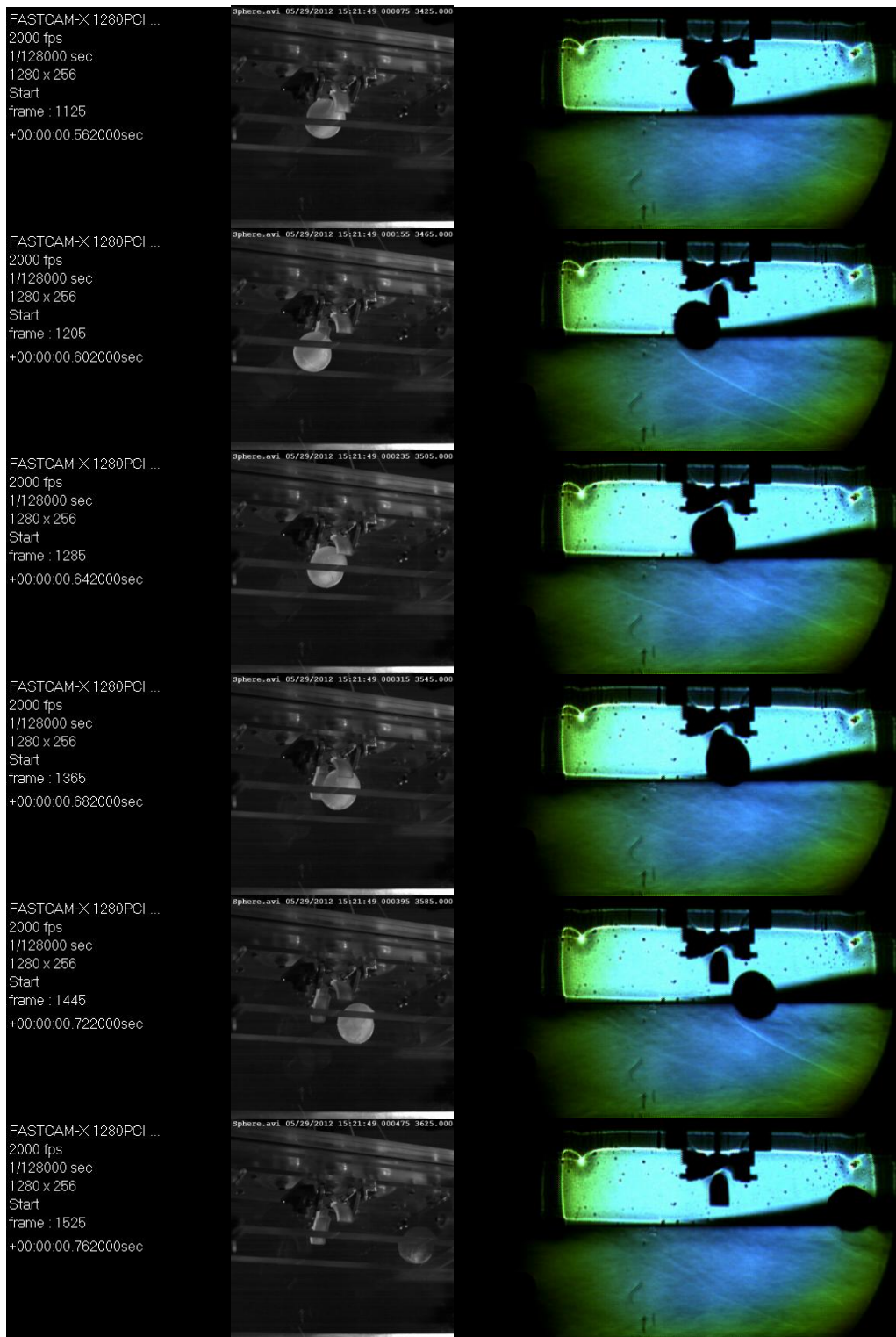


Figure 77. Image sequence of run 529S2. No flow control device used. Frame rate=2kHz, $\Delta t=40$ ms.

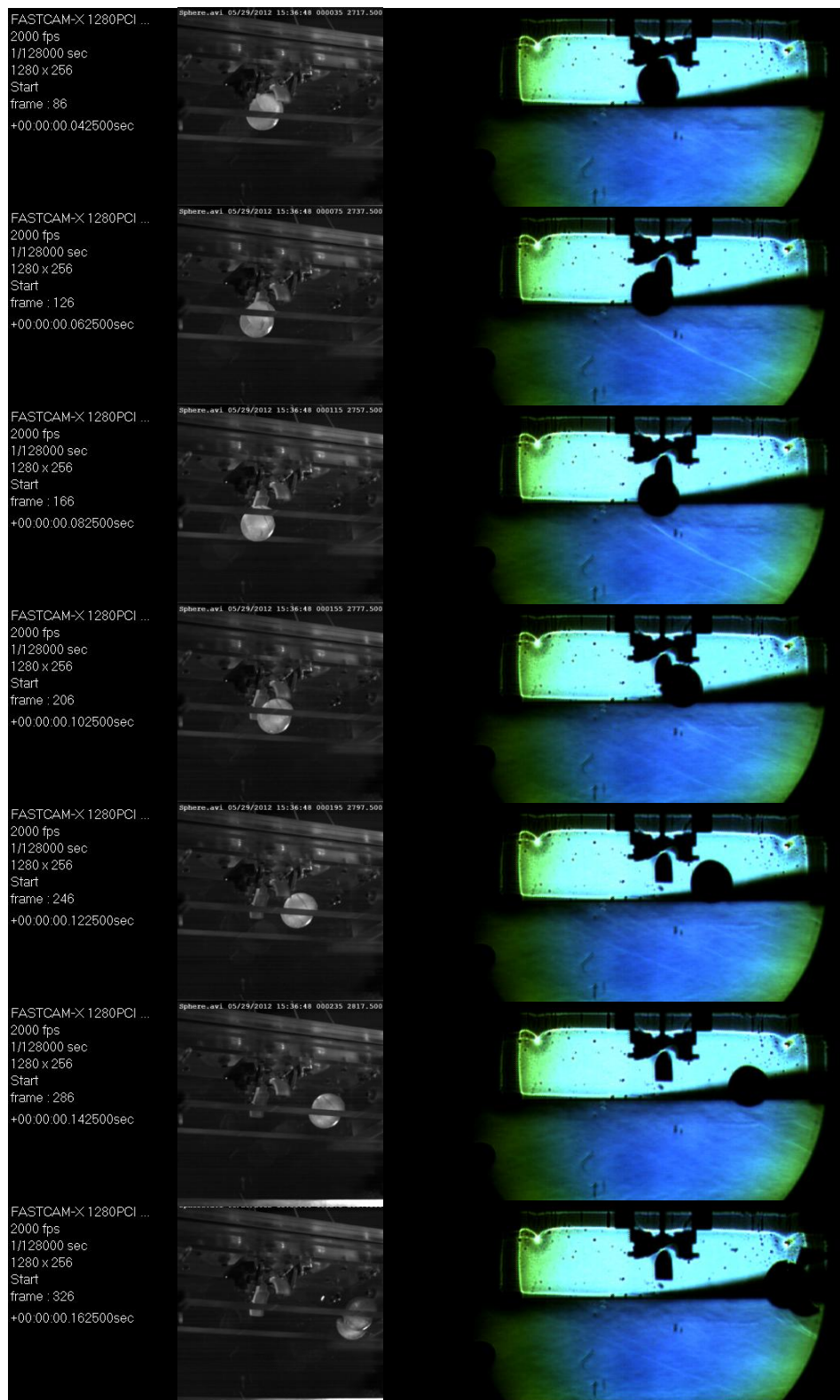


Figure 78. Image sequence of run 529S3. No flow control device used. Frame rate=2kHz, $\Delta t=20$ ms.

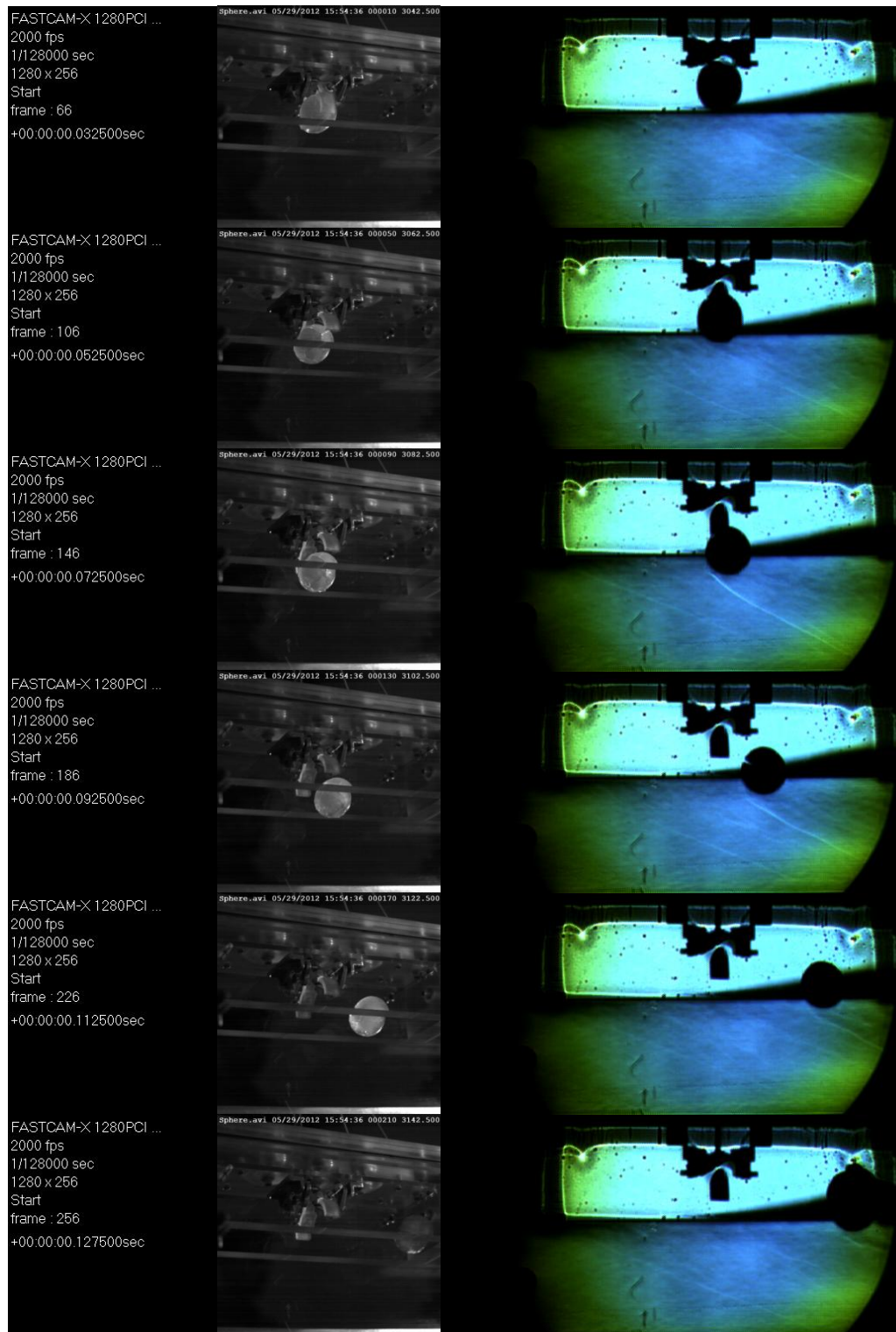


Figure 79. Image sequence of run 529S5. No flow control device used. Frame rate=2kHz, $\Delta t=20$ ms.

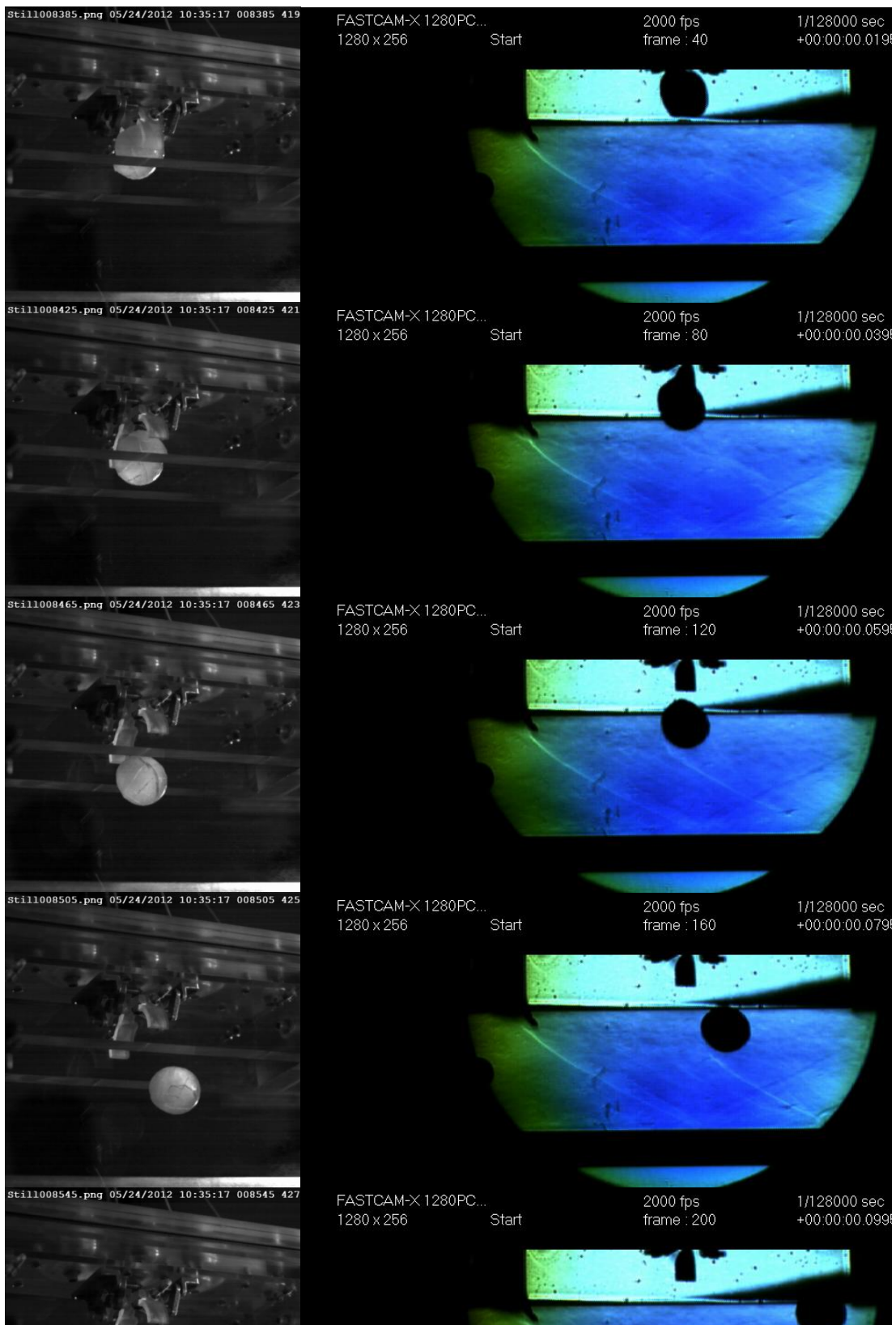


Figure 80. Image sequence of run 524S4. Short Sawtooth flow device used. Frame rate=2kHz, $\Delta t=20$ ms.

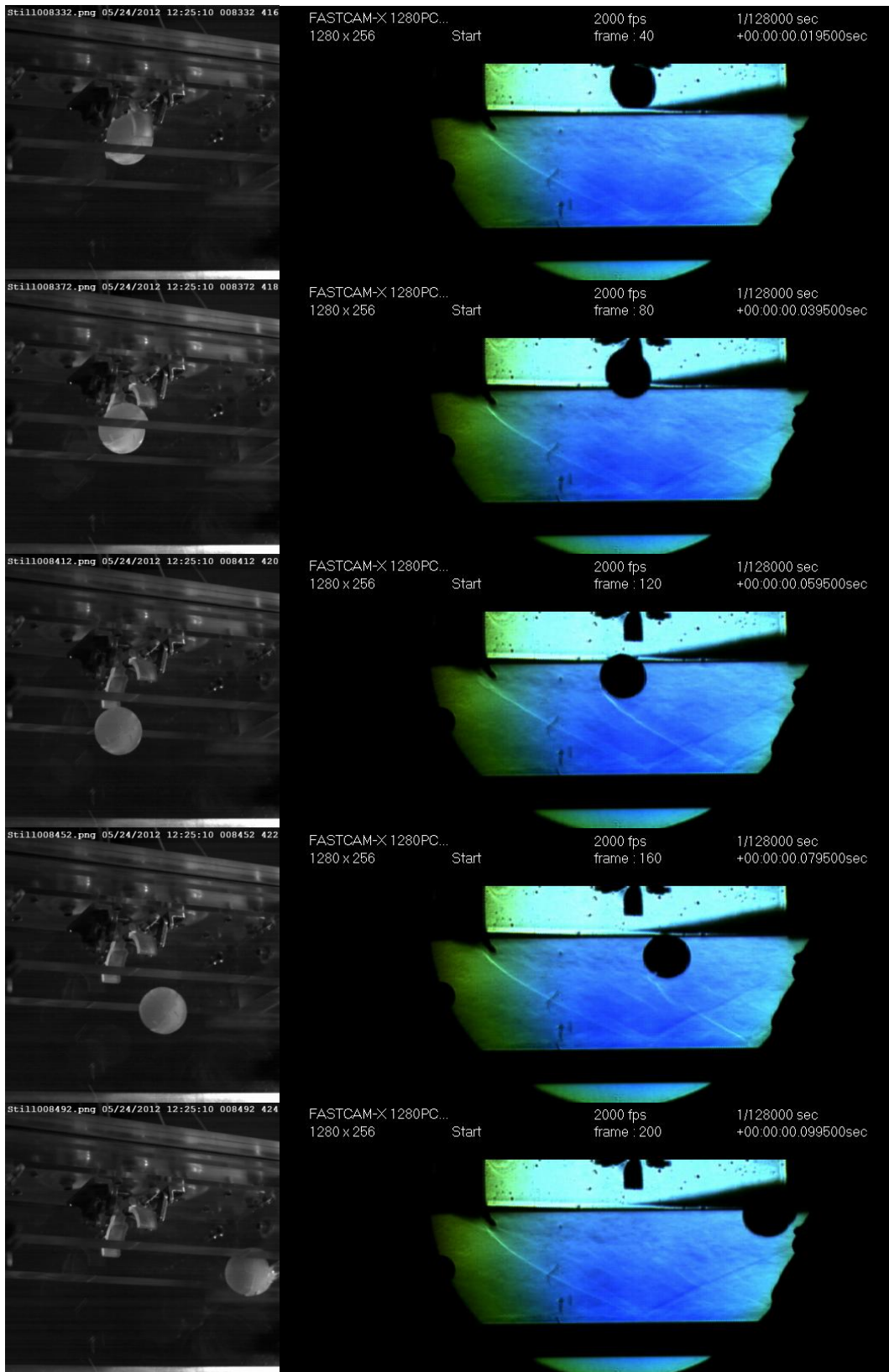


Figure 81. Image sequence of run 524S6. Short Sawtooth flow device used. Frame rate=2kHz, $\Delta t=20$ ms.

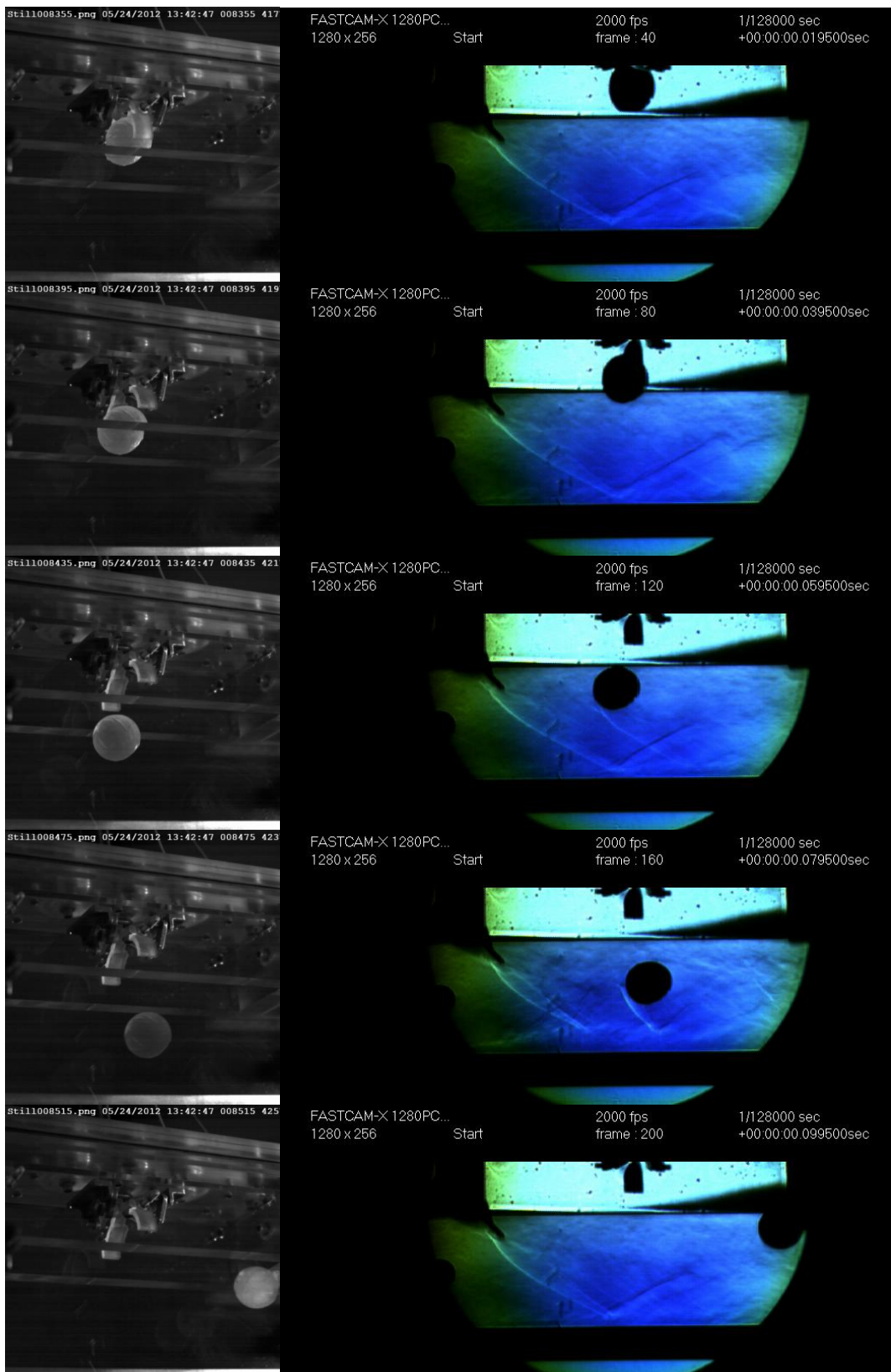


Figure 82. Image sequence of run 524S7. Long Sawtooth flow device used. Frame rate=2kHz, $\Delta t=20$ ms.

Appendix C. $P_{T,sc}=12$ Psia Sphere Run Images

The following figures are the image sequences of the sphere freedrop tests at $P_{T,sc}=12$ Psia. The figures include testing in the clean configuration, with the SST, and the LST installed.

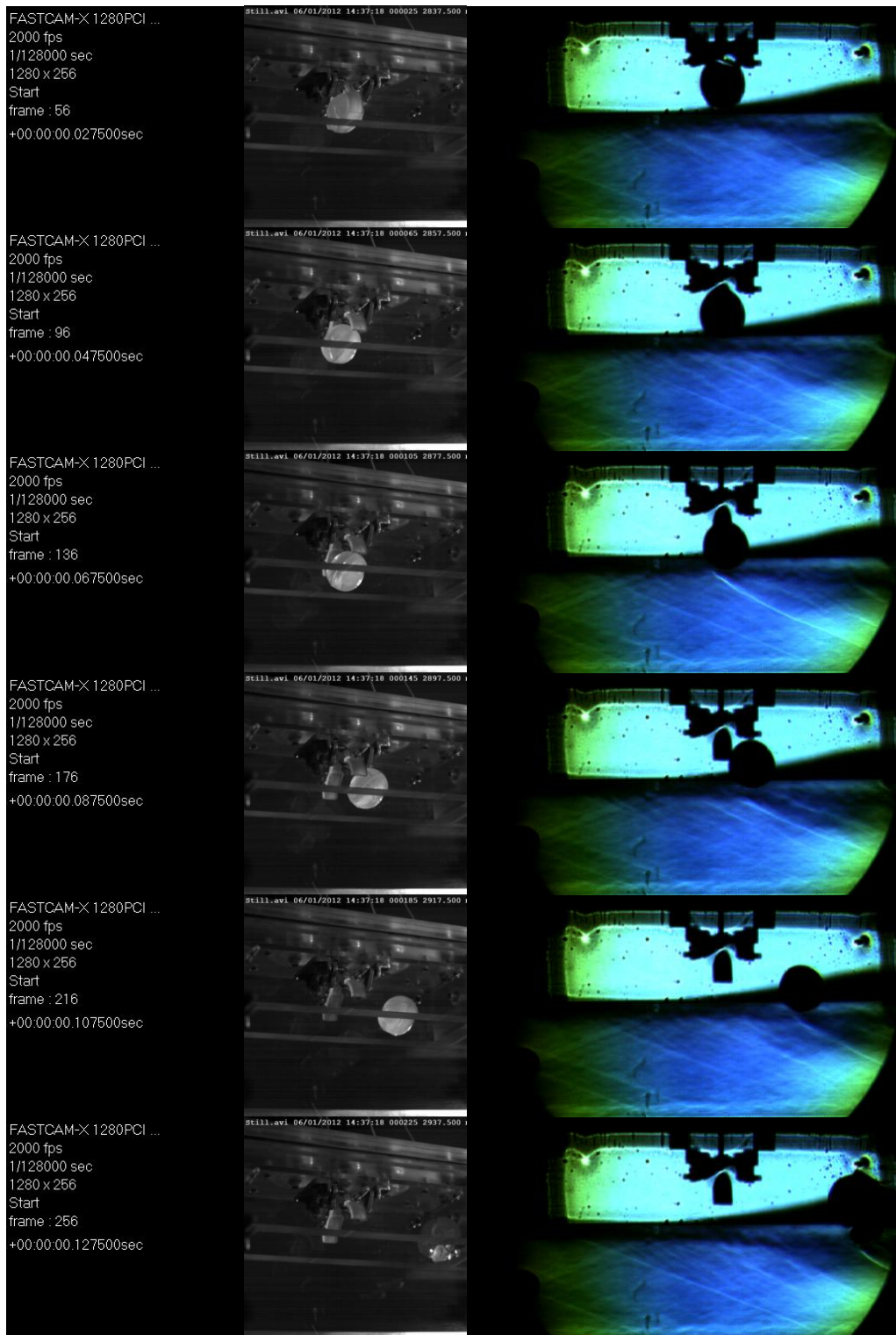


Figure 83. Image sequence of run 601S2. No flow control device used. Frame rate=2kHz, $\Delta t=20$ ms.

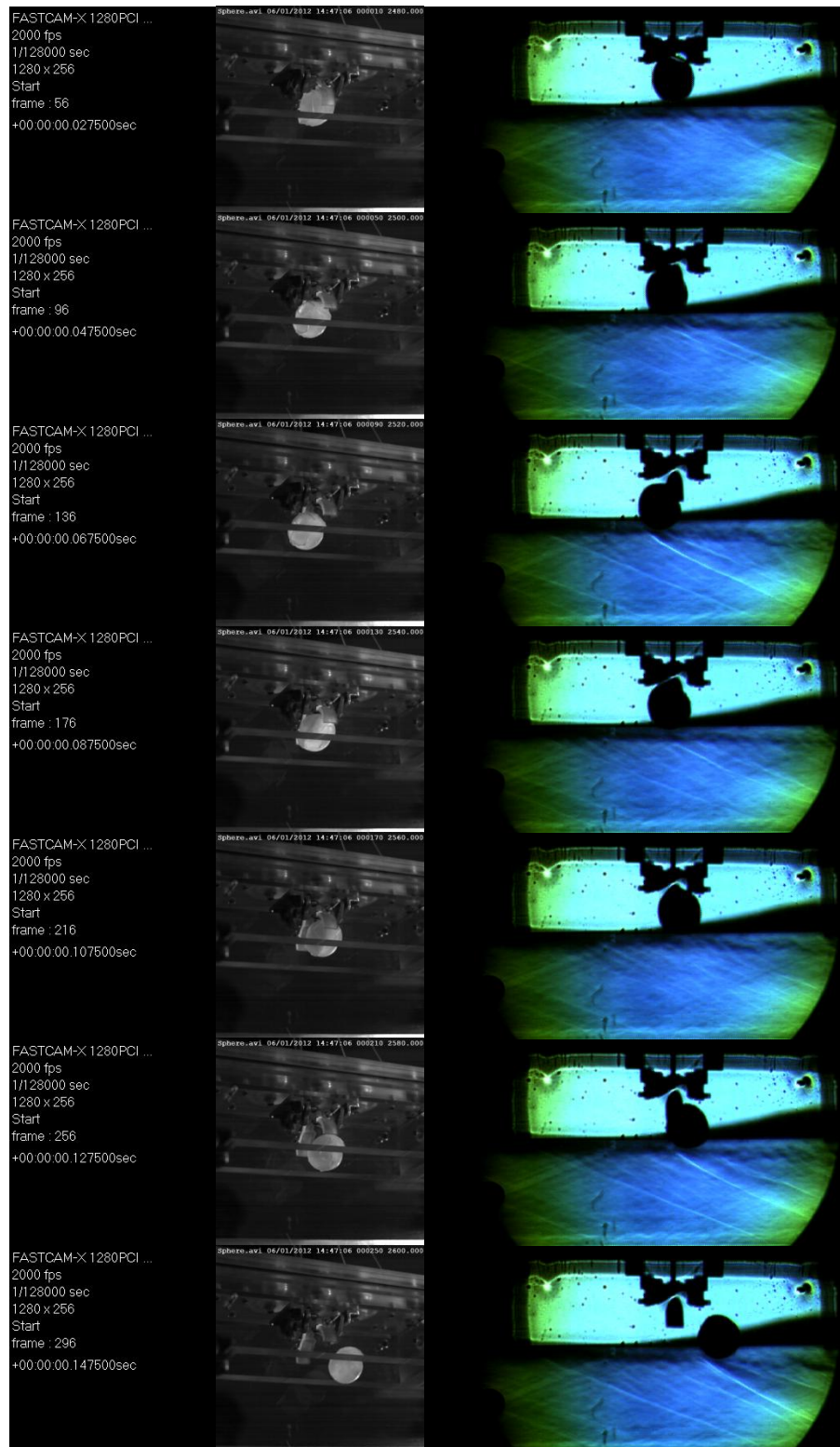


Figure 84. Image sequence of run 601S3. No flow control device used. Frame rate=2kHz, $\Delta t=20$ ms.

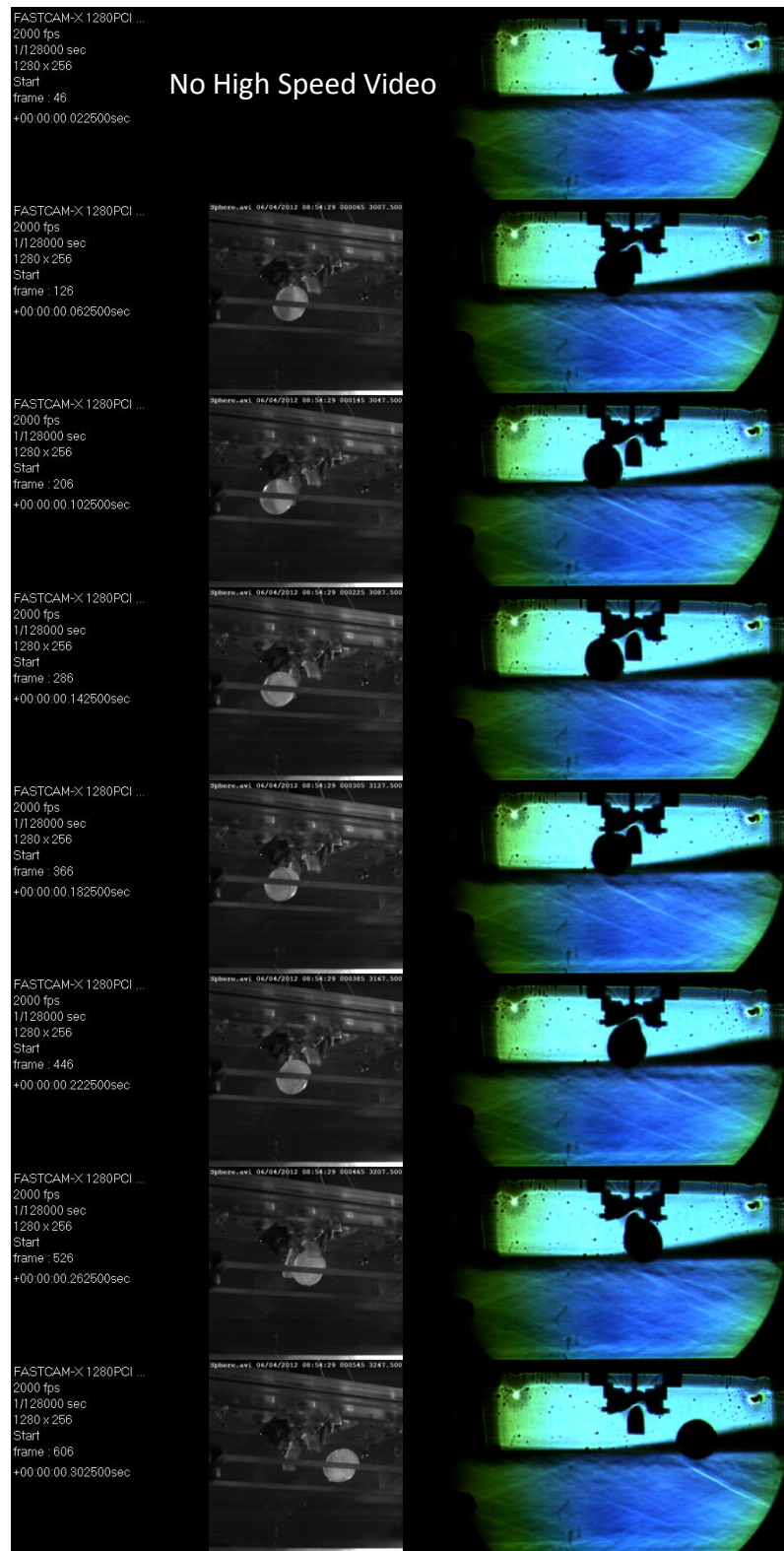


Figure 85. Image sequence of run 604S1. No flow control device used. Frame rate=2kHz, $\Delta t=40$ ms.

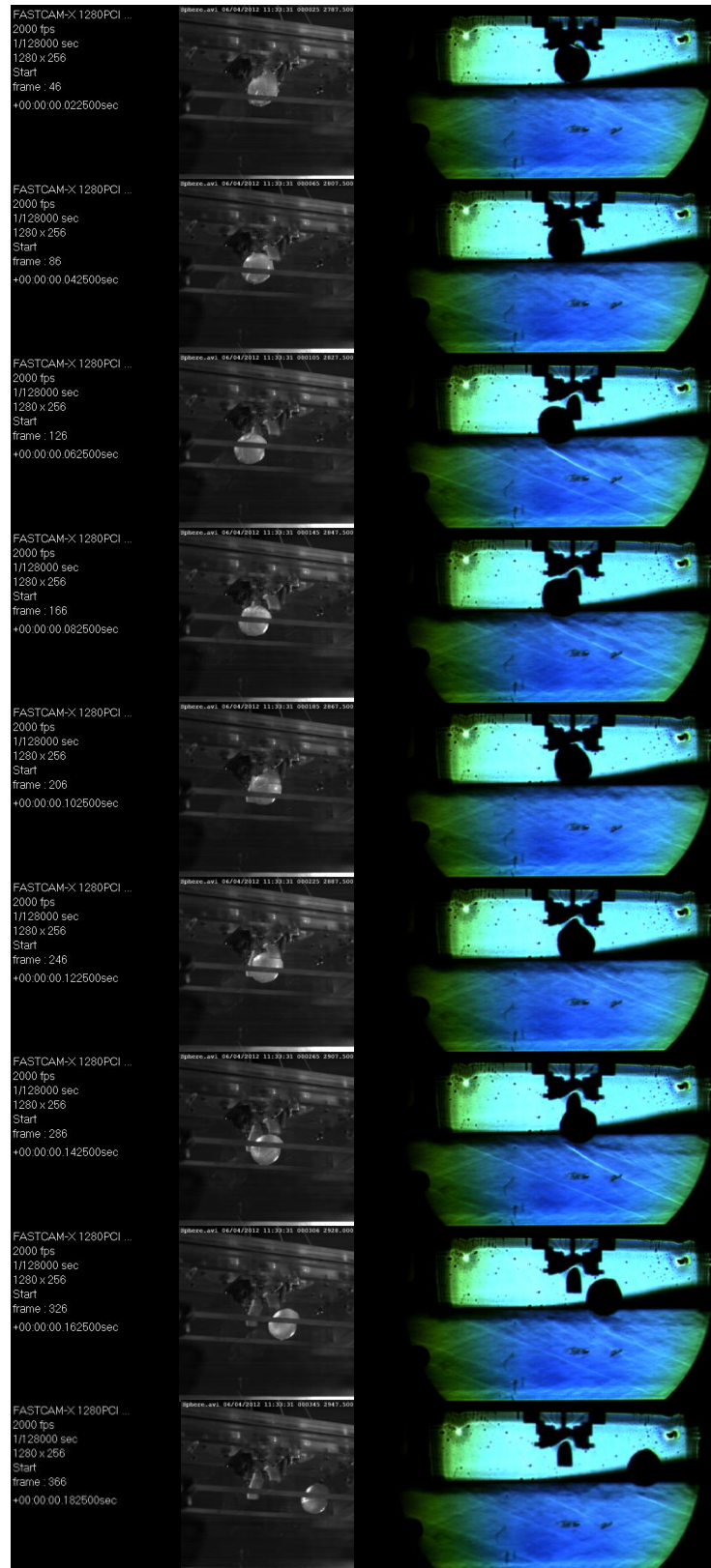


Figure 86. Image sequence of run 604S2. No flow control device used. Frame rate=2kHz, $\Delta t=20\text{ms}$.

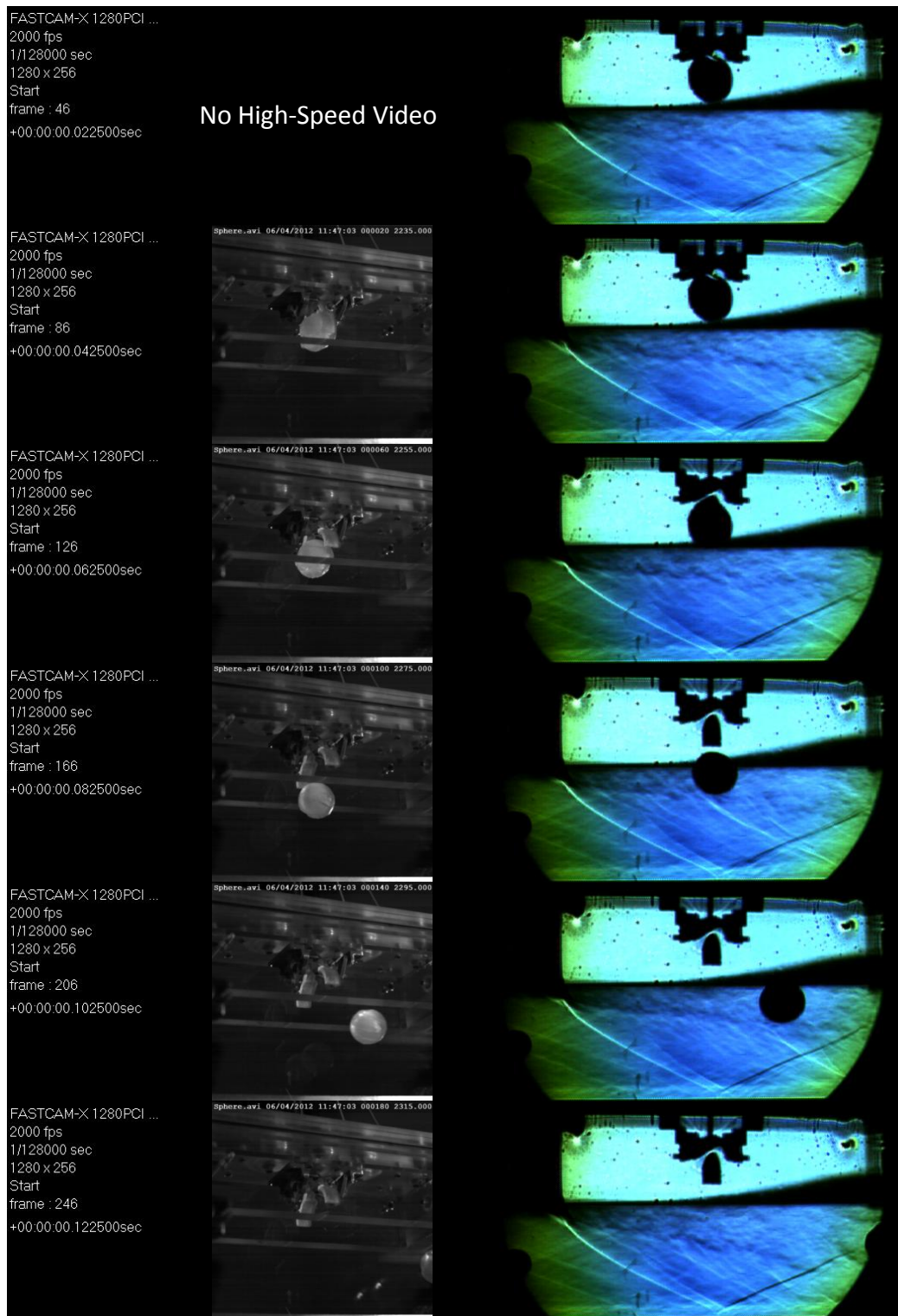


Figure 87. Image sequence of run 604S3. Short sawtooth flow control device used. Frame rate=2kHz, $\Delta t=20\text{ms}$.

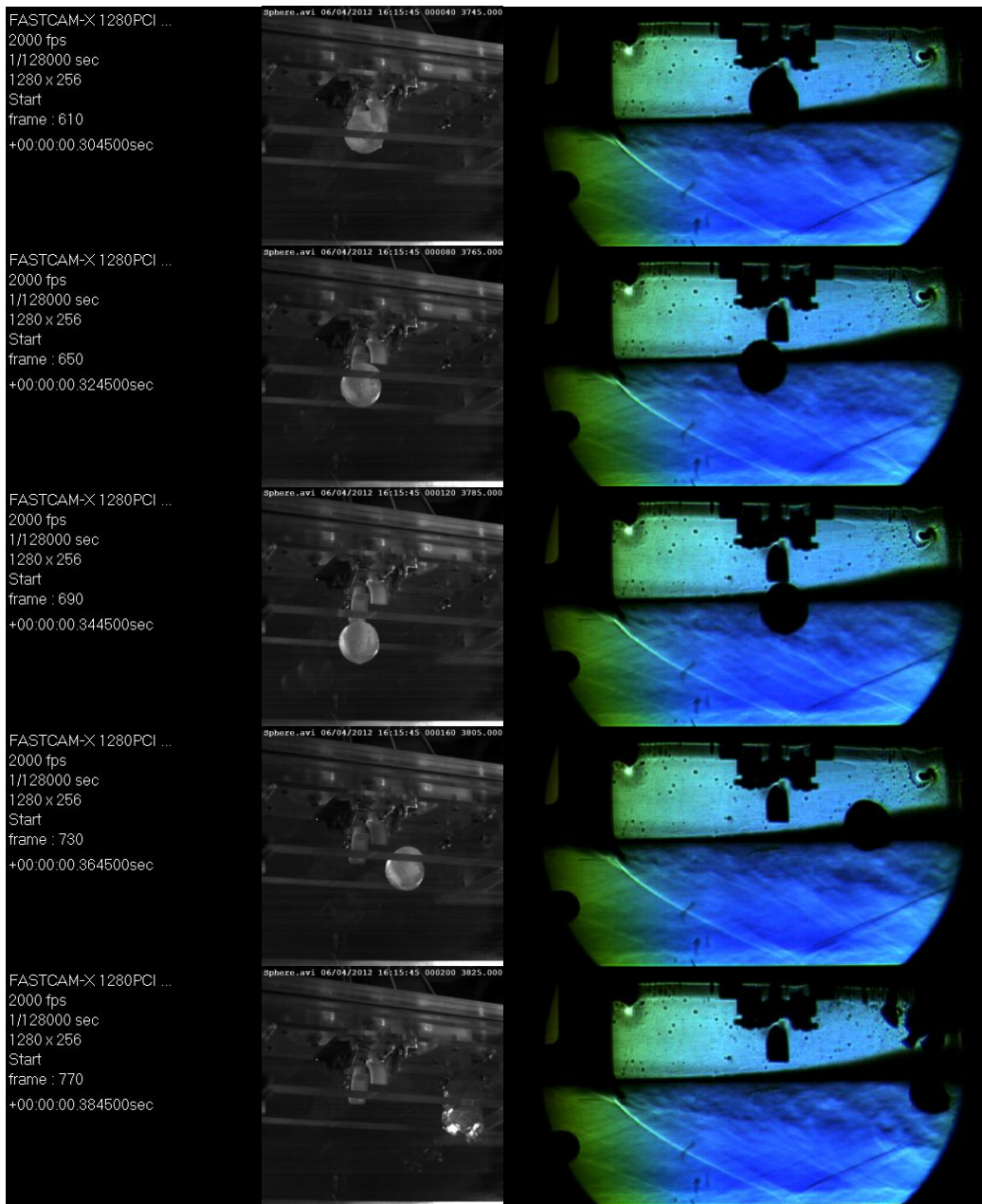


Figure 88. Image sequence of run 604S5. Short sawtooth flow control device used. Frame rate=2kHz, $\Delta t=20\text{ms}$.

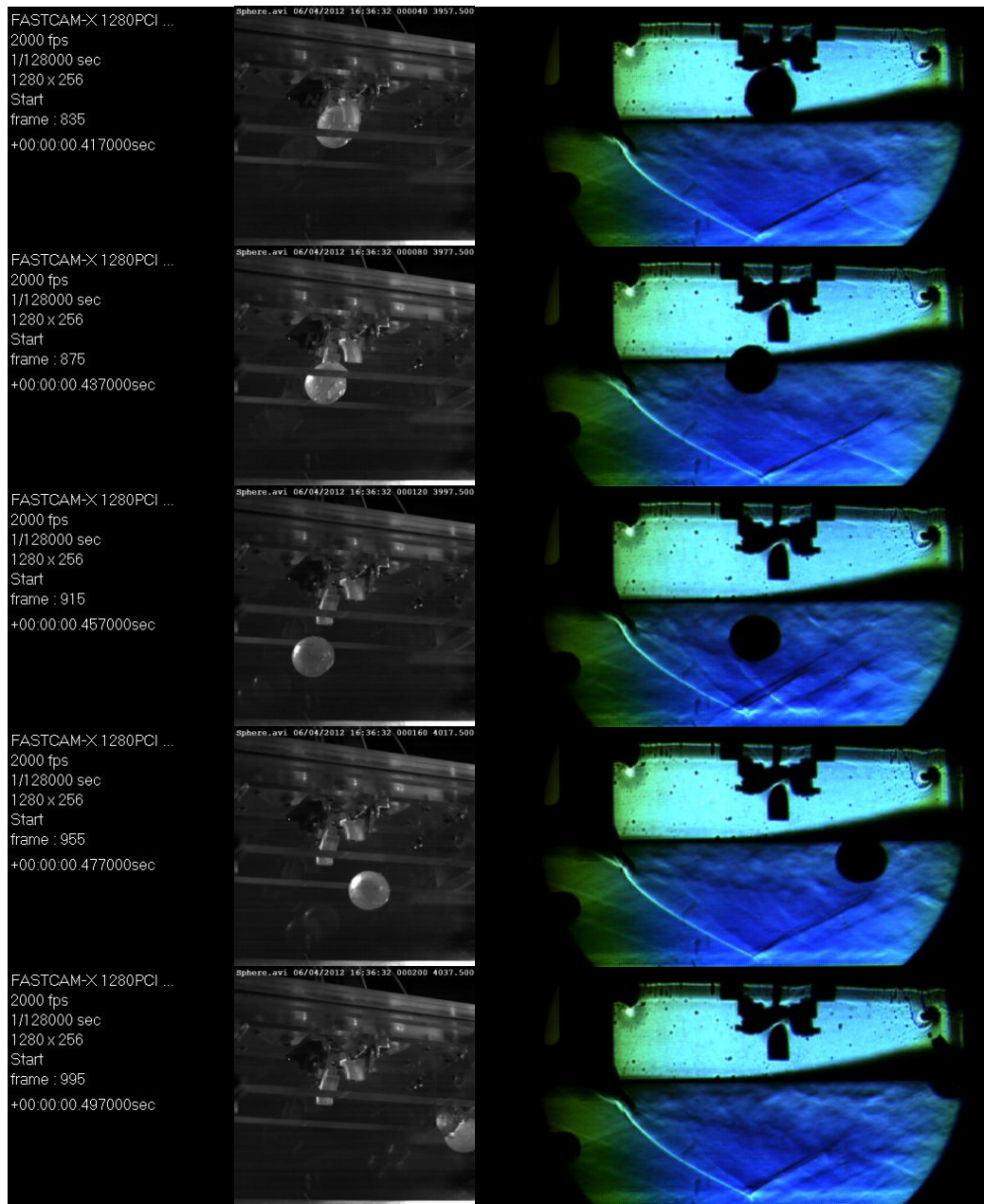


Figure 89. Image sequence of run 604S6. Long sawtooth flow control device used. Frame rate=2kHz, $\Delta t=20\text{ms}$.

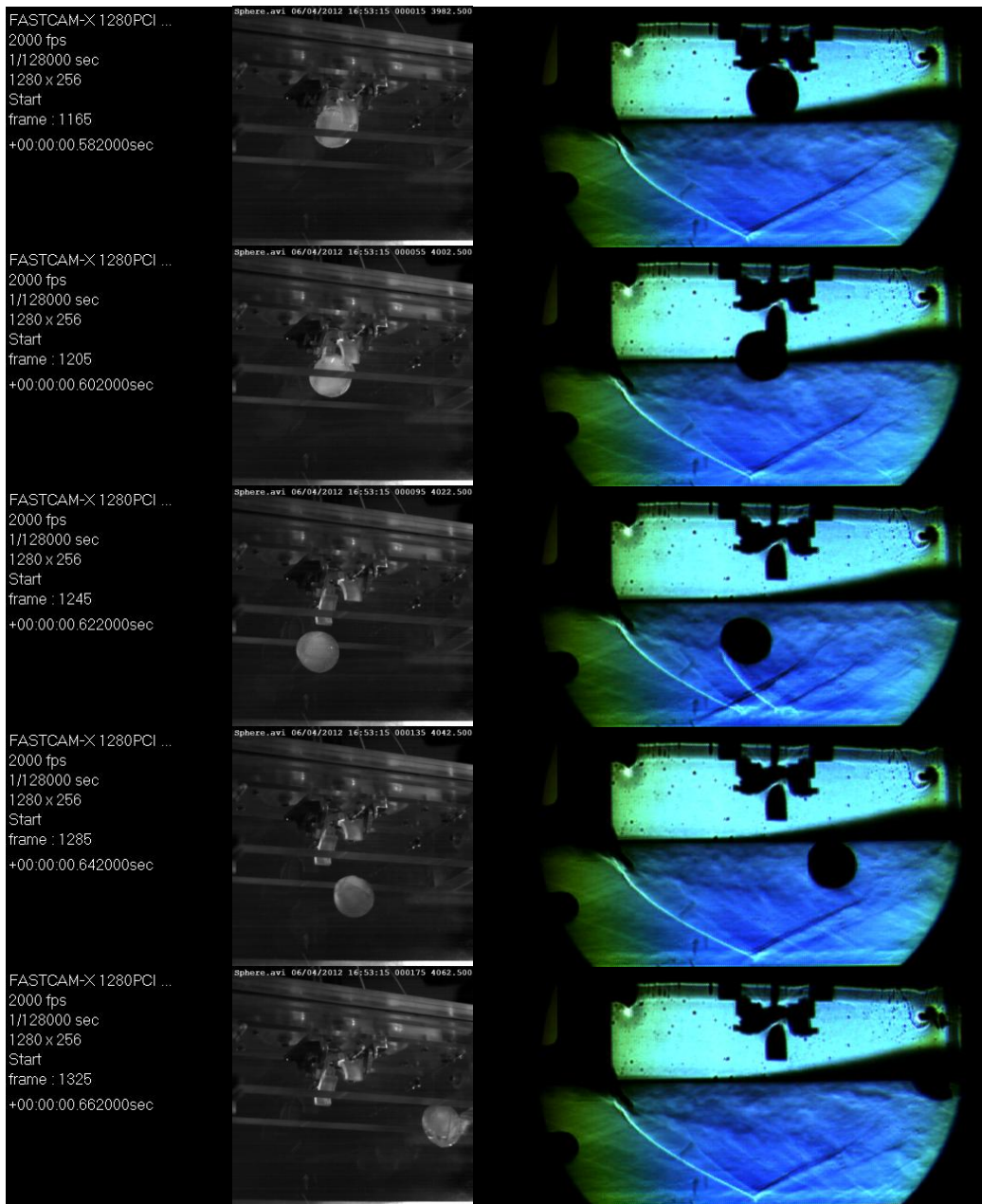


Figure 90. Image sequence of run 604S8. Long sawtooth flow control device used. Frame rate=2kHz, $\Delta t=20\text{ms}$.

Appendix D. $P_{T,sc}=20$ Psia Sphere Run Images

The following figures are the image sequences of the sphere freedrop tests at $P_{T,sc}=20$ Psia. The figures include testing in the clean configuration, with the SST, and with the LST installed.

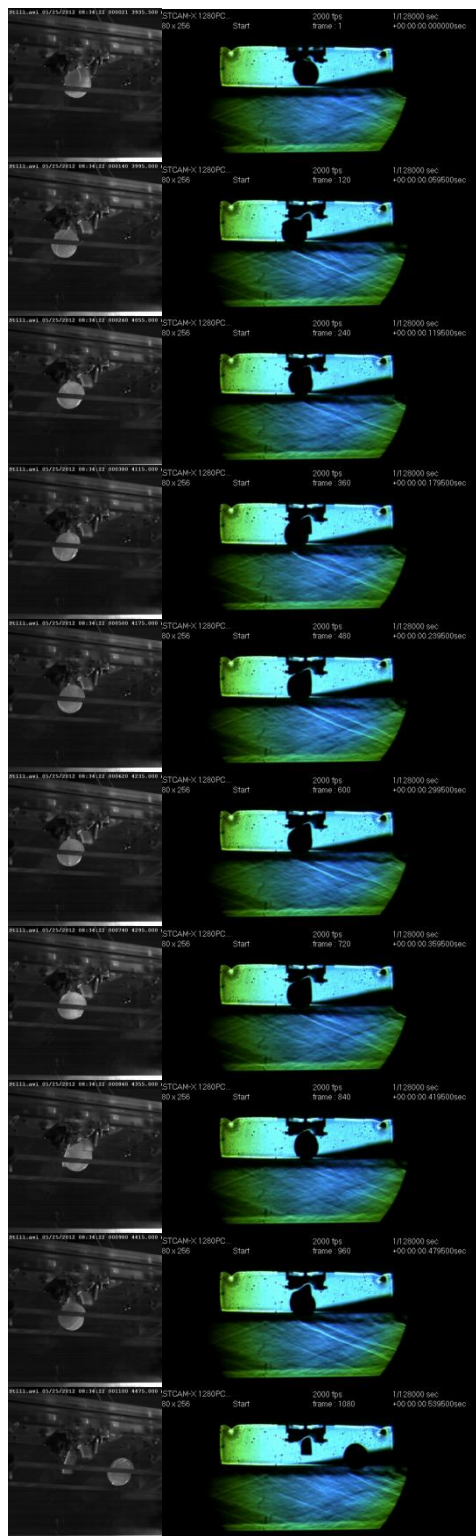


Figure 91. Image sequence of run 525S1. No flow control device used. Frame rate=2kHz, $\Delta t=60$ ms.

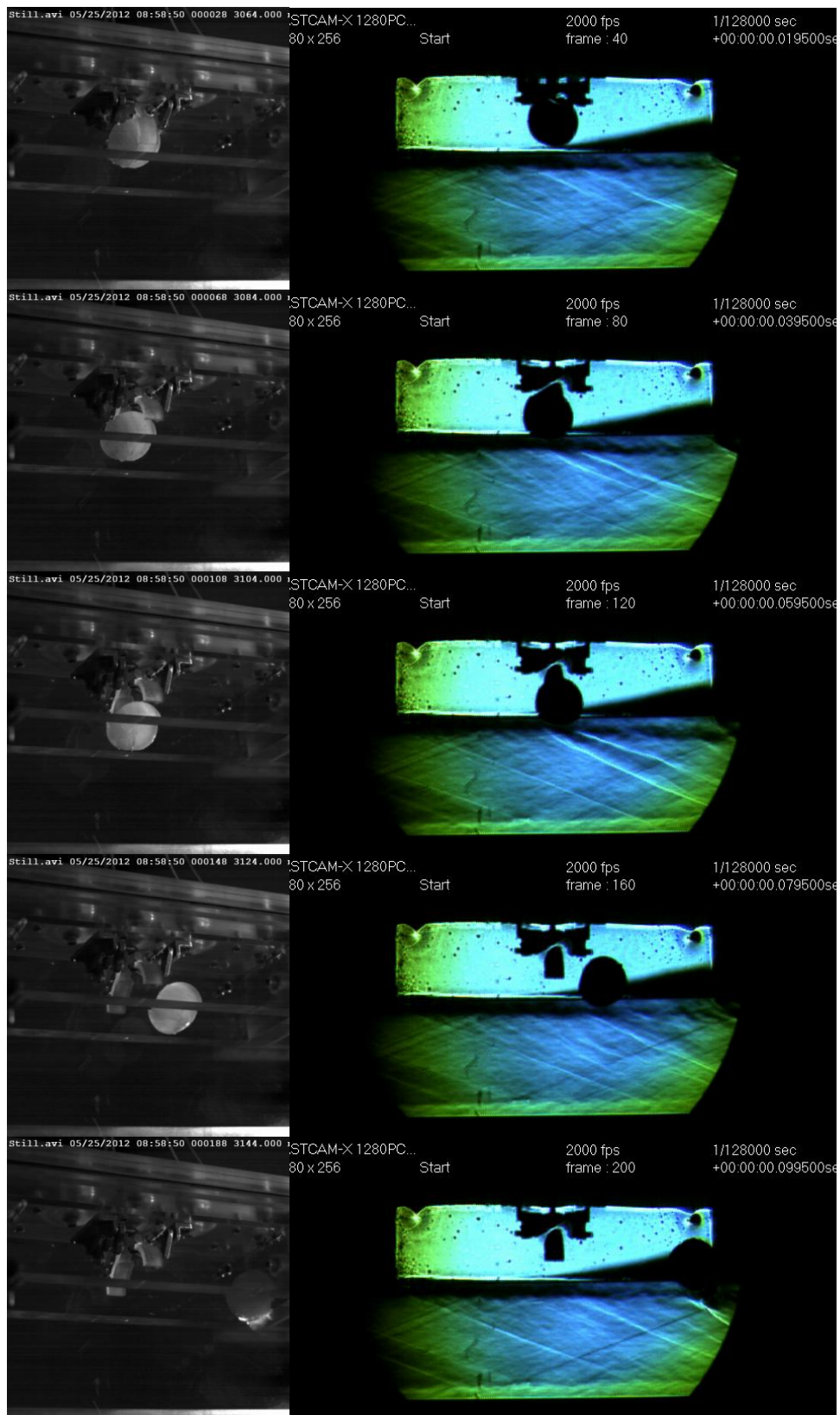


Figure 92. Image sequence of run 525S2. No flow control device used. Frame rate=2kHz, $\Delta t=20$ ms.

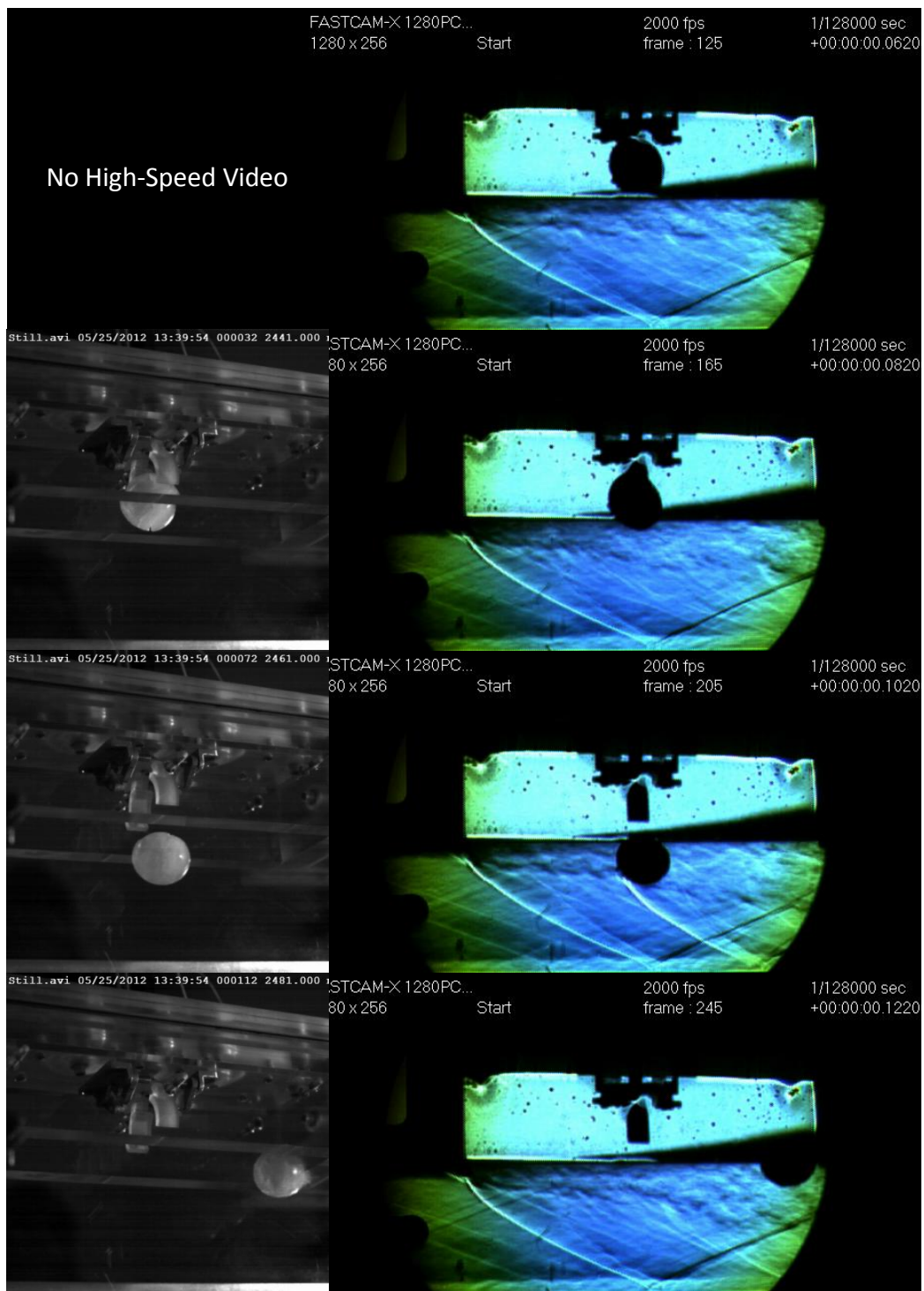


Figure 93. Image sequence of run 525S5. Short sawtooth flow control device used. Frame rate=2kHz, $\Delta t=20\text{ms}$.

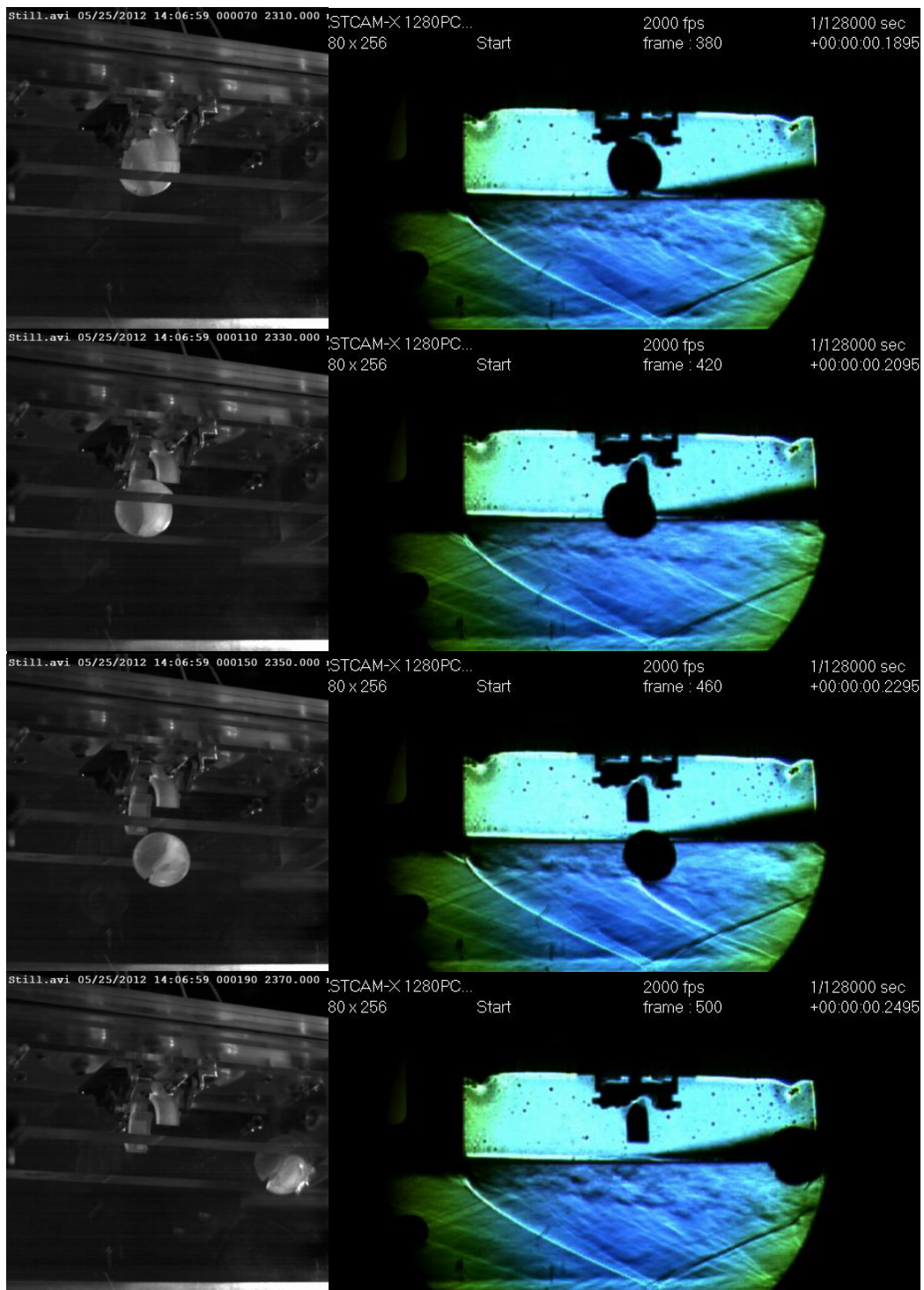


Figure 94. Image sequence of run 525S6. Short sawtooth flow control device used. Frame rate=2kHz, $\Delta t=20\text{ms}$.

Appendix E. Store Run Images

The following figures are the image sequences of the Mk-82 freedrop tests at $P_{T,sc}=4$, 12, and 20 Psia. The figures include testing in the clean configuration, with the SST, and with the LST installed.

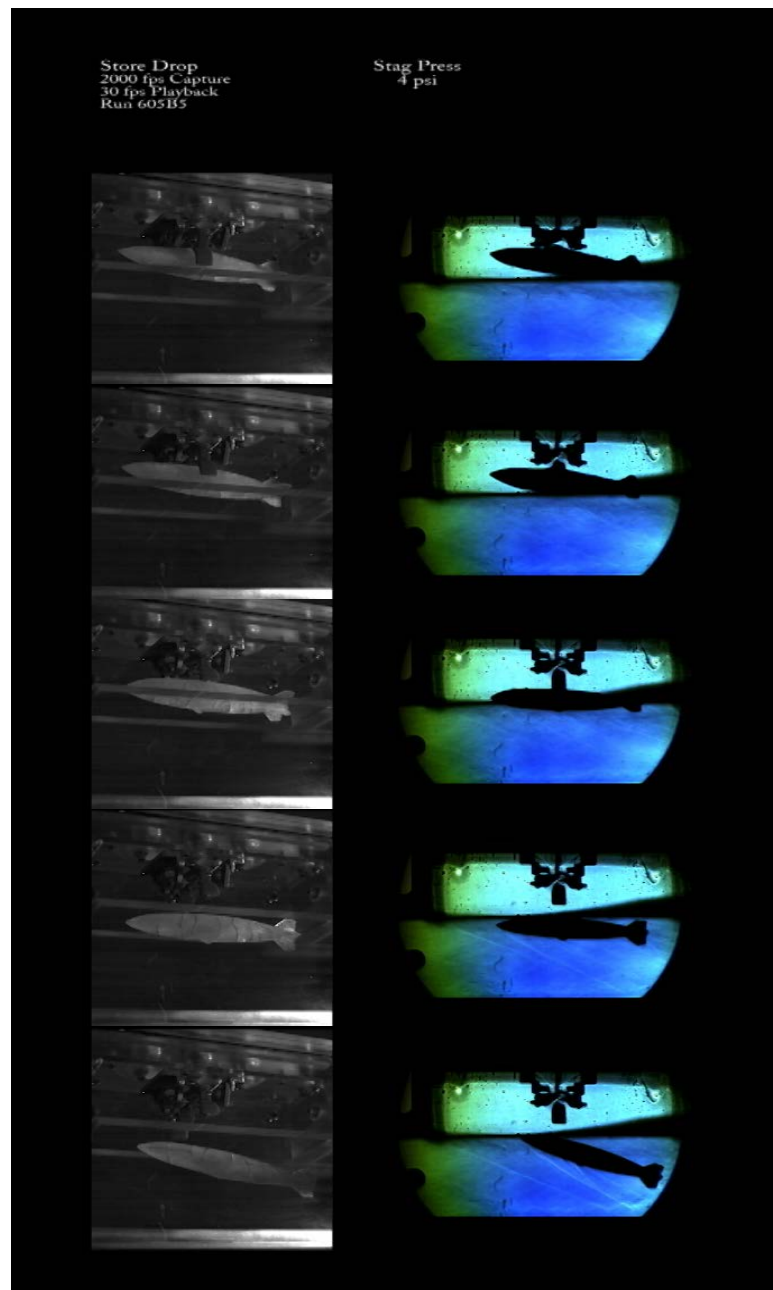


Figure 95. Image sequence of run 605B5. No flow control device used. $P_{T,sc}=4$ Psia. Frame rate=2 kHz, $\Delta t=20$ ms.

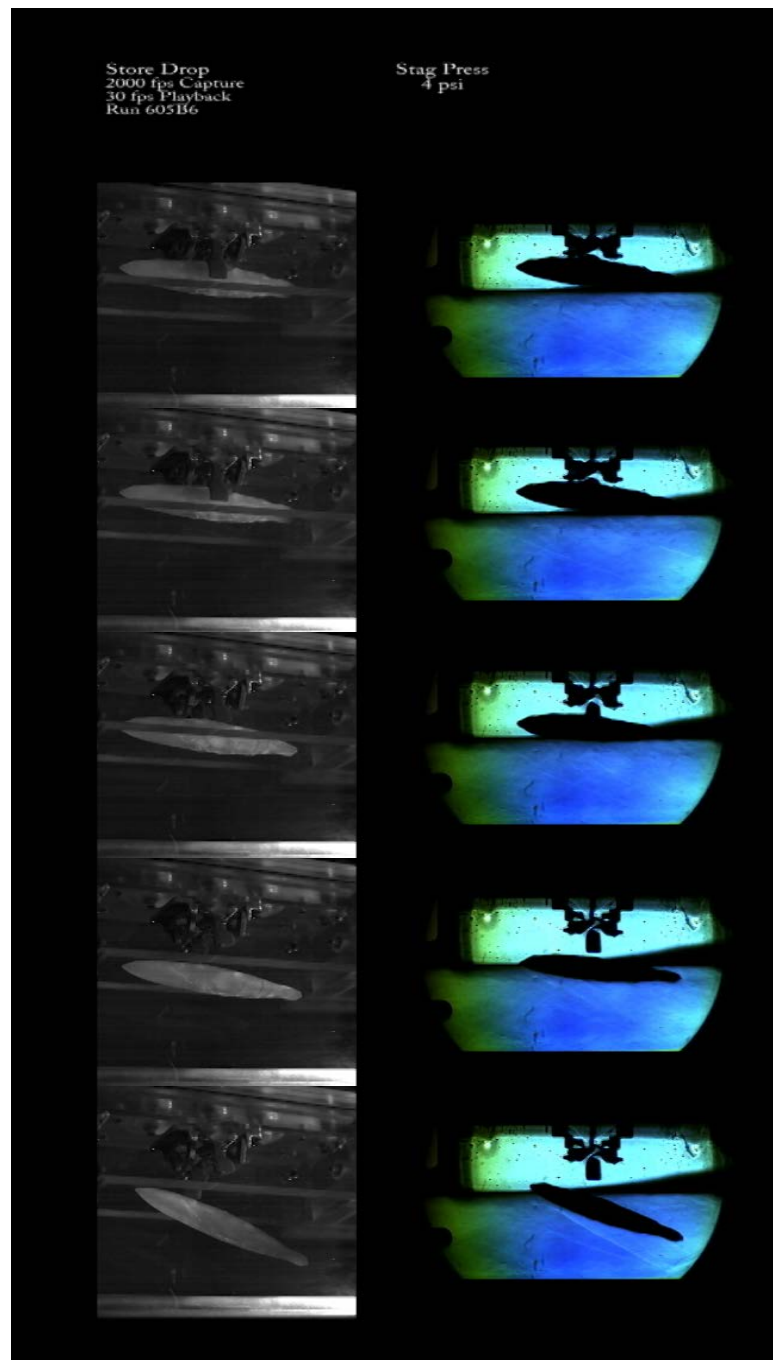


Figure 96. Image sequence of run 605B6. No flow control device used. $P_{T,sc}=4$ Psia. Frame rate=2 kHz, $\Delta t=20$ ms.

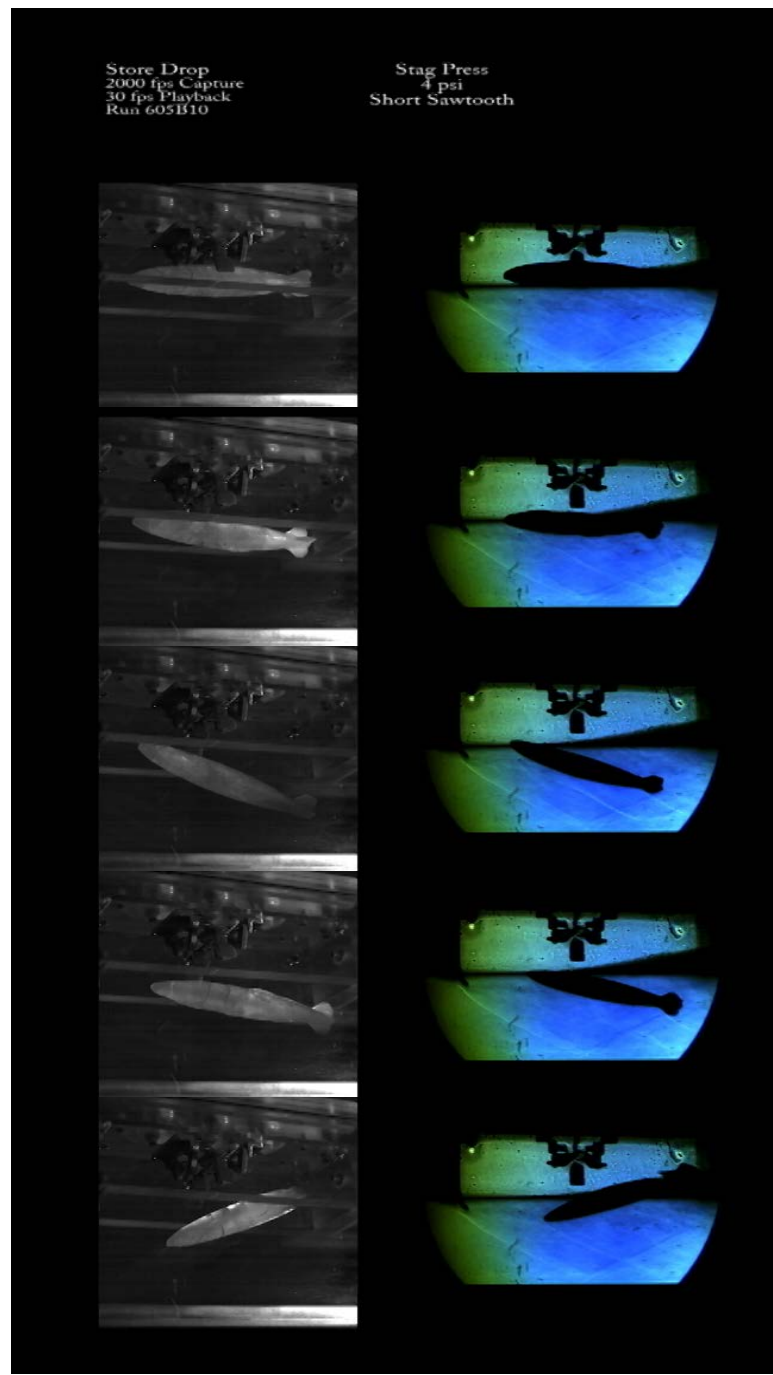


Figure 97. Image sequence of run 605B10. Short sawtooth flow control device used. $P_{T,sc}=4$ Psia. Frame rate=2 kHz, $\Delta t=20$ ms.

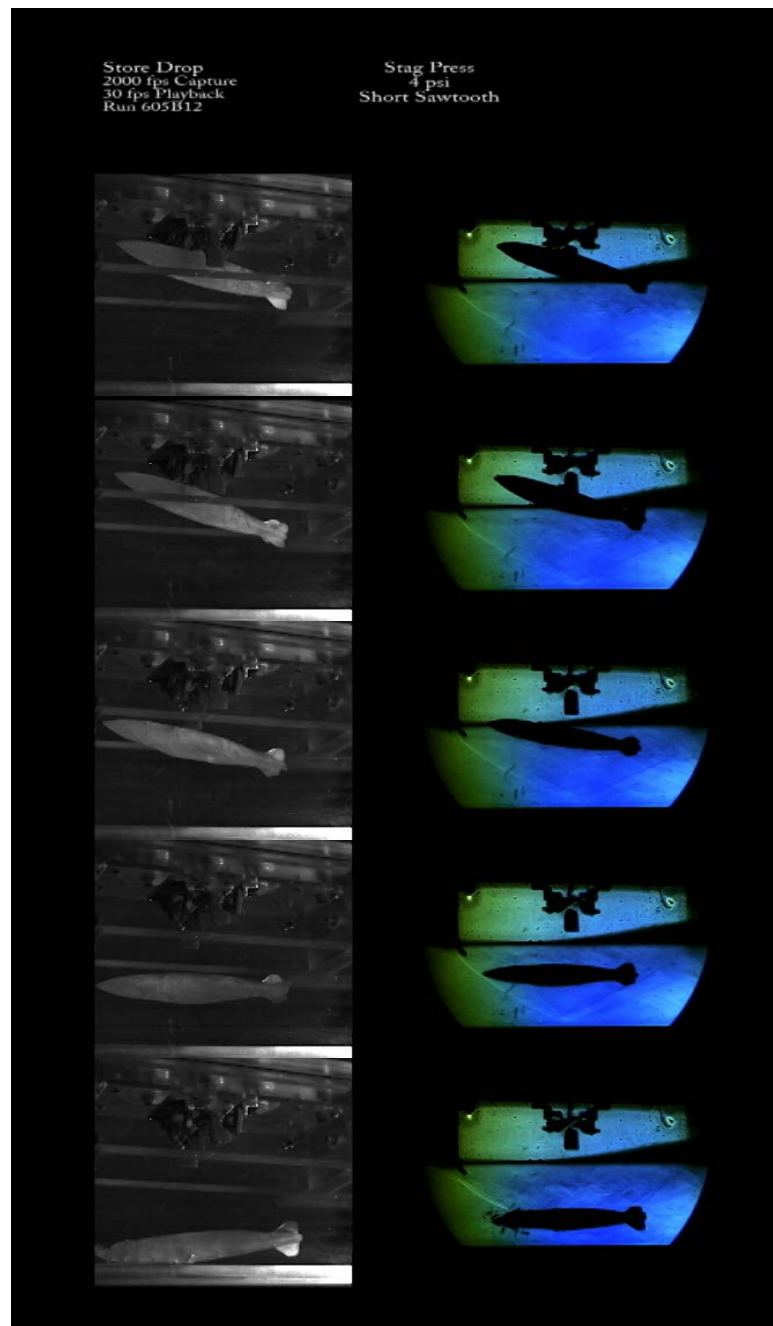


Figure 98. Image sequence of run 605B12. Short sawtooth flow control device used. $P_{T,sc}=4$ Psia. Frame rate=2 kHz, $\Delta t=20$ ms.

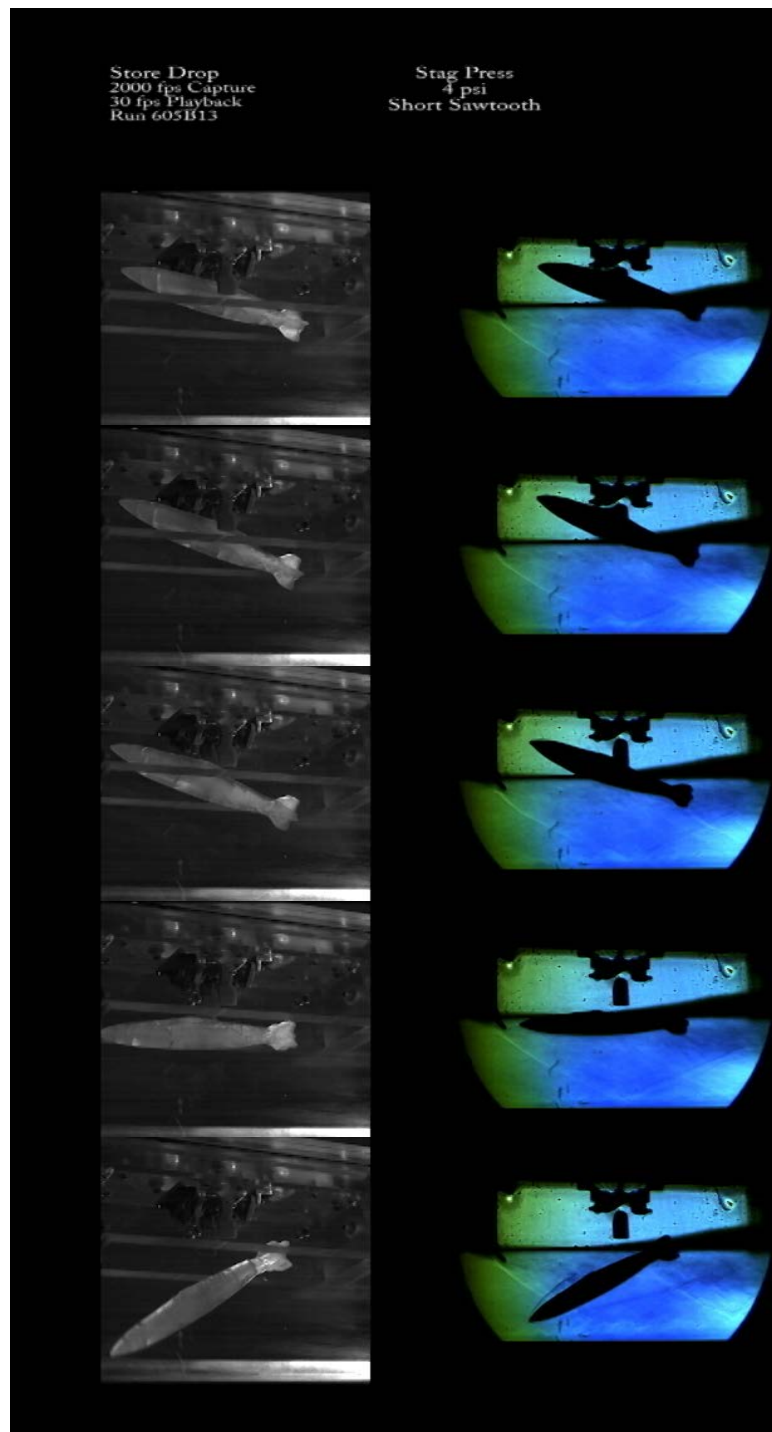


Figure 99. Image sequence of run 605B13. Short sawtooth flow control device used. $P_{T,sc}=4$ Psia. Frame rate=2 kHz, $\Delta t=20$ ms.

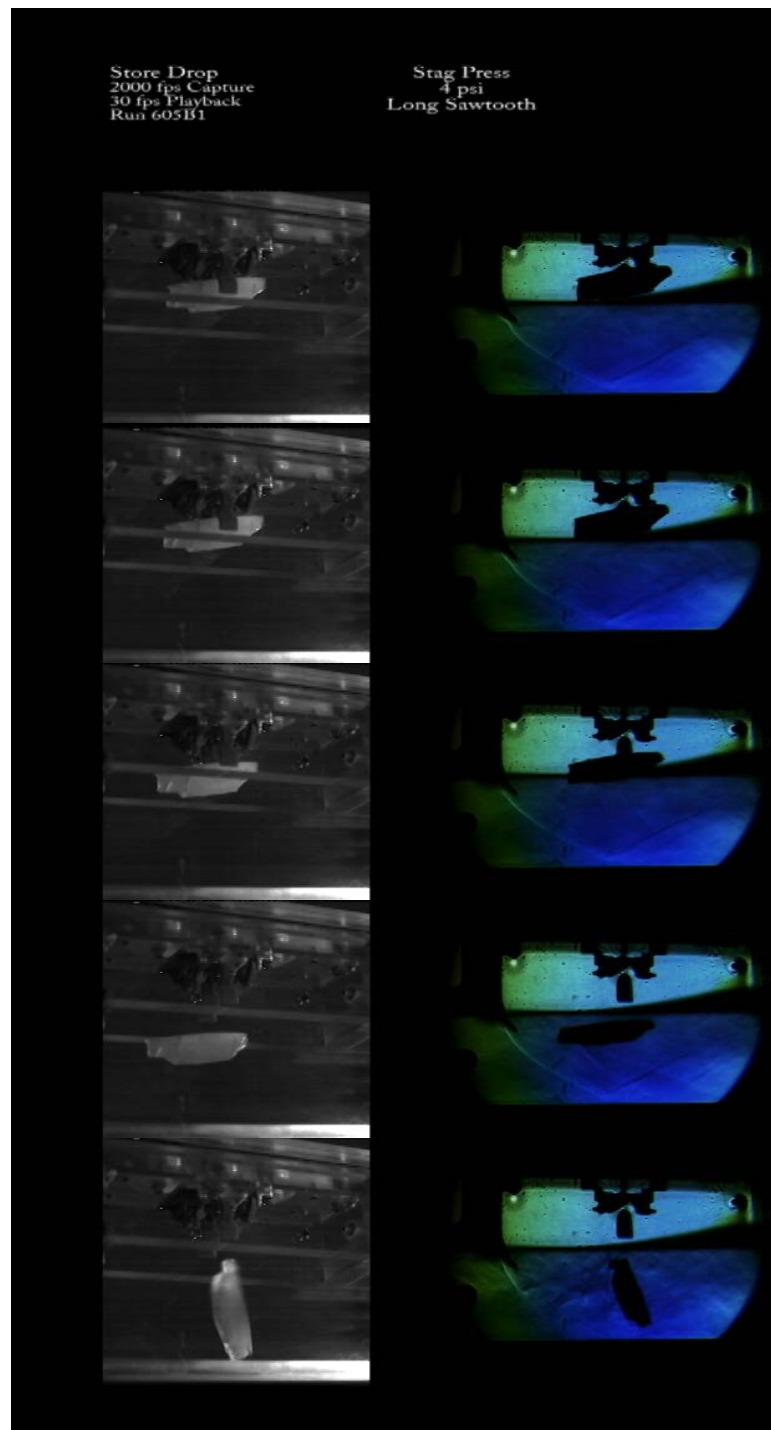


Figure 100. Image sequence of run 605B1. Long sawtooth flow control device used.
 $P_{T,sc}=4$ Psia. Frame rate=2 kHz, $\Delta t=20$ ms.

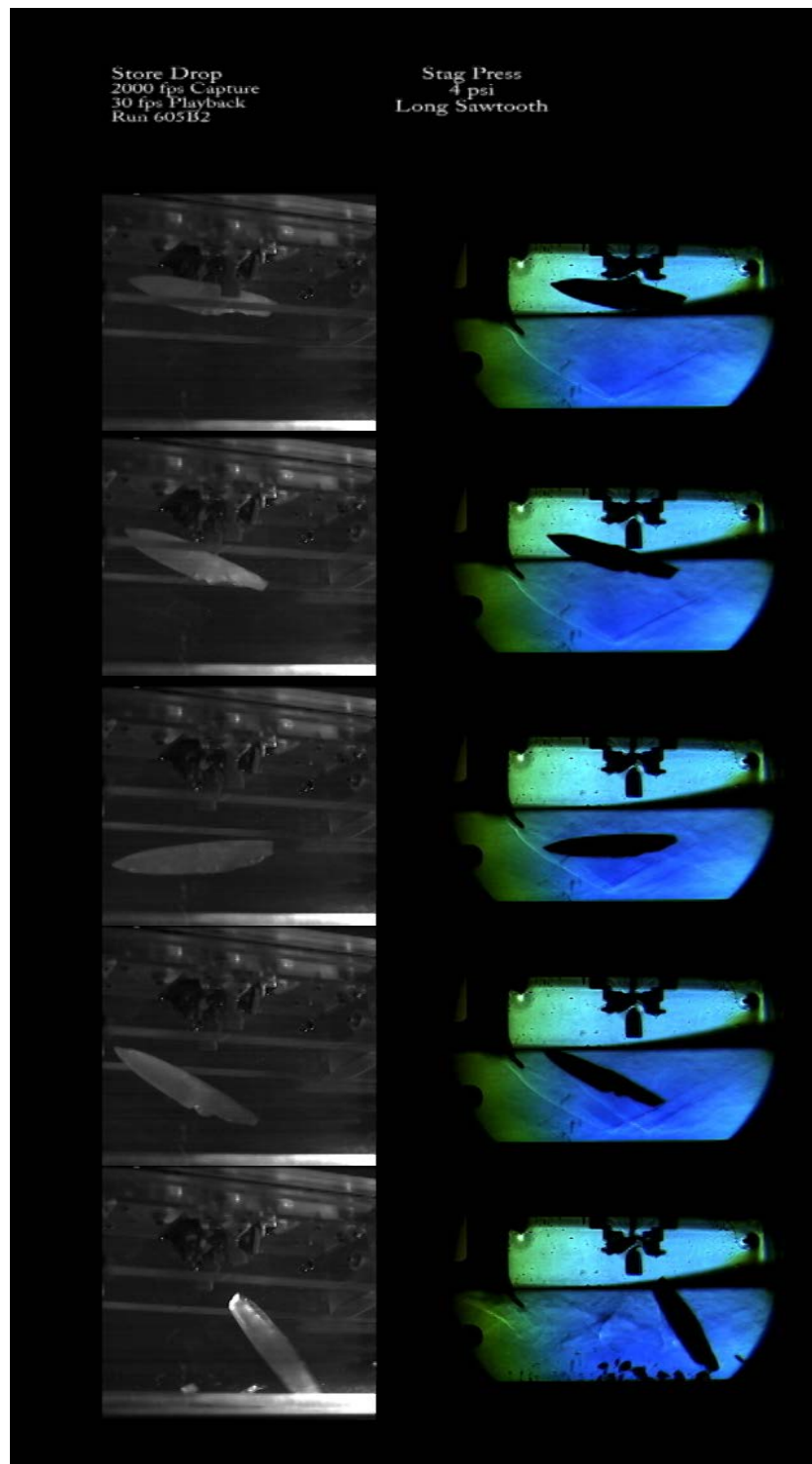


Figure 101. Image sequence of run 605B2. Long sawtooth flow control device used.
 $P_{T,sc}=4$ Psia. Frame rate=2 kHz, $\Delta t=20$ ms.

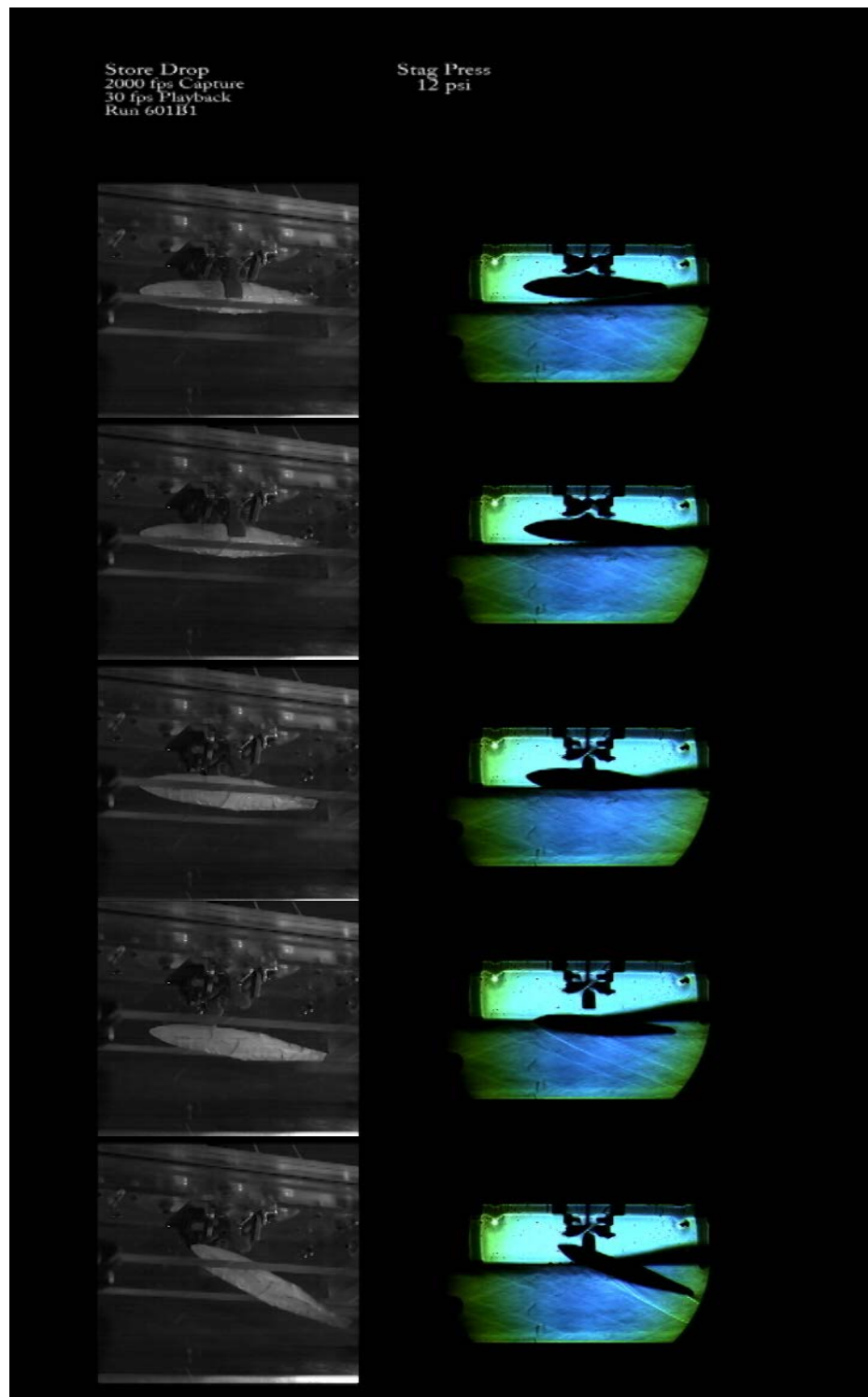


Figure 102. Image sequence of run 601B1. No flow control device used. $P_{T,sc}=12$ Psia. Frame rate=2 kHz, $\Delta t=20$ ms.

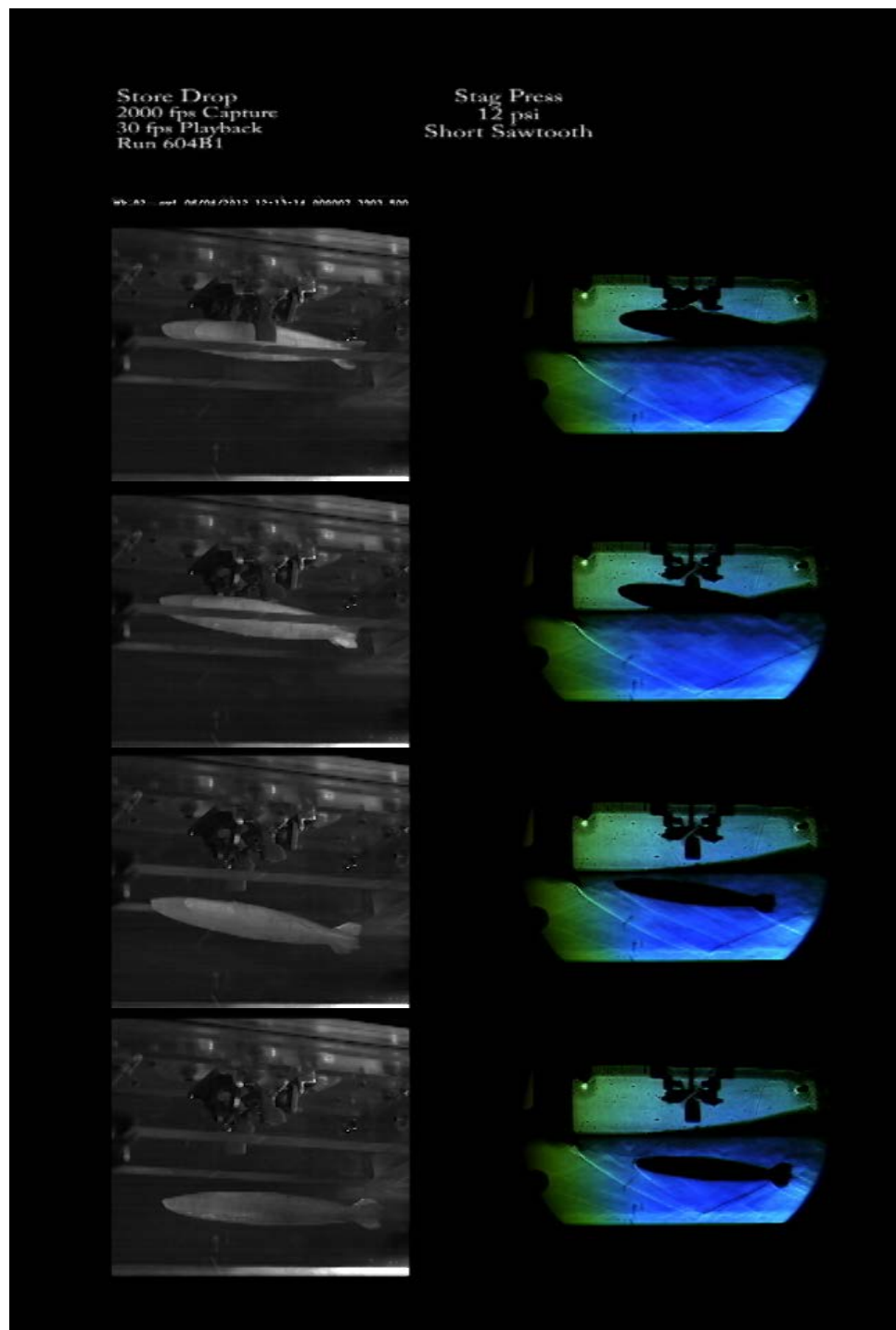


Figure 103. Image sequence of run 604B1. Short sawtooth flow control device used. $P_{T,sc}=12$ Psia. Frame rate=2 kHz, $\Delta t=20$ ms.

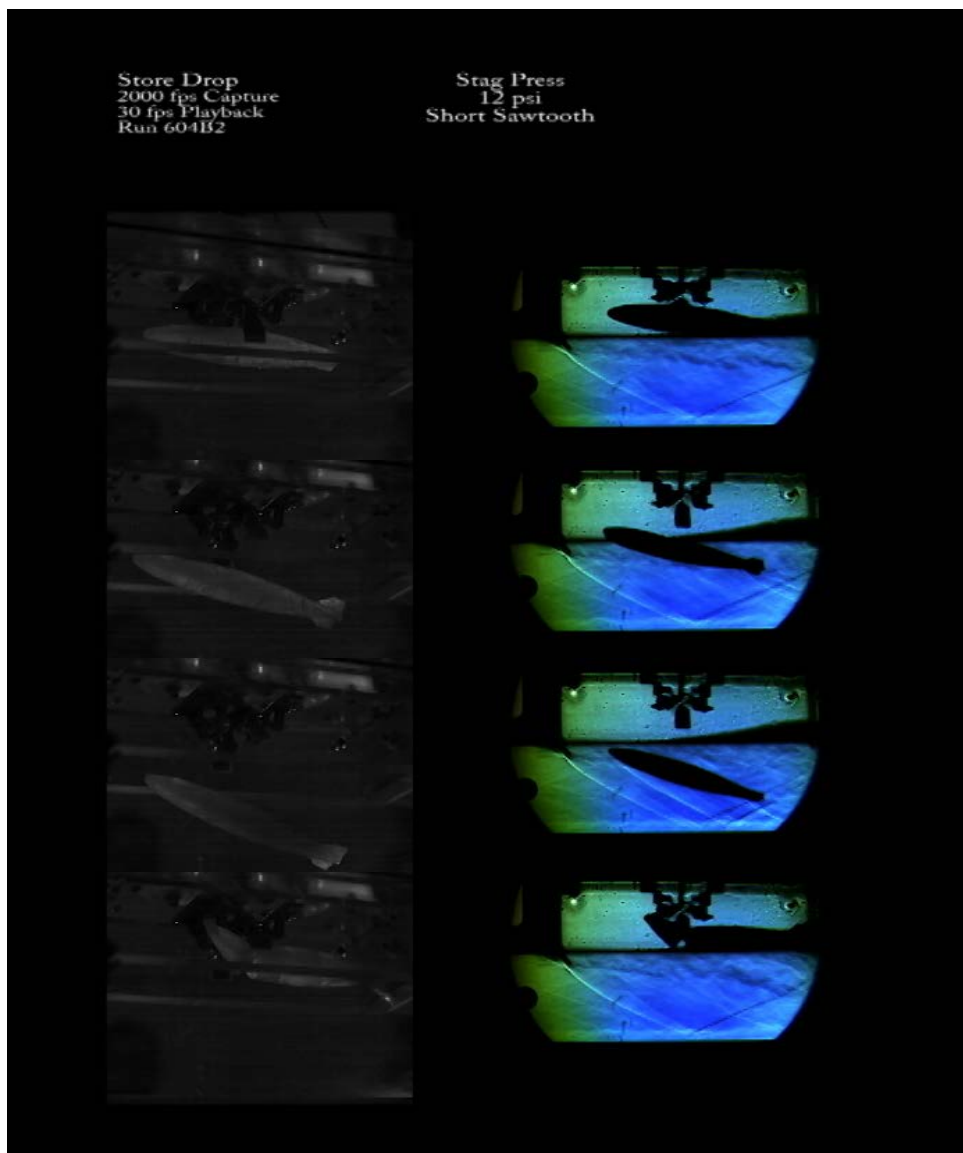


Figure 104. Image sequence of run 604B2. Short sawtooth flow control device used. $P_{T,sc}=12$ Psia. Frame rate=2 kHz, $\Delta t=20$ ms.

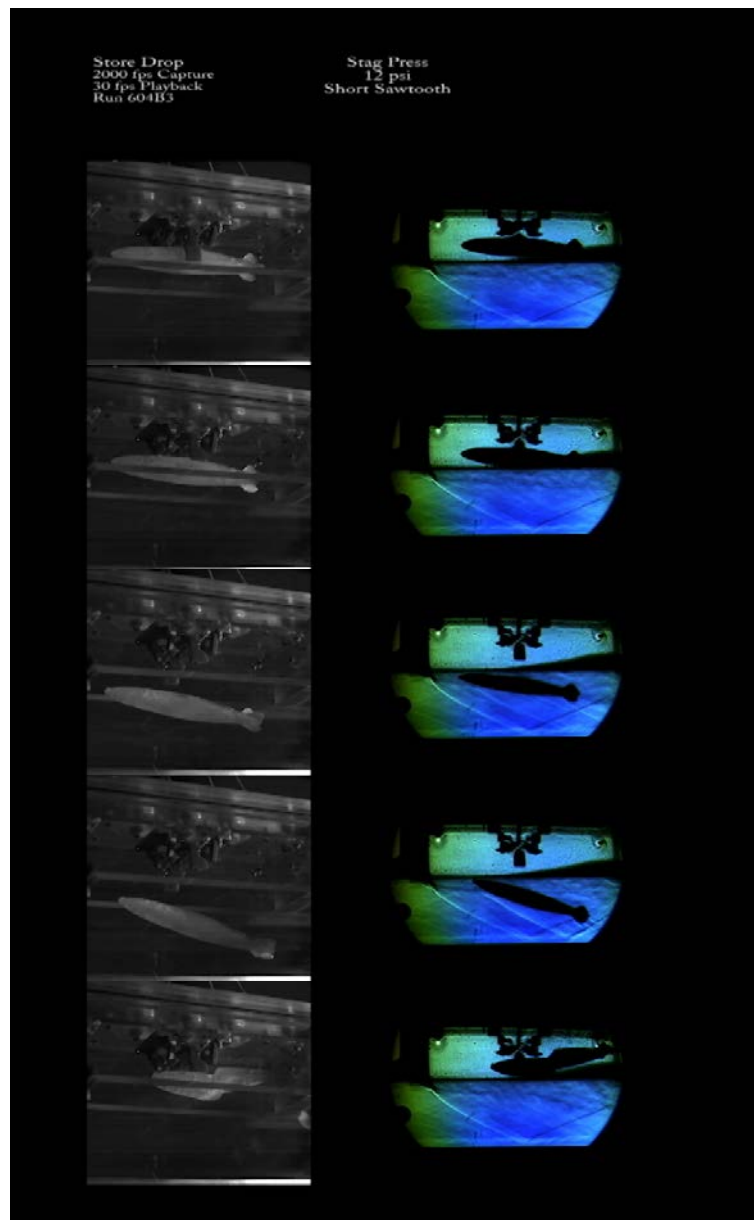


Figure 105. Image sequence of run 604B3. Short sawtooth flow control device used. $P_{T,sc}=12$ Psia. Frame rate=2 kHz, $\Delta t=20$ ms.

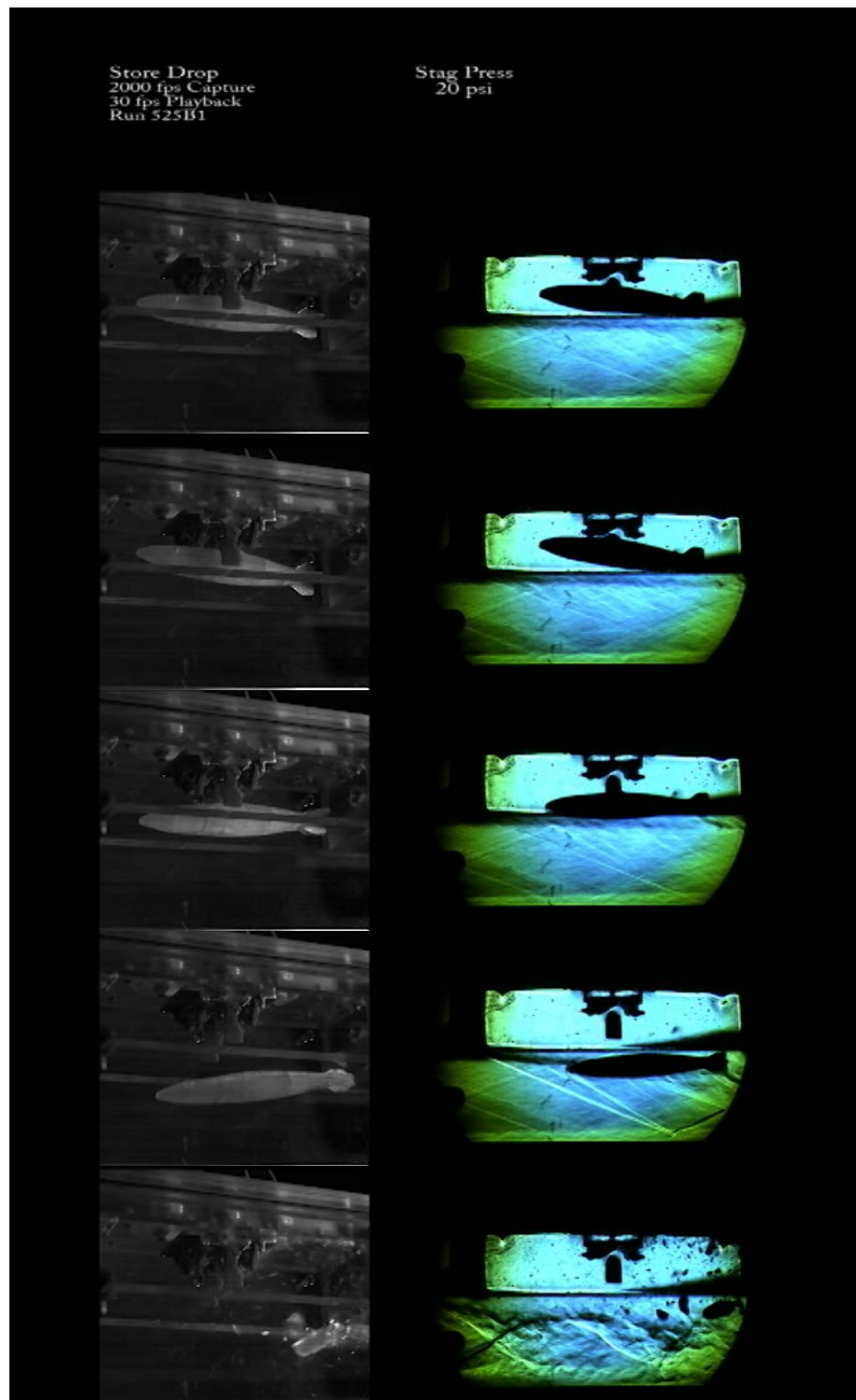


Figure 106. Image sequence of run 525B1. No flow control device used. $P_{T,sc}=20$ Psia. Frame rate=2 kHz, $\Delta t=20$ ms.

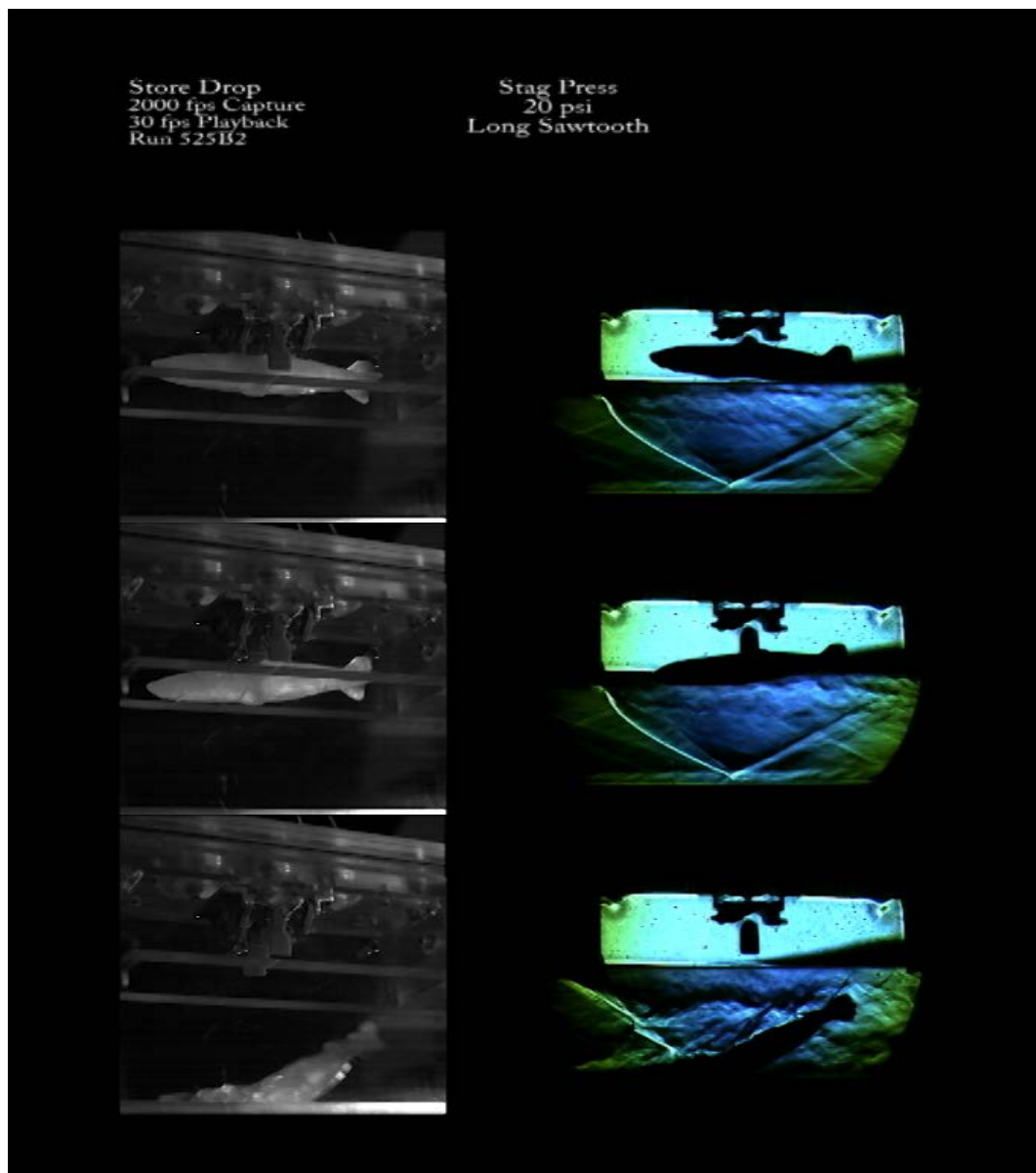


Figure 107. Image sequence of run 525B2. Long sawtooth flow control device used.
 $P_{T,sc}=20$ Psia. Frame rate=2 kHz, $\Delta t=20$ ms.

Appendix F. Transducer Calibration Functions

The following graphically depicts the calibration functions used with the cavity and stagnation pressure transducers.

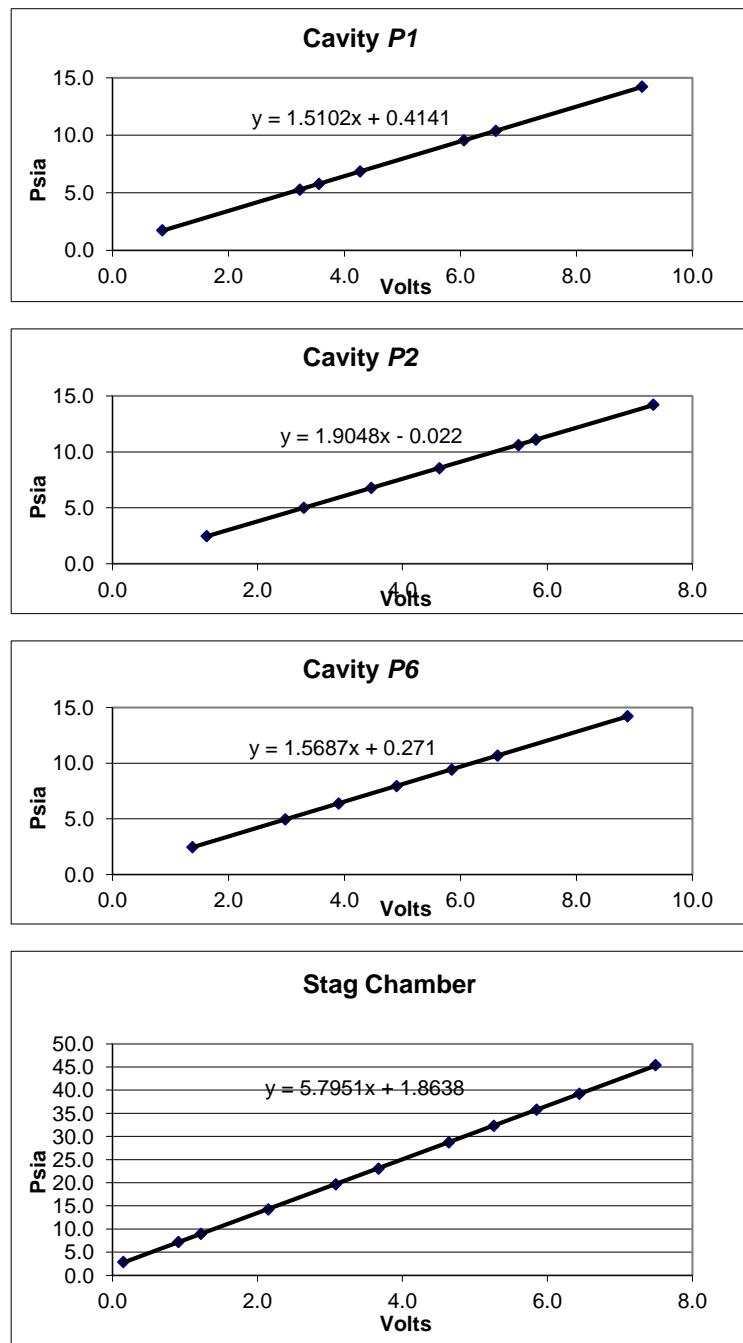


Figure 108. Transducer calibration functions for cavity and stagnation chamber dynamic pressure transducers.

Appendix G. Sample OVERFLOW Inputs (Run CT1B_D)

The following text file provides a sample input file used with OVERFLOW. The input file was used in run CT1B_D, which corresponded with a freedrop test at a total pressure of 4 Psia.

```

$GLOBAL
  NSTEPS = 30000,
  RESTRT= .T.,
  MULTIG = .F., FMG = .T., FMGCYC=150,150,
  FSONWT=2.0, NITNWT=5, DTPHYS=.3247,
  CHIMRA = .T.,
  NQT    = 205,
  NSAVE  = -500,
  ISTART_QAVG = 25000,
$END

$OMIGLB
  I6DOF = 2,
  LFRINGE = 3,
  IRUN = 0,
  DYNMCS = .T.,
$END

$XRINFO
  IDXRAY = 1,
  IGXLIST = 1,2,
  XDELTA = .2
$END

$DCFGLB
  DQUAL = 0.05, MORFAN = 1, NORFAN = 11,
$END

$GBRICK
  OBGRIDS = .F.,
$END

$BRKINP
  NBRICK = 0,
$END

$GROUPS
  WGHTNB = 1., MAXNB = 0, MAXGRD = 0,
$END

$FLOINP
  FSMACH= 3.0, ALPHA = 0.00, REY    = 2.00E4,
  TINF = 190.36,
  XKINF = 1.0E-6, RETINF = 0.1,
$END

$VARGAM      $END

$GRDNAM
  NAME  = 'plate',
$END

$NITERS      $END

$METPRM
  IRHS     = 5,
  ILIMIT   = 3,
  ILHS     = 6,
$END

$TIMACU
  ITIME   = 0,
  DT      = 0.0,

```

```

$END

$SMOACU
  FSO    = 5.0,
$END

$VISINP
  FSOT  = 2.0,
  VISC  = .T.,
  WALLFUN = .T.,
  IDES   = 2,
$END

$BCINP
  IBTYP   =      1,      5,      5,      5,      5,      40,      30,      47,      47,      47,      61,
  IBDIR   =      3,      3,      3,      3,      3,      1,      -1,      2,      -2,      -3,      1,
  JBCS    =      1,     21,     71,     71,    271,      1,      -1,      1,      1,      1,     77,
  JBCE    =     20,     71,    271,    271,      -1,      1,      -1,      -1,      -1,      -1,   265,
  KBCS    =      1,      1,      1,    141,      1,      1,      1,      1,      1,      1,     67,
  KBCE    =     -1,     -1,     61,     -1,     -1,     -1,     -1,      1,      1,     -1,   135,
  LBCS    =      1,      1,      1,      1,      1,      1,      1,      1,      1,      1,     -1,     1,
  LBCE    =      1,      1,      1,      1,      1,     -1,     -1,     -1,     -1,     -1,     -1,    35,
$END

$SCEINP  $END

$SIXINP  $END

$GRDNAM
  NAME  = 'bay',
$END

$NITERS  $END

$METPRM  $END
$TIMACU  $END

$SMOACU  $END

$VISINP  $END

$BCINP
  IBTYP   =      5,      5,      5,      5,      5,  201, 201, 201,
  IBDIR   =      3,      1,     -1,      2,     -2,      1,     -1,      3,
  JBCS    =      1,      1,     -1,      1,      1,      1,     -1,      1,
  JBCE    =     -1,      1,     -1,     -1,     -1,      1,     -1,     -1,
  KBCS    =      1,      1,      1,     -1,     -1,     41,     41,     41,
  KBCE    =     -1,     -1,     -1,     -1,     -1,     41,     41,     41,
  LBCS    =      1,      1,      1,      1,      1,      1,      1,      1,
  LBCE    =      1,     81,     81,     81,     81,     81,     81,     1,
$END

$SCEINP  $END

$SIXINP  $END

$GRDNAM
  NAME  = 'Yen',
$END

$NITERS  $END

$METPRM  $END

```

```

$TIMACU      $END
$SMOACU      $END
$VISINP      $END

$BCINP
  IBTYP      =      5,
  IBDIR      =      3,
  JBCS       =      1,
  JBCE       =     -1,
  KBCS       =      1,
  KBCE       =     -1,
  LBCE       =      1,
  LBCE       =      1,
$END

$SCEINP      $END
$SIXINP      $END

$GRDNAM
  NAME      = 'Yang',
$END

$NITERS      $END
$METPRM      $END
$TIMACU      $END
$SMOACU      $END
$VISINP      $END

$BCINP
  IBTYP      =      5,
  IBDIR      =     -3,
  JBCS       =      1,
  JBCE       =     -1,
  KBCS       =      1,
  KBCE       =     -1,
  LBCE       =     -1,
  LBCE       =     -1,
$END

$SCEINP      $END
$SIXINP      $END

```

Bibliography

- [1] “Doolittle Raid on Japan, 18 April 1942. Raiding Force B-25s on board USS Hornet”. World Wide Web Page, Photo Number NH53421, 2008. URL <http://www.history.navy.mil/photos/events/wwii-pac/misc-42/doolt-a.htm>.
- [2] “The U.S. Navy variant of the F-35 Joint Strike Fighter, the F-35C, conducts a test flight over the Chesapeake Bay”. World Wide Web Page, Photo Number 110211-O-XX000-001.jpg, 2011. URL http://www.navy.mil/view_single.asp?id=97631.
- [3] Bower, W. W., V. Kibens, A. W. Cary, F. S. Alvi, G. Raman, A. Annaswamy, and N. M. Malmuth. “High-Frequency Excitation Active Flow Control for High-Speed Weapon Release (HIFEX)”. *2nd AIAA Flow Control Conference*, AIAA 2004-2513. Portland, Oregon, July 2004.
- [4] Cenko, A. “Lessons Learned in 30 Years of Store Separation Testing”. *47th AIAA Aerospace Sciences Meeting Including The New Horizons Forum and Aerospace Exposition*, AIAA 2009-98. Orlando, Florida, January 2009.
- [5] Cenko, A., R. Deslandes, M. Dillenius, and M. Stanek. “Unsteady Weapon Bay Aerodynamics - Urban Legend or Flight Clearance Nightmare”. *46th AIAA Aerospace Sciences Meeting and Exhibit*, AIAA 2008-189. Reno, Nevada, January 2008.
- [6] Deslandes, R. M. and S. Donauer. “Scaled-Drop-Tests: WYSIWYG or not?” *48th AIAA Aerospace Sciences Meeting Including the New Horizons Forum and Aerospace Exposition*, AIAA 2010-681. Orlando, Florida, January 2010.
- [7] Dix, R. E. and C. Butler. *Cavity Aeroacoustics*. Technical Report AD-A223 853, Air Force Armament Laboratory, Eglin AFB, Florida, 1990.
- [8] Greene, B. G. *Characterization and Control of Carbon Dioxide Seed Particles in Particle Image Velocimetry*. Master’s thesis, Graduate School of Engineering and Management, Air Force Institute of Technology, (AU), Wright Patterson AFB, Ohio, March 2008.
- [9] Harris, F.J. “On the Use of Windows for Harmonic Analysis with the Discrete Fourier Transform”. *Proceedings of the IEEE*, 66(1):51 – 83, January 1978. ISSN 0018-9219.
- [10] Heller, H. H. and D.B. Bliss. “The Physical Mechanism of Flow-Induced Pressure Fluctuation in Cavities and Concepts for their Suppression”. *AIAA 2nd Aero-Acoustics Conference*, AIAA 75-491. Hampton, Virginia, March 1975.

- [11] Heller, H. H., G. Holmes, and E. E. Covert. *Flow-Induced Pressure Oscillations in Shallow Cavities*. Technical Report AD880496, Air Force Flight Dynamics Laboratory, Wright-Patterson Air Force Base, Ohio, 1970.
- [12] Johnson, R. A., M. J. Stanek, and J. E. Grove. “Store Separation Trajectory Deviations Due to Unsteady Weapons Bay Aerodynamics”. *46th AIAA Aerospace Sciences Meeting and Exhibit*, AIAA 2008-188. Reno, Nevada, January 2008.
- [13] Kageyama, A. and T. Sato. “The “Yin-Yang grid”: An Overset Grid in Spherical Geometry”. *Geochem. Geophys. Geosyst*, 5(Q09005), September 2004.
- [14] Keen, K. S., C. H. Morgret, and R. L. Arterbury. *An Analytic Investigation of Accuracy Requirements for Onboard Instrumentation and Film Data for Dynamically Scaled Wind Tunnel Drop Models*. Technical Report AEDC-TR-96-7, Arnold Engineering Development Center, Arnold Air Force Base, Tennessee, 1997.
- [15] Kraft, E. M. “After 40 Years Why Hasn’t the Computer Replaced the Wind Tunnel?” *ITEA Journal*, (31):329–346, September 2010.
- [16] Kraft, N. D. and A. Lofthouse. “Non-Repeatability of Store Separation Trajectories from Internal Weapons Bays due to Unsteady Cavity Flow effects - Lessons Learned from a 2D Investigation”. *49th AIAA Aerospace Sciences Meeting including the New Horizons Forum and Aerospace Exposition*, AIAA 2011-1238. Orlando, Florida, January 2011.
- [17] Krishnamoorthy, L. V., R. Glass, and D.R. Kirk. *Measurement of Drag Characteristics of Mk 82 General Purpose Low Drag Bomb using an Aeroballistic Range Facility*. Technical Report DSTO-TR-0545, Weapons Systems Division Aeronautical and Maritime Research Laboratory, Melbourne, Victoria, Commonwealth of Australia, 1997.
- [18] Lachance, M. “Air Force Basic Research Key to Successful Supersonic Bomb Release”. World Wide Web Page, April 2008. URL <http://www.wpafb.af.mil/news/story.asp?id=123094065>.
- [19] Lawson, S. J. and G. N. Barakos. “Review of Numerical Simulations for High-speed, Turbulent Cavity Flows”. *Progress in Aerospace Sciences*, 47(3):186–216, April 2011.
- [20] Marshall, J. C. “Analytical Evaluation of the Limitations of the Various Scaling Laws for Freedrop Store Separation Testing”. *Fourth JTCA Aircraft/Stores Compatibility Symposium*. Fort Walton Beach, Florida, October 1977.
- [21] Menter, F. R. and C. L. Rumsey. “Assessment of Two-Equation Turbulence Models for Transonic Flows”. *25th AIAA Fluid Dynamics Conference*, AIAA 94-2343. Colorado Springs, Colorado, June 1994.

- [22] Mullin, S. N. “The Evolution of the F-22 Advanced Tactical Fighter”. *1992 Wright Brothers Lecture AIAA Aircraft Design Systems Meeting*, AIAA 92-4188. Hilton Head Island, South Carolina, August 1992.
- [23] Murray, N. E., B. J. Jansen, L. Gui, J. M. Seiner, and R. Birkbeck. “Measurements of Store Separation Dynamics”. *47th AIAA Aerospace Sciences Meeting Including The New Horizons Forum and Aerospace Exposition*, AIAA 2009-105. Orlando, Florida, January 2009.
- [24] Murray, R. C. and G. S. Elliott. “Characteristics of the Compressible Shear Layer over a Cavity”. *AIAA Journal*, 39(5):846–856, May 2001.
- [25] Nichols, R. H. “A Comparison of Hybrid RANS/LES Turbulence Models for a Generic Weapons Bay With and Without a Spoiler”. *26th AIAA Applied Aerodynamics Conference*, AIAA 2008-6229. Honolulu, Hawaii, August 2008.
- [26] Nichols, R. H. and P. G. Buning. *User’s Manual for OVERFLOW 2.1*, August 2008.
- [27] Pulliam, T. H. “High Order Accurate Finite-Difference Methods as seen in OVERFLOW”. *20th AIAA Computational Fluid Dynamics Conference*, AIAA 2011-3851. Honolulu, Hawaii, June 2011.
- [28] R. L. Stallings, Jr. and Jr. F. J. Wilcox. *Experimental Cavity Pressure Distributions at Supersonic Speeds*. Technical Report 2683, NASA Langley Research Center, Hampton, Virginia, 1987.
- [29] Spalart, P. R., S. Deck, M. L. Shur, K. D. Squires, M. Kh. Strelets, and A. Travin. “A new version of detached-eddy simulation, resistant to ambiguous grid densities”. *Theoretical and Computational Fluid Dynamics*, 20:181–195, May 2006.
- [30] Stanek, M. J., G. Raman, V. Kibens, J. A. Ross, J. Odedra, and J. W. Peto. “Control of Cavity Resonance Through Very High Frequency Forcing”. *6th AIAA/CEAS Aeroacoustics Conference and Exhibit*, AIAA 2000-1905. Lahaina, Hawaii, June 2000.
- [31] Welch, P. D. “The Use of Fast Fourier Transform for the Estimation of Power Spectra: A Method Based on Time Averaging Over Short, Modified Periodograms”. *IEEE Transactions on Audio and Electroacoustics*, 15(2):70 – 73, June 1967.

Vita

Lieutenant Commander Thomas J. “T.J.” Flora grew up outside of Newton, Kansas, graduating from Berean Academy Christian High School in 1996. He earned his Bachelors of Science degree in Mechanical Engineering from the University of Kansas and was commissioned into the United States Navy via the ROTC program.

LCDR Flora began naval aviation training at NAS Pensacola and subsequently earned his *wings of gold* in 2003. After completing training in the F-14 Tomcat in VF-101, he was assigned to the Fighting Swordsmen of VF-32. LCDR Flora completed a combat cruise in support of Operation Iraqi Freedom in 2005. Upon returning from deployment, LCDR Flora transitioned with his squadron to the F/A-18F, completing the pre-deployment training cycle prior to the first Super Hornet combat cruise of VFA-32.

LCDR Flora received orders to represent the US Navy as an exchange pilot with the Swiss Air Force, but was medically disqualified prior to execution of those orders. After serving in temporary assignments awaiting medical resolution, he was assigned as a flight instructor with VFA-106, where he served in the safety department.

LCDR Flora was accepted to the Aerospace Engineering Duty Officer program, which began with his enrollment in the AFIT Graduate School of Engineering and Management in August 2010. Upon receiving his Masters of Science degree, LCDR Flora will be assigned to PMA-205, the NAVAIR Training Systems Program Office, as the F/A-18 Training Systems IPT Co-Lead.

REPORT DOCUMENTATION PAGE

Form Approved
OMB No. 0704-0188

The public reporting burden for this collection of information is estimated to average 1 hour per response, including the time for reviewing instructions, searching existing data sources, gathering and maintaining the data needed, and completing and reviewing the collection of information. Send comments regarding this burden estimate or any other aspect of this collection of information, including suggestions for reducing this burden to Department of Defense, Washington Headquarters Services, Directorate for Information Operations and Reports (0704-0188), 1215 Jefferson Davis Highway, Suite 1204, Arlington, VA 22202-4302. Respondents should be aware that notwithstanding any other provision of law, no person shall be subject to any penalty for failing to comply with a collection of information if it does not display a currently valid OMB control number. PLEASE DO NOT RETURN YOUR FORM TO THE ABOVE ADDRESS.

1. REPORT DATE (DD-MM-YYYY)	2. REPORT TYPE	3. DATES COVERED (From — To)	
26-08-2012	Master's Thesis	20 Aug 2010 - 26 Aug 2012	
4. TITLE AND SUBTITLE		5a. CONTRACT NUMBER	
Freedrop Testing and CFD Simulation of Ice Models from a Cavity into Supersonic Flow		5b. GRANT NUMBER	
		5c. PROGRAM ELEMENT NUMBER	
		5d. PROJECT NUMBER	
		5e. TASK NUMBER	
		5f. WORK UNIT NUMBER	
6. AUTHOR(S)		7. PERFORMING ORGANIZATION NAME(S) AND ADDRESS(ES)	8. PERFORMING ORGANIZATION REPORT NUMBER
Thomas J. Flora, LCDR, USN		Air Force Institute of Technology Graduate School of Engineering and Management (AFIT/EN) 2950 Hobson Way WPAFB OH 45433-7765	AFIT/GAE/ENY/12-S15
9. SPONSORING / MONITORING AGENCY NAME(S) AND ADDRESS(ES)		10. SPONSOR/MONITOR'S ACRONYM(S)	
AFRL/RBAI 2145 5th St Wright Patterson AFB, OH 45433 POC: Mr. Rudy Johnson (937) 255-3037, rudy.johnson@wpafb.af.mil		AFRL/RBAI	
		11. SPONSOR/MONITOR'S REPORT NUMBER(S)	
12. DISTRIBUTION / AVAILABILITY STATEMENT			
APPROVED FOR PUBLIC RELEASE; DISTRIBUTION UNLIMITED.			
13. SUPPLEMENTARY NOTES			
This material is declared a work of the U.S. Government and is not subject to copyright protection in the United States.			
14. ABSTRACT			
Weapon release at supersonic speeds from an internal bay is highly advantageous. For this reason, both experimental and numerical methods were used to investigate store separation from a cavity ($L/D=4.5$) into Mach 2.94 flow. The experiment used a piezoresistive pressure transducer, Schlieren and high-speed photography for data acquisition. The computational solution used the OVERFLOW solver. A sphere and a Mk-82, scaled to 1:20, were formed using frozen tap water. The sphere model was freedrop tested experimentally and computationally, while the sub-scale store shaped model was freedrop tested experimentally. The total pressure was varied to alter the dynamic response of the model. Computed spectra of pressure signals were in reasonable agreement with those measured experimentally, while the trajectory and dynamics of the CFD sphere release closely matched the experiment. Two sawtooth spoiler devices were tested for effectiveness at high Mach numbers. Pressure measurements showed a detuning of the Rossiter tones but with an increase in the broadband levels. Furthermore, spoiler testing demonstrated the capability to enhance store separation. Mk-82 shapes were also tested, which proved that the experimental process can be used with representations of actual stores. Reducing the test pressure conditions to sub-atmospheric levels allowed sub-scale models to be accurately scaled in mass and moment of inertia using heavy Mach scaling laws.			
15. SUBJECT TERMS			
Store Separation, Cavity Flow, Freedrop Testing, CFD, Rossiter Modes, Frequency Analysis, Dynamic Scaling			
16. SECURITY CLASSIFICATION OF:		17. LIMITATION OF ABSTRACT	18. NUMBER OF PAGES
a. REPORT	b. ABSTRACT	c. THIS PAGE	U
U	U	U	U
			230
		19a. NAME OF RESPONSIBLE PERSON	Dr. Mark F. Reeder
		19b. TELEPHONE NUMBER (include area code)	(937) 255-3636 x4530; mark.reeder@afit.edu